ISSN 1313 - 0927

# Aerospace Research in Bulgaria

## 34

Bulgarian Academy of Sciences
Space Research and Technology Institute

2022



bl.1, *Acad. G. Bonchev* St.,
1113 Sofia, Bulgaria
tel./fax: (+359 2) 988 35 03,
http://www.space.bas.bg

# AEROSPACE RESEARCH IN BULGARIA

**Founded in 1978**

Volume 34, Sofia, 2022
Space Research and Technology Institute
Bulgarian Academy of Sciences





## Address

AEROSPACE RESEARCH IN BULGARIA
Space Research and Technology Institute
*Acad. Georgi Bonchev* St., block 1, 1113 Sofia, Bulgaria

web-site: http://journal.space.bas.bg
e-mail: journal@space.bas.bg

*Pre-Publication Processing*
Tsveta Srebrova





p-ISSN 1313 – 0927 e-ISSN 2367 – 9522

**This issue of *Aerospace Research in Bulgaria* is published with financial support from the Bulgarian National Science Fund – Contract No КП-06-НП3/60 - 22.11.2021**

*Bulgarian Academy of Sciences* **ISSN 1313 – 0927**

# Aerospace Research in Bulgaria

## 34

## Sofia, 2022

## C o n t e n t s

# С Ъ Д Ъ Р Ж А Н И Е

Bulgarian Academy of Sciences. Space Research and Technology Institute.
Aerospace Research in Bulgaria. 34, 2022, Sofia

DOI: https://doi.org/10.3897/arb.v34.e01

# DEPENDENCE OF THE GLEISBERG CYCLE PERIOD ON THE LENGTH OF WOLF'S NUMBERS SERIES

***Igor Shibaev[1], Aleksandr Shibaev[2]***

*[1]Pushkov Institute of Terrestrial Magnetism, Ionosphere and Radio Wave Propagation*
*Russian Academy of Sciences, Moscow, Russia.*
*[2]Lomonosov Moscow State University, Moscow, Russia*
*e-mail: ishib@izmiran.ru*

***Keywords:*** *"Gleisberg cycle", Wolf numbers, Solar activity, Dalton minimum*

***Abstract***

*The concept of "Gleisberg cycle" arose from the analysis of a small amount of data for a series of Wolf numbers (WSN), which are characterized by varying degrees of reliability and with the key role of cycles 5–7 of the Dalton minimum. Back in the thirties of the last century, when analyzing the first 16 cycles was done, Gleisberg noted the frequency of their maximums in seven to eight cycles, and later gave an updated value of the period — about 80 years. In the works done over the past 60 years, this period is evaluated within 80–110 years. A number of researchers allocate a specific value for the Gleisberg cycle period equals to 88 years. Since different authors analyzed a series of Wolf numbers of different lengths, it makes sense to investigate the influence of the length of the series itself on this period.*

*The paper analyzes the long-period components of WSN versions v1 and v2. The connection between the period and the length of the series is found through the sine approximation of the corresponding fragments. An increase in the sine period from 82 to 110 years (for v1) was obtained with an increase in the length of the series from 18 to 24 cycles and the conditions for the local manifestation of the 88-year harmonic. The initial periodicity of the maximums of seven to eight cycles is transformed into ten to eleven cycles.*

*The WSN series includes recovered data from 1749 to 1849 and further on, regular observation data — reliable data. The dependence of the period on the length of the series, that is, on the share of reliable data, is associated with the inconsistency of the characteristics of the reconstructed and reliable series and casts doubt on the existence of the Gleisberg cycle or "secular" harmonic in the WSN readings in the 1749–2015 interval. Changes in the land cover by temporal analysis.*

## Introduction

The persistent interest in long-period solar activity (SA) cycles, including the Gleisberg cycle (which is often associated with the "secular" cycle), is associated with the manifestation of SA minimum / maximum epochs in everyday life. Back in 1939, Gleisberg, relying on the Zurich series (1750–1928) and smoothing the maximums of the cycles by four values, identified two maximums and two minimums among them, which indicated the long-period component of the series (the Gleisberg cycle) with a frequency of their maximums/minimums of seven to eight cycles [1]. In later works [2, 3] a refined value of the period of about 80 years is given. Such an estimate can be easily obtained by approximating the amplitudes of these sixteen cycles with a sine, the parameters of which are found by the least squares method (OLS). The result, with the best value for the period of 82 years, is presented in Fig. 1, the dots mark the amplitudes themselves, along the horizontal axis of their date. Such an approximation satisfactorily describes no more than 18 cycles and its character is largely determined by cycles 5–7 of the Dalton minimum (MD).

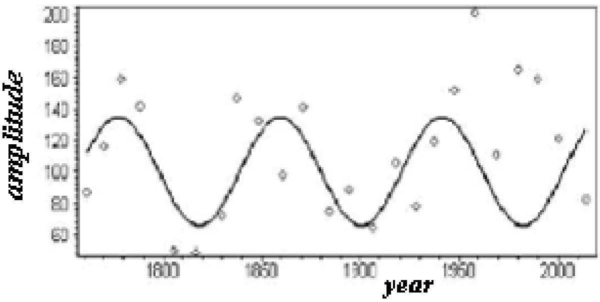


*Fig. 1. Sine approximation of the amplitudes of cycles 1–16*

In the works of various authors on the analysis of the WSN series itself, made over the past 60 years, the period of the Gleisberg cycle is estimated within 80–110 years. Researchers often identify a specific value for the period which is equal to 88 years [4–5]. Since different authors analyzed a series of different lengths, it makes sense to investigate the dependence of the period of the approximating sine on the length of the series itself, and besides this:

- To indicate the reasons for the growth (instability) of the period of the approximating sine.
- Point out the possible asymptotics of this growth.
- To specify more clearly such concepts as "period of the low-frequency component" and "epochs of minimum/maximum SA".

Along with the classical version of the WSN series, its new version is also considered in the work. Since July 2015, the Belgian Center for the Study of the Sun (http://sidc.oma.be) has introduced new rules for calculating the monthly Wolf numbers, according to which the WSN series was recalculated from 1749 to June 2015. The ratio of the cycle maxima in the new v2 and old v1 versions of the WSN series is demonstrated by Fig. 2 [6]. Correction of a significant part of the old version of the series is formal, but the amplitude correction of cycles 10 and 18–24 will affect the "secular" component of the new version. In this work, the presentation of the material and results are given for the old version of the series v1, the results associated with the new version v2 are marked or commented on.

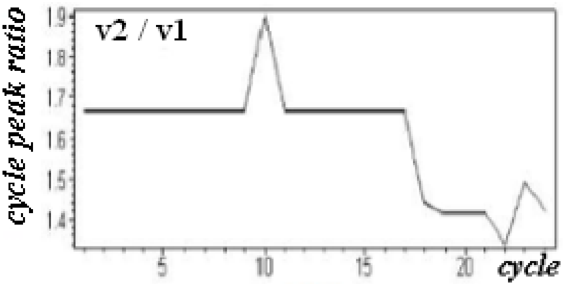


*Fig. 2. The ratio of the maxima of the cycles*

**Initial data**

Most of the results on the analysis of WSN were obtained before 2015, i.e., for version v1, and it is natural to rely on these developments. According to works [7–8], the long-period part of the v1 series, which includes components with a period of more than 24 years, is closely related to the envelope of the cycle maxima and serves as a geometrical place for the mean values of the cycles. This determines the choice of the source material, since Gleisberg analyzed the envelope of the cycle maxima. In this paper, we analyze the long-period components of the series of versions v1 and v2 (smoothed series of monthly Wolf numbers since 1749).

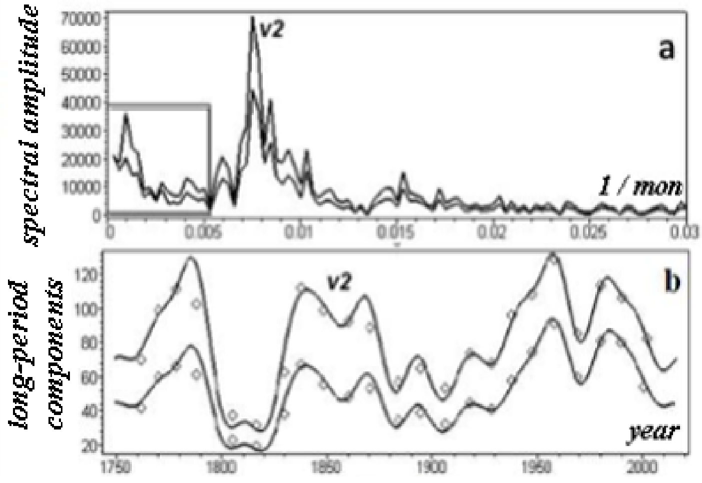


*Fig. 3. Spectrums of WSN (a); long-period components (b)*

The spectra of these series are presented in Fig. 3a, where the Ox axis is in reverse months, and the low-frequency part of the spectrum is labeled. The long-period components corresponding to the marked frequency range are displayed in Fig. 3b. The dots mark the mean values of the cycles which, for the v2 series [6], are well superimposed on the long-period components — the time axis Ox in years.

**Sine-approximation of fragments of long-period components**

Let us compare the approximations of two distinctive lengths of the low-frequency component of the old version of the series: a shortened fragment of eighteen cycles (1749–1954.37) and a long fragment up to the maximum of cycle 24 (1749–2014.376). The result of their approximation for $\sin((2\pi/T) + \varphi)$ is presented in Fig. 4. The period and phase of the sine were found by the least squares method, that is, by the minimum value of the sum squares of deviation (vertical axis) when scanning the corresponding rows with sine. The period was tested within 50–200 years (horizontal axis), phase $0\ldots2\pi$. The series under study were preliminarily reduced to a commensurate scale — after subtracting the mean they were normalized to the square root of the variance. For the first row the smallest deviation is observed at a period of 84 years, for the second — at 110 years, the values of the phases at which the minima were reached are not indicated.

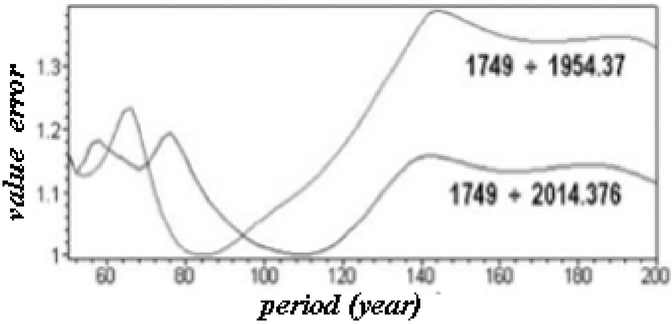


*Fig. 4. Result of approximation of two options of long-period components by a sine*

We use this approach to estimate the period of sine approximation of series of different lengths. The dependence of the period of the approximating sine (vertical axis in years) on the length of the series in cycles (the beginning of the cycle and its maximum) is shown in Fig. 5. The period grows with increasing row length and the 88-year harmonic appears in the old version of the series. The initial periodicity of the peaks of seven to eight cycles was transformed into ten to eleven cycles.

**Results and Discussions**

There are two important points to note:

- The above-mentioned estimate of the period of the Gleisberg cycle of 80–110 years (the results obtained by different authors at different times) coincided well with the ordered growth of the period from 82 to 110 years obtained in the work.
- The conditions for the local manifestation of the 88-year harmonic are clearly traced.

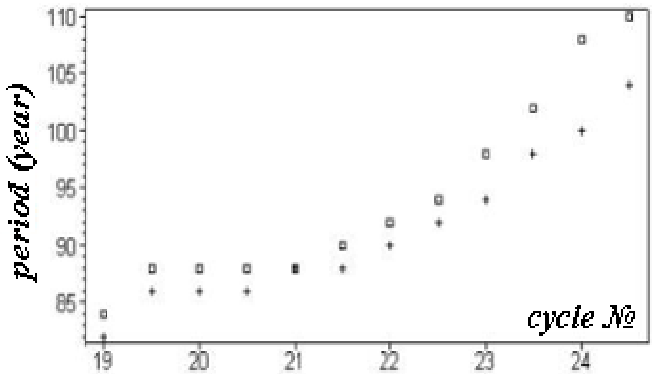


*Fig. 5. Dependence of an approximating sine period on length of WSN; v2 – (+)*

It is clear that the instability (growth) of the estimate of the period of the "secular" harmonic complicates the interpretation and extrapolating it to the external time interval and identifying the SA minimum/maximum epochs. This behavior can be associated with an increase in the proportion of reliable data (cycles) in the analysis. Recall that the original series of monthly average Wolf numbers consists of the reconstructed series $W_{rest}$ (from 1749 to 1849) and a reliable series of $W_{tool}$ (regular instrumental observations from 1849 to the present), i.e. $W = W_{rest} \cup W_{tool}$. Combining fragmentary data [9] with different density of observations, amplitude resolution and scaling will break the consistency of temporal fragments of different scales (for example, the structure of cycles and their relationship). All this manifested itself during the formation of the restored series. In the above mentioned works [7, 8] significant differences in the behavior of the series $W_{rest}$ and $W_{tool}$ are shown, the properties of the region of cycles 5–7 were significantly "distinguished". With a series length of 18–19 cycles, a certain balance of properties of the restored and reliable parts is still preserved, and the Dalton minimum determines the formation and local manifestation of the 88-year to 90-year harmonic. A further increase in the proportion of reliable data shifts this balance in favor of the $W_{tool}$ series with a smoother and more ordered long-period component (Fig. 3b), which leads to an increase in the period. When analyzing only the $W_{tool}$ series, the period of the approximating sine is 150 years [10], this corresponds to the periodicity of the maxima of fourteen cycles, and we have, as it were, the saturation of the period with the leveling of the role of the Wrest series, which corresponds to the concept under consideration. We simply state the same period for the new version $W_{tool}$ equal to 131 years [6], taking into account the formal nature of the transformation of a significant group of cycles. Strictly speaking, the inconsistency of the parameters of the reliable and reconstructed series casts doubt on the existence of the Gleisberg cycle or "secular" harmonic in the WSN readings in the interval 1749–2015.

A different situation arises if one relies on the "good" data of the $W_{tool}$ series to reconstruct the "bad" data of the $W_{rest}$ series. Then we get "consistent" (probably without the Dalton minimum) behavior of the long-period part over the entire interval of 1749–2015 and an "adjusted" estimate of the average values of the cycles of the reconstructed series. This scenario concretizes concepts such as the "period of the low-frequency component" and "epochs of minimum/maximum SA". An example of such an extrapolation, with a period of the approximating sine of the $W_{tool}$ series of 150 and 131 years, is demonstrated in Fig. 6.

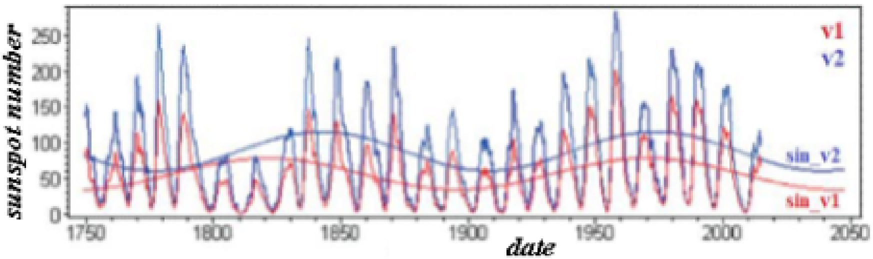


*Fig. 6. Review of series v1, v2 and extrapolation of their sine approximations*

**Conclusion**

As noted above, the concept of "Gleisberg cycle" arose from the analysis of small amount of data for a series of Wolf numbers of different reliability and with the key role of cycles 5–7. This fragment, with a low SA, coincided with a period of lower than average global temperatures. This justifies the presence of the Dalton minimum although such a connection is not obvious. Volcanic activity and elevated $CO_2$ levels may have a greater impact on climate than SA change [11]. Weather anomalies ("year without summer") in Europe and America in 1816, caused by the eruption a year earlier of the Tambora volcano on the Indonesian peninsula Sumbawa, are the confirmation of this [12]. The temperature and SA in the recent past correlate in a different way: the temperature of the Earth has noticeably increased against the background of a rapid decrease in average activity and, since about 1970, the influence of the Sun on the climate could not be significant [13]. With such a variety of situations, the plot presented in Fig. 6 is quite real. It should be expected that the agreement of the parameters of the reliable and reconstructed series will correct, first of all, the Dalton minimum, towards an increase in its values, and will change (cancel) the concept of the "Gleisberg cycle". It is reasonable not to speak about the "Gleisberg cycle" tied to the MD, but about the long-period component corresponding to the $W_{tool}$ series and the corrected $W_{rest}$ series. Note that a critical attitude to the restored series is expressed by many authors in the works of the 1978 symposium — [14]. An attempt to balance the timing characteristics of the cycles of the same series at the expense of the "lost" cycle was undertaken in the work [15]. When analyzing the fractal properties of the series of the annual ring widths of eleven sequoias [16], the Dalton minimum did not appear.

Finally, we note that the closeness of the amplitude characteristics of cycles 8 and 9 to the parameters of reliable cycles allows us to speak about the consistency of the 150-year harmonic (generated by cycles 10–24) and the WSN readings since 1835.

The authors would like to sincerely thank V. N. Ishkov for the attention and support of the theme.

**References**


1. Gleissberg, W. A long-periodic Fluctuation of the Sun-spot Numbers. *Observatory*, 1939, 62, 158–159.
2. Gleissberg, W. Die Persistenz des 80 Jahrigen Sonnenfleckenzyklus Durch 16 Jahrhunderte. *İ.Ü. Fen Fak. Mecm. Seri C.*, 1955, 20, 263–271.
3. Gleissberg, W. Secularly Smoothed Data on the Minima and Maxima of Sunspot Frequency. *Solar Physics*, 1967, 2, 231–233.
4. Feynman, J., S. B. Gabriel. Period and phase of the 88-year Solar cycle and the Maunder minimum: evidence for a chaotic Sun. *Solar Physics*, 1990, 127, 2, 393–403.
5. Peristykh, A. N., P. E. Damon. Persistence of the Gleissberg 88-year solar cycle over the last ~12,000 years: Evidence from cosmogenic isotopes. *JGR*, 2003, 108, A1, 1003–1005. DOI:10.1029/2002JA009390.
6. Shibaev, A. The characteristics of old and new versions of month Wolf numbers range and there uniformity are compared. *Proceedings of 12th Scientific Conference with International Participation "Space, Ecology, Safety" SES'2016*, Sofia, Bulgaria, 2017, 73–76. (In Russian).
7. Shibaev I. G. Estimation of the reconstructed part of the Wolf series and the possibility of its correction. *Solar System Research*, 2008, 42, 1, 63–71.
8. Shibaev, I. G. Reconstruction of the Dalton Minimum using the 150-year harmonic and characteristics of reliable series of Wolf Numbers. *Proceedings of 12th Scientific Conference with International Participation "Space, Ecology, Safety - SES'2016"*, Sofia, Bulgaria, 2017, 68–72. (In Russian).
9. Hathaway, D. H. The Solar Cycle. Living Rev. *Solar Phys.*, 2015, 12, 4, 10–11. https://doi.org/10.1007/lrsp-2015-4.

10. Ishkov, V. N., I. G. Shibaev. Cycles of solar activity: general characteristics and modern boundaries of forecasting. *Izvestiya Rossiiskoi Akademii Nauk. Seriya Fizicheskaya*, 2006, 70, 10, 1439–1442.
11. Wagner, S., E. Zorita, The influence of volcanic, solar and CO2 forcing on the temperatures in the Dalton Minimum (1790–1830): a model study. *Climate Dynamics*, 2005, 25, 205–218. DOI 10.1007/s00382-005-0029-0.
12. Schurer, A. P., G. C. Hegerl, J. Luterbacher *et al.* Disentangling the causes of the 1816 European year without a summer. *Environ. Res. Lett.*, 2019, 14, 11. https://doi.org/10.1088/1748-9326/ab3a10.
13. Krivova, N. A., S. K. Solanki. Solar variability and global warming: a statistical comparison since 1850. *Advances in Space Research*, 2004, 34, 361–364.
14. McCormac, B. *Solar-Terrestrial Influences on Weather and Climate. Proceeding of a Symposium*. Dordrecht, Holland, Springer, 1978, The Ohio State University, Columbus, Ohio, 24–28 August 1978, 348 p.
15. Usoskin, I. G., K. Mursula, G. A.Kovaltsov. The lost sunspot cycle: Reanalysis of sunspot statistics. *A&A*, 2003, 403, 2, 743–748.
16. Otsuka, K., G. Cornelissen, F. Halberg. Chronomics of tree rings gauge climate change. *Geophysical Processes and Biosphere*, 2009, 8, 1, 63–72. (In Russian).

## ЗАВИСИМОСТЬ ПЕРИОДА ЦИКЛА ГЛЯЙСБЕРГА ОТ ДЛИНЫ РЯДА ЧИСЕЛ ВОЛЬФА

***Иг. Шибаев, Ал. Шибаев***

### Резюме

Понятие «цикл Гляйсберга» возникло из анализа небольшого объема данных с различной степенью достоверности и с ключевой ролью минимума Дальтона. Сглаживая максимумы циклов Цюрихского ряда (1750–1928 гг.) по четырем значениям Гляйсберг выделил среди них два максимума и два минимума, которые и указывали на длиннопериодную составляющую ряда с периодичностью максимумов/минимумов в семь–восемь циклов.

В работе анализируются длиннопериодные компоненты ряда WSN версий v1 и v2. Связь периода и длины ряда находится через синус-аппроксимацию соответствующих фрагментов. Для v1 получен рост периода синуса с 82 до 110 лет при увеличении длины ряда от 18 до 24 циклов, т. е. периодичность максимумов трансформируется в десять–одиннадцать циклов. Неустойчивая (растущая) оценка периода «вековой» гармоники затрудняет её интерпретацию и экстраполяцию на внешний временной интервал.

Ряд WSN включает восстановленные данные с 1749 по1849 г. и далее данные регулярных наблюдений – достоверные данные. Зависимость периода от длины ряда, т. е. от доли достоверных данных, связана с несогласованностью характеристик восстановленного и достоверного рядов и ставит под сомнение существование «цикла Гляйсберга» или «вековой» гармоники в показаниях WSN на интервале 1749–2015 гг.

Bulgarian Academy of Sciences. Space Research and Technology Institute.
Aerospace Research in Bulgaria. 34, 2022, Sofia

DOI: https://doi.org/10.3897/arb.v34.e02

# WITHIN-FIELD MAPPING OF WINTER WHEAT BIOPHYSICAL VARIABLES USING MULTISPECTRAL IMAGES FROM UAV

***Georgi Jelev, Petar Dimitrov, Eugenia Roumenina***

*Space Research and Technology Institute — Bulgarian Academy of Sciences*
*e-mail: g_jelev@abv.bg, petarkirilov@mail.bg, roumenina@space.bas.bg*

***Keywords:*** *Winter Wheat, LAI, fAPAR, fCover, UAV, Multispectral Camera*

***Abstract***

*The paper presents the results from a study aiming to map the dynamic of biophysical variables of winter wheat crops in different phenological growth stages (PGSs) using multispectral camera data acquired by Unmanned Aerial Vehicle (UAV). The studied biophysical variables are Leaf Area Index (LAI), fraction of Absorbed Photosynthetically Active Radiation (fAPAR) and fraction of vegetation cover (fCover). During agricultural year 2016/2017, 4 field campaigns (FCs) were carried out in 6 farmer-managed fields sown with two winter wheat varieties. During the FCs, 8 UAV flight missions were accomplished. Linear and exponential regression models were designed and evaluated to derive predictive equations for the biophysical variables of the crops based on a set of vegetation indices (VIs). The best predictor for all biophysical variables was OSAVI (RMSE was 0.90 $m^2/m^2$, 0.07 and 0.08 for LAI, fAPAR, and fCover respectively). The chosen models were used to compose maps of LAI, fAPAR, and fCover of the studied fields. The maps correspond well with the spatial distribution of the values of the respective biophysical variables measured during the respective field campaign.*

## Introduction

Leaf Area Index (LAI), fraction of Absorbed Photosynthetically Active Radiation (fAPAR), and fraction of vegetation Cover (fCover) are biophysical variables of the vegetation cover which are among the major indicators of its status. To evaluate their spatial change, the products LAI, fAPAR, and fCover are formed, using multispectral aerial and satellite data [1–3]. These products are validated by ground-based measurements of the same parameters on test fields located in various parts of the world. On the territory of Bulgaria, the LAI and FAPAR products from the MERIS satellite sensor were tested on winter wheat fields located in north-east Bulgaria [4]. The new satellite mission Sentinel 2 of the European Space Agency features good spectral, spatial, and temporal resolution [5]. The data from it are already used in precision agriculture, but there are still some limitations related mostly to the days with cloud cover during the image-taking. For this reason, sometimes the farmers cannot obtain information about their fields for weeks on end.

Quite often, when a certain problem arises, the farmers would wish to immediately obtain information about its progress so as to be able to take informed decision.

The technologies for remote determination of the crops' status using unmanned aerial vehicle (UAV) are increasingly used in precision agriculture [6]. Scientists develop and evaluate different models for timely deriving of information about the dynamics of the agronomic parameters of agricultural crops during major phenological phases from images obtained by UAV cameras [7–12]. The studies were carried out on one or several adjacent experimental fields of similar small size which are not managed by farmers.

This study was carried out on fields of various sizes managed by farmers carrying out their agrotechnical activities. Its main objective is within-field mapping of the change of LAI, fAPAR, and fCover of winter wheat crops during different phenological growth stages using data from UAV-borne multispectral camera.

## Study area and materials

### *Study fields*

This study was carried out on 6 farmer-managed fields or Units (Us) sown with winter wheat (*Triticum aestivum L.*). They are located on the territory of Zlatia test site, Municipality of Knezha, Pleven region, Bulgaria, Fig. 1, which is part of the north-west planning district of Bulgaria. The Units were spatially grouped in two areas and were managed by two different farmers — U1, U2, and U3 were located on the land of the town of Knezha, and U4, U5, and U6 — on the land of the village of Enitsa. The units feature different area: U1 — 150 ha, U2 — 86 ha, U3 — 10 ha, U4 — 48 ha, U5 — 78 ha, and U6 — 7 ha. Units 1 to 3 were sown with *Anapurna* variety while units 4 to 6 were sown with *Enola* variety. The altitude varies between 80 and 190 m a.s.l. The winter wheat crops were grown on three types of soil [13]. Epicalcic Chernozems Siltic, Endocalcic Chernozem Pachic Siltic (Units 1, 2, and 3), and Haplic Cambisol Eutric Siltic (Units 4, 5, and 6). These are among the most widespread soils in North-west Bulgaria and they are suitable for growing of winter wheat.

## Data acquisition and processing

In the study, we used data from field measurements and observations and imagery obtained from Parrot Sequoia UAV multispectral camera as well as data from the two farmers managing the fields. The data were obtained as a result of the implementation of the TS2AgroBG Project.

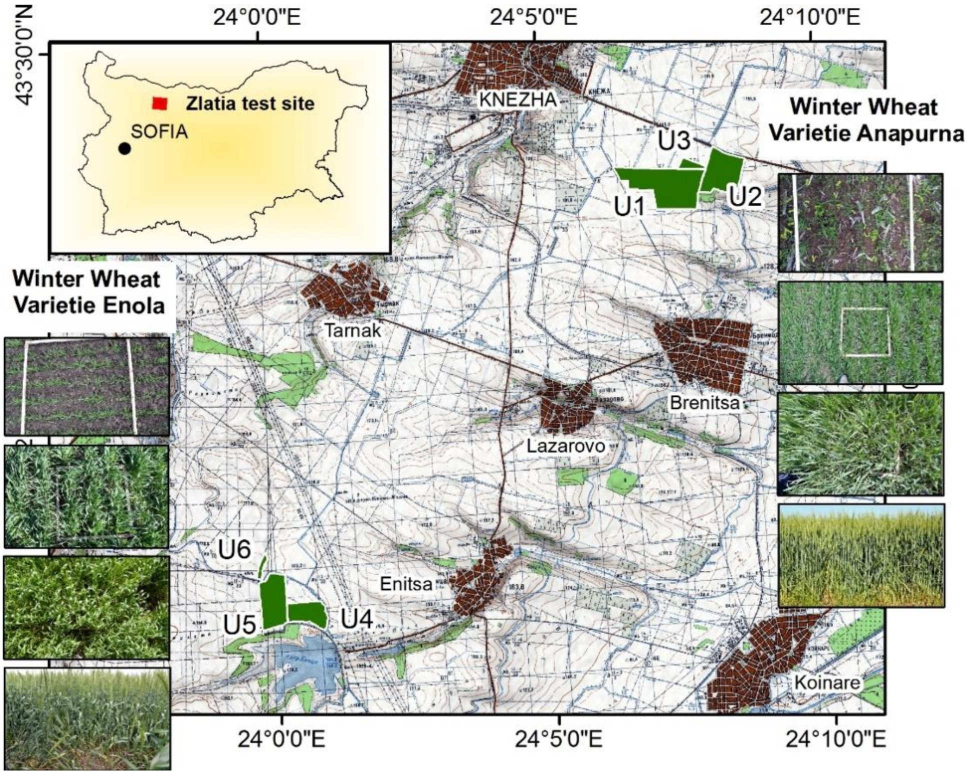


*Fig. 1. Location of the Units (U1, U2, U3, U4, U5 and U6) on which the study was carried out in the Zlatia test site, Bulgaria. (Base map source: http://web.uni-plovdiv.bg/vedrin)*

*Field data*

During agricultural year 2016/2017, 4 field campaigns (FCs) were carried out aiming to collect data about the studied units. They were carried out during 4 major phenological growth stages (PGSs) of the crops, as follows: Tiller production before wintering — FC 1 (07–11.11.2016), Tiller production after wintering — FC 2 (20–24.03.2017), Stem elongation — FC 3 (24–28.04.2017), and Anthesis — FC 4 (15–19.05.2017). To determine the PGS, Zadoks decimal code [14] was used.

The predecessors on the observed Units were sunflower (U1, U2, U3) and maize (U4, U5, U6) which are suitable for growing of winter wheat. On all Units, pre-sowing preparation was carried out and, during sowing, the soil was fertilized with Diammonia phosphate (DAP) — 250 kg/ha in U1, U2, and U3 and 260 kg/ha in U4, U5, and U6. The winter wheat was sown on 03.10.2016 and 09.10.2016, within the optimal terms for its growth in this region of Bulgaria, but for U6 where it was sown later, on 25.10.2016. Units 1, 2, and 3 were sown with 500 seeds per m$^2$, Units 4 and 5 — with 550 seeds per m$^2$, and U6 — with 580 seeds per m$^2$.

During the restoration of winter wheat vegetation after wintering (05.03.2017 and 26.02.2017), spring fertilization with *Urea* was carried out with 180 kg/ha (U1, U2, U3) and 250 kg/ha (U4, U5, U6). There was significant difference in the type of spring fertilization of wheat crops carried out on 25.03.2017. The crops in Units 1, 2, 3 were fertilized with *Ammonium nitrate* (150 kg/ha). On the wheat in Units 4, 5 and 6, foliar fertilization was applied during PGS Tiller production.

On the territory of the studied Units, a total of 30 (Fig. 1) elementary sampling units (ESUs) sized 20×20 m were outlined. Three elementary sub-sampling units sized 1 $m^2$ were determined within each ESU to perform phenological observations and measurements using the instrument AccuPAR PAR/LAI Ceptometer LP-80. The data from these measurements were averaged for each ESU and were used to determine LAI ($m^2$ $m^{-2}$), fAPAR and fCover [15]. The obtained data are summarized on Table 1 at Unit level for the units sown with *Anapurna* and *Enola* variety. The distribution of the values of the ground-measured biophysical crop variables for Unit 6 is provided separately because of the differences in the phenological development due to its later sowing, as compared to Units 4 and 5.

*Table 1. Descriptive statistics for the ground-measured biophysical crop variables recorded during the 4 carried out field campaigns*

| **Range, Mean and Std. dev.** | **Code Unit** | **Phenological growth stages** | **LAI** | **fAPAR** | **fCover** |
|---|---|---|---|---|---|
| Range | U1, U2, U3 | Z20 | 0.08–0.41 | 0.13–0.34 | 0.03–0.13 |
| | U4, U5 | Z20 | 0.04–0.22 | 0.12–0.24 | 0.02–0.07 |
| | U6 | Z00 | 0 | 0 | 0 |
| Mean | U1, U2, U3 | Z20 | 0.19 | 0.20 | 0.06 |
| | U4, U5 | Z20 | 0.09 | 0.15 | 0.04 |
| | U6 | Z00 | 0 | 0 | 0 |
| Std. dev. | U1, U2, U3 | Z20 | 0.09 | 0.06 | 0.03 |
| | U4, U5 | Z20 | 0.06 | 0.04 | 0.02 |
| | U6 | Z00 | 0 | 0 | 0 |
| Range | U1, U2, U3 | Z21 to 26 | 0.57–1.54 | 0.38–0.63 | 0.23–0.47 |
| | U4, U5 | Z21 to 26 | 1.04–2.62 | 0.49–0.79 | 0.35–0.65 |
| | U6 | Z20 to 24 | 0.14–0.35 | 0.16–0.25 | 0.06–0.14 |
| Mean | U1, U2, U3 | Z21 to 26 | 0,94 | 0,48 | 0,33 |
| | U4, U5 | Z21 to 26 | 1,86 | 0.68 | 0.53 |
| | U6 | Z20 to 24 | 0.25 | 0.21 | 0.10 |

| | | | | | |
|---|---|---|---|---|---|
| Std. dev. | U1, U2, U3 | Z21 to 26 | 0.29 | 0.07 | 0.07 |
| | U4, U5 | Z21 to 26 | 0.43 | 0.09 | 0.08 |
| | U6 | Z20 to 24 | 0.10 | 0.04 | 0.04 |
| Range | U1, U2, U3 | Z31 to Z33 | 2.27–5.30 | 0.70–0.92 | 0.64–0.91 |
| | U4, U5 | Z31 to Z34 | 3.36–7.88 | 0.77–0.95 | 0.74–0.97 |
| | U6 | Z31 to Z33 | 2.21–2.81 | 0.68–0.72 | 0.59–0.66 |
| Mean | U1, U2, U3 | Z31 to Z33 | 3,45 | 0,83 | 0,78 |
| | U4, U5 | Z31 to Z34 | 6,19 | 0.91 | 0.93 |
| | U6 | Z31 to Z33 | 2,46 | 0.70 | 0.62 |
| Std. dev. | U1, U2, U3 | Z31 to Z33 | 0.81 | 0.06 | 0.08 |
| | U4, U5 | Z31 to Z34 | 1,23 | 0.05 | 0.07 |
| | U6 | Z31 to Z33 | 0.31 | 0.02 | 0.04 |
| Range | U1, U2, U3 | Z65 | 2.43–5.86 | 0.72–0.92 | 0.65–0.94 |
| | U4, U5 | Z65 to 69 | 3.65–7.09 | 0.85–0.94 | 0.81–0.95 |
| | U6 | Z65 to 69 | 3.45–3.73 | 0.83–0.88 | 0.80–0.87 |
| Mean | U1, U2, U3 | Z65 | 3,81 | 0,84 | 0,82 |
| | U4, U5 | Z65 to 69 | 5,03 | 0.91 | 0.92 |
| | U6 | Z65 to 69 | 3,59 | 0.86 | 0.84 |
| Std. dev. | U1, U2, U3 | Z65 | 0.99 | 0.06 | 0.09 |
| | U4, U5 | Z65 to 69 | 1,11 | 0.02 | 0.04 |
| | U6 | Z65 to 69 | 0.14 | 0.03 | 0.03 |

***UAV System and Flight Missions***

Here, during each field campaign, 2 UAV missions were carried out, Table 2, using the *Specialized Unmanned Aerial Vehicle (SUAV) senseFly eBee Ag* including the drone *Parrot Sequoia* multispectral camera, Table 3, plus a sunshine (light) sensor [16], navigation, and image processing software. Before each UAV mission a flight plan was drawn and simulation of the flight was carried out. The products from the imaging were georeferenced using data from the on-board GPS in UTM coordinate system, zone 35, datum World Geodetic System (WGS) 1984. The ultimate generated product was orthophoto mosaic for the studied Units. To georeference the photomosaic with maximum precision, the coordinates of 13 geographical control points (GCPs) were used which were measured by GNSS Leica GS08. The GCPs were determined before the carrying out of the two UAV missions being marked by fixed clearly discernible white markers sized 25×25 cm$^2$.

All UAV missions were accomplished at flight altitude of 265 m on clear sunny days, during the period between 11:00 a.m. and 02:00 p.m. local time, at wind velocity below 5 m/s.

*Table 2. Dates of the carried out UAV flight missions and PGSs of the winter wheat crops in the studied Units*

| Flight mission/ID | Flight date UAV | Unit (U) | Phenological Growth Stage |
|---|---|---|---|
| Mission 1/M1 | 07.11.2016 | U1 and U3 | Tiller production, (Z20) |
| | 11.11.2016 | U2 | |
| Mission 2/M2 | 10.11.2016 | U4, U5 and U6 | U4, U5 – Tiller production, (Z 20), U6 – Unspr \outed Z00 |
| Mission 3/M3 | 21.03.2017 | U1, U2 and U3 | Tiller production: Zadoks 21 to 26 |
| Mission 4/M4 | 22.03.2017 | U4, U5 and U6 | Tiller production: U4, U5 – Z21 to Z26, U6 – Z20 to 24 |
| Mission 5/M5 | 25.04.2017 | U1, U2 and U3 | Stem elongation: Z31 to Z33 |
| Mission 6/M6 | 26.04.2017 | U4, U5 and U6 | Stem elongation: U4, U5 – Z31 to Z34, U6 – Z31 to Z32 |
| Mission 7/M7 | 15.05.2017 | U4, U5 and U6 | Anthesis: U4 – Z65, U5 – Z69, U6 – Z65 to 69 |
| Mission 8/M8 | 18.05.2017 | U1, U2 and U3 | Anthesis (flowering): Z65 |

*Table 3. Spectral bands for the Parrot Sequoia UAV camera used in the study*

| Channel name | Green (Bg) | Red (Br) | Red edge (Bre) | Near IR (Bnir) |
|---|---|---|---|---|
| Central wavelength (nm) | 550 | 660 | 735 | 790 |
| Bandwidth (nm) | 40 | 40 | 10 | 40 |
| Spatial resolution (m/pixel) | 0.20 | 0.20 | 0.20 | 0.20 |

## Methodology

The maps of the crops' biophysical variables in the studied Units were composed in 2 stages. During the first one, regression models for LAI, fAPAR and fCOVER were designed, and during the second one, the relevant maps were composed.

**Designing of regression models for LAI, fAPAR, and fCOVER**

*Methods*

We used regression analysis in order to find predictive equations for the biophysical variables based on a set of vegetation indices (VIs), Table 4, and the four spectral bands. Linear and exponential models were developed using one predictor at a time and thus all VIs/bands were evaluated for their predictive capability. The 2016–2017 growing season data were used for model calibration and leave-one out cross validation. ESUs with significant weed coverage were omitted from the dataset.

*Table 4. List of spectral vegetation indices used in this study and formulas for their calculation*

| Vegetation Index | Formulae | Reference |
|---|---|---|
| Chlorophyll Index green (CIg) | (NIR / Green) – 1 | [17, 18] |
| Chlorophyll Index red edge (CIre) | (NIR / Red edge) - 1 | [17, 18] |
| Difference Vegetation Index (DVI) | NIR - Red | [19] |
| Green Infrared Percentage Vegetation Index (GIPVI) | NIR/(NIR + Green) | |
| Green Normalized Difference Vegetation Index (gNDVI) | (NIR – Green) / (NIR + Green) | [20] |
| Green Normalized Difference Vegetation Index 1 (gNDVI 1) | (Red edge – Green) / (Red edge + Green) | |
| Modified Triangular Vegetation Index 2 (MTVI2) | $\frac{1.5*[1.2*(NIR-Green)-2.5*(Red-Green)]}{\sqrt{(2*NIR+1)^2-(6*NIR-5\sqrt{Red})-0.5}}$ | [7] |
| Normalized Difference Vegetation Index (NDVI) | (NIR – Red) / (NIR + Red) | [21] |
| Normalized Difference Vegetation Index 1 (NDVI 1) | (Red edge – Red) / (Red edge + Red) | |
| Optimized Soil-Adjusted Vegetation Index (OSAVI) | (1+0.16)*(NIR - Red) / (NIR + Red + 0.16) | [22] |
| Red edge Normalized Difference Vegetation Index (reNDVI) | (NIR –Red-edge) / (NIR + Red-edge) | [23] |
| Simple Ratio (SR) | NIR / Red | [19] |
| Simple Ratio 1 (SR 1) | Red-edge / Red | |
| Simple Ratio 3 (SR 3) | NIR / Red-edge | [23] |
| Vegetation Index green (VIg) | (Green – Red) / (Green + Red) | [24] |
| Wide Dynamic Range Vegetation Index (WDRVI) | (0.3 * NIR – red) / (0.3 * NIR + Red) | [25] |

The performance of the models was evaluated based on the Root Mean Square Error (RMSE):

1) $$\text{RMSE} = \sqrt{\frac{\sum_i (y_i - \hat{y}_i)^2}{n}},$$

where: $y_i$ is the measured value for the i-th observation and $\hat{y}_i$ is the predicted value for i derived from a model calibrated with all observations except i. Relative RMSE ($RMSE_r$) was calculated as percentage of the mean of the measured values.

*Results*

Table 5 shows the error statistics of the regression equations derived by each predictor. For each combination of biophysical variable and predictor two models, i.e. linear and exponential, were developed and the one with lower error were selected and considered for the comparison in Table 5. For all biophysical variables the best predictor was OSAVI. The relationships with OSAVI were exponential, Fig. 2. The corresponding regression equations are shown in Table 6.

*Table 5. Root mean square errors (RMSE) and relative Root mean square errors (RMSEr) from the leave-one-out cross validation of the regression models. Model type is either linear (lin), or exponential (exp). For each biophysical variable the three lowest RMSE/RMSEr values are shown in bold.*

| Predictor | LAI | | | fAPAR | | | fCover | | |
|---|---|---|---|---|---|---|---|---|---|
| | **Model type** | **RMSE [$m^2/m^2$]** | **$RMSE_r$ [%]** | **Model type** | **RMSE [-]** | **$RMSE_r$ [%]** | **Model type** | **RMSE [-]** | **$RMSE_r$ [%]** |
| Green band | lin | 2.08 | 68.8 | lin | 0.26 | 38.9 | lin | 0.31 | 50.4 |
| Red band | lin | 2.19 | 72.6 | lin | 0.27 | 39.7 | lin | 0.33 | 52.8 |
| Red edge band | exp | 1.22 | 40.5 | lin | 0.14 | 20.2 | lin | 0.17 | 27.3 |
| NIR band | exp | **0.96** | **31.7** | lin | 0.08 | 12.0 | lin | 0.09 | 14.6 |
| CIg | lin | 1.39 | 46.1 | lin | 0.13 | 18.9 | lin | 0.16 | 26.7 |
| CIre | lin | 1.39 | 46.0 | lin | 0.11 | 16.8 | lin | 0.13 | 21.2 |
| DVI | exp | **0.94** | **31.3** | lin | **0.08** | **11.3** | lin | **0.09** | **14.0** |
| GIPVI | exp | 1.40 | 46.4 | exp | 0.12 | 17.1 | lin | 0.17 | 27.1 |
| gNDVI | exp | 1.40 | 46.4 | exp | 0.12 | 17.1 | exp | 0.16 | 25.9 |
| gNDVI1 | lin | 1.79 | 59.5 | lin | 0.19 | 28.3 | lin | 0.24 | 39.7 |
| MTVI2 | exp | 0.99 | 32.7 | exp | **0.07** | **10.1** | exp | **0.09** | **13.8** |
| NDVI | exp | 1.47 | 48.7 | exp | 0.12 | 17.1 | exp | 0.15 | 25.0 |
| NDVI1 | exp | 1.75 | 58.2 | exp | 0.17 | 25.0 | lin | 0.22 | 36.4 |
| OSAVI | exp | **0.93** | **30.8** | exp | **0.07** | **10.0** | exp | **0.08** | **13.1** |
| reNDVI | lin | 1.35 | 44.7 | lin | 0.09 | 13.7 | lin | 0.11 | 18.2 |

| | | | | | | | | | |
|---|---|---|---|---|---|---|---|---|---|
| SR | lin | 1.52 | 50.4 | lin | 0.13 | 19.7 | lin | 0.17 | 28.1 |
| SR1 | lin | 1.80 | 59.6 | lin | 0.19 | 27.4 | lin | 0.24 | 38.6 |
| SR3 | lin | 1.39 | 46.0 | lin | 0.11 | 16.8 | lin | 0.13 | 21.2 |
| VIg | lin | 1.91 | 63.2 | lin | 0.20 | 29.0 | lin | 0.25 | 40.1 |
| WDRVI | exp | 1.48 | 49.1 | exp | 0.11 | 16.8 | exp | 0.16 | 25.5 |

*Table 6. Regression model selected for the mapping of the biophysical variables*

| **Biophysical variable** | **Regression equation** |
|---|---|
| LAI | LAI = 0.00193 * exp(OSAVI * 9.31558) |
| fAPAR | fAPAR = 0.05485 * exp(OSAVI * 3.32069) |
| fCover | fCover = 0.01119 * exp(OSAVI * 5.20752) |

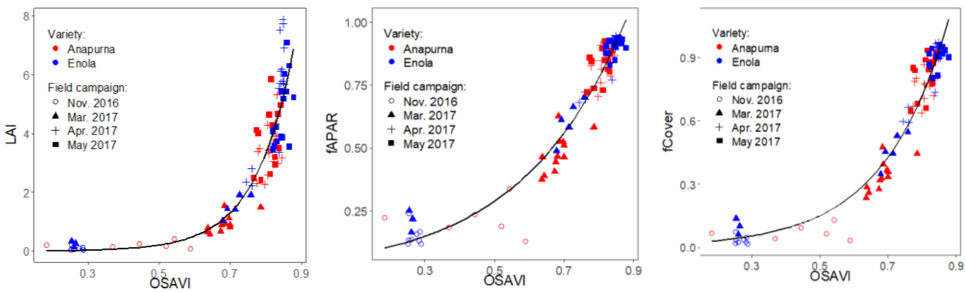


a) b) c)

*Fig. 2. Scatter plots of biophysical variables LAI (a), fAPAR (b), and fCover (c) and OSAVI showing the exponential regression fit*

## Composing of maps of LAI, fAPAR, and fCOVER

In the beginning of this stage, a geodatabase was composed. It included: the boundaries of the studied Units, soil maps, digital elevation model (DEM), the data from the carried out field campaigns, and the images obtained from all UAV flight missions; Crop Calendar containing information about the agrotechnical measures carried out by the farmers, and data about the initial and final dates of occurrence of the major phenological phases of the winter wheat crops for each individual Unit. Input into the geodatabase were also the designed regression models for calculation of the crops' biophysical variables, as well as the results from the processing and analysis of the multispectral UAV images.

The maps of the crops' biophysical variables were composed in the following steps. Initially, the orthophoto mosaic of the multispectral images obtained from each UAV flight mission was cropped along the boundaries of each Unit. Out of them, the vegetation index OSAVI for each pixel was calculated and a raster image was obtained, on which the respective regression model for LAI, fAPAR and fCOVER was applied successively, Table 6. The raster layer thus calculated was reclassified into 5 classes with previously fixed boundaries. As a result, a raster layer was obtained which was used to draw a separate map for each biophysical parameter, Fig. 3, 4, and 5.

## Results and discussion

The crops studied during the observed agricultural year 2016/2017 do not differ significantly in their phenological growth, but for those in Unit 6. In it, due to the later sowing, a delay in the dates of the mass occurrence of PGS *Germination Z 0–1* and *Stem elongation Z 31 to 34* was observed, as compared to the other crops.

Maps of LAI, Fig. 3, were composed, obtained by applying a regression model based on the OSAVI vegetation index, Table 6, on images from *Parrot Sequoia* UAV multispectral camera acquired during the carried out UAV flight missions, Table 2.

On them, the obtained values of LAI and their distribution during PGSs *Tiller production, Stem elongation,* and *Anthesis* comply with the ground-measured ones during the carried out FCs, Fig. 3, Table 1.

On the map of LAI, Fig. 3, drawn using images from UAV missions 3 and 4, one can easily distinguish between Units 1, 2, 3, and 6, from one hand, which feature lower LAI values (0.15–1.5 $m^2/m^2$) and Units 4 and 5, from the other hand (LAI between 0.15–3.0 $m^2/m^2$). This coincides with the ground-measured values of LAI which are within the same limits, Table 1. The same differences are also observed on the maps composed for PGS *Stem elongation* Fig. 3b, Table 1. The average value of LAI by data obtained from ground-based measurements in U1, U2, and U3 is 3.45 $m^2m^{-2}$, while in U4 and U5 it is much higher — 6.19 $m^2/m^2$, being lowest again in U6 — 2.46 $m^2/m^2$.

The recorded values of LAI on the maps where the crop is in PGS *Anthesis,* Fig. 3c, are identical with those on the maps for PGS *Stem elongation,* Fig. 3b. The only exceptions are U6, the southern part of U1, and the western part of U4 where the values are higher. This is also confirmed by the data from the ground-based measurements, Table 1, but for U4 and U5 where a certain decrease of the average values of LAI by 1.17 $m^2/m^2$ is observed. This inconsistency of the modeled LAI with ground measurements at PGS Anthesis may be explained with the lower sensitivity (saturation issues) of the exponential model at high LAI values.

The reasons for the established differences in the values of the crops' LAI in U1, U2 and U3 compared to those in U4 and U5 are complex. Probably, they are due not only to the fact that they have been sown with different varieties of winter wheat but also because they differ in the applied spring fertilization as described in Section *Field data*. On U4 and U5, in the end of March 2017, foliar feeding of wheat was also carried out. The grain yield is classified in the *feed wheat category* in the crops of winter wheat variety *Anapurna*, and *normal bread wheat* category for variety *Enola*.

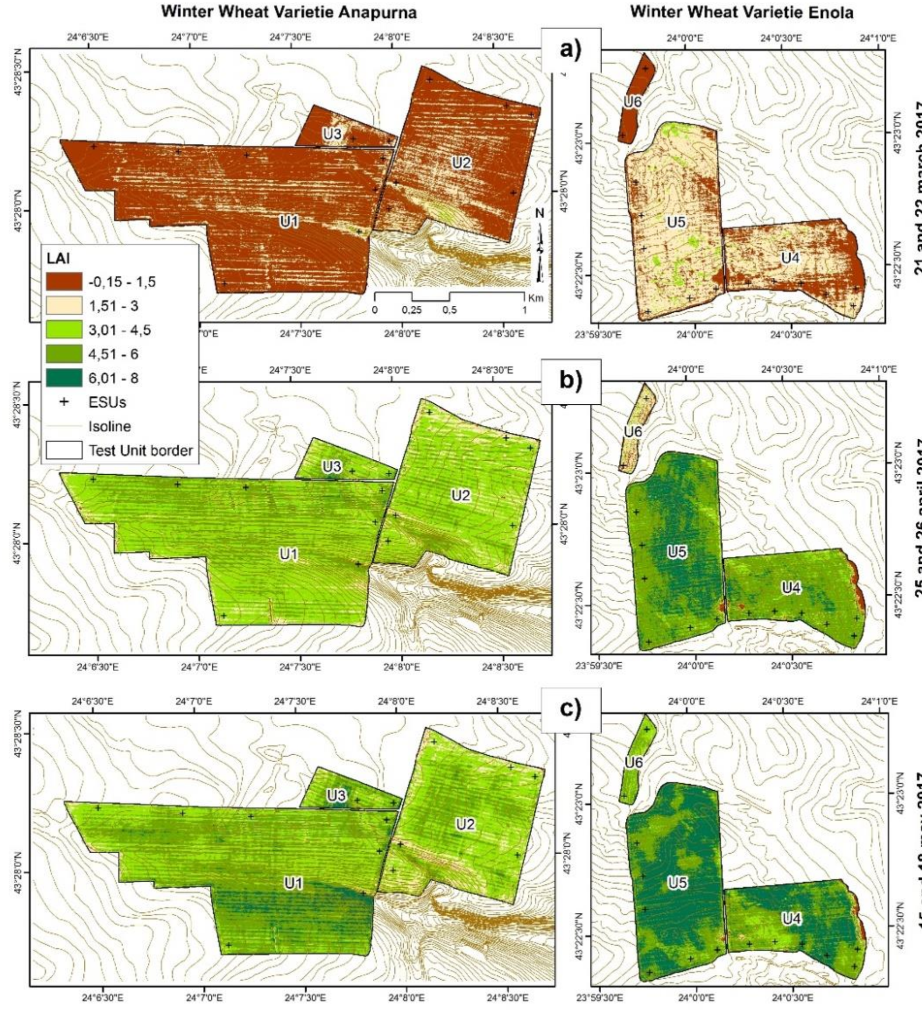


*Fig. 3. Maps of LAI of winter wheat crops in the studied Units composed by applying a regression model based on the OSAVI vegetation index on images from Parrot Sequoia UAV multispectral camera obtained from UAV flight missions: a) missions 3 and 4, FGS Tiller production, b) missions 5 and 6, FGS Stem elongation, and c) missions 7 and 8, FGS Anthesis*

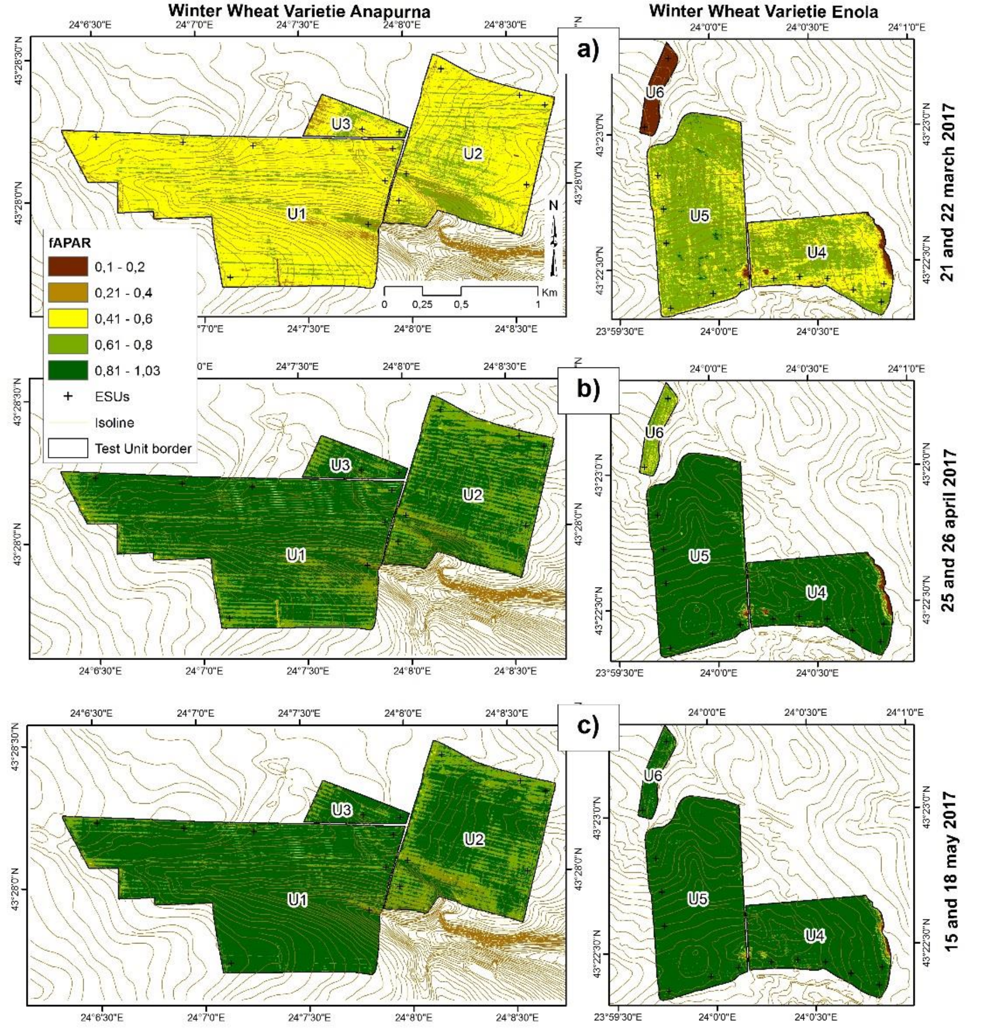


*Fig. 4. Maps of fAPAR of winter wheat crops in the studied Units composed by applying an regression model based on the OSAVI vegetation index on images from Parrot Sequoia UAV multispectral camera obtained from UAV flight missions: a) missions 3 and 4, FGS Tiller production, b) missions 5 and 6, FGS Stem elongation, and c) missions 7 and 8, FGS Anthesis*

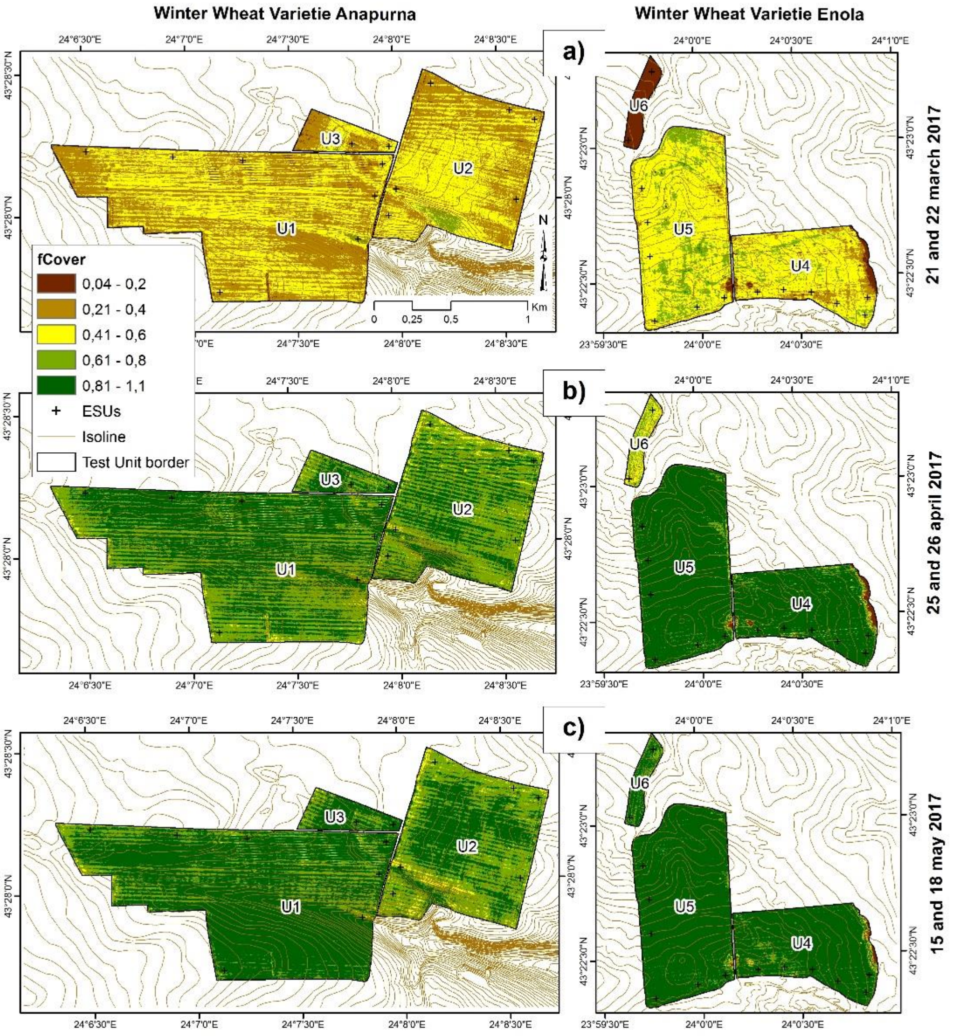


*Fig. 5. Maps of fCOVER of winter wheat crops in the studied Units composed by applying an regression model based on the OSAVI vegetation index on images from Parrot Sequoia UAV multispectral camera obtained from UAV flight missions: a) missions 3 and 4, FGS Tiller production, b) missions 5 and 6, FGS Stem elongation, and c) missions 7 and 8, FGS Anthesis*

On the drawn maps of the other two biophysical variables it may be seen that the recorded values of fAPAR and fCover on U1–U3 differ from those on U4–U5, Fig. 4 and 5, only in PGS *Tiller production: Zadoks 21 to 26,* Fig. 4a and 5a.

In Unit 6, in PGSs *Tiller production* and *Stem elongation*, the crop features lower values of both variables, Fig. 4a, 4b and 5a, 5b.

## Conclusions

The best predictor for all studied biophysical variables, was OSAVI — RMSE, for LAI is 0.90 $m^2/m^2$, for fAPAR — 0.07, and for fCover — 0.08.

The composed maps for LAI, fAPAR and fCOVER obtained by applying the respective regression model, based on the vegetation index OSAVI, on images from *Parrot Sequoia* UAV multispectral camera, correspond well with the spatial distribution of the values of the respective parameter, measured during the given field campaign.

Clearly expressed tendencies in the change of LAI values are observed. They increase up to PGS *Stem elongation*, whereas the rate of increase with the winter wheat crops of the *Anapurna* variety is smaller. The change is insignificant between PGSs *Stem elongation* and *Anthesis*.


## Acknowledgments

This study was conducted as part of the "Testing Sentinel-2 vegetation indices for the assessment of the state of winter crops in Bulgaria (TS2AgroBg)" project funded by the Government of the Republic of Bulgaria through ESA Contract 4000117474/16/NL/NDe under the Plan for European Cooperating States.

We pay our gratitude also to the farmers Mr. Nikolai and Tihomir Milovski, Mr. Svetlin Ilchovski, and the agronomist Mrs. Polina Marinska for the provided data and the carried out useful discussions.


## References


1. Fang, H., F. Baret, S. Plummer, G. Schaepman-Strub. An overview of global leaf area index (LAI): Methods, products, validation, and applications. *Reviews of Geophysics*, 2019, 57 (3).
2. Wójtowicz, M., A. Wójtowicz, J. Piekarczyk. Application of remote sensing methods in agriculture. *Communications in Biometry and Crop Science*, 2016, 11(1), 31–50.
3. Wenjuan, Li, M. Weiss, F. Waldner, *et al.* A Generic Algorithm to Estimate LAI, FAPAR and FCOVER Variables from SPOT4_HRVIR and Landsat Sensors: Evaluation of the Consistency and Comparison with Ground Measurements. *Remote Sensing*, 2015, 7 (11), 15494–15516.
4. Roumenina, E., P. Dimitrov, L. Filchev, G. Jelev. Validation of MERIS LAI and FAPAR products for winter wheat-sown test fields in North-East Bulgaria. *International Journal of Remote Sensing*, 2014, 35 (10), 3859–3874.
5. Weiss, M., F. Baret. S2ToolBox Level 2 products: LAI, FAPAR, FCOVER. *INRA*, 2016, V1.1, 53.

6. Shanmugapriya, P., S. Rathika, T. Ramesh, P. Janaki. Applications of Remote Sensing in Agriculture — A Review. *Int.J.Curr.Microbiol. App. Sci.*, 2019, 8(1): 2270–2283.
7. Haboudane, D., J. Miller, E. Pattey, *et al.* Hyper-spectral vegetation indices and novel algorithms for predicting green LAI of crop canopies: modeling and validation in the context of precision agriculture. *Remote Sensing of Environment*, 2004, 90, 337–352.
8. Sugiura, R., N. Noguchi, K. Ishii. Remote-sensing technology for vegetation monitoring using an unmanned helicopter. *Biosyst. Eng.*, 2005, 90, 369–379.
9. Hunt, E., W. Hively, S. Fujikawa, *et al.* Acquisition of NIR-green-blue digital photographs from unmanned aircraft for crop monitoring. *Remote Sensing*, 2010, 2(1), 290–305.
10. Schirrmann, M., A. Giebel, F. Gleiniger, *et al.* Dammer. Monitoring Agronomic Parameters of Winter Wheat Crops with Low-Cost UAV Imagery. *Remote Sensing*, 2016, 8(9), 706.
11. Holman, F., A. Riche, A. Michalski, *et al.* High Throughput Field Phenotyping of Wheat Plant Height and Growth Rate in Field Plot Trials Using UAV Based Remote Sensing. *Remote Sensing*, 2016, 8 (12), 1031.
12. Yue, J., H. Feng, X. Jin, *et al.* A Comparison of Crop Parameters Estimation Using Images from UAV-Mounted Snapshot Hyperspectral Sensor and High-Definition Digital Camera. *Remote Sensing*, 2018, 10(7), 1138.
13. Kolchakov, V., M. Kercheva, M. Banov, *et al.* Complex evaluation of winter wheat growing conditions in Northwestern Bulgaria. *Proceedings of the 10-th International Soil Congress "Successful Transformation toward Land Degradation Neutrality: Future Perspective"*, 17–19 June 2019, Ankara, Turkey, 10, 482–487.
14. Zadoks, J., T. Chang, C. Konzak. A decimal code for the growth stages of cereals. *Weed Research*, 1974, 14, 415–421.
15. Decagon Devices. AccuPAR PAR/LAI Ceptometer, Model LP-80. Operator's Manual Version June 20, 2014, 78.
16. Parrot Sequoia. Available online: https://community.parrot.com/t5/Sequoia/bd-p/Sequoia (accessed on 18.12.2019).
17. Gitelson, A., Y. Gritz, M. Merzlyak. Relationships between leaf chlorophyll content and spectral reflectance and algorithms for non-destructive chlorophyll assessment in higher plant leaves. *Journal of Plant Physiology*, 2003, 160, 271–282.
18. Gitelson, A., G. Keydan, M. Merzlyak. Three-band model for noninvasive estimation of chlo-rophyll, carotenoids, and anthocyanin contents in higher plant leaves. *Geophysical Research Letters*, 2006, 33, L11402.
19. Jordan, C. Derivation of leaf-area index from quality of light on the forest floor. *Ecology*, 1969, 50, 663–666.
20. Gitelson, A., Y. Kaufman, M. Merzlyak. Use of a green channel in remote sensing of global vegetation from EOS-MODIS. *Remote Sensing of Environment*, 1996, 58, 289–298.
21. Rouse, J., R. Haas, J. Schell, D. Deering. Monitoring vegetation systems in the great plains with ERTS. *In: Third ERTS Symposium, NASA SP-351*, 1973, vol. 1, NASA, Washington, DC, 309–317.

22. Rondeaux, G., M. Steven, F. Baret. Optimization of soil-adjusted vegetation indices. *Remote Sensing of Environment*, 1996. 55(2), 95–107.
23. Gitelson, A., M. Merzlyak. Spectral reflectance changes associated with autumn senescence of Aesculus hippocastanum L. and Acer platanoides L. Leaves. Spectral features and relation to chloro-phyll estimation. *Journal of Plant Physiology*, 1994, 143, 286–292.
24. Gitelson, A., Y. Kaufman, R. Stark, D. Rundquist. Novel algorithms for remote estimation of vegeta-tion fraction. *Remote Sensing of Environment*, 2002, 80, 76–87.
25. Gitelson, A. Wide Dynamic Range Vegetation Index for Remote Quantification of Biophysical Charac-teristics of Vegetation. *Journal of Plant Physiology*, 2004, 161. 165–173.

## КАРТОГРАФИРАНЕ НА БИОФИЗИЧНИ ПРОМЕНЛИВИ НА ПОСЕВИ ОТ ЗИМНА ПШЕНИЦА С ИЗПОЛЗВАНЕ НА МНОГОКАНАЛНИ ИЗОБРАЖЕНИЯ ОТ БЛА

***Г. Желев, П. Димитров, Е. Руменина***

**Резюме**

В статията са представени резултати от проведено изследване с цел картографиране на динамиката на биофизични променливи на посеви от зимна пшеница в различни фенологични фази чрез използване на данни, получени от безпилотен летателен апарат (БЛА) с многоканална камера. Изследваните биофизични променливи са индекс на листната повърхност (LAI), дял на абсорбираната фотосинтетично активна радиация (fAPAR) и дял от повърхността на почвата, покрита с растителност (fCover). През селскостопанската година 2016/2017 са проведени 4 полеви кампании (ПК) в 6 полета, стопанисвани от фермери, засети с два сорта зимна пшеница. В рамките на ПК са реализирани 8 полетни мисии с БЛА. Съставени и оценени са линейни и експоненциални регресионни модели за изчисляване на биофизичните променливи на посевите на базата на набор от вегетационни индекси (ВИ). Като най-добър предиктор за всички биофизични променливи е определен OSAVI (RMSE е 0.90 $m^2/m^2$, 0.07 и 0.08, съответно за LAI, fAPAR, и fCover). Избраните модели са използвани за съставяне на карти на LAI, fAPAR и fCover на изследваните полета. Картите в значителна степен отговарят на пространственото разпределение на стойностите на съответната биофизична променлива измерени по време на дадената полева кампания.

Bulgarian Academy of Sciences. Space Research and Technology Institute.
Aerospace Research in Bulgaria. 34, 2022, Sofia

DOI: https://doi.org/10.3897/arb.v34.e03

# POLARIMETRIC ANALYSIS OF ALOS PALSAR DATA (POL-SAR) OVER TEST AREAS IN NORTH-WEST BULGARIA — POLARIMETRIC DESCRIPTORS, DECOMPOSITIONS AND CLASSIFICATIONS

***Zlatomir Dimitrov***

*Space Research and Technology Institute — Bulgarian Academy of Sciences*
*e-mail: zlatomir.dimitrov@space.bas.bg*

***Keywords:*** *POL-SAR, Polarimetry, ALOS1 PALSAR, Polarimetric coherences, Polarimetric decompositions*

***Abstract***

*This study is focused on utilizing full-polarimetric L-band radar data from ALOS PALSAR (JAXA) by means of Polarimetry (POL-SAR), over mountainous test sites in Bulgaria. General aim is to show feasibility of the Polarimetry to describe natural targets, which exhibits various scattering mechanisms in respect to their bio-physical and geometrical properties. Firstly, the importance of Covariance and Coherent matrices is shown which is followed by calculation of the polarimetric coherences with their particular significance. The mathematical and physical model based decompositions are applied to describe backscattering media from scattering mechanisms. Radar indices resulted from H/A/α-decomposition showed randomization of scattering mechanisms over forest areas, whilst two major scattering mechanisms are observed mainly in crop lands. A comparison is made between polarimetric descriptors from acquisitions in different seasonality over mountainous forest and agricultural lands. Polarimetric segmentations and classifications are applied, with 8 (H/A) and 16 (H/A/α) components. Finally, a forest mask is proposed based on relevant polarimetric descriptors. Study showed good utilization and importance of the full-polarimetric L-band SAR data, derived from ALOS PALSAR, in natural targets and forest areas. This report resulted from a course GEO414 — "Polarimetrie" held at the University of Jena, Lehrstuhl für Fernerkundung, in the framework of ERASMUS+, with the kind support of — Dr. T. Jagdhuber (DLR) and Prof. C. Schmullius.*

## Introduction

Radar polarimetry (POL-SAR) is essential technique in polarimetric SAR analysis exploiting relation of polarization states to the geometrical properties and physical state of the scattering objects within scattering media [1]. The type of polarimetric content from dual- or quad-polarimetric datasets is essential for the accuracy of natural media classifications [2]. The Advanced Land Observing Satellite (ALOS) is Japan's most successful full-polarimetric EO satellite by its Phased Array L-band SAR (PALSAR) instrument launched in 2006 [3]. Due to better sensitivity of L-band to the vegetation, moreover by means of polarimetry at the forest volume, PALSAR is preferable instrument for forest structure information extraction [1, 4]. To link SAR observables with structure of the scattering media, target decomposition theory is introduced where modeling the backscatter with certain reflection symmetry is derived [5]. Benefits of model based approach for scattering power decomposition gives better understanding of volume backscatter and discrimination of vegetation from oriented urban areas using PALSAR PLR data [6]. Thus, an advanced approaches for modeling depolarization of soil-trunk double bounce scattering are proposed focusing on extended Fresnel scattering [7].

In this study general application of Polarimetry (POL-SAR) is considered with emphasis on natural targets. Utilization of ALOS1-PALSAR full-pol SAR data is made in mountainous and flat area with variety of land cover. Outcomes of the polarimetric coherences over natural scattering media is considered. Accent is given on decomposition theorems such as Eigen-based (H/A/α) and physical model based (Yamaguchi-3, Freeman-2) including variety of polarimetric descriptors and radar indices (e.g. RVI). Polarimetric segmentations and classifications are involved where, finally, a Forest/Non-forest mask is proposed. Processing and analysis of PALSAR scenes is performed within PolSARPro v.5 (software by IETR, Prof. E. Pottier) without geocoding in Radar geometry. Geocoding is made in ESA-SNAP.

This report is resulted from the Master course — GEO414 "Polarimetrie", held at the University of Jena (FSU-Jena), Lehrstuhl für Fernerkundung, with the kind support of lecturer Dr. Thomas Jagdhuber and Prof. Christiane Schmullius.

The report was also presented in Bulgarian on the Seventeenth International Scientific Conference "Space, Ecology, Safety" — SES 2021, Sofia, 20–22 October 2021, held online, at Space Research and Technology Institute — BAS.

**Polarimetry basics**

The formulation of POL-SAR begins with the Maxwell's laws for electromagnetic waves crossing over the Stokes parameters. General statement of the Jones vector formalism considers the important property of the Electric vector orientation in space [5]. The polarization ellipse of the Electric vector defines general property in polarimetry, namely — *linear, circular* and *elliptical* polarization states [8]. Hence, the polarimetric states of the emitted and received chirp is formulated as a Scattering (Sinclair's) matrix considering linear basis (*H, V)* where:

$$(1) \qquad [S] = \begin{bmatrix} S_{hh} & S_{hv} \\ S_{vh} & S_{vv} \end{bmatrix}$$

In general, polarimetric theory assumes *reciprocity* that considers equilibrium of the cross-pols — $S_{hv} = S_{vh}$. Physical process of the backscatter considers two types of scattering targets — deterministic (or coherent) and non-deterministic (or natural/distributed). Considering the point target vector, *coherent targets* are point scatterers, the amplitude of the point target vector holds most of the backscattered energy; whereas, at the *natural targets* — backscattered energy is distributed over individual backscatterers thus vector sum is random [5]. Therefore, describing scattering process from natural media in the case of reciprocity, the Second order statistics is defined in terms of two rang-3 Hermitian matrices [8] such as:

- Covariance Matrix — **[C3]**

$$(2)\quad \overrightarrow{k_{3L}} = \begin{pmatrix} S_{HH} & \sqrt{2}S_{XX} & S_{VV} \end{pmatrix}^T \to [C] = \langle \overrightarrow{k_{3L}} \cdot \vec{k}_{3L}^{*T} \rangle = \begin{bmatrix} C_{11} & C_{12} & C_{13} \\ C_{21}^* & C_{22} & C_{23} \\ C_{31}^* & C_{32}^* & C_{33} \end{bmatrix} =$$

$$\begin{bmatrix} |S_{HH}|^2 & \sqrt{2}S_{HH}S_{XX}^* & S_{HH}S_{VV}^* \\ \sqrt{2}S_{HH}^*S_{XX} & 2|S_{XX}|^2 & \sqrt{2}S_{XX}S_{VV}^* \\ S_{HH}^*S_{VV} & \sqrt{2}S_{XX}^*S_{VV} & |S_{VV}|^2 \end{bmatrix},$$

where: $S_{XX} = S_{HV} = S_{VH}\ is\ cross-polarized\ scattering\ for\ monostatic\ systems.$

- Coherence Matrix — **[T3]:**

$$(3)\quad \overrightarrow{k_{3P}} = \frac{1}{\sqrt{2}}(S_{HH}+S_{VV} \quad S_{HH}-S_{VV} \quad S_{HV}+S_{VH})^T \to [T] = \langle \overrightarrow{k_{3P}} \cdot \vec{k}_{3P}^{*T} \rangle = \begin{bmatrix} T_{11} & T_{12} & T_{13} \\ T_{21}^* & T_{22} & T_{23} \\ T_{31}^* & T_{32}^* & T_{33} \end{bmatrix}$$

$$= \frac{1}{2}\begin{bmatrix} |S_{HH}+S_{VV}|^2 & (S_{HH}+S_{VV})(S_{HH}-S_{VV})^* & 2(S_{HH}+S_{VV})S_{XX}^* \\ (S_{HH}+S_{VV})^*(S_{HH}-S_{VV}) & |S_{HH}-S_{VV}|^2 & 2(S_{HH}-S_{VV})S_{XX}^* \\ 2(S_{HH}+S_{VV})^*S_{XX} & 2(S_{HH}-S_{VV})^*S_{XX} & 4|S_{XX}|^2 \end{bmatrix}$$

Important is to be stated, that the [$T_3$] and [$C_3$] are derived from Pauli and Lexicographic target vectors respectively. Those matrices are the starting point for polarimetric analysis in natural media, in order to describe depolarization.

## Study area and polarimetric SAR data

In this survey, polarimetric SAR data from ALOS-1 PALSAR (JAXA) — PLR datasets are used, provided via PI proposal from ESA Third Party mission. The test area (AOI) is selected according to the test sites from the Author's PhD study, located in the North-West Bulgaria, along Stara Planina mountain massif and the Danube River valley. It comprises forest areas in rugged terrain with steep slopes, also characterized with many agricultural lands with crop types for the time of acquisitions — maize, corn, and sunflower. Rural areas are small, neighboring with reservoirs and standing water bodies. Many grasslands are also common in the forest areas.

*Table 1. Scene parameters of ALOS PALSAR –full polarimetric (PLR) SAR data acquisition parameters, over selected test sites*

| PARAMETERS | SCENE - 1 | SCENE - 2 | SCENE - 3 |
|---|---|---|---|
| **Date of acquisition** | 2007-05-10 | 2007-11-10 | 2009-05-15 |
| **Product type** | PLR_SLC_1P | PLR_SLC_1P | PLR_SLC_1P |
| **Orbit** | Ascending | Ascending | Ascending |

| | | | |
|---|---|---|---|
| **Polarimetric channels** | HH, HV, VH, VV | HH, HV, VH, VV | HH, HV, VH, VV |
| **Azimuth Res.** | 3.57063 [m] | 4.03544 [m] | 4.03577 [m] |
| **Range Res.** | 9.36852 [m] | 9.47558 [m] | 9.47558 [m] |
| **Incidence angle** | 23.937 [deg] | 23.944 [deg] | 25.764 [deg] |
| **Lines** | 1 344 | 1 344 | 1 216 |
| **Rows** | 24 320 | 24 512 | 22 528 |
| **Type and format** | Level 1.1 / CEOS | Level 1.1 / CEOS | Level 1.1/CEOS |
| **Test site in PhD** | TS20 | TS20 | TS21 |
| **Comment over the selected chip** | Forest area and a bit of agricultures. | Forest area and a bit of agricultures. | Large agricultural diversity, forests. |
| **Meteo situation in the time of acquisition** | In Spring; Clear and calm weather, no rain. T.16°C; Hum.59%. | Cold Autumn, wind and rain; Severe weather. T.3°C; Hum. 69%. | Warm Spring, with precipitation. Calm and wet weather. T.20°C; Hum. 78%. |
| **Referent MODIS imagery in the day of acquisition** |  |  |  |

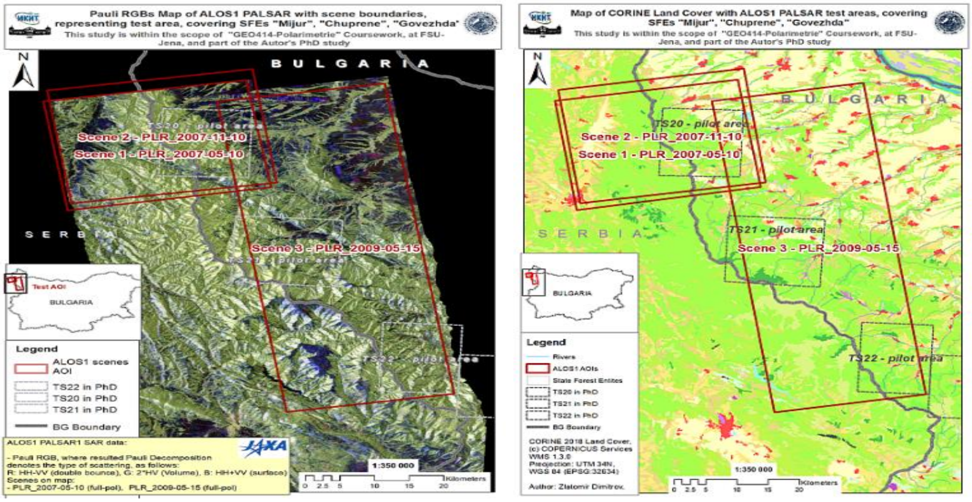


*Fig 1. Test sites boundaries, resulted from ALOS1 scenes footprint are presented, over two Pauli-Basis (RGB) from two PALSAR acquisitions (left), over CORINE land cover (right). The test sites boundaries from Author's PhD study are also pictured, in greyish dashed.*

## Polarimetric Methods Applied and Results

### Analysis via single matrix elements

On first instance analysis is made via Sinclair's elements from scattering matrix [$S_2$], valid for coherent targets only [5]. Testing correlation of the matrix elements in between showed low correlation at $S_{11}$ vs. $S_{12}$, correlation at $S_{11}$ vs. $S_{22}$, and best correlation between $S_{12}$ vs. $S_{21}$ which is true for monostatic systems.

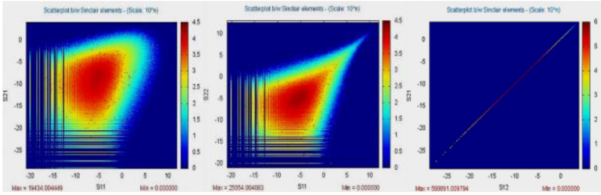

*Fig. 2. Correlative plots between Sinclair's elements of [S]; from left to right: S21~S11, S22~S11, S21~S12*

The on-screen analysis between Scene-1 and 2 showed general difference within normalized radar cross-section, in-between the co-pol and cross-pol channels of [$S_2$] mainly over non-forest area. Geometric distortions — foreshortening in mountainous forest gives high backscatter, with differences more than 5 dB. Highest backscatter difference is observed over agricultural lands where some of the crops produces high backscatter toward sensor in Sinclair's elements with polarizations HH and VV; whilst, the HV & VH decreased with more than 20 dB (see Fig. 3).

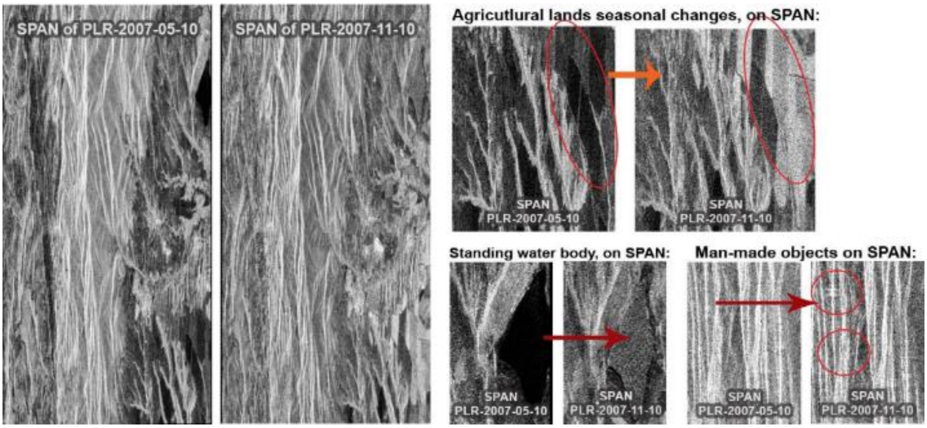


*Fig. 3. Total backscattered power — SPAN of scattering matrix [S], comparison between Scene — 1 and 2 in two different areas of land cover types that exhibits differences in the backscatter power, registered by the sensor (©ESA/JAXA – PALSAR)*

The analysis by means of SPAN — representing the total backscattered power, revealed lower backscatter in forest areas, because of the leaf-off in forest. Over the standing water body in November's scene a strong backscatter toward sensor is observed, which points out a rough surface, possibly caused by a rainfall.

Direct interpretation of [$C_3$] and [$T_3$] matrix elements showed following dependencies in vegetation (see Fig. 4): registered backscatter intensity on $C_{11}$ representing HH-polarization is equal with the $T_{11}$; more than 19 dB is observed between $C_{11}$ and $C_{22}$, representing Volume backscatter. Above 10 dB difference is observed between $C_{22}$ and $T_{22}$, and $C_{22}$ and $T_{33}$ over distributed targets, although the calculated total power in SPAN is very high (ab. 0 dB). That leads to strong backscatter toward sensor, from natural targets. The $C_{33}$ representing VV polarization in common cases is higher than $C_{11}$ over distributed targets.

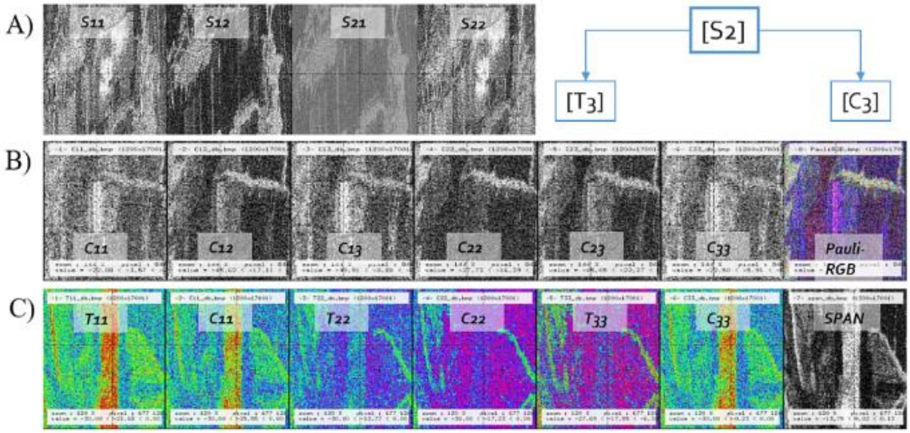


*Fig. 4. Matrix elements representation over agriculture — A) Sinclair's (Scattering Matrix) elements; B) Second order statistics of Covariance matrix elements, with Pauli-Basis; C) Second order statistics of Coherence matrix elements, with SPAN* (©ESA/JAXA – PALSAR)

Analyzing urban areas, where the degree of depolarization is very low, high backscatter is observed with almost equal intensity of $T_{11}$, $C_{11}$ $T_{22}$, but lower in $C_{33}$.

Therefore, considering the $[T_3]$ and $[C_3]$ matrix elements, it could be concluded that Coherency matrix is preferable in Polarimetric analysis of non-deterministic (distributed) targets, due to its direct interpretation of scattering mechanisms. In spite, usage of Covariance matrix should be prompt, when aiming the direct interpretation of the polarimetric channels information.

### Polarimetric speckle filtering

In polarimetric analyses speckle filtering is essential in order to reduce the ambiguities between systematical noise and useful information. In general case it is some kind of tradeoff between spatial accuracy and characteristic noise suppression [8]. Variety of polarimetric filtering techniques exists, where the mono-temporal non-adaptive/adaptive polarimetric speckle filters are related to the spatial domain, where incoherent averaging is performed to the $[T_3]$ and $[C_3]$ [9].

To test polarimetric speckle filtering over the PALSAR polarimetric imageries, two type of filters are used: BOXCAR and Refined Lee. Result is presented in Fig. 5, where different size of averaging windows is used, over coherent and non-coherent targets [9].

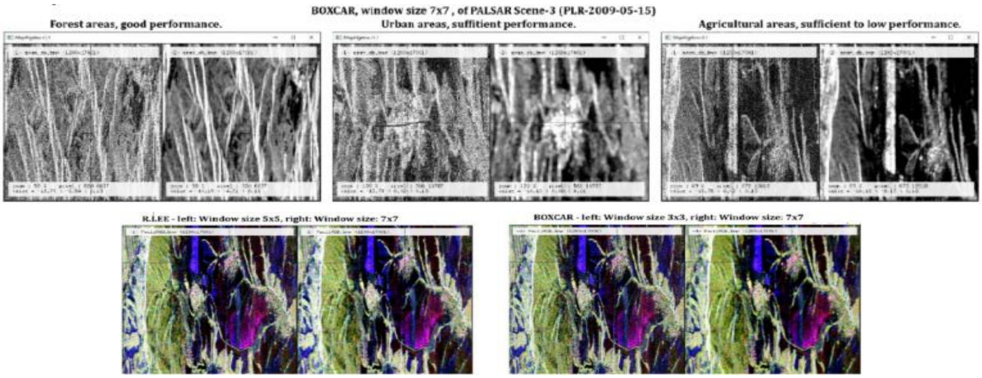


*Fig. 5. Speckle filters BOXCAR and R. Lee — applied over coherent and non-coherent targets, using SPAN and Pauli-Basis (Pauli-RGB) of Scene-3, with different windows*

Window sizes of 5×5 or 7x7 are found to be reasonable over natural targets.

**Polarimetric coherences — analysis in *HH, VV* and *LL, RR* basis**

Polarimetric coherences are complex correlation coefficients between off-diagonal complex Hermitian matrices elements, with indexes — $H_{12}$, $H_{13}$, $H_{23}$ where "H" is element from $[T_3]$ or $[C_3]$. Correlation coefficients could be calculated either in Linear (*HH, VV*) or in Circular (*LL, RR*) basis [8]. Formulation of the correlation coefficients for natural targets, tested in the study, is:

$$(5)\quad \gamma_{HH\pm VV} = \gamma_{T12} = Ro12 = \frac{\langle T_{12}\rangle}{\sqrt{\langle T_{11}\rangle\langle T_{22}\rangle}} = \frac{\langle (S_{hh}+S_{vv})(S_{hh}-S_{vv})^*\rangle}{\sqrt{\langle |S_{hh}+S_{vv}|^2\rangle\langle |S_{hh}-S_{vv}|^2\rangle}}$$

$$(6)\quad \gamma_{(HH+VV)HV} = \gamma_{T13} = Ro13 = \frac{\langle T_{13}\rangle}{\sqrt{\langle T_{11}\rangle\langle T_{33}\rangle}} = \frac{\langle 2(S_{hh}+S_{vv})S_{XX}{}^*\rangle}{\sqrt{\langle |S_{hh}+S_{vv}|^2\rangle\langle 4|S_{XX}|^2\rangle}}$$

$$(7)\quad \gamma_{(HH-VV)HV} = \gamma_{T23} = Ro23 = \frac{\langle T_{23}\rangle}{\sqrt{\langle T_{22}\rangle\langle T_{33}\rangle}} = \frac{\langle 2(S_{hh}-S_{vv})S_{XX}{}^*\rangle}{\sqrt{\langle |S_{hh}-S_{vv}|^2\rangle\langle 4|S_{XX}|^2\rangle}}$$

$$(8)\quad \gamma_{HHVV} = \gamma_{C13} = Ro13 = \frac{\langle C_{13}\rangle}{\sqrt{\langle C_{11}\rangle\langle C_{33}\rangle}} = \langle S_{hh}S_{vv}^*\rangle/\sqrt{\langle |S_{hh}|^2\rangle\langle |S_{vv}|^2\rangle}$$

$$(9)\quad \gamma_{RRLL} = \gamma_{CCC} = C.C.C.\,and\ |C.C.C.| = \frac{\langle C_{lr}\rangle}{\sqrt{\langle C_{ll}\rangle\langle C_{rr}\rangle}} = \frac{\langle S_{ll}S_{rr}^*\rangle}{\sqrt{\langle |S_{ll}|^2\rangle\langle |S_{rr}|^2\rangle}}$$

Correlation coefficients are calculated with size of the averaging window — 7x7, for whole PALSAR — PLR data.

**Analysis of Ro12, Ro13 and Ro23, derived from $[T_3]$:**

Statistics have been calculated, showing mean value of coherences ab. 0.16, pointing out low coherence between particular scattering mechanisms; see table.

*Table 2. Statistics and distribution of the Correlation coefficients based on [T3], of Scene-3*

| Modulus of: | **Ro12 ($\gamma_{HH \pm VV}$)** | **Ro13 ($\gamma_{(HH+VV)HV)}$)** | **Ro23 ($\gamma_{(HH-VV)HV}$)** |
|---|---|---|---|
| Max | 0.9633 | 0.8844 | 0.9165 |
| Mean | 0.1806 | 0.1548 | 0.1604 |
| Median | 0.1713 | 0.1557 | 0.1521 |
| Histograms | 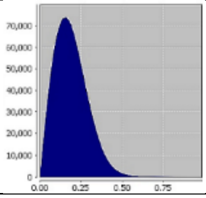 | 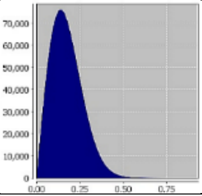 | 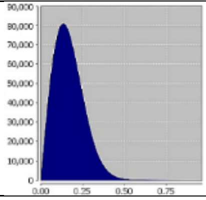 |

Highest correlation at the modulus of the correlation coefficients is found over agricultural areas, where the phase shows better consistency than the modulus, with good object's delineation. From the three coherences, the **Ro12($\gamma_{T12}$)** — shows the best polarimetric correlation, with modulus of ab. 0.67–0.81 over crops (Fig. 6).

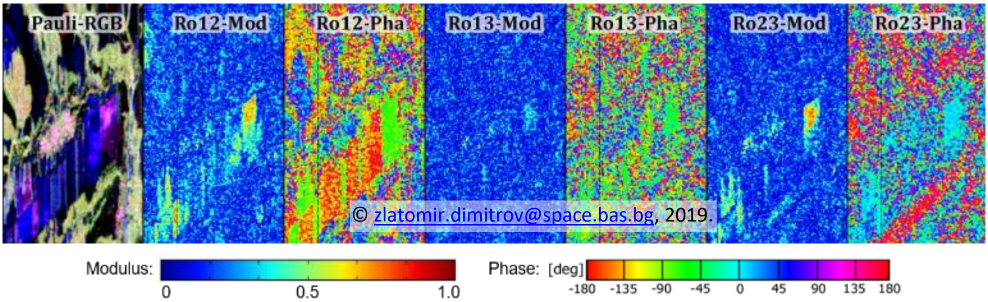


*Fig. 6. Polarimetric correlation coefficients, derived from — [T3]: Ro12, Ro13 and Ro23 with Pauli Decomposition* *(©ESA/JAXA – PALSAR)*

In forest and urban areas low coherence is observed. Phase is showing good consistency and distinct landcover objects are recognizable. In sparse or non-forest areas, angle between scattering mechanisms is: -90 deg (yellowish in Fig. 6). Over agricultural areas the phase angle is homogenous (green and red), where crops could be delineated. Over forest areas, phase keep random values. The **Ro23($\gamma_{T23}$)** also shows good polarimetric correlation over some distinct agricultural areas, with modulus of 0.5. Phase of Ro23 suggests changes in forest structure over flat forest with values of -170 deg (reddish in Fig. 6). Phase over neighboring agriculture varies from -45 to 45 deg (bluish in Fig. 6). Interestingly, the **Ro13($\gamma_{T13}$)** in general is noisy, except at the high mountain. There, phase angle delineates very well grassland from forest, with values below 130 deg; modulus shows less consistency (see Fig.7).

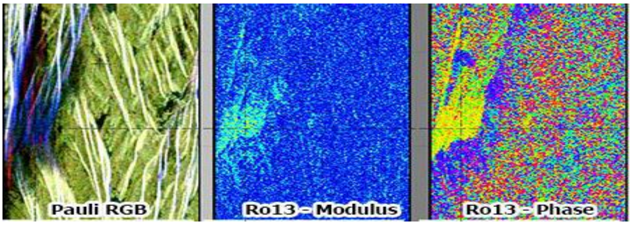


*Fig. 7. Top hill area in the mountains on Scene-3, which exhibits surface scattering. This is the only area where the modulus of Ro13 is showing values ab. 0.6. In spite, grassland could be easily delineated from forest. (©ESA/JAXA – PALSAR).*

**Interpretation** of the complex polarimetric coherences derived from [$T_3$], should reveal the apposition of scattering mechanisms within the scattering media. Higher modulus (amplitude) of polarimetric coherence means equal input of those scattering mechanisms. Phase angle suggests the height of the scattering phase centers — e.g. vertical location of canonical scattering mechanisms. Hence, the high values of Ro12 ($\gamma_{T12}$) should express equal contribution of the Dihedral and Surface scattering. Over natural media such as forests, input of scattering mechanisms is highly varying, thus modulus trends to zero; phase angle is random, which suggests different height of the canonical scattering mechanisms. The top-hill area where Ro13 ($\gamma_{T13}$) modulus is high is due to presence of surface scattering.

**Analysis of Ro13, C.C.C and Normalized C.C.C, derived from [$C_3$]:**

Contrariwise, the polarimetric coherences derived from [$C_3$] are showing higher correlation, whilst the Ro13 ($\gamma_{C13}$) shows highest mean correlation at all.

*Table 3. Statistics and distribution of the Correlation coefficients based on [C3], of Scene-3*

| Modulus of: | **Ro13 ($\gamma_{HHVV}$)** | **C.C.C ($\gamma_{LLRR}$)** |
|---|---|---|
| Max | 0.9971 | 0.9363 |
| Mean | 0.4261 | 0.1806 |
| Median | 0.4118 | 0.1713 |
| Histograms | 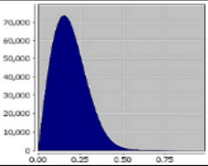 | 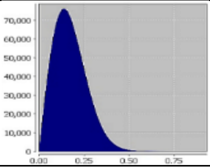 |

The **Ro13($\gamma_{HHVV}$)** derived from [$C_3$] allows direct interpretation on polarization result from correlation of HH vs. VV at target vector. Considering the Ro13 ($\gamma_{HHVV}$), highest coherence is observed over deforested areas in the mountains, or over crops where values in the modulus reaches up to 0.98! Thus, those areas are very well recognizable. Thus, phase of Ro13 ($\gamma_{HHVV}$) is circulating around zero degrees, with exception over natural media. Over forest modulus drops, showing no correlation. Considering the modulus of the polarimetric coherence in circular basis — *LL,RR*, shows high correlation at non-forest areas — especially agriculture where values are ab. 0.84, despite very low values over forest areas. The phase of the Circular Correlation Coefficient **(C.C.C.)** there, is much more consistent with homogenous trend about 180 deg, over grassland and crops. The Normalized C.C.C. showed exactly the opposite trend in modulus — high values over forest areas.

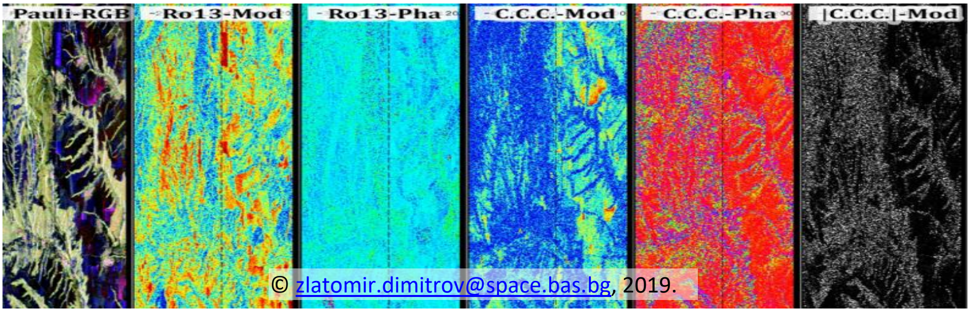


*Fig. 8. Polarimetric coherences derived from Coherency matrix, Scene-3* (©ESA/JAXA – PALSAR)

Considering direct **interpretation**, the Ro13 ($\gamma_{HHVV}$) shows high correlation over areas with surface scattering, e.g. grasslands and agriculture. In such scattering media, energy loss is not so much, thus the depolarization is less and phase angle between HH and VV vectors stays almost constant. This is not the case in forest areas where volume scattering is accompanied by strong depolarization and energy loss. Interestingly, switching into *LL,RR* basis the C.C.C. ($\gamma_{LLRR}$) delineates very well forest from non-forest area, which is a result from helix backscatter in the media.

**Polarimetric Decompositions — mathematical and physical based**

Polarimetric decompositions express the measured backscattered signal in scattering matrix, as a sum of particular responses of simple canonical objects [5]. Considering coherent deterministic targets, a coherent decomposition theorems exists, such as Pauli, Kroager, via Scattering matrix. Considering non-deterministic targets, where complete depolarization is observed, the incoherent decompositions are applied via Hermitian matrices. Those decomposition theorems are based either on physical model such as Freeman-Durden, Van-Zyl or based on mathematical based approach such as Eigen-based — H/A/alpha. Decomposition theorems are summarized on the diagram below in Fig. 9 [8]. Should be noted that for incoherent decomposition theorems because presence of non-deterministic scatterers averaging is needed according to the coherence test based on Touzi criterion [5].

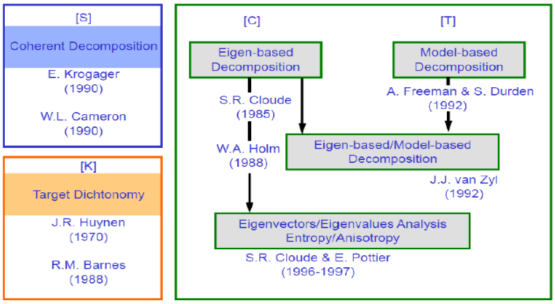


*Fig. 9. Summary of Polarimetric Decomposition Theorems [8]*

**Pauli coherent Decomposition, via [$S_2$]**

The Pauli coherent decomposition theorem is a coherent decomposition theorem, used to describe deterministic targets via [$S_2$]. It express the measured scattering matrix in the Pauli basis, with the following assumption [10]:

(10) Dihedral scattering, or Double Bounce: $\boldsymbol{DB} = \frac{1}{2}\langle|S_{HH} - S_{VV}|^2\rangle$

(11) Volume scattering, or Dihedral rotated by $-{}^{\pi}/_{4}$ : $\boldsymbol{VOL} = 2\langle|S_{XX}|^2\rangle$

(12) Surface, or odd scattering (Single bounce): $\boldsymbol{SB} = \frac{1}{2}\langle|S_{HH} + S_{VV}|^2\rangle$

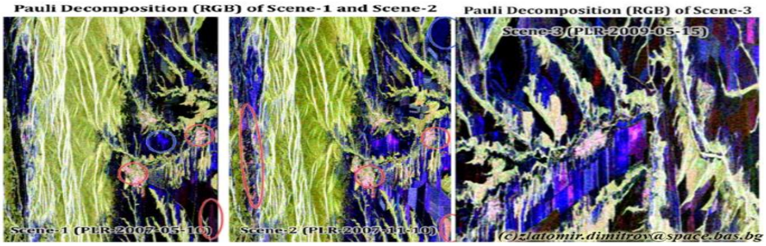


*Fig. 10. Pauli coherent Decomposition applied on whole three scenes in different seasonality. In general: Bluish depicts general odd scattering (or Surface), Reddish — even scattering (double bounce), Greenish — multiple scattering (volume). (©ESA/JAXA – PALSAR).*

The Pauli decomposition could be related to the Pauli-Basis (*Pauli-RGB*). The Pauli-coherent decomposition is useful tool in polarimetric analysis because it gives a raw idea over mixture of scattering mechanisms within the backscatter.

From the theorem applied, the following dependencies were observed: at Scene-1 general surface scattering (SB) is observed over crops, bare soils, and some grassland. At Scene-2, and 3, situation is the same with contribution of particular surface scattering from the standing water body due to heavy rainfall at the time of acquisition! The agri-fields was observed to exhibits strong SB and pure DB, for instance from maize or winter crops; some particular agri-fields exhibits bluish to green color, possibly due to mixture of surface and helix scattering. Urban areas in all cases exhibits strong DB mixed with helix scattering (trees nearby). Of course, non-deterministic scatterers such as forest areas exhibits general volume and helix. Interestingly, during leaf-off period on Scene-2 (due to autumn) more DB scattering could be observed over forest revealing direct backscatter from trunks.

**Eigen-based incoherent decomposition — H/A/α, via [$T_3$]**

Derived from the diagonalization of the Coherency matrix, the Eigen-based decomposition represents [$T_3$] — as a sum of three individual [$T_1$] matrices. Those Hermitian matrices are derived from the eigenvectors ($u_i$) which elements are related to the eigenvalues ($\lambda_i$) where: $\infty < \lambda_1 < \lambda_2 < \lambda_3 < 0$ [10] used as Eigenvalues — RGB. Due to the orthogonality, each eigenvalue concerns pure scattering mechanism depicted by α, and orientation around Radar Line Of Sight (RLOS) by β. For interpretation, three well known functions of the eigenvalues are defined related to the physical properties of the scattering media:

(13) Entropy ($H$): $H = -\sum_{i=1}^{3} p_i log_3(p_i),\ p - probability: p_i = \lambda_i / \sum_{k=1}^{3} \lambda_k$

(14) Anisotropy ($A$): $A = \frac{\lambda_2 - \lambda_3}{\lambda_2 + \lambda_3}$

(15) Mean_alpha_angle ($\alpha$): $\bar{\alpha} = \sum_{i=1}^{3} p_i \alpha_i$

**Entropy** (as in Thermodynamics) is a measure of randomness within the scattering media; **Anisotropy** shows the significance of the second and third scattering mechanisms; **α-angle** controls the change of the scattering mechanisms.

**Interpretation** of Eigen-based decomposition could be performed either by analyses of H/A/α or by the eigenvectors-eigenvalues ($\lambda_i$) and their pseudo probabilities ($p_i$) despite all complement to each other [10]. Hence, at Scene-3, the calculated Eigenvalues-RGB image is showing equilibrium with the Pauli-decomposition (RGB) and consistency with the dominant scattering mechanisms.

Close analysis at the mountainous hilly area (peak "Mijur", see Fig. 11 — UP) at bluish areas on Eigenvalues-RGB, entropy (H) show low values pointing to isotropic surfaces with surface scattering (S). That is confirmed on alpha angle with values close to zero. In that case, the pseudo probability ($p_1$) shows importance of the first eigenvalue; Anisotropy is low, confirms that only one scattering mechanism contributes to the total power. Interesting situation with a close look over the neighboring **reddish strip** on Eigenvalues-RGB shows presence of strong dihedral scattering (D) with high H, A and $p_2$; α — angle points out *isotropic dipole* (**NOT dihedral [10]*) with values of 48 deg; *β* — is homogenous at that area showing small variations around RLOS with ab. 9.8 deg. Contrariwise, at the neighboring **forest area** (greenish on Eigenvalues-RGB), H — increases dramatically pointing out complete randomness of the scattering media; *α* — shows high consistency with this with values near 45 deg pointing to randomly oriented dipoles; *β* — lies within interval 28–90 deg, showing variations of orientation along RLOS; in forest area — $p_1$, $p_2$ and $p_3$ show importance of the second and third scattering mechanisms.

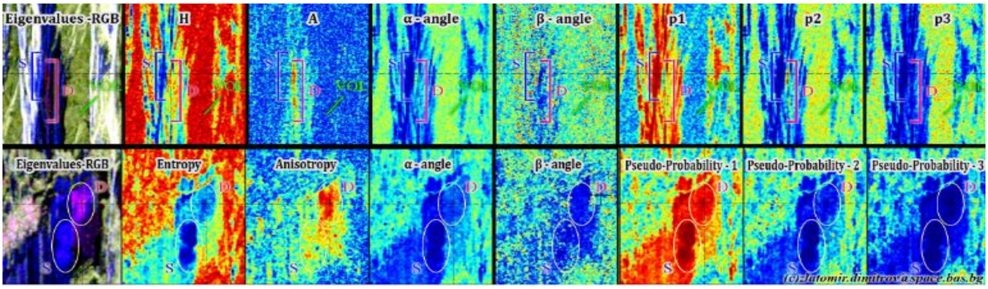


*Fig. 11. UP: Hilly area in the mountains near peak "Mijur", with bare grasslands and forest areas. DOWN: Agricultural area (Agri-area-2) with variety of crops at bottom of Scene-3, with urban area and sparse forest area (©ESA/JAXA – PALSAR)*

Over **agriculture area** (Fig. 11 — Agri-area-2), the bluish crops exhibits surface scattering (S) with very low H, $\alpha$-points to isotropic surface, and $p_i$ are showing significance of only one scattering mechanism. Whilst the magenta cropland exhibits very high Anisotropy (ab. 0.84) where $\alpha$ — shows values ab. 30 deg which trends to isotropic dipole; the $p_1$ shows one major scattering mechanism. **Sparse forest** follow same dependencies observed over forests in spite of the third scattering mechanism is less important ($p_3$). The **urban areas** exhibits small entropy which is improper interpretation possibly due to the higher averaging.

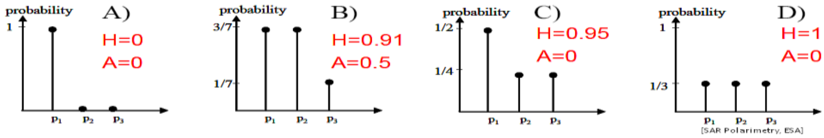


*Fig. 12. Contribution of scattering mechanisms to the backscatter based on probabilities, depicted from Entropy (H) and Anisotropy (A) [10]*

From the stated above it is clear that $p_i$, H and A control the number of scattering mechanisms (Fig. 12). To account for their contribution and thus to relate them to the physics of the scattering media, combinations of H and A are considered:

**A)** Only one mechanism, when H = 0, A = 0 : (1-H)(1-A)
**B)** Two major equal mechanisms, when H > 0.9, A > 0.5 : (HA)
**C)** Two mechanisms unequally strong, when H > 0.9, A = 0: (1-H)A
**D)** Three mechanisms equally strong, when H = 1, A = 0 : H(1-A)

Hereupon, the first dependency — **A)** contributes to the analysis stated above at Scene-3 over the mountainous hilly area (near peak "Mijur", see Fig. 13 — top), proving the availability of only one scattering mechanism over the bluish strip (S). Whilst, at neighboring reddish strip, the second dependency — **B)** proves the availability of two major scattering mechanisms, which leads to *isotropic dipoles*.

Forests areas exhibit three equal scattering mechanisms, according to dependency — **D**) where entropy is showing complete randomness of the scattering media.

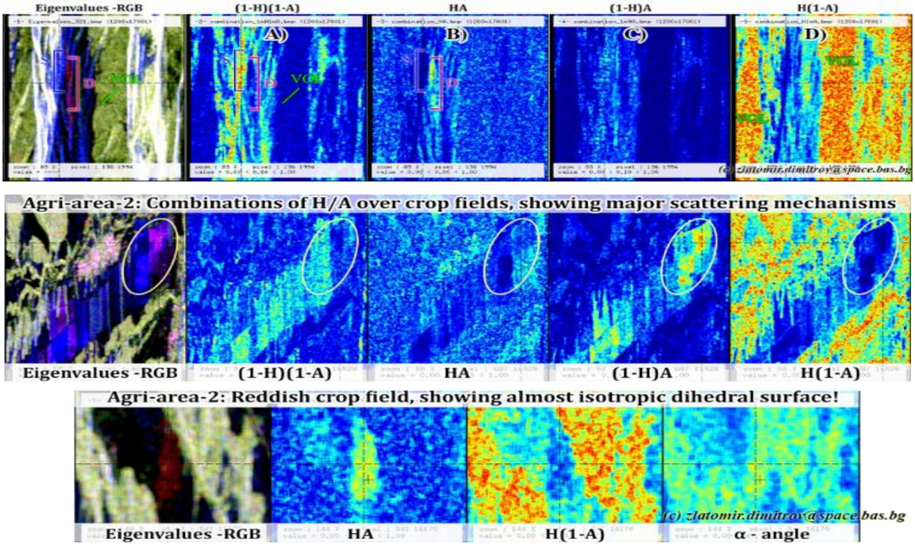


*Fig. 13. On Scene-3 — Top: Mountainous area near peak "Mijur"-reddish stripe that exhibits dihedral surrounding isotropic surfaces in bluish; middle: Agri-area-2, crop fields with diversity of H/A; bottom: Reddish crops having pure dihedral (©ESA/JAXA – PALSAR)*

Considering bottom of Scene-3 (Agri-area-2), whole H/A — combinations are observed where the magenta colored crops on Eigenvalues-RGB are kind of *anisotropic surface* with two mechanisms unequally strong (Fig. 13 — middle). A neighboring agri-field colored in pure-reddish on Eigenvalues-RGB (see Fig. 13 — bottom) should be an *isotropic dihedral* surface (*with $\alpha \approx 90°$ [10]*), showing high consistency with — **B)**. Despite, the $\alpha$-angle is ab. 45 deg, therefore it points to — pure volume scattering constructed from oriented dipoles [8, 10].

**Shannon Entropy and Radar Indices from Eigen-based decomposition**

Measuring the degree of randomness according to the degree of depolarization is also part or the mathematical model of Eigenbased-decomposition where the eigenvalues set of parameters allows the following formulations [8]:

(16) Shannon Entropy (**SE**): **I** − intensity, **P** − polarimetric phase contribtion :

$$\mathrm{SE} = SE_I\{Tr[T_3]\} + SE_p\left\{\frac{Det(T_3)}{Tr[T_3]}\right\}$$

(17) Radar Vegetation Index (**RVI**): $\mathrm{RVI} = \frac{4\lambda_3}{(\lambda_1+\lambda_2+\lambda_3)}, RVI \in (0, \frac{4}{3})$

(18) Pedestal Height (**PH**): $\mathrm{PH} = \frac{min(\lambda_1, \lambda_2, \lambda_3)}{max(\lambda_1, \lambda_2, \lambda_3)} = \frac{\lambda_3}{\lambda_1}, PD \in (0, 1)$

Shannon Entropy accounts about the randomization within scattering media by its intensity and polarimetric contribution term; RVI — accounts for the homogeneity in the orientation of the canonical objects; PD — accounts for the strength of backscattered power of the non-polarized signal [8]. Another SAR indices exists in addition and show the de-polarization within the scattering media, such as — *Polarization fraction* and *Perplexity*. Consistency of those indices depends on the wavelength, and full polarimetry to be provided. **Important:** polarimetric descriptors derived from H-A-α theorem are roll-invariant — they doesn’t rely on the rotation of the polarization ellipse around RLOS.

Shannon entropy normalized fractions — $SE_I$ and $SE_P$ — are showing particular sensitivity to the type and geometry of scattering media. Besides, high values on $SE_I$ well delineate coherent targets (like — build-up areas) but also foreshortenings.


*Fig. 14. Shannon Entropy — Intensity and Phase components, showing correlation with — build-up area (left), with foreshortening and forest density (right) (©ESA/JAXA – PALSAR)*

It is observed that $SE_I$ varies with the forest density, with values < 0.45 where changes relates also with variations in SPAN (see Fig. 14). Contrariwise, the polarimetric contribution term (e.g. Phase) is related to the degree of polarization, and shows high values |— e.g. *random oriented dipoles* in forest [10]. The $SE_P$ shows no-sensitivity on geometric distortions. Indication of depolarization due to anisotropic surfaces is showed over the *Perplexity index*, which correlates with — $SE_P$. The *Pedestal Height (PH)* index shows high degree of depolarization — $PH < 0.5$.

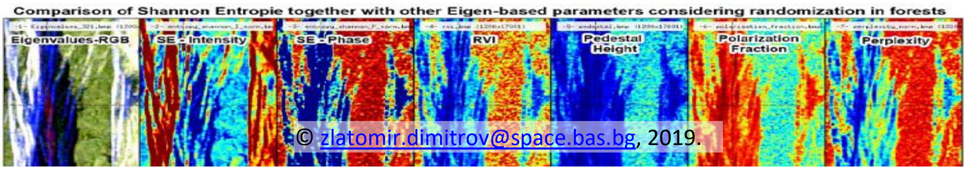


*Fig. 15. Comparison of Shannon Entropy ($SE_I$ and $SE_P$) with other SAR indices – RVI, PH, Polarization Fraction, and Perplexity accounting for depolarization in natural media*

Over Agricultural areas same dependencies are observed where the isotropic surfaces (with one/two major scattering mechanisms — bluish from the Eigenvalues — RGB) are having highest — $SE_I$, and *Polarization fraction*, and lowest — $SE_P$, *RVI* and *Perplexity index*. Considering *RVI*, over each forest type it shows high values — RVI > 0.45 (Fig. 16).

A **comparison between** Shannon Entropy — SE, and Neuman's Entropy — H — over *isotropic Bragg surfaces* (e.g. agricultural fields in bluish at Eigenvalues — RGB), H is very low contrary to the highest $SE_I$. Nonetheless, over such areas the H and $SE_I$ have same texture patterns in between. Over forest $SE_P$ have consistency with H, due to complete randomization. Could be concluded that, both entropies Neumann and Shannon — are not equal, but consistency in between is found due to physical meaning, when considering the both $SE_I$ and $SE_P$.

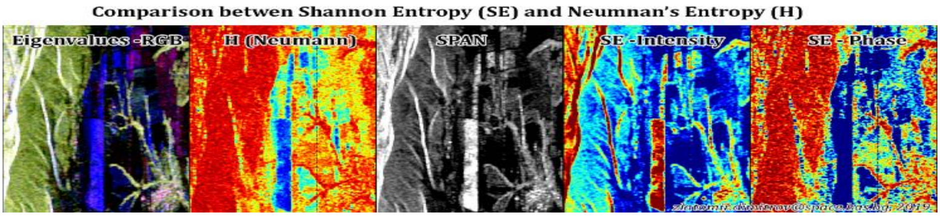


*Fig. 16. Comparison, between Neumann's Entropy (H) and Shannon Entropy (SE — $SE_I$ and $SE_P$); $SE_I$ relate its changes with SPAN; SE — complements with H (©ESA/JAXA – PALSAR)*

**Model-based incoherent decompositions**

Model based decompositions describe well polarimetric measurements from natural scatterers. Scattering models considers intrinsic properties of the canonical scattering mechanisms — e.g. Dipole (by means of its orientation), Bragg, Dihedral, Sphere, and Helix.

**Yamaguchi-3 — component polarimetric decomposition — via [$T_3$]:**
The Yamaguchi-3 (three) component scattering model relates polarimetric SAR measurements with three general orthogonal scattering mechanisms, imposing reflection symmetry conditions with scattering powers — $P_S$, $P_D$, $P_V$ [6], where:

- Bragg-scattering (odd-bounce) from rough surface — $\boldsymbol{P_S}$ (β,fS) ;
- Even-bounce (DB) scattering from orthogonal surfaces — $\boldsymbol{P_D}$ (α,fD);
- Volume-scattering from cloud of randomly oriented dipoles — $\boldsymbol{P_V}$. (fV);

Yamaguchi proposed the probability distribution function, where to represent more uniformly oriented dipoles (oriented along RLOS, on angle ψ [8]), which is more consistent with the backscatter from the natural scattering media, and better describe the volume scattering [6].

Analysis via the three powers — $P_S$, $P_D$, and $P_V$ show better representation of the scattering mechanisms over forest areas and agriculture, where constructed RGB correlates well with the Eigenvalues-RGB and Pauli-RGB on Scene-3. As seen from Yamaguchi-RGB in comparison with Eigenvalues-RGB (Fig. 17), the particular colors representing scattering mechanisms are more distinguishable and saturated.

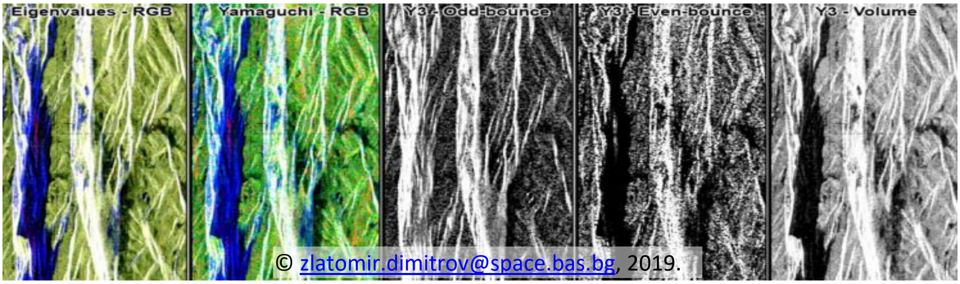


*Fig. 17. Mountainous area near peak "Mijur": Yamaguchi's three-component incoherent Polarimetric Decomposition, based on physical scattering model, by — Odd and Even Bounce, and Volume* (©ESA/JAXA – PALSAR)

Clear example is that within the forests are recognizable reddish patches with certain dihedral scattering, where $P_D \approx 2*(P_S, P_V)$, which is mostly consistent with vertical oriented dipoles (e.g. tree trunks). Moreover, the analysis over agricultural areas showed better recognition of the DB with values ab. -11 dB that is unlike via the Eigenbased — decomposition parameters (descriptors).

**Freeman-2 — component polarimetric decomposition — via [$C_3$]:**

The Freeman-2 (two) component polarimetric decomposition scattering model is initially intended to depict solely volume scattering from forest areas [5, 10]. Thus, selected contributing scattering mechanisms are only two, where:

- *First scattering mechanism*: volume scattering, contributed from random volume of dipoles with reflection symmetry;
- *Second scattering mechanism*: ground scattering contributed either — from dihedral from surfaces with different dielectric constants (e.g. DB from ground-trunk), or from Bragg-scattering of rough surfaces.

Hence, the second order statistics represented from Covariance matrix, is:

(19) $[C_3] = C_{3G} + C_{3V}$

Therefore, two power contributors of the total backscattered power are defined:

(20) $SPAN = P_G + P_V, where: P_G = P_G(f_G, \alpha), P_G = P_G(f_V, \rho), \quad \alpha, \rho \in ¢$

Here, $\alpha$ — controls the type of backscatter (i.e. Bragg or DB) and is sensitive to the forest density, whereas the $\rho$ — is sensitive to the type of randomly oriented dipoles.

At scene-3, this two-component decomposition is showing in general poor discrimination between areas with one or two major scattering mechanisms. Nevertheless, over agricultural areas good discrimination is made of isotropic surfaces, where the strongest power in the ground contribution $P_G$ is from Bragg-scatter, with values ab. -3 dB. Urban areas are well delineated with values ab. -6 dB.

In spite, good consistency of the volume contribution $P_V$ is found over forest areas with values ab. -5.5 dB, but over sparse forest it could drop up to -9.8 dB (Fig. 4).

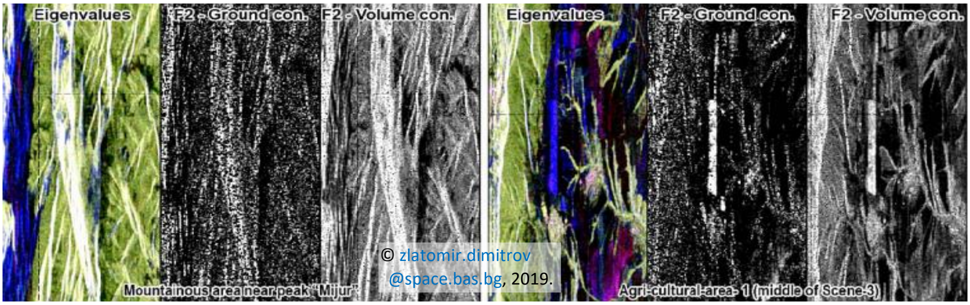


*Fig. 18. Preview of Freeman-2 component physical polarimetric scattering model, over hilly mountainous location and agricultural fields, relating ground and volume contribution to the physics of the scattering process (©ESA/JAXA – PALSAR)*

**Comparison of polarimetric descriptors in two different acquisitions**

A comparative analysis is made of whole polarimetric descriptors derived from Scene-1 and Scene-2 over same geographic area, with different seasonality.

**Comparison between H/A/α decomposition components (descriptors)**

Comparative analysis considers the Eigen-based derived polarimetric descriptors — Eigenvalues-RGB, H, A, α-angle, RVI and PH. First comparison includes the interesting difference observed on decomposition parameters, over the **standing water body** located on bottom of both scenes. Due to intense raining, the eigenvalue — $\lambda_1$ (blue) is showing kind of a Bragg-backscatter, whereas H is very low; A — points out significance of the second and third scattering mechanisms, in spite $\alpha$-confirms isotropic Bragg-surface. Completely the opposite is situation on Scene-1 (spring acquisition, calm weather) where, H — shows highest degree of randomness, maybe due to wind on that area, A — is meaningful, $\alpha$ — points out to anisotropic dihedral surface, with values > 45 deg (Fig. 19 — top).

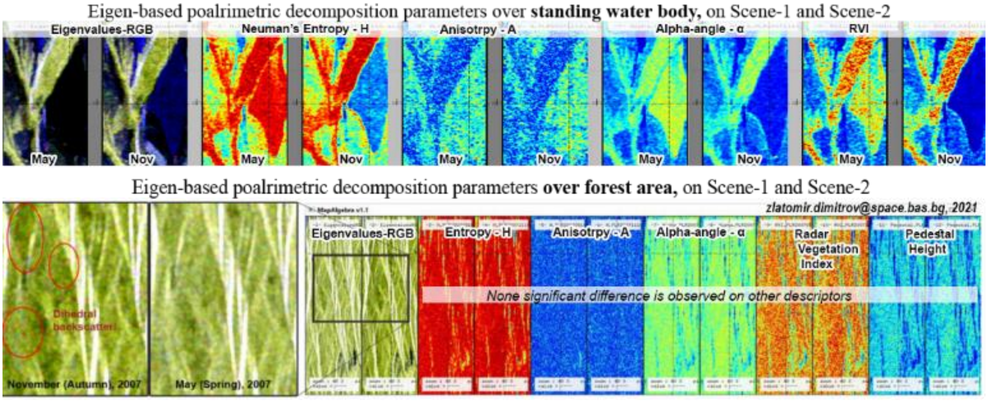


*Fig. 19. Comparison of the Eigen-based decomposition, of scene-1 and scene-2 — top: example on Lake; bottom: example on forest area. At the November acquisition due to higher penetration a Dihedral backscatter is more recognizable. (©ESA/JAXA – PALSAR)*

At the comparison over **forest areas**, the Eigenvalues-RGB on late autumn image (Scene-2) show distinct lower backscatter, rather than the spring one (Scene-1). Due to the higher penetration within the forest volume on Scene-2, particular reddish pixels are recognizable that suggests dihedral backscatter — i.e. from trunks. The rest of the parameters represent already observed high degree of randomness. Small increase in values is observed at autumn image (Scene2) on — $\alpha$, RVI and PH, without distinct difference. Solely on RVI visible change is recognizable in forest.

Most of the difference between polarimetric descriptors are namely at the **agricultural areas**. On spring acquisition (Scene-1) uncultivated fields (pastures) caused low values in Eigenvalues, thus is black. Entropy is much higher, whilst Anisotropy suggests contribution from second and third scattering mechanisms.

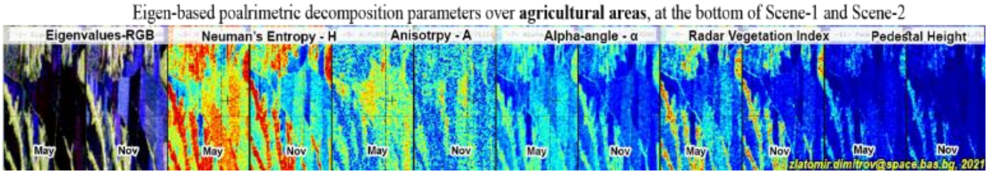


*Fig. 20. Comparison of the Eigen-based decomposition, of scene-1 and scene-2: example on crop lands (©ESA/JAXA – PALSAR)*

In spite, on autumn's acquisition (Scene-2), most of the fields have been already planted with winter crops that have already sprouted. Transition of high Entropy values to lower ones is observed here, along change of the physical properties of the scattering media that is observed also at A, $\alpha$-angle and RVI. Interestingly, the Pedestal Height over this area is less affected and stays quasi constant.

**Comparison between Freeman-2 decomposition components**

The comparison between Freeman2 decomposition parameters gives another point of view that complement to the above analysis, by emphasizing on forest areas.

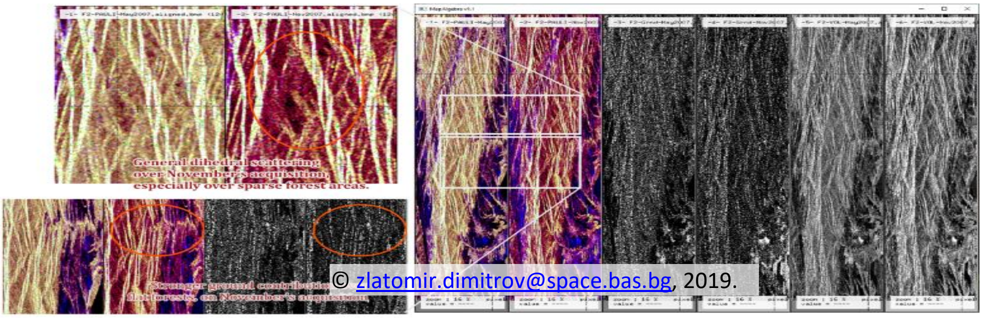


*Fig. 21. Comparison between Freeman-2-decomposition, scenes — Scene 1- May, 2007 (first column) and Scene 2 — November, 2007 (second column). Example over forest areas showing leaf-off period, and increased dihedral scattering and ground contribution.*
*(©ESA/JAXA – PALSAR)*

It is obvious the reduced volume backscatter contribution from the forest areas, observed at November's acquisition (Scene-2) — see Fig. 21. Comparing the pseudo-Pauli-RGBs, the November's image is darker, due to higher ground contribution to the total backscatter, due to leaf-off period in forest. Thus, general dihedral scattering is observed on Scene-2, especially over sparse forest areas. In flat forest, manmade objects are recognizable, in respect to May's image (Scene-1). Interesting fact is that the foreshortening strips from the November's acquisition are brighter, rather than May's acquisition. In spite of that, Scene-2 ground contribution gives better representation of the urban areas, due to fade out of vegetation at the resolution cell. Whereas the largest heterogeneity in backscatter is observed over agricultural areas. Ground contribution is far higher on November's image, rather than May's acquisition, due to phenological crop status for this period.

**Polarimetric segmentations and classifications**

Polarimetric segmentations are part from POL-SAR classifications, which sample polarimetric data by distribution algorithm (e.g. Wishart) of the second order statistics — $[T_3]$ and $[C_3]$ [8, 11]. Number of classes are determined from polarimetric data, but mostly they constitutes of 8 or 16 — classes, from Wishart distribution.

**Polarimetric segmentation in H-A and H-A-α panes:**

Firstly, the H-α plane is analyzed, which shows importance of the classes — 2, 3, 5, 6, 7 and 8, over Scene-3. General polarimetric segmentation into 8 — real classes is presented on Table-4. Refer to that according also to the segmentation applied in Fig. 22 — left, interpretation shows that most occurrences are in vegetation class (5). At the surface roughness propagation class (8), isotropic Bragg surfaces have less occurrences having more anisotropic character. The branch/crown structure class (3) shows most occurrences resulted from correlation between H and α. The cloud isotropic needles classes (6) follows up, probably due to large scale forest areas whole over the scene, consisted of randomly oriented dipoles. Class (2) also comprises isotropic dihedral backscatter from forest.

*Table 4. The H/α — segmentation pane classes, of major scattering mechanisms from polarimetric data, which breaks into 8-regions (classes) with enumeration [11]*

| | | | | | |
|---|---|---|---|---|---|
| 1 | Dihedral scatterer | 4 | Dipole | 7 | Bragg Surface |
| 2 | Forestry DB | 5 | Vegetation | 8 | Surface Roughness propagation effects |
| 3 | Branch / Crown structure | 6 | Cloud of Anisotropic Needles | 9 | No feasible region |

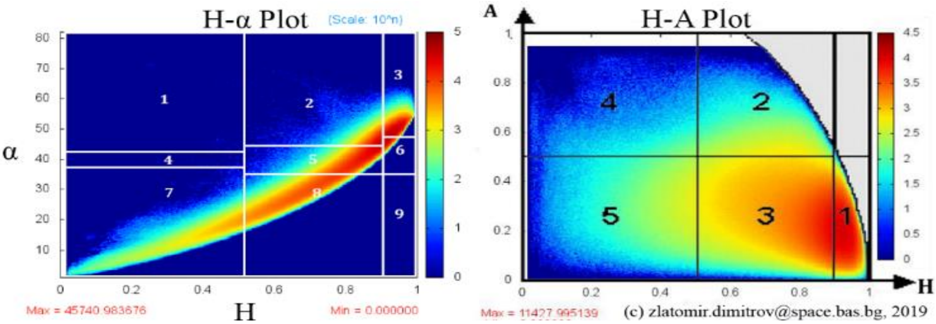


*Fig. 22. Left: H-α segmentation plot (segmentation plane), showing frequency distribution in respect to the type of the scattering media; Right: The H-A segmentation plane for Scene-3, showing the character of the scattering media (surface)*

Further analysis concerns the H-A segmentation plane, which is another approach for representing physical properties of the scattering media in respect to the type of backscatter. As seen from Fig. 22 — right, and Table-5, classes are:

*Table 5. Th H/A — segmentation pane classes, with contribution mainly from least significant scattering mechanisms [8]*

| | | | | | |
|---|---|---|---|---|---|
| 1 | Random scatterers | 3 | Random surfaces | 5 | Bragg surfaces |
| 2 | Random anisotropic scatterers | 4 | Two scattering mechanisms | *[Jagdhuber, T., GEO414]* | |

From the H-A plane presented above calculated for Scene-3, could be stated that in general the scattering media is constituted by random scatterers (class-1) and the random surfaces (class-3), which are in the sake of large scale forest areas, mixed up with agricultures. Bragg surfaces have less occurrences in class-4, related with bare fields, and some particular crops on Scene-3 (see Eigen-based decomposition).

Concurrent classifications using classes from the segmentation panes are applied. The H-A-α classification shows most distinct separation between classes. Forests as random scatterers are well delineated (electric bluish, Fig.23), which is thus so also on H-A, and A-α (light-green and dark-green colors). Bragg surfaces in H-A-α are colored in pure red color, whilst anisotropic surfaces are well recognized. Scattering delineation at H-α classification is based on α-angle, thus Bragg surfaces are more distinct here (dark-blue), whilst the rest is mixed up. The H-A shows different delineation due to Anisotropy. The anisotropic surfaces (magenta colored fields at Eigenvalues-RGB) are well classified at the *H-A* and *A-α* classifications.

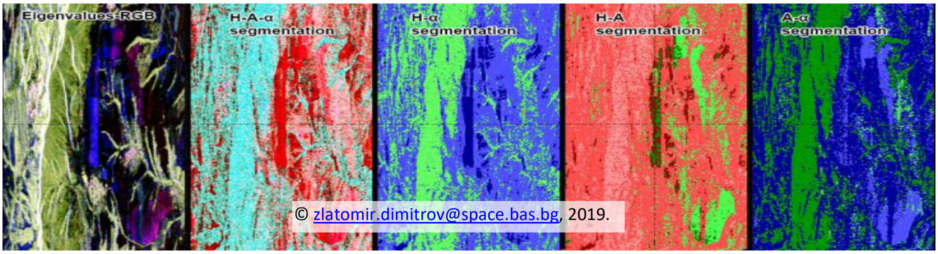


*Fig. 23. Comparison of — form left to right: Eigenvalues-RGB, H-A-α, H-α, H-A, and A-α classifications over particular segmentation, on agricultural area -2 with surrounding forest areas, located at the bottom of Scene-3 (©ESA/JAXA – PALSAR)*

**Polarimetric Classifications using Wishart classifier:**

In purpose of the analysis, the following unsupervised Wishart classifications are calculated [11]:

- H-α Wishart — composited of 8-stable clusters (classes)
- H-A-α Wishart — composited of 16 stable clusters (classes), same prerequisites, but more comprehensive due to including information from Anisotropy.

Advantage of the *H-A-α* Wishart classification with 16-classes is the discrimination of the second and third scattering mechanisms. Anisotropy allows to split clusters to smaller ones, with more distinct separation in physical manner. Starting point of the analysis is classification based on Pauli-Decomposition, from the Wishart H-α or H-A-α classifiers. The Pauli's H-α classification improperly classifies dihedral scattering (e.g. urban areas). Good separation of anisotropic and Bragg surfaces is present at the Pauli H-A-α classification. As seen in Fig. 24, Wishart classifications are detailed, thus hardly is interpretation of resulted clusters, especially the 16-classes one. In spite, performance of the both classifications over forest areas is straightforward, where particular sensitivity is observed for the sparse forest and deforested areas. The benefit from Anisotropy, which discriminates the second and third scattering mechanisms from is obvious, with a close look at mountainous area near "Peak Mijur". Considering the already discussed reddish strip, which exhibits contribution of two equal major mechanisms, is well separated at the 16-classes classifications, whilst is not at the 8-classes one (Fig. 24 — top).

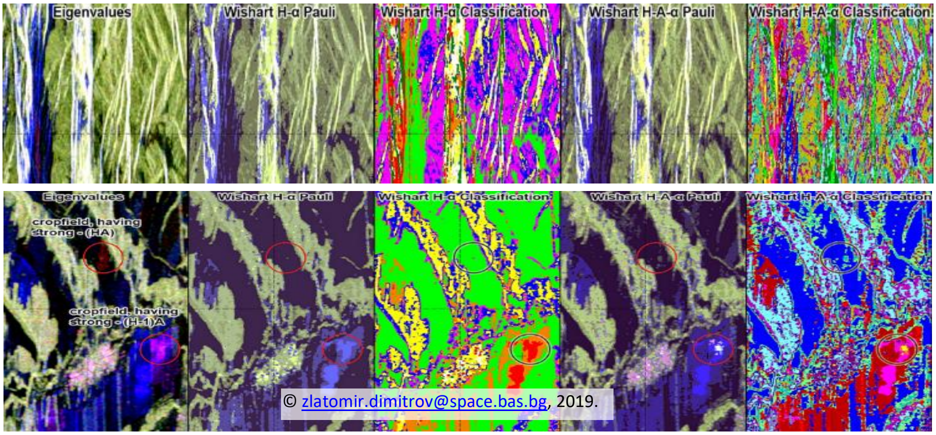


*Fig. 24. Top: Comparison over mountainous area of peak "Mijur" on Scene-3 showing better performance of the H-A-α — 16-classes in regard to the 8-classes one; bottom: Crop fields near Agri-area-2 on Scene-3 having different physical origin of the backscatter (©ESA/JAXA – PALSAR)*

The same is observed over agricultural areas (Fig. 24 — bottom), considering already discussed pure reddish crop on Eigenvalues (related to an isotropic dihedral surface that exhibits two equally strong scattering mechanisms), and magenta-one (related to an anisotropic dihedral surfaces with two unequally strong mechanisms).

### Forest mask proposal, based on derived polarimetric descriptors

Forest is kind of a scattering media consisted of randomly oriented dipoles, inducing high degree of depolarization, with three equal scattering mechanisms at target vector. This leads to the general conclusion that most discriminative polarimetric descriptors should be such polarimetric parameters showing high degree of depolarization and randomization, such as — *RVI*, *Pedestal height*, *Perplexity*. In spite, in non-deterministic targets multiple scattering occurs, which induces phase differences, pointing out to different height of the phase centers. This was already observed on the phases of polarimetric coherences, and $SE_P$. Therefore, based on conducted polarimetric analysis of whole PALSAR scenes, the following discrimination of polarimetric descriptors **to delineate forest area,** could be done:

*Table 6. Selected Polarimetric descriptors, which pixels represents the forests areas, and could be used to generate – **Forest/Non-forest Mask** (©ESA/JAXA – PALSAR)*

| *Pauli-Basis* | **C.C.C. Mod** | **C.C.C. Pha** | **\|C.C.C.\|** | **YMG3-VOL** | **H** | ***α*** |
|---|---|---|---|---|---|---|
|  | 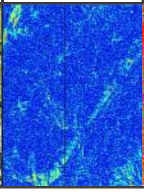 | 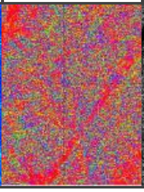 |  | 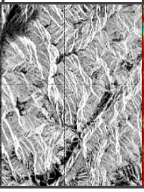 | 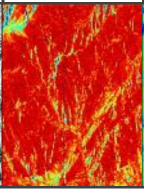 | 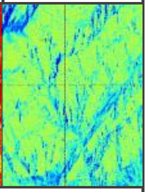 |
| | | | | | | |
| ***pp₃*** | **H(1-A)** | ***SE_P*** | **RVI** | **Per-plexity** | **PH** | **Polariz. Fraction** |
| 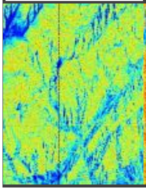 | 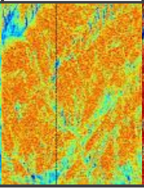 | 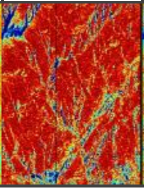 | 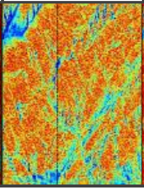 | 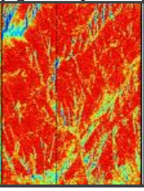 | 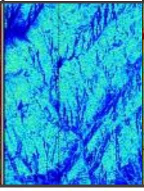 | 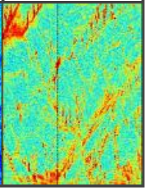 |

*Table 7. Values and intervals of selected Polarimetric descriptors that delineates forest from non-forest pixels, derived from on-screen analysis, over whole PALSAR PLR scenes*

| *Descriptor* | *Values / Interval* | | *Descriptor* | *Values / Interval* |
|---|---|---|---|---|
| **C.C.C. Mod** | < 0.42 | | **H(1-A)** | > 0.6 |
| **C.C.C. Pha** | ∈ -150 – 150 [deg] | | ***SE_P*** | > 0.88 |
| **\|C.C.C.\|** | > 1.1 [dB] | | **RVI** | > 0.7 |
| **YMG3-VOL** | > -12 dB | | **Perplexity** | > 2.5 |
| **H (Neumann)** | > 0.8 | | **PH** | > 0.26 |
| ***α*-angle** | ∈ 38.0 -53.0 [deg] | | **Pol. Fract.** | < 0.6 |
| ***pp₃*** | > 0.17 | | | |

## Conclusion

General conclusion from the conducted polarimetric study is that POL-SAR provides extensive information about biophysical and geometrical properties of the scattering media. Natural targets like forest and agricultural areas are well described by the thorough analysis of incoherent Polarimetric decompositions. Resulting polarimetric descriptors are main tool for characterization of the scattering media.

Considering Speckle filtering in vegetation areas algorithms without edge preservation (e.g. BOXCAR) are reasonable to obey introducing artifacts. In spite, adaptive filtering with edge preservation (e.g. R. Lee) is important where certain geometry is present (e.g. in urban areas). In spite, the low modulus of Polarimetric coherences is due to presence of non-deterministic targets where complex scattering persists. At those areas, higher phase differences points out different location of the active phase centers — i.e. scattering mechanisms.

From the Eigen-based mathematical decomposition theorem one could concluded that isotropic areas produce mostly surface scattering with general contribution of odd-bounce. Forest areas are related to random oriented dipoles ($\alpha \approx 45°$) which gives complete randomness whilst anisotropic surfaces (e.g. agriculture) resulted with two scattering mechanisms with equal probabilities. Urban areas resulted with two unequal scattering mechanism, possibly due to averaging of non-deterministic (e.g. trees) with deterministic (e.g. buildings) targets. Combinations of H/A is of great benefit in analysis of agricultural areas where to relate the observed physics to the scattering media. From the Yamaguchi-3 component physical decomposition could be concluded that scattering mechanisms are well depicted within natural scattering media. The Freeman-2-component polarimetric decomposition is well utilized over forest areas and other natural media via its volume contribution. In spite, the ground contribution gives good results in the delineation of rough isotropic surfaces with Bragg-backscatter.

From comparison of two acquisitions, could be concluded that changes in the physics of the backscatter due to seasonality — like leaf-off in forests or other environmental conditions, could be fully analyzed by means of derived polarimetric descriptors. Prompt analysis of the phenology changes in crops is more suitable to be done by Eigen-based decomposition theorem and concurrent Radar indices.

Considering Polarimetric segmentation, most discriminative is the scattering derived from random surfaces. Good discrimination is achieved also over isotropic Bragg surfaces especially with propagation effects which also is related to non-deterministic targets. Problems in Wishart classification algorithms mainly concerns the misclassification of the pixels with equal characteristics aiming the edge value of the clusters. As observed, to the forest area five classes are dedicated from the 8-classes classification, whilst at the 16-classes one, the number of forest classes got doubled. Therefore, increasing number of classes by means of anisotropy leads to further maze and fragmentation of the land cover classes, especially over forest areas with varying density. Nevertheless, one could concluded that the isotropic and Bragg surfaces are well classified by both unsupervised Wishart classifications.

Finally, randomization in natural media could be exploited to derive Forest/Non-forest mask from polarimetric descriptors of full polarimetric SAR data.

**Acknowledgment**

I would like to sincere thank Dr. T. Jagdhuber for supporting my interest in Polarimetry during the course GEO414 that resulted in writing this paper. Wish to thank also Prof. C. Schmullius, *Lehrstuhl für Fernerkundung,* for the giving me this precious opportunity to take part at the Courses of MSc in Geoinfromatics, at FSU-Jena, in the framework of the ERASMUS+ program. Wish also to thank my tutor in Bulgaria Prof. E. Roumenina for supporting me during my PhD. I acknowledge also to ESA and JAXA for providing me with PALSAR PLR data.

## References

1. Le Toan, T., S. Quegan, M.W.J. Davidson, *et al.* The BIOMASS mission: Mapping global forest biomass to better understand the terrestrial carbon cycle. *Remote Sensing of Environment*, 115, 2011, 2850–2860, DOI:10.1016/ j.rse.2011.03.020.
2. Ainsworth, T. L., J. P. Kelly, J.-S. Lee. Classification Comparisons Between Dual-Pol and Quad-Pol SAR Imagery. *Proceedings of ISPRS Journal of Photogrammetry and Remote Sensing*, 64, 2009, 464–471.
3. Rosenqvist, A., M. Shimada, N. Ito, M. Watanabe. ALOS PALSAR: A pathfinder mission for global-scale monitoring of the environment. *IEEE TRANSACTIONS ON GEOSCIENCE AND REMOTE SENSING*, 45, 2007, 3307–3316.
4. Erxue, C., L. Zengyuan, T. Xin, F. Fengyun. FOREST STRUCTURE INFROMATION EXTRACTION FROM POARIMETRIC ALOS PALSAR DATA. *PI No. 315. Institute of Forest Resources Information Technique*, CAF, 2009, 6 p.
5. Cloude, S. R., E. Pottier. A Review of Target Decomposition Theorems in Radar Polarimetry. *IEEE Trans. Geoscience and Remote Sensing*, vol. 34, 1996, 498–518.
6. Yamaguchi, Y., S. Akinobu, R. Sato, H. Yamada, J. Yang. A New Four-component Scattering Power Decomposition Applied to ALOS-PALSAR PLR Data Sets. Niigata University, Japan, 2010, 4p.
7. Jagdhuber, T. An Approach to Extended Fresnel Scattering for Modeling of Depolarizing Soil-Trunk Double-Bounce Scattering. *MDPI, Remote Sens.*, 8, 818, 2016, 25 p. doi:10.3390/rs8100818.
8. Jagdhuber, T., C. Schmullius. SAR Polarimetry — Theory and Applications. *Lecture and Exercise (Course materials with closed access), GEO-414 Masterkurs*, Friedrich-Schiller-Universität-JENA, 2019, 305 p.
9. López-Martínez, C, L. Ferro-Famil, E. Pottier. 3. SPECKLE FILTERING. *PolSARPro Tutorials*, Part-I, Chapter-3, ESA, 2005, 12 p.
10. López-Martínez, C, L. Ferro-Famil, E. Pottier. 4. POLARIMETRIC DECOMPOSITIONS. *PolSARPro Tutorials*, Part-I, Chapter-4, ESA, 2005, 28 p.
11. López-Martínez, C, L. Ferro-Famil, E. Pottier. 5. POLARIMETRIC SAR DATA CLASSIFICATION. *PolSARPro Tutorials*, Part-I, Chapter-5, ESA, 2005, 14 p.

# ИЗПОЛЗВАНЕ НА ПОЛЯРИМЕТРИЯ (POL-SAR) НА ТЕСТОВИ РАЙОНИ В СЕВЕРОЗАПАДНА БЪЛГАРИЯ – ПОЛЯРИМЕТРИЧНИ ДЕСКРИПТОРИ, ДЕКОМПОЗИЦИИ И КЛАСИФИКАЦИИ

***З. Димитров***

**Резюме**

Статията представя приложение на Поляриметрия (POL-SAR) в планински и равнинен тестови райони в Северозападна България, с изображения в пълна поляриметрия от спътниковата система в микровълнов канал – L – ALOS1 PALSAR на Японската космическа агенция (JAXA). Приложени са всички основни методи в поляриметрията, като са изчислени множество поляриметрични дескриптори, като резултат от поляриметрични декомпозиции и поляриметрични кохерентности. Анализирано е поведението на поляриметричните параметри при различни видове разсейващи обекти, свързвайки механизмите на разсейване с вида на разсейващата среда. Направено е сравнение в планински горски територии от две дати на заснемане – май (през пролетта) и ноември (през есента). Приложени са поляриметрични сегментации и класификации с 8 и 16 класа. Накрая е предложена маска на горската територия, на база на поляриметричните дескриптори. Статията е разработена по линия на положен Курс – GEO414, към обмен по програма ЕРАЗЪМ+ на ЕС в Университета в Йена, Германия. Докладът е представен на поредната Седемнадесета международна научна конференция „Космос, Екология, Сигурност (Space, Ecology, Safety) –SES 2021“.

Bulgarian Academy of Sciences. Space Research and Technology Institute.
Aerospace Research in Bulgaria. 34, 2022, Sofia

DOI: https://doi.org/10.3897/arb.v34.e04

# IONIZING RADIATION SENSOR FOR NANOSATELLITES, MICRODRONES AND SMALL UNMANNED GROUND VEHICLES

***Rositsa Miteva[1], Svetoslav Zabunov[2], Garo Mardirossian[2], Todor Kunchev[3], Roxandra Pamukoff-Michelson[4]***

[1]*Institute of Astronomy with National Astronomical Observatory — Bulgarian Academy of Sciences, e-mail: rmiteva@nao-rozhen.org*
[2]*Space Research and Technology Institute — Bulgarian Academy of Sciences*
[3]*Faculty of Medicine — Sofia University*
[4]*Department of Preventive Medicine, Faculty of Public Health, Medical University — Sofia*

***Keywords:*** *Ionizing radiation sensor, Radiological dosimetry unmanned system*

***Abstract***

*The purpose of this paper is to present an ionizing radiation sensor suitable for nanosatellites, small drones and other types of unmanned vehicles. When implemented on an airborne or ground-based unmanned vehicle the sensor is beneficial in disaster management scenarios such as inspection of buildings and facilities for ionizing radiation contamination and measurements of the ionizing radiation dose.*

*Herein, a design and laboratory tests of the sensor are presented. The instrument is a lightweight module having low power consumption suitable for nanosatellite platforms and for mobile use by having it installed in an unmanned system (airborne or ground-based).*

*For test purposes a 36-rotor drone was developed along with a mobile ground based unmanned vehicle. With all implementations the radiological sensor is directly connected to the main processor unit of the platform. In the case of the drone and ground-based vehicle systems the processor unit is the microcontroller of the autopilot.*

*Experimental results of laboratory measurements of different radiation sources are shown and discussed. The experimental setup demonstrates a few advances related to specific problems encountered in the existing ionizing radiation measurement systems.*

## Introduction

The need for space research in the area of ionizing radiation sources on the one hand, and the ever rising requirements for nuclear safety and readiness for nuclear disaster management define new technological limits that should be overcome by the radiation measurement instrumentation.

We have focused our research and development efforts on investigating the possibility to realize a lightweight ionizing radiation sensor for use on such platforms as nanosatellites and very small unmanned aerial vehicles — also known as micro-drones — having total weight of less than or equal to 250 g. Other platforms that could benefit from this type of sensor are unmanned ground-based vehicles with very small sizes and weights.

The novel sensor described herein is vibration resistant, lightweight, PIN photodiode based and uses the microprocessor of the host system in order to minimize weight, complexity, cost and failure rate.

**State of the art**

For the purpose of nuclear disaster management and radiation inspection within buildings there have been developed robotic platforms of various kinds. These systems are categorized into two major groups: airborne and ground systems. Water vessels employed for this task are rare. Examples of ground based robots for radiological surveying are the CARMA 2 platform, the JAEA-3 robot, and the Quince robot among others. Most such platforms are equipped with a Geiger Müller tube for γ- and β-surveying. There are some advanced designs employing solid state sensors. Connor et al. [1] have compiled a good overview of the existing airborne radiation mapping systems. The most elaborate developments in the field have been commenced after the Fukushima Daiichi nuclear disaster in 2011 [2–4].

The literature shows that the existing airborne platforms are above 0.9 kg while the ground-based systems are over 10 kg [5]. Due to their significant weights and sizes such ground vehicles are hardly usable in narrow corridors and rooms. The airborne counterparts, on the other hand, are totally inapplicable in closed spaces. In order to solve this discrepancy we established a total weight for an airborne system to be below 500 g and of a ground-based platform to be below 2 kg. It is obvious that the airborne systems impose more stringent requirements on the ionizing radiation sensor weight. We concluded that a sensor of 10 g weight or less shall be suitable for all systems without exceeding the limit for the payload weight.

We chose to compare our design with the Liulin family of ionizing radiation sensors [6–7] for their proven qualities. Liulin instruments are developed at the Space Research and Technology Institute — Bulgarian Academy of Sciences. We were to choose between two technologies as those were evaluated to deliver higher reliability, lower weight, spectrum analyser capabilities and detection of the broadest variety of particle types.

Both technologies are solid state and do not use tubes or high voltages, which is a great benefit. The first method is implemented in the Liulin devices, this is the PIN photodiode technology [8–9] and eventually we developed our sensor after that approach. The second technology that was considered is the scintillation sensor using photodiode readout. This method was decided to be implemented in our next prototype and testing stage.

**Ionizing radiation sensor**

With our current choice of technology we can achieve spectral identification of the radioactive sources along with radiation dose measurements. Further, the PIN photodiode based sensor can detect fast neutrons with energies above 1 MeV, accelerated protons and heavy ions besides beta and gamma rays.

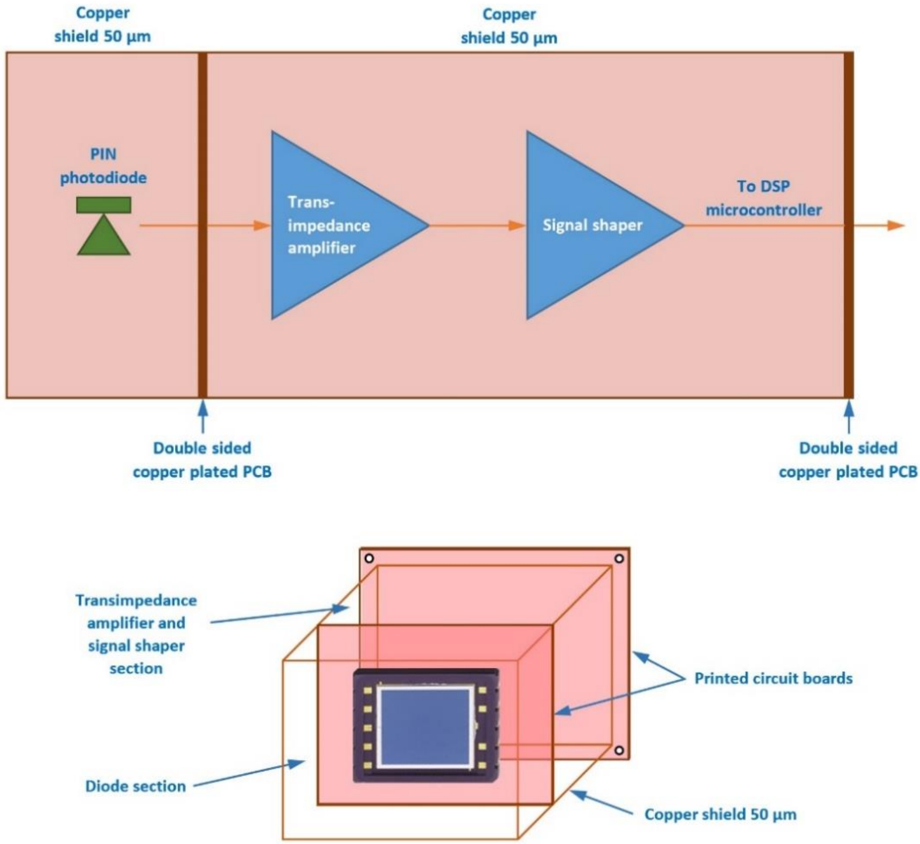


*Fig. 1. Ionizing radiation sensor diagram and 3D model. The sensor enclosure consists of two compartments — one for the PIN photodiode and one for the electronics*

The sensor enclosure was built using copper foil and printed circuit boards (PCBs) to achieve the required 10 g weight (see Fig. 1). The shielding stops incident light and electromagnetic interference and keeps the sensor interior isolated from air contaminants and moisture. The shielding foil is only 50 µm thick and allows the sensitivity of gamma rays to be well below 60 keV. Beta particles are also let through the shielding. The sensor does not use a dedicated microcontroller nor any kind of digital electronics circuitry — it is a purely analogue device. The sensor is connected directly to the host platform control board.

The PCBs form two interior sections (Fig. 1). In the front compartment the PIN photodiode is deployed. This section is completely sealed — no light nor air may penetrate or exit. The employed PIN photodiode is Hamamatsu S5107 with 100 $mm^2$ active area. The thickness of the sensitive silicon volume is 0.3 mm. This diode has 30 V max reverse voltage. We chose to bias it with 28 V.


*Fig. 2. A typical Americium-241 (top) and Uranium-238 (bottom) ionization events*

The second compartment hosts the transimpedance amplifier and the signal shaper. The backmost PCB is used to mount the sensor to the host platform by means of four springs. Such a sprung suspension (see Fig. 4 and 5) guarantees no interference by vibrations coming from the host platform. Due to the very thin shielding the sensor is prone to registering vibrations as parasitic signals. The analogue signal is connected to an analogue to digital converter (ADC) of the host system using shielded cable. The shaper filter central frequency is 16 kHz. A 12-bit ADC mode with the maximum sampling frequency for our test microcontroller of 530 kHz gives high enough resolution for the apparatus to work without additional circuitry such as sample and hold modules, threshold detectors, etc. The signal is purely digitally processed in the host system and a detailed image of the signal is received and visualized in our test setup (see Fig. 2). Due to the very high oversampling rate the digital signal processing that follows is made efficient and accurate.

We computed the noise voltage RMS to be 15 mV. Americium-241 60 keV gamma ray in Fig. 2 (top) generates a signal with 120 mV positive amplitude. By measuring only the positive part of the shaped impulse and adjusting channel 1 to correspond to 60 keV gamma ray energy we record the first 512 channels of ionizing radiation particle energies (Fig. 3). Fig. 2 (bottom) shows a typical Uranium-238 gamma event.

## Experimental Test

Our laboratory tests were carried out with 5 different radioactive sources. Table 1 gives account on the radioactive sources measurements by showing the counts per minute our device has registered for each source.

Fig. 3 demonstrates the spectra of the background radiation and the test radioactive sources in 512 channels. All sources except Americium-241 have wide spectra.

*Table 1. Tested radioactive materials*

| Radioactive source | Counts per minute |
|---|---|
| Background | 5 |
| Americium-241 | 590 |
| Radium-226 | 1239 |
| Uranium-238 | 48 |
| Thorium-232 | 54 |
| Potassium-40 | 15 |

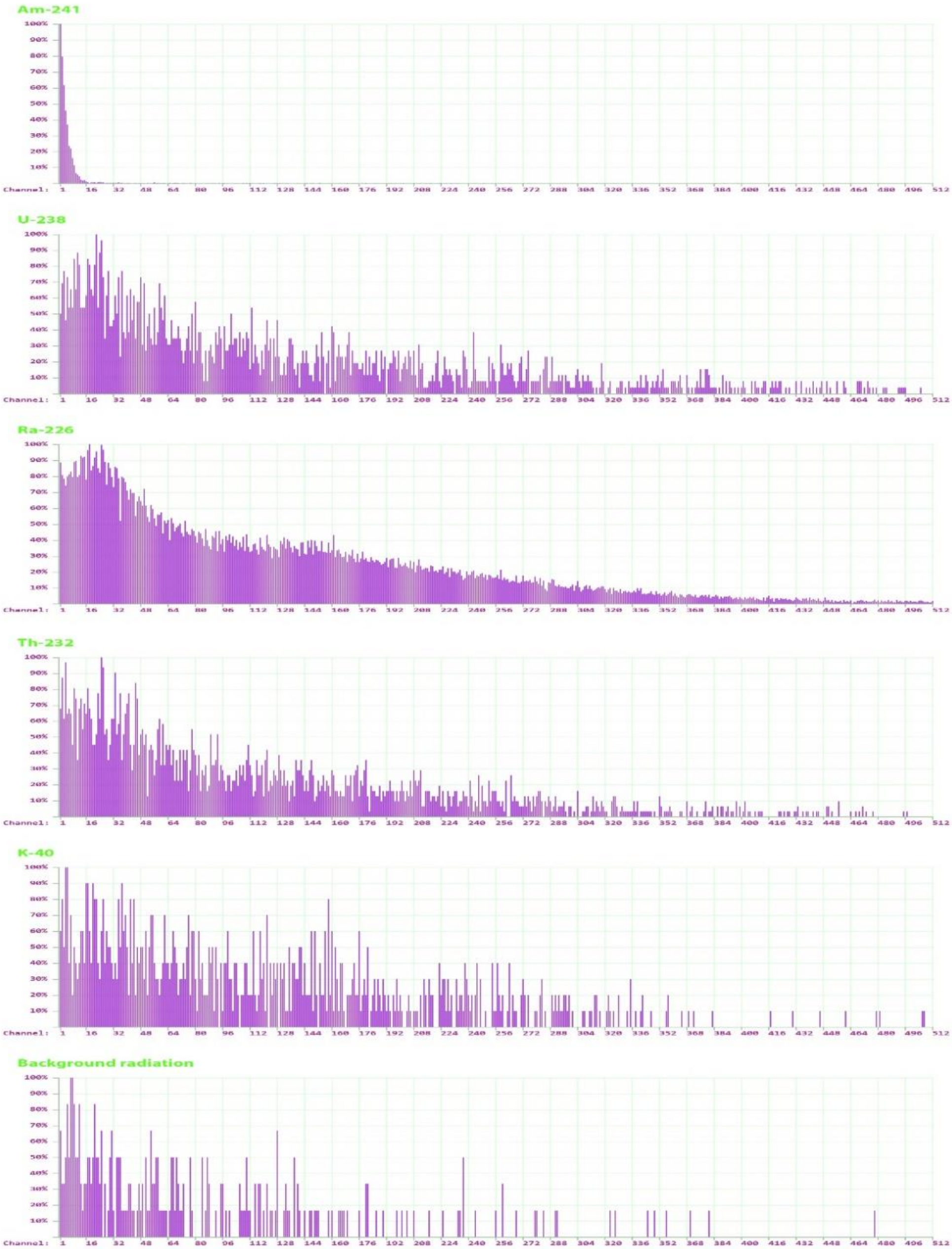


*Fig. 3. Spectra of Am-241, U-238, Ra-226, Th-232, K-40, the background radiation*

Some characteristic spectra are shown in Fig. 3. It becomes clear that the sensor is suitable for identification of radioactive sources. What also should be mentioned is that besides Potassium-40 and Americium-241 all other sources have daughter nuclides, most of which are already in dynamic equilibrium. A good example is the daughter nuclide Bismuth-214 in the Radium-226 and Uranium-238 samples. A registered drawback of the PIN photodiode sensor is its low sensitivity to high energy gamma rays.

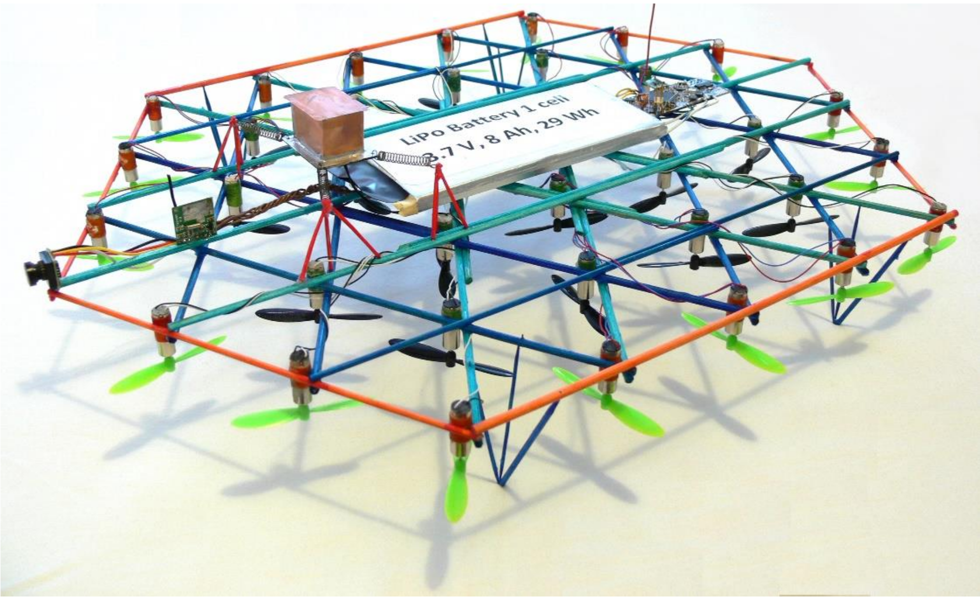


*Fig. 4. A 36-rotor drone designed for indoor surveying of ionizing radiation sources. The sensor is mounted on sprung suspension.*

**Conclusions and future work**

Nanosatellites are becoming increasingly accessible platforms for scientific research. Specifically they are suitable for space ionizing radiation research and can be used as testbeds for small sized innovative ionizing radiation sensors. Furthermore, potential nuclear disasters require preparedness for disaster management using state of the art unmanned systems for ionizing radiation measurements. The avoidance of human involvement in such cases is obligatory.

We envisage the implementation of our sensor on an airborne platform, namely our XZ series 36-rotor micro-drone (Fig. 4) specifically developed for that purpose. Another ongoing experiment is a ground–based small unmanned vehicle being used as a test platform for our sensor (Fig. 5).

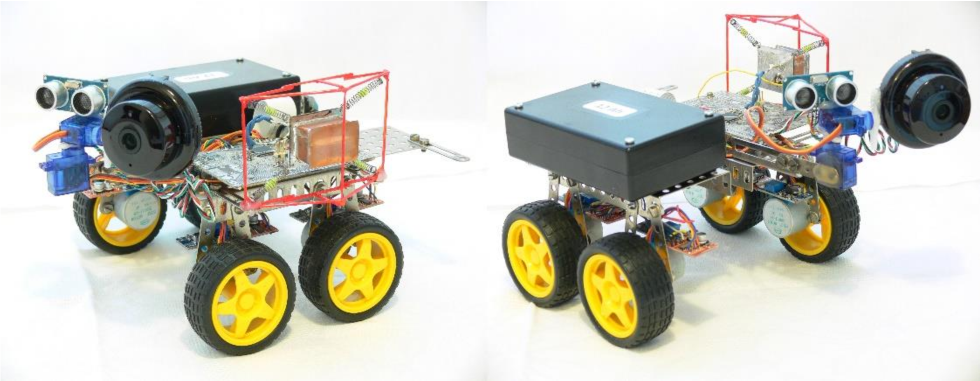

*Fig. 5. The radiation sensor mounted on a small and lightweight ground-based unmanned vehicle for testing purposes. The sensor is installed on the right deck of the vehicle by the use of sprung suspension.*

By our further research and development we aim at lowering the devices initial and maintenance costs, achieving smaller sizes and weights but at the same to obtaining higher resistance of the used electronics to ionizing radiation — specifically we assume implementing a radiation resistant microcontroller from the same family of MCUs [10].

Certain improvements to the navigation system within confined spaces is desirable too [11–14].

We intend to increase the ionizing radiation sensor sensitivity to high energy gamma rays. This can be achieved by implementing a scintillator as the sensor element instead of a PIN photodiode.

**Acknowledgements**

We would like to thank prof. Jordanka Semkova from Space Research and Technology Institute — Bulgarian Academy of Sciences for giving us precious comments all the way through our exciting research.

**References**

1. Connor, D., P. G. Martin, T. B. Scott. Airborne radiation mapping: overview and application of current and future aerial systems. *International Journal of Remote Sensing*, Vol. 37, 2016, Iss. 24, pp. 5953–5987.
2. Kawatsuma, S., M. Fukushima, T. Okada. Emergency response by robots to Fukushima-Daiichi accident: summary and lessons learned. *Industrial Robot: An International Journal*, Vol. 39, Iss. 5, pp. 428–435.

3. Kawatsuma, S., R. Mimura, H. Asama. Unitization for portability of emergency response surveillance robot system: Experiences and lessons learned from the deployment of the JAEA-3 emergency response robot at the Fukushima Daiichi Nuclear Power Plants. *ROBOMECH J.*, vol. 4, no. 1, Feb. 2017, pp. 1–7.
4. Nagatani, K. *et al.* Emergency response to the nuclear accident at the Fukushima Daiichi Nuclear Power Plants using mobile rescue robots. *J. Field Robot*, vol. 30, no. 1, Jan./Feb. 2013, pp. 44–63.
5. Lauria, M. *et al.* Design and Control of a Four Steered Wheeled Mobile Robot. *IECON 2006 — 32nd Annual Conference on IEEE Industrial Electronics*, Paris, France, 2006, pp. 4020–4025.
6. Semkova *et al.* Charged particles radiation measurements with Liulin-MO dosimeter of FREND instrument aboard ExoMars Trace Gas Orbiter during the transit and in high elliptic Mars orbit. *Icarus*, 303, 2018, pp. 53–66.
7. Dachev, T. P., J. V. Semkova, B. T. Tomov, *et al.* Overview of the Liulin type instruments for space radiation measurement and their scientific results. *Life Sciences in Space Research*, 2015, 4, pp. 92–114.
8. Seco, J., B. Clasie, M. Partridge. Review on the characteristics of radiation detectors for dosimetry and imaging. *Physics in Medicine and Biology*, 59(20), 2014, pp. R303–R347.
9. Shrivastava, S., R. Henry. Process Simulation and Analysis for PIN Detector. *IEEE Circuits and Systems International Conference on Testing and Diagnosis, ICTD*, 28–29, April 2009, pp. 1–4
10. Leite, F. G. H. *et al.* Ionizing Radiation Effects on a COTS LowCost RISC Microcontroller. *2017 18th IEEE Latin American Test Symposium (LATS)*, 2017, pp. 1–4.
11. Filipov, F. F. *Erforschung und Implementierung von Technologien für die Navigation in Innenräumen*. TU-Sofia — Verteidigung zur Erlangung des Doktor Titels, Sofia, 2017.
12. Zakaria, A. H., Y. M. Mustafah, J. Abdullah, N. Khair, T. Abdullah. Development of Autonomous Radiation Mapping Robot. *2016 IEEE International Symposium on Robotics and Intelligent Sensors, IRIS 2016*, 17–20 December 2016, Tokyo, Japan, pp. 81–86.
13. Kim, D., H. Woo, Y. Ji, *et al.* 3D Radiation Imaging Using Mobile Robot Equipped with Radiation Detector. *Proceedings of the 2017 IEEE/SICE International Symposium on System Integration*, Taipei, Taiwan, December 11–14, 2017, pp. 444–449.
14. Dudar, A. M., D. G. Wagner, G. D. Teese. AUTONOMOUS MOBILE ROBOT FOR RADIOLOGIC SURVEYS. *United States Patent Office*, Patent Number: 5, 324, 948, Date of Patent: Jun. 28, 1994.

# СЕНЗОР ЗА ЙОНИЗИРАЩО ЛЪЧЕНИЕ ПРЕДНАЗНАЧЕН ЗА НАНОСПЪТНИЦИ, МИКРО-ДРОНОВЕ И МАЛКИ ДИСТАНЦИОННО УПРАВЛЯВАНИ НАЗЕМНИ ПЛАТФОРМИ

***Р. Митева, С. Забунов, Г. Мардиросян, Т. Кунчев, Р. Памукова-Майкълсън***

**Резюме**

Целта на настоящата публикация е да представи сензор за йонизиращо лъчение, подходящ за наноспътници, микро-дронове и други видове платформи, които се управляват дистанционно. Поставен на борда на микро-дрон сензорът е подходящ при борба с бедствия като например инспекция на сгради, в които има радиоактивно замърсяване.

В статията са представени дизайн и лабораторни тестове на предложения сензор. Инструментът е много лек и има нищожна консумация на електрическа мощност. Това го прави приложим в наноспътници и мобилни системи, на борда на които няма хора.

За целта на тестване беше разработен специализиран 36-роторен дрон, а също така и мобилна наземна платформа с дистанционно управление.

Експериментални резултати на лабораторните измервания на различни радиоактивни източници са представени и дискутирани. Експерименталната постановка показва подобрени резултати в сравнение със съществуващата техника.

Bulgarian Academy of Sciences. Space Research and Technology Institute.
Aerospace Research in Bulgaria. 34, 2022, Sofia

DOI: https://doi.org/10.3897/arb.v34.e05

# DIGITAL SIGNAL PROCESSING IN RADIOSOLARIZ PROJECT USING SSE2

***Svetoslav Zabunov***

*Space Research and Technology Institute — Bulgarian Academy of Sciences*

***Keywords:*** *Radio Telescope Signal Processing, Digital Signal Processing, Streaming Single Instruction — Multiple Data Extensions 2*

***Abstract***

*This paper aims at elaborating on the digital signal processing techniques used in data manipulation in the radioSolariz solar radio-telescope project.*

*Focus is drawn on the implementation of different digital signal processing algorithms through the use of streaming single instruction — multiple data extensions 2. This complementary instruction set to general purpose personal computer microprocessors offers increased computational power by realizing parallel processing. The benefit is a higher data throughput while lowering the electrical power consumption of the digital signal processing computer.*

*Optimized code fragments are shown along with original code snippets and these are discussed and analysed. Future work and implementation of other modern parallel processing technologies are envisaged.*

## Introduction

The radioSolariz project was conceived in 2019 [1] and the first prototype has been developed a year later to start collecting radio data starting from late 2020. The telescope called radioSolariz is a solar radio telescope that collects data from radio waves emitted by the Sun in the meter and decameter radio bands. The telescope's station general block diagram is shown in fig. 1. The station consists of antennas, a radio receiver and a general purpose personal computer. The radio receiver digitizes the received signal from the antennas and transfers it to the personal computer. There, using the software of radioSolariz, the signal data is processed by means of digital signal processing (DSP) techniques [2–5].

All digital processing tasks may be executed on the general purpose processor, the central processing unit (CPU) of the utilized computer, by employing standard instructions. This approach was implemented in the first software prototype. Later, for the need of improving the performance of the system, a new approach was devised — implementation of the streaming single instruction — multiple data extensions 2 (SSE2) [6–7].

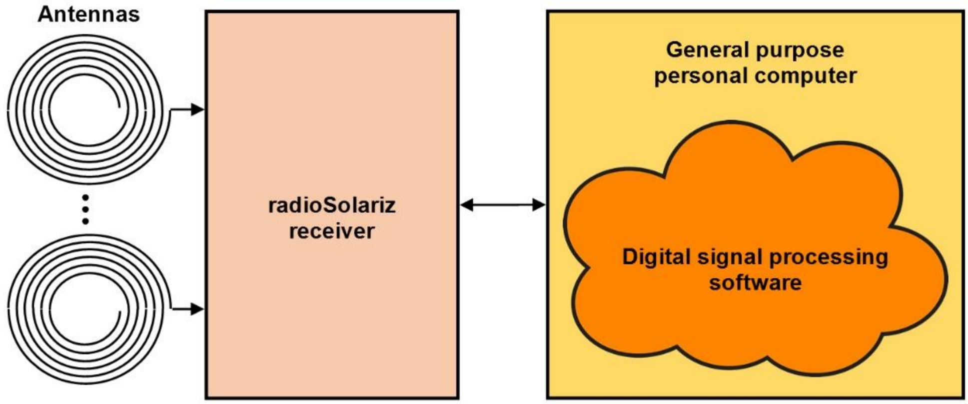


*Fig. 1. RadioSolariz station general block diagram*

**Digital signal processing using streaming single instruction — multiple data extensions 2**

What is SSE2? It is an instruction set, or more precisely an extension to the standard Intel architecture IA-32 instruction set of the CPU of the IBM-PC family personal computers. This instruction set, as its name suggests, is meant for parallel processing of data realized through the technique called single instruction, multiple data (SIMD). What this means is that a single instruction may be executed on an array of similar data, thus avoiding the process of decoding multiple instructions and saving power and transistors in the CPU by doing so. Another benefit is that the instruction set controls a parallel processing co-processor inside the main processor that can perform several operations in parallel.

SSE2 was first introduced by Intel with the initial version of the Pentium 4 processor in 2000. This instruction set is not the first parallel processing instruction set introduced by Intel. It is an improvement of the earlier SSE instruction set, and completely replaces the MMX instruction set (MMX is officially an initialism that has no meaning and is trademarked by Intel). Later in 2004 Intel introduced an extension of SSE2 called SSE3, which never reached the popularity of its predecessor. There is a SSE4 version also.

SSE2 extends the 70 instructions of the SSE model by 144 new instructions. SSE2 was implemented in the processors of the competing processor manufacturer Advanced Micro Devices (AMD). This happened in 2003 when the company introduced the Opteron and Athlon 64 AMD64 64-bit CPUs.

Digital signal processing in radioSolariz involves data preconditioning, spectral decomposition, filtering, signal power level extraction, data compression, etc. All these calculations involve processing of large amounts of data using the same operations, hence they are good candidates for parallelization. Nevertheless, the initial variant of the software relied on the classical instruction set x87 floating point unit (FPU) that is programmatically scalar and maybe parallelized implicitly by the CPU to some extent, depending on the underlying processor architecture and algorithm structure.

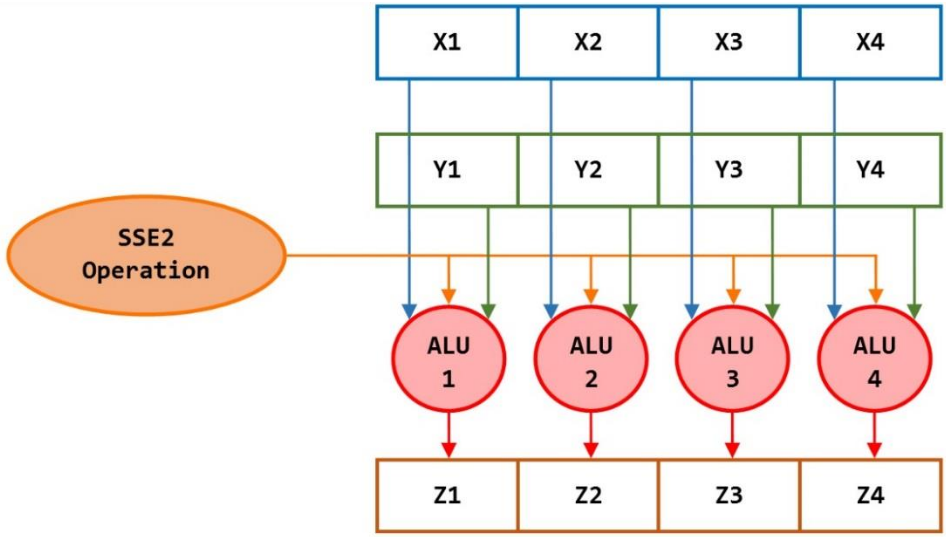


*Fig. 2. Structure of streaming single instruction — multiple data extensions 2 operations on floating point 32-bit data*

FPU (x87) instructions calculate intermediate results with 80 bits of precision. Such a precision is required only by numerically unstable algorithms that were not used in the radioSolariz software.

On the other hand, SSE2 floating point instructions offer the capability to perform four operation in parallel on 32-bit floating point data due to the presence of four SSE2 arithmetic and logical units (ALUs) for each processor core (see Fig. 2) or two operation in parallel on 64-bit floating point data. For the purposes of radioSolariz digital signal processing 32-bit floating point data suffices. Thus theoretically a fourfold increase in data throughput can be achieved. Due to implicit parallelism realized by the CPU on regular x87 instructions the improvement in performance is lower, but still meaningful. For this reason the second variant of the software uses extensively SSE2 instructions to perform calculations on large datasets.

Fig. 3 shows an implementation both using x87 and SSE2 instructions of a summation function that finds the sum of all elements of an array. The code in the top section of Fig. 3 is the standard x87 code while the bottom section of the same figure represents the SSE2 code. Both code snippets are representative of the respective instruction sets implementations in C++ programming language. It is visible that both codes are short, clear to read and require no comments. There are no cumbersome code constructs when implementing SSE2 instructions in C++. All these benefits let the author translate most of the computationally intensive code to SSE2 and still keep it well readable and understandable, yet easy to debug.

```
float  vSum;
size_t i;

for (i = 0; i < length; ++i)
  vSum += pInput [i];

*pResult = vSum;
```

```
XMVECTOR vSum = XMVectorZero ();
size_t   i;

for (i = 0; i < (length >> 2); ++i)
  vSum = XMVectorAdd (vSum, pInput [i]);

*pResult = XMVectorGetX (vSum) + XMVectorGetY (vSum) +
           XMVectorGetZ (vSum) + XMVectorGetW (vSum);
```

*Fig. 3. C++ code for realizing an array sum calculation using x87 instruction set (top) and SSE2 instruction set (bottom)*

Another example of an optimization using SSE2 instructions is the function used to calculate the base 10 logarithm of the signal power. The two code snippets of the original code and the optimized code are shown in Fig. 4. Here we can observe that the original code is shorter. More complex calculations require more local temporary variables to store the intermediate results. This can be avoided, but the code expression would become so hard to read that the maintenance of the code would be compromised.

In both examples a theoretical maximum improvement of the performance is four times. Tests showed real improvement of performance close to this estimation — 3.5 times. This figure varies over different processors the code is tested on, because each processor family realizes super scalar parallelism to different extent.

Many other functions that operate on large arrays of data in the radioSolariz software were optimized in a similar way and showed similar levels of performance benefits.

It was possible to realize a second level of parallelization by running as many programme threads as the number of cores were in the microprocessor, because SSE2 ALUs are present in each core of the CPU. Our final tests were executed on an 8 core processor. The final maximum theoretical performance improvement in this case is 32 times.

```
float  fVerySmallNumber = 1e-38f;
size_t i;

for (i = 0; i < length; ++i)
  pOutput [i] = log10f (pInputReal [i] * pInputReal [i] +
                        pInputImaginary [i] * pInputImaginary [i] +
                        fVerySmallNumber);
```

```
XMVECTOR vVerySmallNumber = XMVectorReplicate (1e-38f);
size_t   i;
XMVECTOR vRR;
                                XMVECTOR vII;
XMVECTOR vRRplusII;

for (i = 0; i < (length >> 2); ++i)
{
  vRR         = XMVectorMultiply (pInputReal [i], pInputReal [i]);
  vII         = XMVectorMultiply (pInputImaginary [i], pInputImaginary
[i]);
  vRRplusII   = XMVectorAdd (vRR, vII);
  vRRplusII   = XMVectorAdd (vRRplusII, vVerySmallNumber);
  pOutput [i] = XMVectorLog10 (vRRplusII);
}
```

*Fig. 4. C++ code for base 10 logarithm of the signal power calculated using x87 instruction set (top) and SSE2 instruction set (bottom)*

## Conclusions

A several times increase in performance was observed by implementing SSE2 instructions instead of standard x87 instructions in the software. The author is encouraged to continue improving the software of the telescope through the implementation of new modern parallel processing hardware and software techniques in the next versions of the radioSolariz telescope, such as Field programmable gate arrays (FPGA) implementation [8].

## References


1. Zabunov, S., R. Miteva. Online Real-time Visualization of radioSolariz Spectrum and Spectrogram, *Proceedings of the SES-2020 conference*, ISSN 2603-3313, 2020, pp. 69–74.
2. Fog, A. *Optimizing software in C++: An optimization guide for Windows, Linux and Mac platforms*. Technical University of Denmark, 2021, Copyright © 2004–2021.
3. Canu, S., R. Flamary, D. Mary. Introduction to optimization with applications in astronomy and astrophysics. *HAL archives-ouvertes*, hal-01346134, 2016, pp. 1–36.

4. Patterson, D., J. Hennessey. *Computer Organization and Design: The Hardware/Software Interface*. Morgan Kaufmann, 2nd edition, 1997, 916 p.
5. Knuth, D. E. *The Art of Computer Programming, v. 2, Semi-numerical Algorithms*. Addison-Wesley, 2$^{nd}$ edition, 1998, 784 p.
6. Tian, X., H. Saito, S. V. Preis, *et al.* Effective SIMD Vectorization for Intel Xeon Phi Coprocessors. *Scientific Programming*, vol. 2015, Article ID 269764, 14, 2015, pp. 1–14, https://doi.org/10.1155/2015/269764
7. Nyland, L., M. Snyder. Fast trigonometric functions using Intel's SSE2 instructions. *Intel tech. rep.*, 2004, pp. 1–11.
8. Andraka, R. A survey of CORDIC algorithms for FPGAs. *FPGA'98, the proceedings of the ACM/SIGDA sixth international symposium on Field Programmable Gate Arrays*, 1998, pp. 191–200.

## ЦИФРОВА ОБРАБОТКА НА СИГНАЛИ В RADIOSOLARIZ ЧРЕЗ SSE2

**С. Забунов**

**Резюме**

Настоящата публикация цели да доразвие темата за цифровата обработка на сигнали в проекта radioSolariz. Проектът radioSolariz представлява радиотелескоп, предназначен за наблюдение на Слънцето в метровия и декаметровия радиообхвати. Цифровата обработка на сигнали в телескопа се използва за първична и вторична обработка на данните в radioSolariz.

Обърнато е внимание на приложението на различни алгоритми за цифрова обработка на сигнали чрез използване на streaming single instruction – multiple data extensions 2. Този допълнителен набор инструкции предлага подобрена изчислителна производителност, реализирана чрез паралелна обработка на данните. Предимствата са както в увеличената производителност, така и в намалената консумация на електроенергия.

Представени са алгоритмични програмни фрагменти едновременно от оригиналния и от оптимизирания код. Примерите са дискутирани и анализирани. Направен е преглед на идеите за бъдеща работа чрез приложение на модерен хардуер и софтуер за паралелна обработка на данни.

Bulgarian Academy of Sciences. Space Research and Technology Institute.
Aerospace Research in Bulgaria. 34, 2022, Sofia

DOI: https://doi.org/10.3897/arb.v34.e06

# DESIGN OF A FLAP FOR STRAIGHT WING OF UNMANNED AERIAL VEHICLE

***Konstantin Metodiev***

*Space Research and Technology Institute — Bulgarian Academy of Sciences*
*e-mail: komet@space.bas.bg*

***Keywords:*** *Airfoil, Fowler flap, simFlow, Autodesk Inventor, Mugin*

***Abstract***

*In the paper hereby, design of a single stage Fowler flap is proposed. The flap is meant to increase lifting abilities of a straight wing at low speeds. It is applicable to small-sized remotely controlled unmanned aerial vehicles widely available to hobbyists.*

*The design process included thorough analysis of flow around a wing foil in case of both retracted and deployed flap. To obtain aerodynamic coefficients values at different angles of attack and Reynolds numbers was a primary goal. In addition, a linkage mechanism was developed to make it possible for the flap to move along a complex path.*

*Various plots and charts are depicted thereafter with sole purpose of providing better understanding of the idea.*

## Introduction

For a few years, the Space Research and Technology Institute has been in possession of a Chinese unmanned aerial vehicle called Mugin-3 3220 mm V-tail [1]. For lack of documentation, making minor changes to the airframe out of pure necessity can hardly be implemented and the local maintenance team can only speculate about the real facts. For the reason that the wing is not equipped with high-lift devices, not to mention the mysterious airfoil, it has been found necessary, for the sake of improving airplane handling characteristics, to carry out preliminary research as to what the airplane performance would be if the aforementioned improvements had been introduced. To start with, a single stage Fowler flap could be attached to the wing right between the fuselage and the tail rod.

The study hereby comprises two stages: analysis of flow around an airfoil and design of a flap actuating linkage. The former stage aims at working out values to aerodynamic coefficients whilst the latter one yields a linkage through which the flap moves. Eventually, the design is applied to a CAD model shown in Fig. 1 for testing purposes. The model resembles the Chinese Mugin-3 as closely as possible.

*Fig. 1. Project "Flight of Fancy" Λ-tail UAV, [2]*

**Method**

A few major stages during design process are described below.

**Flow analysis**

In order to carry out computational fluid dynamics research, trial version of SimFlow [3], an OpenFoam [4] graphical front end, was used. The OpenFoam bundle contains solvers for numerical solution of continuum mechanics problems. In this particular study case, a solution to Reynolds averaged Navier-Stokes equations was found within a Cartesian computational grid refined locally in an area that is close to the airfoil contour. The fluid is assumed incompressible inasmuch as the flow speed is low enough. Boundary conditions at the airfoil contour imply that no fluid is allowed through and the static pressure gradient takes the value of zero. A k–ω SST turbulence model was chosen according to what is recommended in a tutorial available online, [5]. This model is said to be capable of predicting flows with severe pressure gradients and tendency to separation. Prior to starting iterations, reference values are set, such as freestream velocity and nominal airfoil area (chord length times unit span). Eventually, the iterative process continues until the numerical solution, precisely aerodynamic forces and moment coefficients, complies with a certain convergence criterion.

**Mechanical design**

For purpose of linkage design, trial version of Autodesk Inventor [6] was employed. Tools for building an electronic mock-up of virtually any kind of machine and/or mechanism are available within Inventor's integrated development environment. In this way, developer is able to devise and validate both shape and functionality before the model is built. What is more, Inventor introduces modules for structural and modal analysis implemented by means of the Finite Element Method in order to make the 3D design plausible even more.

The flap chord is 20% times the airfoil chord length. The flap is attached to the wing right next to the fuselage. Apart from guiding rods at both ends, an actuating mechanism is put together and attached to the flap middle. Shape and dimensions of each part are adjusted within Inventor assembly for the flap to meet design requirements in particular. In this way, the mechanism ensures the flap attitude control. Both flap layout and actuating mechanism are shown in Fig. 2.

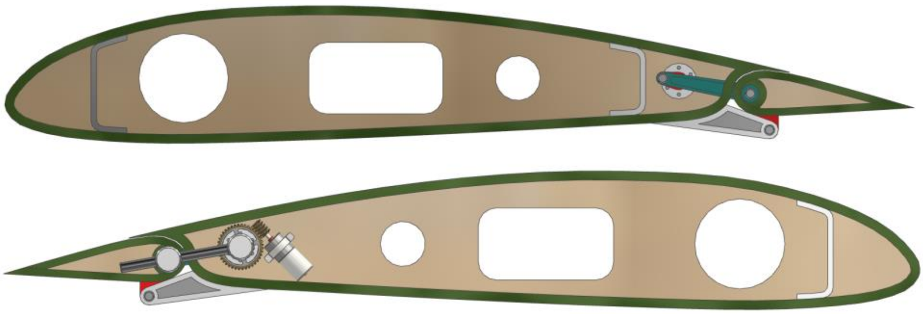

*Fig. 2. Layout of the flap deployment mechanism, airfoil used in Mugin-3*

The four-bar linkage used in the study hereby, obeys the Grashof's law. For at least one link to be capable of making a full revolution, following inequality has to be fulfilled:

$$s + l \leq a + b \quad (1)$$

where variables stand for following: s — the shortest link, l — the longest link, a, b — remaining links. If the shortest link is adjacent to the fixed link, the mechanism is called "a crank rocker four-bar linkage," Fig. 3. In the current project, the shortest link, which is also attached to the worm gear, is able to perform a full revolution.

Flap weight and aerodynamic load are supported by the guiding rod. Forces and moments needed to keep the flap in motion are supported by mere linkage. A triggering device of choice might be applied to the leading crank such as worm gear. To opt for a self-locking actuating device is highly recommended. A worm gear is considered irreversible statically if the lead angle is sufficiently small. The lead angle (a.k.a. helix angle) is defined as an angle between the helix and the worm axis.

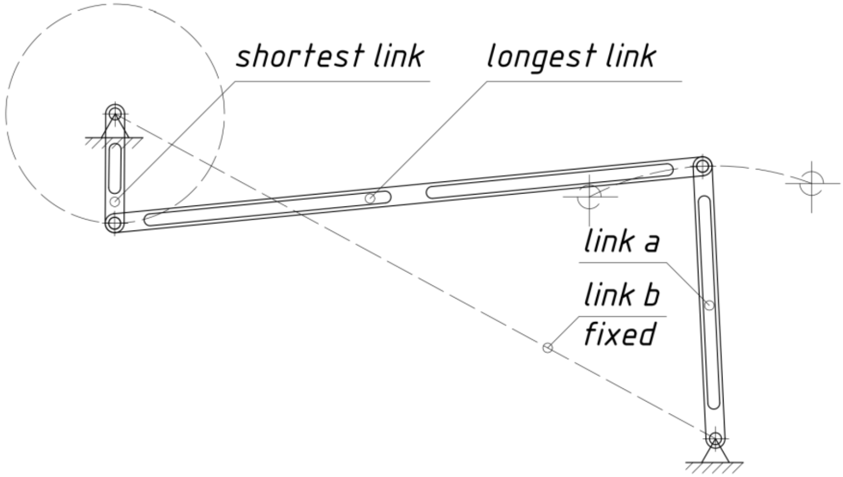


*Fig. 3. A crank rocker four-bar linkage*

**Results**

In Fig. 4 static pressure distribution is depicted in case of deployed flap. The airfoil meets the flow at 5 degrees angle of attack. Red zones show high pressure values as opposed to blue ones. Stagnation points are distinguishable clearly at airfoil and flap leading edges.

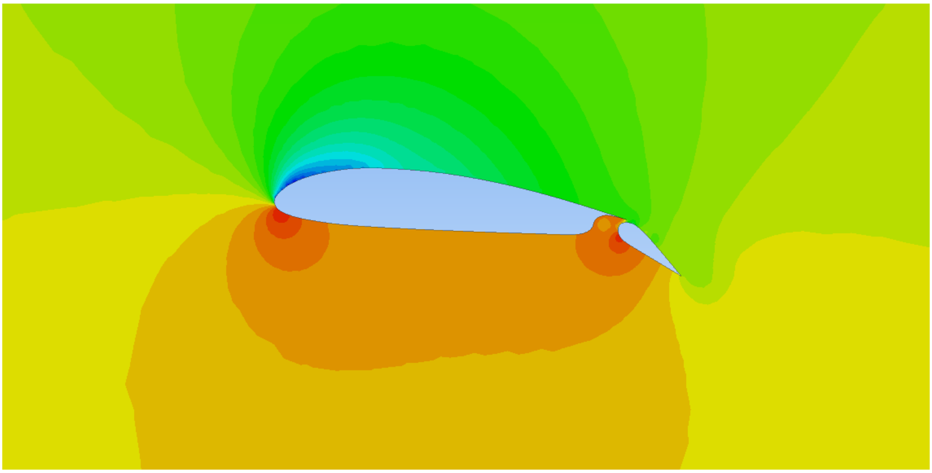

*Fig. 4. Static pressure contours, $\alpha = 5$ deg, $Re = 2.66E+06$*

In Fig. 5, drag polar is shown in case of airfoil with retracted flap. The biggest lift-to-drag ratio ~50 occurs at angle of attack $\alpha \approx 5$ deg.

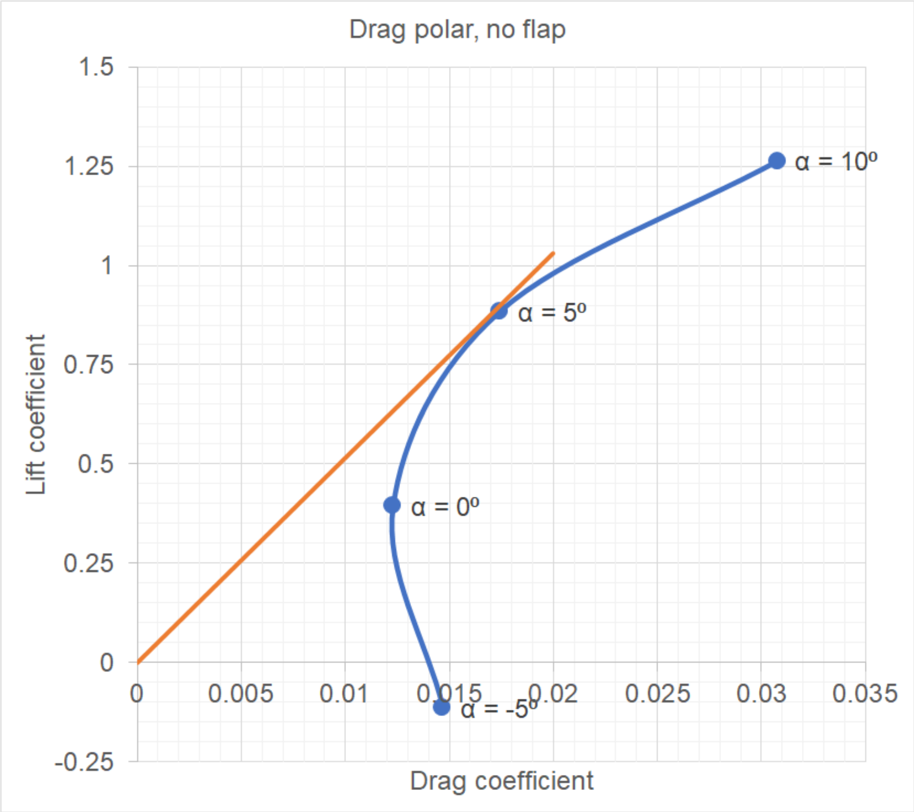


*Fig. 5. Mugin-3 airfoil drag polar, Re = 2.66E+06*

It must be noted that SimFlow simulation worked out a numerical solution to three-dimensional problem, i.e., a wing with unit span, without taking into consideration drag due to lift effects whatsoever. Hence, the obtained numerical results are attributive to the parasitic drag only (predominantly pressure drag). On the other hand, drag coefficient of a finite span wing is augmented by the lift induced drag.

In Fig. 6, the lift force coefficient is shown in terms of angle of attack, so is the pitching moment measured at the airfoil leading edge. In addition, lift force coefficient in case of extended flap at 30 deg is depicted as well. There is a good agreement between numerical results and theoretical statements. The lift coefficient related to deployed flap (red curve) is “shifted” along the ordinate as expected. This chart conforms to a high lift device. Another favorable condition is slope of the moment coefficient curve. It is desirable for the slope to be somewhat negative, for this condition signifies the airfoil damping abilities. An airfoil with constant pitching moment coefficient, worthy of being mentioned, is NACA 23012.

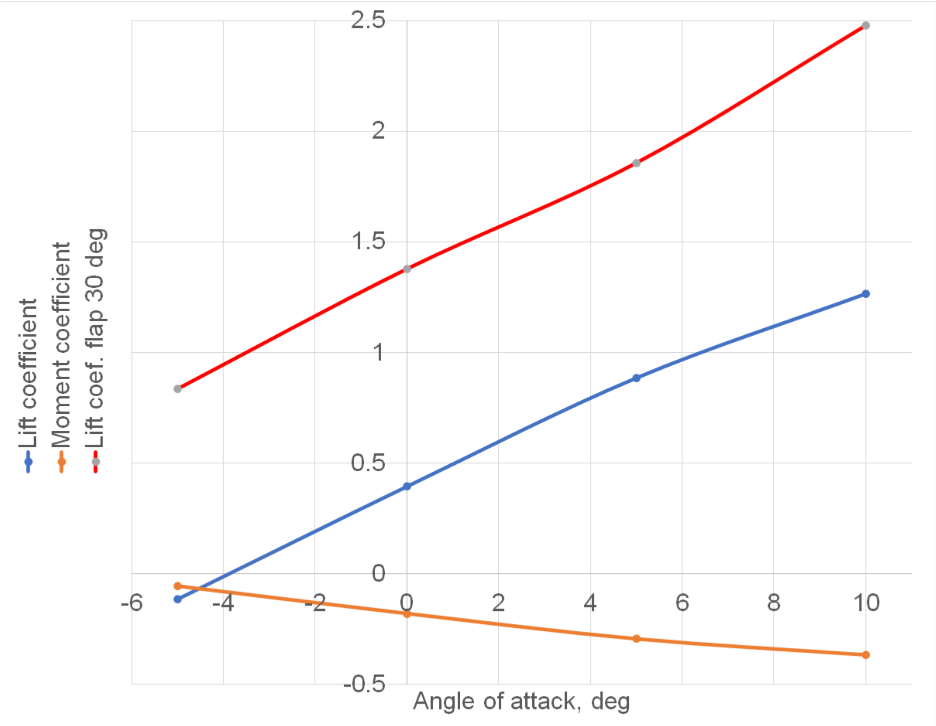


*Fig. 6. Lift force and moment coefficients versus angle of attack, Re = 2.66E+06*

In the current study, to carry out fluid simulations within permissible values of angle of attack, without exceeding the critical value, was considered sufficient. In case of low values of angle of attack, the lift coefficient is said to be barely affected by Reynolds number variations. On the other hand, the stall angle of attack increases as the Reynolds number does.

In Fig. 7 flap deployment/retract sequence is depicted, so is the linkage schematic. The cycle starts from the upper left picture and turns in either clock or counterclockwise direction, whichever is preferable, for instance either 1-2-3-4-1 or 1-4-3-2-1. It is thanks to the four-bar linkage that the actuating motor is not expected to reverse direction. In order to retract the flap, the motor might keep on rotating instead. It takes the input crank exactly one revolution to deploy and retract the flap in succession. Safety stops might indicate that flap extended to an end position and issue a signal accordingly. The linkage dead-centers, that is to say a configuration at which the transmission ratio is minimum, coincide with flap end positions (either retracted or deployed). Taking into consideration the worm gear irreversibility, all these compose a kinematic lock. Consequently, it is permissible for the onboard control system to switch off motor power supply whenever the flap is at rest.

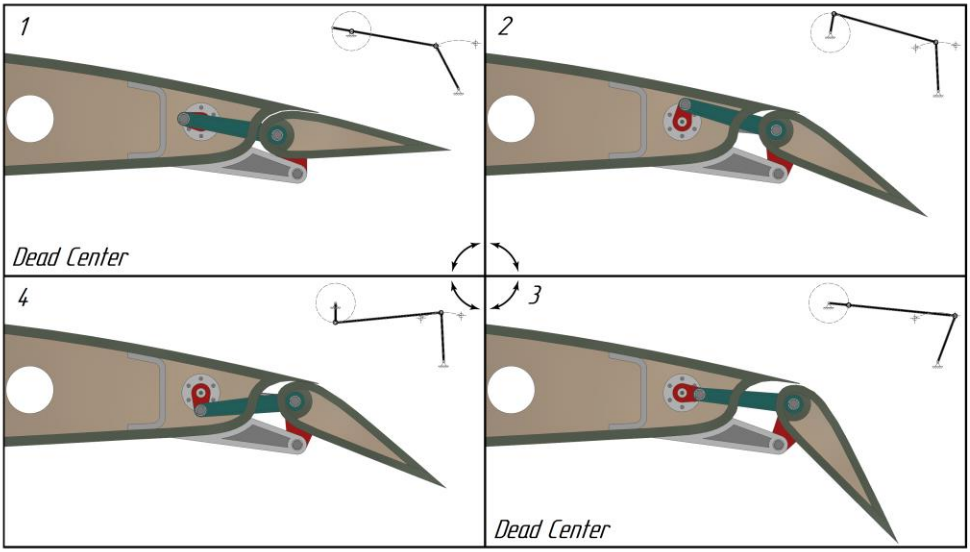


*Fig. 7. Flap deployment/retract sequence*

**Conclusion**

Distinctive features of Fowler flap performance are increased wing planform area, chord length, and airfoil camber. Fowler flap also assists in boundary layer control. Notably, among others, this flap produces the biggest additional lift. Both one- and two-segmented designs are widely used on contemporary airplanes. However, a sophisticated linkage is required to set the flap in motion. For example, a four-bar linkage is used on Boeing 747SP and Boeing 787. In 747SP, the flap is attached to the rocker [7].

Proposed CAD model of the UAV is freely available to everybody for downloading by following link [2].

Further project development might be implementing a microcontroller-based control system that either deploys or retracts the flap whenever an impulse signal is passed from the ground radio transmitter. Presumably, an external interrupt handling routine is worth a thought.

## References

1. https://www.muginuav.com/product/new-mugin-3m-uav-v-tail-platform-frame-kit/
2. https://grabcad.com/library/flight-of-fancy-1
3. https://sim-flow.com/
4. https://www.openfoam.com/
5. https://help.sim-flow.com/userguide/wing/
6. https://www.autodesk.com/products/inventor/overview
7. Rudolph, P., High-Lift Systems on Commercial Subsonic Airliners, NASA CR 4746, 96


## ПРОЕКТ НА ЗАДКРИЛКА ЗА ПРАВО КРИЛО НА БЕЗПИЛОТЕН САМОЛЕТ


***К. Методиев***



**Резюме**

В настоящата статия е предложен проект на едностепенна задкрилка на Фаулер. Задкрилката е предназначена за повишаване на носещите свойства на право крило при ниски скорости. Тя е приложима за малки дистанционно управляеми безпилотни самолети, широко разпространени при любители.

Процесът на проектиране включва детайлен анализ на флуидно течение около крилен профил за случаите на прибрана и отворена задкрилка. Целта е да се получат стойностите на аеродинамичните коефициенти за различни ъгли на атака и числа на Рейнолдс. В допълнение е разработен лостов механизъм, с помощта на който задрилката се задвижва по сложна траектория.

Показани са различни графики и диаграми с цел идеята на проекта да бъде разбрана по-добре.

Bulgarian Academy of Sciences. Space Research and Technology Institute.
Aerospace Research in Bulgaria. 34, 2022, Sofia

DOI: https://doi.org/10.3897/arb.v34.e07

# AEROSPACE SYSTEMS "AERIAL LAUNCH" AT THE MODERN STAGE

***Pavel Penev, Nikolay Zagorski***

*Space Research and Technology Institute — Bulgarian Academy of Sciences*
*e-mail: ppenev@space.bas.bg*

***Keywords:*** *Aerospace systems, Aerial launch, Small satellites*

***Abstract***

*The need for the emergence and use of aerospace systems (ASS) "Aerial launch" by the leading countries has been formulated. The types of ASS and the types of military space systems are revealed, as well as the connection between them. The functioning and perspective ASS "Aerial launch" with civil and military applications is analyzed. Based on a systematic analysis, a structure of ASS "Aerial launch" for the conditions of the Republic of Bulgaria, its advantages, disadvantages and main properties is proposed. Based on the performed modeling, a scheme of operation of ASS "Aerial launch" and stages of the flight of the MiG-29UB carrier aircraft for launching a nanosatellite (nanosatellites) into orbit in the conditions of our country is proposed.*

## Introduction

The name of the systems "Aerial launch" is associated with the launch into space of an aircraft launch vehicle (LV) with a satellite or satellites carried by an aerodynamic aircraft (AC), which performs a flight at an altitude of not less than 10,000 m in the atmosphere on Earth, as a result of which the satellite (satellites) are launched into orbit.

Unlike ground-based and sea-launched LV, air-launched ones do not have to traverse the densest layers of the atmosphere and consume a significant amount of fuel. In this case, starting from a carrier aircraft at a certain altitude, the LV reduces the loss of speed due to the fact that it does not pass through the lower dense layers of the atmosphere.

Account should also be taken of the fact that ground-based or sea-launched LV consumes a significant mass of fuel to reach the altitude and flight speed that an air-launched LV already has when launched by a carrier aircraft.

Another circumstance that contributes to the increasing relevance of the "Aerial launch" systems is that in the 90 s of the twentieth century, as a result of the rapid development of high technology, the concept of "small satellite" (small satellite) appeared. This term refers to an artificial satellite of the Earth (ASE) with a relatively small mass and dimensions, which have been declining in recent years. At present, these miniaturized spacecraft (SCs), also known as cubesat, due to their several times lower value, reduced power consumption and time to create them compared to conventional satellites, are launched into orbit by means of LV dozens of satellites simultaneously.

According to the company “Arianaspace”, the classification of small satellites by indicator “mass” is as follows: small satellite 500–100 kg; microsatellite 100–10 kg; nanosatellite 10–1 kg; picosatellite — less than 1 kg [3]. The small mass-size characteristics of these satellites ensure their placement on board aviation LVs.

As a result of the above, as well as the commercialization of space activity [9], in the last 20 years an unconventional approach to launching small satellites into orbit has been actively applied — through a system known as “Aerial launch”. In this system, the role of the first stage of LV for launching a satellite (satellites) into orbit is played by the carrier aircraft. In particular, the set of functionally interconnected and co-operating carrier aircraft, aircraft carrier and satellite/s designed to be launched into orbit around the Earth, as well as ground command center and surveillance equipment, forms an ASS “Aerial launch”.

During the operation of the ASS “Aerial launch”, the small satellite (satellites) with a relatively small mass is taken out (brought out) in Low Earth Orbits up to an altitude of 600–800 km.

The concept of creation and use of small satellites has passed through various space programs in recent decades (TACSAT, ORS, System F6, etc.), on the basis of which it is corrected and improved [8].

Modern projects “Aerial Launch” have an innovative character, because they incorporate digital and other high technologies, including robotics excellence.

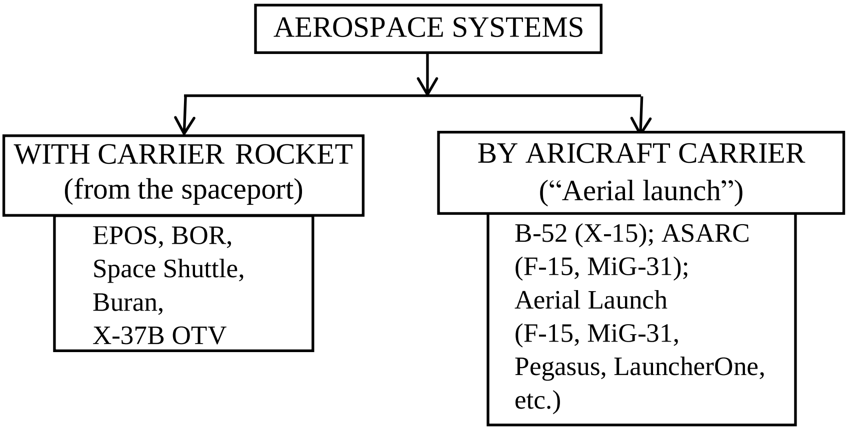


*Fig. 1. Types of aerospace systems*

In a broader sense, ASS operates not only with the use of carrier aircraft. Therefore, they can be considered as a set of functionally interconnected and coordinated operating aircraft carrier or classic LV, SC or rockets of the class "Air-to-Space", space and airport infrastructure designed to solve various target tasks in Space (Fig. 1).

These systems are created at the intersection of aviation and aerospace by combining the advantages and disadvantages of aircraft and missiles.

**Problem status and area of research**

In the early 60's of the twentieth century were gradually built, and in the following decades were established military space systems (MSS) of the United States and the Soviet Union (Fig. 2), representing a set of functionally interconnected and coordinated means of space, air and ground based designed to solve various target tasks of a military nature in and out of Space.

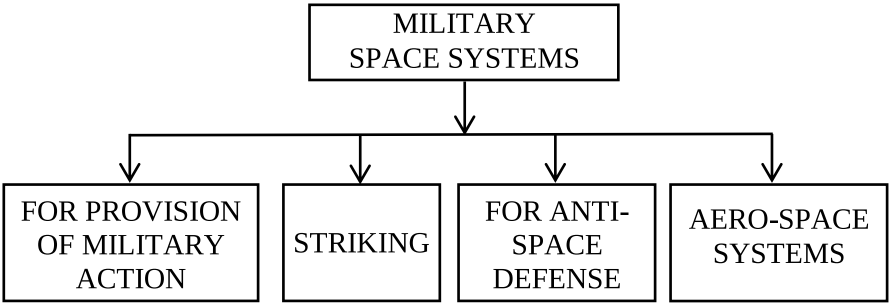


*Fig. 2. Types of military space systems*

Aerospace systems used for military purposes are the latest type of MSS.

In the early 60`s of the twentieth century in the United States began the actual construction of ASS as a type of MSS, whose main dynamic component is the manned missile aircraft X-15 (Fig. 3).

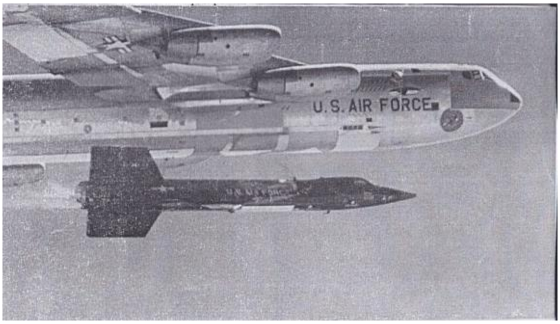


*Fig. 3. Launch of the X-15A rocket plane from space by a B-52 carrier aircraft*

This rocket plane (cosmoplane), mounted on a wing pylon on the right wing of a specially adapted B-52 bomber, is released at near-sonic speed by the carrier aircraft and from a height of 8.5 miles (13.7 km) at M = 0,8 launched into space by turning on its rocket engine [5]. The rocket plane reaches a hypersonic speed (about 7000 km/h) and an altitude of 80–108 km, and for this purpose its engine is turned on for up to 85 s. After reaching its dynamic ceiling, the X-15 rocket launches a ballistic descent, enters the dense layers of the atmosphere, performs planning, lowering and landing on two skis (rear chassis) and a landing gear on the bottom of a dried salt lake in the United States.

Similar activities for the creation of ASS are carried out in the USSR, finalized with the world's first automatic landing at an airport after a space flight on 15.11.1988 of the MSS for repeated use "Buran".

Simultaneously with the X-15 program, the Pentagon conducts research in the field of space defense and considers as one of the possible approaches to this issue the creation of an air-based anti-satellite missile system (ASARC), providing the launch of "Air-to-Space" missiles for destruction of SC. In the period from 1977 to 1986 on the basis of the F-15 fighter was created ASARC, known by the abbreviation ASAT (Anti-Satellite), whose full designation is ASM-135 ASAT. The complex [5] as a carrier aircraft includes the modernized F-15A fighter, armed with a two-stage solid propellant rocket and a small self-guided interceptor with an infrared self-targeting system for low-orbit spacecraft (Fig. 4).

*Fig. 4. ASAT anti-satellite missile system with F-15A carrier aircraft*

The range of the anti-satellite missile of ASARK "ASAT" is about 1000 km, and can intercept spacecraft at altitudes up to 560 km (350 miles) above the Earth's surface.

Of the modern "Aerial launch" programs for launching satellites into orbit via LV, the only one that really works is the American "Pegasus". For its realization, the launch of LV "Pegasus" is carried out by a specially equipped modified passenger plane L-1011 Stargazer of the company "Lockheed Corporation" (Fig. 5). The Pegasus launch vehicle is three-stage, runs on solid fuel and is located under the fuselage of the launch aircraft, with a launch mass of 18,600 kg and a length of 15.5 m. The separation of the rocket from the aircraft is at an altitude of about 12,000 m at a speed corresponding to 0.8 M. The mass of the payload launched into low Earth orbit from the LV "Pegasus" is up to 360 kg.


*Fig. 5. Separation of the Pegasus satellite launch vehicle from the L-1011 Stargazer to launch into space*

The world's first launch of a satellite with air-launched LV took place on April 5, 1990. [5] The Pegasus launch vehicle of the American corporation Orbital Sciencec Corporation was launched by a modified B-52 bomber (from the X-15 Program), and the Pegsat and NavySat satellites were launched into low Earth orbit, respectively the Earth's magnetosphere and to ensure communication with the US Navy. The cost of launching this missile is about 11 million dollars.

The further launch of satellites under the Pegasus program is carried out by the new L-1011 Stargazer carrier of Lockheed Corporation. In April 1995, the first launch of the Pegasus-H rocket by the L-1011 Stargazer carrier was carried out.

The Orbital Sciences Corporation also created the LV Pegasus XL, which has an increased starting weight (23.13 tons) and length compared to the base model [5]. The payload mass, launched into low Earth orbit by the Pegasus XL, is up to 443 kg, and the release parameters of the rocket from the carrier aircraft (altitude and velocity) are close to those of the LV Pegasus. The cost of launching a satellite into space with a LV Pegasus XL is $ 40 million (as of 2014). Until October 11, 2019, inclusive, 44 launches of PH from the "Pegasus" series were performed, of which three were unsuccessful and two with partial success (in a lower orbit).

Of the ASS with LV, the most current at the present stage are the X-37B OTV space unmanned shuttles, which are essentially orbital aircraft launched into orbit using a classic LV from a spaceport and landing at an airport as an aircraft (Fig. 6). Their mission is shrouded in secrecy, and the sixth X-37B OTV reusable spacecraft, currently launched on May 17, 2020, is currently in space. These space unmanned shuttles largely replace aerospace ships repeated use of the Space Shuttle program after 2011.

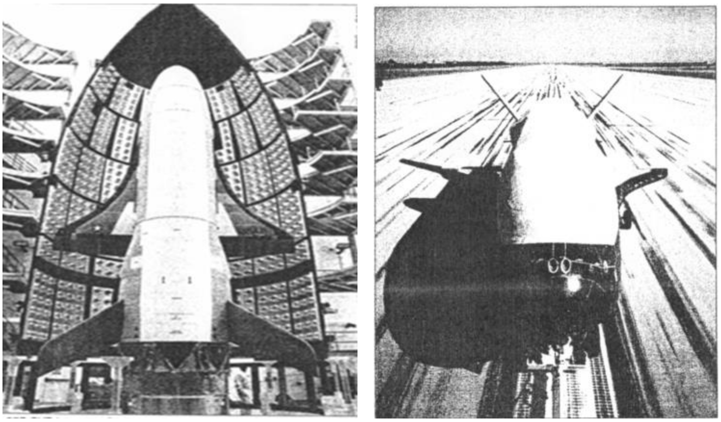

*Fig. 6. Orbital plane reusable X-37B OTV, prepared for mounting rocket (left) and track the aerodrome (right)*

The development of ASS “Aerial launch” with civil applications with solid fuel LV continues. The American company “Virgin Orbit” uses for this purpose a modified Boeing 747 aircraft, called “Cosmic Girl”, under whose left wing a two-stage LV “LauncherOne” with liquid fuel and a length of 21.3 m is suspended on a pylon. The payload that can bring this pH into a low orbit is about 500 kg, and in a polar or close to it — up to 300 kg. This allows the output of a solar synchronous orbit (SSO) up to 300 kg payload.

On May 25, 2020, Virgin Orbit performed a failed test in which the LV fell into the ocean. On January 17, 2021, a second successful experiment was performed, launching 10 small satellites into Earth orbit (Fig. 7). The Boeing 747 Cosmic Girl successfully separates the LauncherOne RN from its board with these 10 nanosatellites — experimental satellites of NASA’s ELaNa educational program.

*Fig. 7. Launcher One successfully launched with 10 nanosatellites from Boeing 747 Cosmic Girl*

According to experts from the company “Virgin Orbit”, if the scheme of operation of this ASS works successfully, it is planned to launch into Earth orbit satellites with a mass of up to 300 kg worth 12 million USD, which is possible at 10–12 space launches per year.

In the second decade of the XXI century, the Spanish company “Celestia Aerospace” began work on ASS for launching nanosatellites. The authors of the idea rely on the MiG-29UB carrier aircraft, ie of a two-seater training fighter, included in the SALS (Sagitarius Airborne Launch System).

According to the authors of the idea [10], the carrier rocket of nanosatellites is of two types: heavy, launching 16 nanosatellites and light — 4 nanosatellites (Fig. 8). The SALS system is expected to launch nanosatellites into orbit around the Earth at an altitude of 400–600 km. Each of the nanosatellites weighs up to 10 kg and is cubic in shape with an edge length of up to 10 inches (25.4 cm).

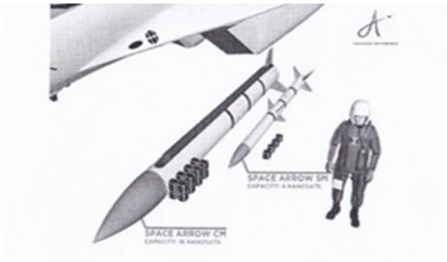


*Fig. 8. Carrier aircraft MiG-29UB and both variants of satellite launch vehicle (according to “Celestia Aerospace”)*

According to Celestia Aerospace, the use of the SALS system requires the MiG-29UB carrier with a LV under the wing to reach an altitude of up to 20,000 m after take-off from the airport. The conditions for the start of the LV, according to [4], are an altitude of 20,000 m; flight speed corresponding to M = 2.2 (i.e. supersonic start), as for the pitch angle the data are theoretical — 65°. At the pre-specified altitude, the Space Arrow SM/CM rocket is separated with its payload on board (i.e. nanosatellite or nanosatellites). Then the LV by starting its engine on solid fuel, and later by inertia, reaches an altitude of 400 to 600 km above the Earth in accordance with the flight program. At this estimated altitude, the nanosatellite (s) are separated and entered into orbit.

From the analysis of the considered issues in the civil and military spheres it follows that at the existing level of development of high technologies and for the considered aircraft-carriers, ASS “Aerial launch” can be an effective means of delivering payload to orbit around the Earth, if the mass it is up to 500 kg and the LV is hypersonic.

## Research method

In order to realize the functioning of the ASS “Aerial launch”, it should have the structure shown in Fig. 9. As can be seen, the ASS “Aerial launch” consists of interconnected components — components that together form its structure.

The main method for studying ASS “Aerial launch” is the theory of systems analysis.

The system has a purpose for which it functions, as well as management, thanks to which its constituent components function purposefully and coherently [7].

The structural connections of different nature between the components of the system ensure the preservation of the properties of the ASS “Aerial launch” when the conditions in the atmosphere and in space change.

The purpose of the ASS “Aerial launch” is the desired result of the operation of the system — launching into orbit a small satellite (satellites) with a specific purpose (e.g. observation).

The presence of management is an inalienable attribute of any system. For this purpose, ASS “Aerial launch” operates a management system at different hierarchical levels. In this case, the central control body is the ground command center (Fig. 9), connected with direct and feedback, both with the carrier aircraft and with ground (ship) surveillance means. At the carrier level, control is performed by the pilot, exchanging information with the ground command center on the necessary control effects.

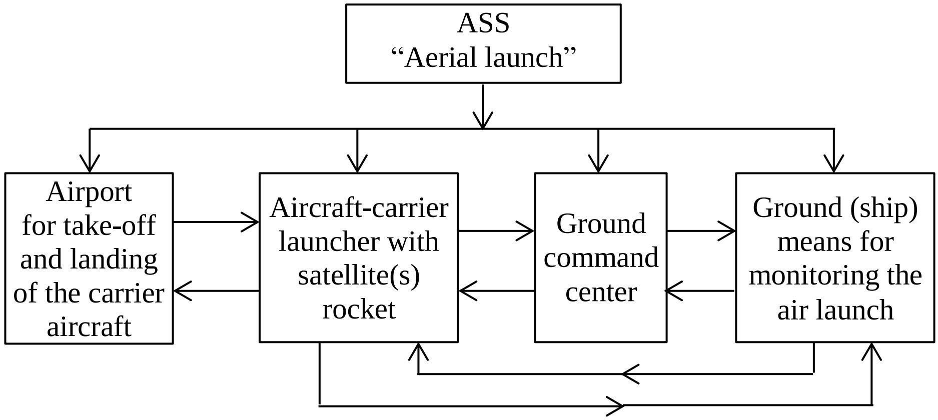


*Fig. 9. ASS “Aerial launch” structure*

The analysis of the state of the problem related to the functioning of various “Aerial launch” systems outlines the following advantages of ASS compared to traditional systems for launching satellites into Space:

- For the functioning of ASS it is not necessary to have or build a specialized stationary ground expensive infrastructure with numerous service personnel as a spaceport with its two main subsystems — technical complex and launch complex;

- Independence of the ASS from the geographical location at the start of the LV with a satellite (satellites) on board, i.e. ASS is not “attached” to the spaceport;

- Selection of the launch point and the possibility of launching satellites into orbit around the Earth in a wide range of directions (inclinations of the orbit to the plane of the equator);

- Use of the initial speed of the LV given by the carrier aircraft after its separation at the respective launch height;

- A significant reduction in the time required for the preparation and launch of aviation LV compared to traditional LV from a spaceport;

- Multiple use of the main components of the ASS;

- Several reductions in the cost of launching one kilogram of payload through the ASS compared to the traditional use of a launch complex from a three-stage LV spaceport;

- Reduction of the harmful impact of the exhaust gases from the LV of the ASS “Aerial launch” in comparison with the classic vertical start of the LV from the spaceport.

Regarding the advantage of ASS to reduce the value of launching one kilogram of payload, the analyzes show that according to [10], space activity becomes profitable by reducing the relative value of launching payload into space to values less than $ 3,000 per kilogram.

Along with the obvious advantages of the ASS over the traditional systems for launching satellites into space, there are certain disadvantages of the ASS “Aerial launch”:

- The operation of the ASS ensures the launch of a limited payload into Space;

- The operation of the ASS ensures the launch of a satellite only in low Earth orbit;

- For the launch of a satellite from the ASS into higher orbits, a significant reduction in the mass of its payload is required;

- Complexity of calculations and the creation of aviation LV, the construction of which can withstand hypersonic speeds (aerodynamics, heating, thermal protection, etc.).

Based on the above advantages and disadvantages, the following properties of ASS “Aerial launch” can be defined and confirmed in practice:

- *Flexibility;*

- *Quick reaction to a created situation;*

- *Functioning in a time scale close to the real one;*

- *Multiple use of the main components of the system (the only one-time component is the LV of the aircraft);*

- *A wide range of realized inclinations of the satellite's orbit to the plane of the Equator;*

- *Lower financial value of the aerial launch compared to the traditional launch in space from a spaceport;*

- *Environmental friendliness;*

- *Versatility, i.e. solving a wide class of tasks of civil and military nature.*

**Need for an aerospace system "Aerial launch" in the conditions of the Republic of Bulgaria**

Our country has highly qualified space specialists and significant experience in the creation and use of space equipment, its own satellites "Bulgaria 1300-I", "Bulgaria 1300-II", "Meteor-Priroda", etc. [3], as well as in conducting space experiments. For all spacecraft and relevant space equipment in which there is Bulgarian participation, their launch into orbit in the past and now is carried out through foreign LV, as the Republic of Bulgaria does not have a spaceport with the relevant infrastructure.

When creating the ASS "Aerial launch", the Bulgarian Air Force not only owned and used MiG-29 fighters to solve various tasks, but also gained over 30 years of experience in the flight and technical operation of these aircraft. In addition, the country has developed airport infrastructure; there is a modern system for command and control of the Air Force; There is an anti-aircraft range of the Shabla Air Force, which is well situated geographically on the Black Sea coast, considerable experience has been gained from its use and, if necessary, temporary restrictions on navigation can be introduced.

Based on the above, it can be considered that for the conditions of the Republic of Bulgaria the project "Aerial launch" can be aimed at launching a low Earth orbit of a small satellite (satellites) for remote sensing through the appropriate LV, suspended under the body of the MiG-29UB (or if possible under the wing).

Most likely, the creation of the LV and its integration with the MiG-29UB carrier will be carried out in another country, due to the lack of experience in our country on this issue.

The creation of the small satellite/s can be done with the participation of Bulgarian scientists and specialists with experience in space research or on their behalf from another country.

The following merits of realization in the conditions of the Republic of Bulgaria of ASS "Aerial launch" with aircraft carrier MiG-29UB are outlined:

- The MiG-29UB training fighter, as a carrier aircraft and a main component of the ASS, is available for use in our country due to the fact that it has been mastered by the flight and engineering staff;

- The presence of two engines of the MiG-29UB aircraft, increasing its reliability, provide a high practical ceiling and the possibility of launching into orbit around the Earth a greater payload than that of a single-engine carrier aircraft;

- The larger geometric dimensions of the MiG-29UB aircraft in comparison with the single-engine fighters allow "suspension" under the body or wing of the LV with larger dimensions;

- Existence and accumulated experience in the use of the Shabla Air Force range, as well as its good location on the Black Sea coast in terms of possible missile launches;

- The crew of the MiG-29UB launch vehicle chooses the direction and the place of launch of the LV;

- There is a possibility for exporting the trajectory of the flight of the LV and the areas of fall of its detachable elements (exhaust stages, front fairings, etc.) from the territory of the Republic of Bulgaria over sea areas with limited navigation;

- Environmental safety (possibility to impose prohibition zones due to falling degrees of LV at its launch into space);

- Mobility of the ASS, enabling the launch of a satellite (s) into orbit from the territory of another applicant country, which is important for commercial launches, including at equatorial latitudes.

The disadvantages of the ASS with the MiG-29UB carrier in the conditions of the Republic of Bulgaria do not differ from those mentioned above for this system in the section "Research method" of the article.

From the above it is clear that for the successful operation of ASS "Aerial launch" in the conditions of the Republic of Bulgaria, in accordance with Fig. 9, it should be specified to the following components:

- Aviation (MiG-29UB carrier aircraft);

- Rocket (LV, respectively under the body or wing of the aircraft);

- Space (satellite/satellites, located at the front of the PH);

- Ground, including a command center or command post that processes incoming information and controls the carrier aircraft and ground (ship) surveillance equipment.

In February 2020, Space Research and Technology Institute-Bulgarian Academy of Science adopted a "Concept for the implementation of the Aerial Launch project for launching a small satellite (small satellites) into Earth orbit in the conditions of the Republic of Bulgaria" [5], as for the purpose is to model the trajectory of the MiG-29 carrier aircraft and the LV with a small satellite (small satellites). The analysis of the results shows [2–4] the theoretical possibility to use a MiG-29 aircraft and a solid fuel pH, with a length of not more than 4.5 m, with a mass of 600 or 1200 kg (in place of the undercarriage tank) for launching nanosatellites (1–10 kg) into low Earth orbit. The three conditions for launching the LV from the MiG-29 aircraft are altitude and flight speed and pitch angle of the carrier aircraft when separating the LV with the satellite, depending on the flight mode.

Scheme of operation of ASS “Aerial launch” and flight stages for launching a small satellite (satellites) into orbit around the Earth in the conditions of the Republic of Bulgaria

The scheme of functioning of ASS “Aerial launch” in the conditions of our country includes the following stages:

- Preparation of LV, respectively of its three stages;
- Installation in LV of a payload — small satellite (small satellites);
- Pre-flight inspection and testing of the on-board LV systems and the small satellite (small satellites);
- Suspension of the LV under the body (half-wings) of the carrier aircraft and pre-flight inspection and testing of the LV systems and the aircraft;
- Departure of the MiG-29UB carrier from the airport and set to a height of 12,000 m – 13,000 m;
- Flight of the aircraft carrier MiG-29UB to the launch zone of the LV to Space, located in the area of the anti-aircraft range of the Air Force near Shabla;
- “Acceleration” by the aircraft carrier MiG-29UB at supersonic speed, performing the so-called. “Diving” with a negative pitch angle and subsequent set of heights (Fig. 10);
- Execution by the aircraft carrier MiG-29UB of the calculated dynamic maneuver “Gorka” (Fig. 10) and separation from the aircraft, for example by catapult or spring mechanism, of LV by actions of the pilot-operator;
- Reaching a safe distance and overshoot between the MiG-29UB carrier aircraft and LV (Fig. 10);
- Control of the flight of the aircraft carrier and LV before and after the launch area of the radar surveillance system of the Air Force;
- Autonomous start of the first stage of LV (Fig. 10);
- Separation of the first stage from the LV, its descent by parachute (or controllable flight to the area of fall) with a view to reuse and autonomous inclusion of its second stage (Fig. 10);
- Separation of the second stage from LV and autonomous inclusion of its third stage (Fig. 10);
- Reaching the third degree of LV at the first cosmic speed (and higher) and output of the calculated orbit of a small satellite (small satellites) — Fig.10;
- Flight of the carrier aircraft to the airport for landing and landing.

As can be seen from Fig. 10, the three conditions for launch of a missile module from a MiG-29UB aircraft, according to the performed modeling, are: altitude 15 km, number M = 0.9 and pitch angle 20°–25° at subsonic launch, and altitude 15 km, number M = 1.7 and pitch angle 30°–35° for supersonic start.

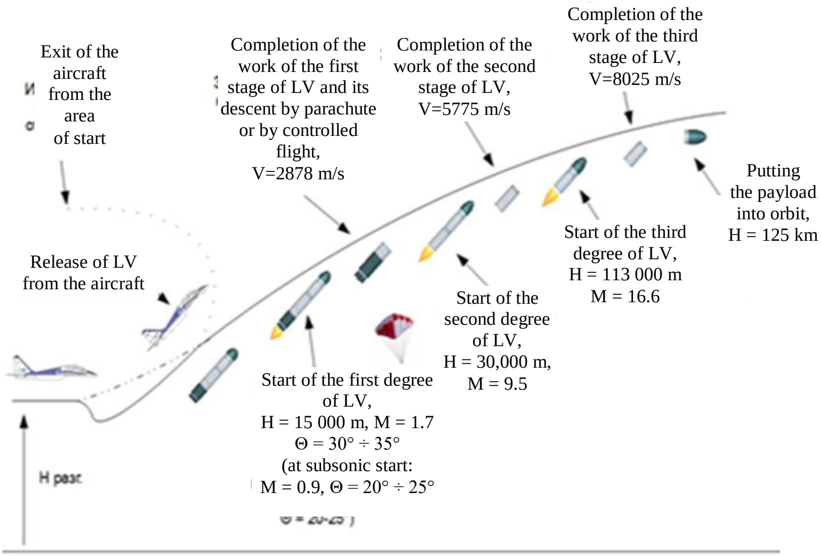


*Fig. 10. Scheme of operation of ASS "Aerial launch" in supersonic flight mode of the MiG-29UB aircraft for launching the launch vehicle (continuous line) and in subsonic flight mode (broken line)*

A detailed engineering and navigational calculation is needed to determine the mass of fuel on the carrier aircraft in order to be able to launch the LV.

**Conclusion**

The idea of implementing the "Aerial Launch" program to launch spacecraft into Low Earth Orbit over the past few decades, given current trends in space, is periodically proposed as a way to radically facilitate access to space for many countries.

The development of ASS "Aerial Launch" with civilian and military applications continues, which is associated with a series of successes and failures. According to Elon Reeve Musk, the success of the famous LV "Falcon 1" previously required at least four failed attempts.

The creation and use of the ASS "Aerial Launch" can reduce the cost of launching a payload and make space flights commercially efficient.

The relatively low value of the "Aerial Launch" project for the conditions of the Republic of Bulgaria is mainly related to the circumstances that its implementation envisages the use of already established reliable aviation equipment (MiG-29UB), which our country has had and successfully operated for decades, as well as its own landfill with adjacent water area with a suitable geographical location, above which to realize its purpose ASS "Aerial Launch".

The creation and operation of the ASS "Aerial Launch" is important not only in the launch of a small satellite (small satellites). Before launching a large satellite into space, scientists and specialists can check some of its equipment on a small satellite (cubsat) launched into orbit by the ASS "Aerial Launch".

With the success of the "Aerial Launch" project, it is possible for the Republic of Bulgaria to independently launch small satellites into space in Low Earth Orbit, both for the needs of the country and at the request of other countries.

## References


1. Badiagin, A. A. *et al.* Proektirovanie samoletov. M., Mashinostroenie. 1972. (in Russian)
2. Yordanov, D. V. Izvejdane na malki izsledovatelski spatnetsi po mnogostepenna shema ot samolat-nositel. Sofia, IKI-BAN, spisanie "Aerokosmicheski izsledvania v Bulgaria", 1996, № 12, pp. 130–136. (in Bulgarian).
3. Mardirossian, G. Introduction to Cosmonsutics. Marin Drinov Acad. Publ. House, 2012, 261 p. ISBN 978-954-322-519-4 (in Bulgarian).
4. Yordanov, D., P. Penev, Air launch options from MiG-29 aircraft. Space research and Technology Institute, SPACE, ECOLOGY, SAFETY, SES 2020, Proceedings 2020, pp. 124 (in Bulgarian).
5. Kardashev, M. A. Vozdushnoi start. Moskva. Novoe vreme. 2016. 355 p. ISBN 978-5-903462-98-8 (in Russian).
6. Kontseptsia za realizirane na proekt "Vazdushen start" za mizvejdane v okolozemna orbita ot samolet-nositel na malak spatnik (malki spatnetsi) v usloviata na Republika Bulgaria. P. Penev, D. Yordanov, Sofia, IKIT-BAN, Sektsia "Aerokosmicheski sistemi za upravlenie", 26.02.2020. 43 p. (in Bulgarian).
7. Lebedev, A. Osnovi sinteza sistem letatelnih apparatov, Moskva, Mashinostroenie. 1987. 224 p. (in Russian).
8. Marshalov, K. Osnovnie napravlenia razvitia kosmicheskih optiko-elektronnih sredstv Voorujennih sil USA, Zarubejnoe voennoe obozrenie, 2015, kn. 12, pp. 80–82 (in Russian).
9. Penev, P. Kosmos i sigurnost, IK "Vital", 2014, 390 p., ISBN 978-954-8259-94-1 (in Bulgarian).
10. Google. LIII Mejdunarodna nauchno-prakticheska konferentsia, Novosobirsk, 2015, V. Korneev i dr. Analiz sistem vozdushnogo starta kosmicheskih obektov (in Russian).
11. http://celestiaaerospace.com
12. https://hicomm.bg/space/nanospytnici-politat-kym-drugite-planeti.html
13. https://bg.wikipedia.org/wiki/CubeSat
14. https://ru.wikipedia.org/wiki/%D0%9A%D0%A1-172

# АЕРОКОСМИЧЕСКИТЕ СИСТЕМИ „ВЪЗДУШЕН СТАРТ” НА СЪВРЕМЕННИЯ ЕТАП

***П. Пенев, Н. Загорски***

**Резюме**

Формулирана е необходимостта от появата и използването от водещите държави на аерокосмически системи (АКС) „Въздушен старт”. Разкрити са видовете АКС и видовете военнокосмически системи, както и връзката между тях. Анализирани са функциониращите и перспективни АКС „Въздушен старт” с граждански и военни приложения. На основата на системния анализ е предложена структура на АКС „Въздушен старт” за условията на Република България, нейните предимства, недостатъци и основни свойства. На базата на извършено моделиране е предложена схема на функциониране на АКС „Въздушен старт” и етапи на полета на самолет-носител МиГ-29УБ за извеждане на наноспътник (наноспътници) в околоземна орбита в условията на нашата страна.

Bulgarian Academy of Sciences. Space Research and Technology Institute.
Aerospace Research in Bulgaria. 34, 2022, Sofia

DOI: https://doi.org/10.3897/arb.v34.e08

# ROLE OF POWER RESERVE IN PARALLEL HYDRAULIC MOVEMENTS OF AIRCRAFT CONTROLS

***Dimitar Jordanov[1], Nikolay Zagorski[1], Stanislav Tsholakov[2]***

*[1]Space Research and Technology Institute – Bulgarian Academy of Sciences*
*[2]Technical University – Sofia*
*e-mail: dimitar.v.jordanov@gmail.com*

***Keywords:*** *Transport aircraft, Parallel hydraulic drives, Hydraulic booster*

***Abstract***

*A parallel booster control of transport aircraft controls has been modeled and the positive role of the power reserve for the operation of the structure with permissible operating differences in the pressures of the supply systems has been demonstrated.*

## Introduction

Parallel hydraulic drives are typical of large transport aircraft, in which one body (for example, a rudder for height or direction) deviates from several hydraulic boosters. Each of these hydraulic boosters is powered by a separate hydraulic system and, of course, there are acceptable differences in the operation of the drive devices. The control unit that drives these devices is the element through which, in real conditions, the common work is redistributed between the individual hydraulic boosters. Some (faster) work with overload, and others (slower) work with supporting efforts. In the vicinity of the end positions, there are significant differences in the strokes of the individual devices. The theory of hydraulic propulsion of aircraft controls recommends that hydraulic boosters be selected with a 50% power reserve and a 20% speed margin, with possible desynchronization within acceptable limits. In practice, such a stock of all modes and structures cannot always be provided, especially for controls such as movable stabilizers for maneuverable supersonic aircraft. In these organs, some limitations in their efficiency are possible (for example, limitation of the range of deviation due to power causes of supersonic speeds) all shunting aircraft. During the flight tests of the MiG-25 aircraft, there is a known case in which it is impossible to bring a differentially deflected horizontal stabilizer out of the extreme position, and the situation ends in a crash. Events for this reason in flight practice are called “biting the control lever”.

**Study area**

The research idea is to check by modeling the efficiency of the power reserve of the hydraulic boosters, with the allowable for the practice difference in the pressure of the supply hydraulic systems of 10% ... 15%. For transport aircraft, this should ensure that the “stop” phenomenon is eliminated before the rudder reaches the end of the available range due to high hinge torque. “Biting the controls in extreme positions” for the handlebars is impossible because the regulations do not allow them to be overcompensated, as in the case of controllable stabilizers. Possible rudder overcompensation can occur due to incorrect adjustment and operation of servo compensators.

**Model of hydraulic booster**

The developed computer model of parallel drive of controls from three steering units aims to study the work in case of differences in the pressure of the working fluid in the feed hydraulic systems, leading to synchronization disorders. This type of propulsion is provided by the spoilers, the rudder of the A-320 aircraft and the controls of most heavy transport aircraft.

Fig. 1 shows a model of a steering unit, implemented through the software package “Matlab-Simulink”. Its operation is the basis of the parallel multi-booster drive. Fig. 2 shows the same unfolded model for the “BOOSTER” subsystem. The load is simulated by the product of four multipliers (Fig. 2): spring stiffness C = 2330 N/mm, stroke of the actuator- *y(mm) = f(t)*, coefficient $K_p$ and additional multiplier (*±1*) , formed by a unit for conditional transition on a signal from the distribution valve.

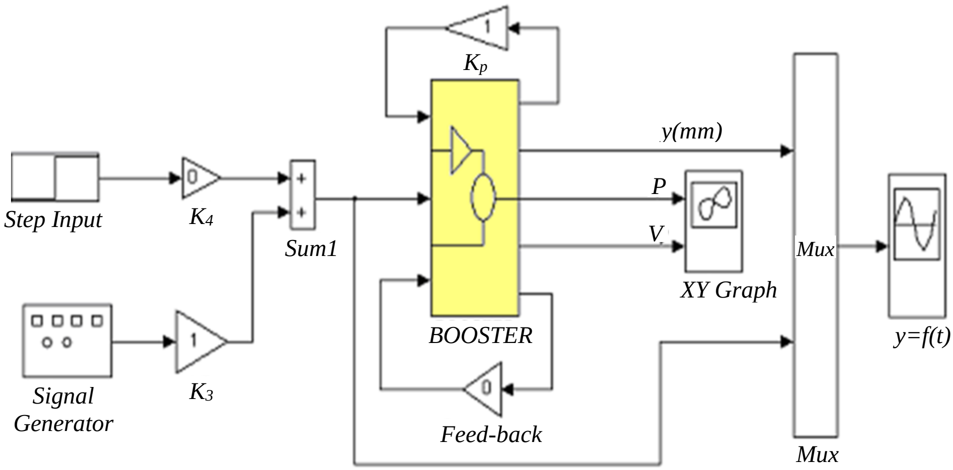


*Fig. 1. Model of steering unit, realized through software package “Matlab-Simulink”*

The input signals (Step input, Signal Generator) in the model are formed from standard Simulink sources, by appropriate adjustment. The results are visualized graphically as a transient process of displacement $y = f(t)$ and the dependence of the speed of movement on the load $V = f(P)$. By changing the value and the sign in the amplifier $K_p$, the degree of load and its direction with respect to the movement of the actuator is simulated. At $K_p > 0$ the load is counteracting. If $K_p < 0$ the power steering model mimics an auxiliary load. The operation of the rudders with axial compensation below 28% is characterized by the fact that in case of deviation from the neutral position the counteracting force increases according to an approximately linear law. Returning to a neutral position of such a governing body is a supportive effort, decreasing from a maximum value to zero. Cyclic deflection of the rudder in the whole range is characterized by successive phases of operation with counteracting and supporting load on the power steering. The change of the nature of the load in the end positions in the model is performed automatically by the *Switch1* unit (Fig. 2).

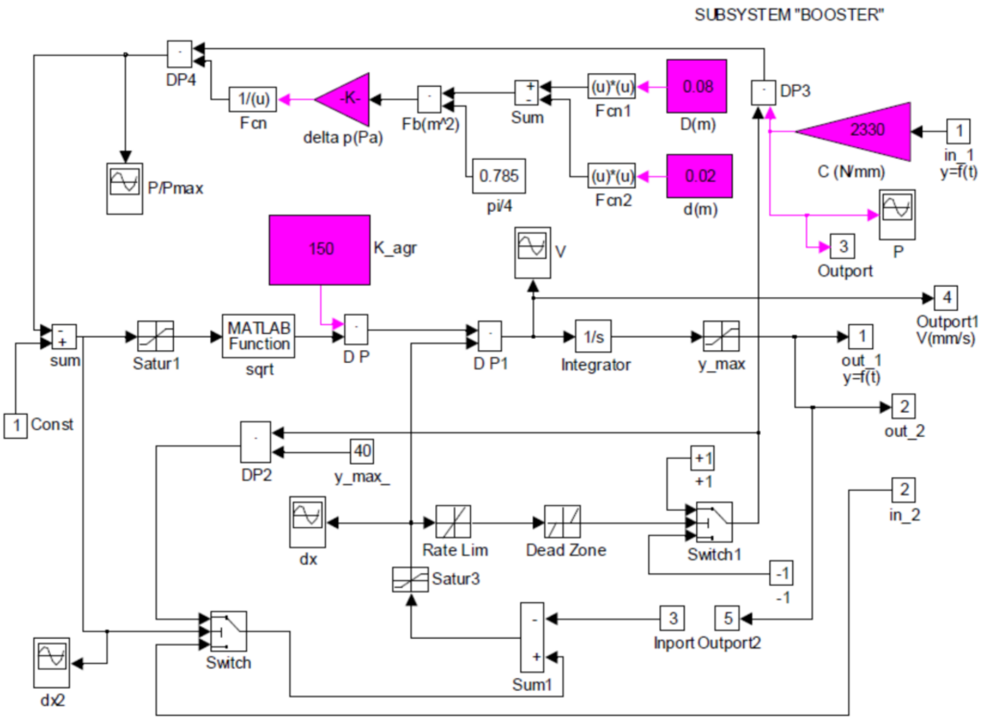


*Fig. 2. Model of the BOOSTER subsystem*

The possibilities of the model are to study different cases of load on the handlebars and steerable stabilizers. If the amplifier $K_p$ is set to a factor $K_p < 1$, the aircraft control is a controllable stabilizer of subsonic speeds with overcompensation. It is characteristic of such controls that the deviation from the neutral position is associated with supporting efforts, and the return with counter-forces (as opposed to alternating phases for the rudders). The absolute value of the coefficient $K_p$ can mimic the overload of the hydraulic booster $\left(|K_p| > 1\right)$ or work with a reserve of power capabilities $\left(|K_p| < 1\right)$. For example, a properly selected power steering in its operating range together with an aircraft rudder has a load factor $\left(|K_p| < 0{,}67\right)$ in the model. Overloading of the power steering is simulated with a factor $K_p > 1$.

Fig. 1 shows the limit cases for counteracting the load on the handlebars $\left(K_p = 1\right)$, when at the very end of the range of deflection of the handlebars, forces are obtained from the hinge moment equal to the power capabilities of the power steering. The feedback can be switched off by setting the Feed-back amplifier (Fig. 1) to 0 and thus recording the static load characteristics of the hydraulic booster similar to a test bench.

**Basic idea of the model**

It is known that the speed *V* of movement of the actuator is determined by the following factors:

• Difference between the pressures in the discharge and drain highways;

• The condition of the channels and the associated hydraulic resistance;

• The area of the piston;

• The opening of the channels for the passage of liquid through the distribution device (slide stroke $\Delta x$);

• The degree of load, as a ratio of the current to the maximum load $P/P_{max}$ for the power steering.

The first three factors in modeling can be conditionally assumed to be constant (piston size, working fluid pressures, coefficient of resistance of the slide) and determine the so-called maximum speed gain *K*, where:

1) $$K = \frac{1}{F_p}\sqrt{\frac{p_H - p_C}{2K_d}}.$$

The physical nature of the coefficient K is the speed of the actuator (*mm/s*) at one stroke of the slide and is the slope of the throttle characteristic in the absence of load. It depends on the difference between the pressure of the discharge and drain lines, the size of the piston and the hydraulic characteristics of the switchgear. For each specific model of the hydraulic booster, this is a known value. Depending on the purpose of the power steering, the shaping of the channels and the profiling of the switchgear, the coefficient K does not exceed a value of $150\ (1/s)$ and usually occurs in the range $K = 10 \ldots 125\ (1/s)$. In the model of Fig. 8, this is the constant $K_{agr} = 150\ (1/s)$, which corresponds to a booster with high speed. The other two factors, when operating the power steering as a tracking system, change the speed of movement of the actuator along its course. If the load is not taken into account, the speed is determined mainly by the stroke of the gate $\Delta x$, which is the difference between the input signal and the feedback signal. This difference in the impact with a stepped input signal at the input of the power steering changes, as at the beginning and end of the process is zero (the cross-section of the gate when the feedback is variable).

The main idea for modeling the movement of the actuator under variable load is realized by representing the speed V as a product of three multipliers:

- the constant $K = K_{agr}$;
- the movement of the slide $\Delta x$;
- $\sqrt{(1 - P/P_{max})}$.

2) $$V = \Delta x K \sqrt{(1 - P/P_{max})}.$$

After integration (block integrator in Fig. 2) at the output of the model is registered the movement of the actuator "*y*" in *mm*. It is limited for the specific model in the range $\pm 40\ mm$.

The maximum load that the hydraulic booster is able to take depends on the size of the piston and the difference between the pressures of the working fluid on both sides and does not depend on the stroke of the slide. Data on the geometric dimensions (constants $D = 0{,}08\ m$ and $d = 0{,}02\ m$) and pressure ($\Delta p = 19700000\ Pa$) are entered in the model, which determine $P_{max} = 92{,}8\ kN$.

The model can be readjusted for different sizes, fluid pressures or loads. The reconfiguration points of the model in Fig. 2 are colored.

## Modeling results

The operation of the model of a power steering is presented with the results of the following graphs. Figure 3 shows *the static load characteristic of the hydraulic booster* $V = f(P)$ at $x = x_{max} = const$. For this purpose, the model is tuned by ***switching off the feedback*** and setting the input signal from the "*Signal Generator*" block with rectangular polarity changing signals — frequency *0.5 Hz* (*3,14 1/s*) and amplitude *1,5 mm*. Operating time of the model $t = 2{,}5\ s$. The coefficient $K_p$ is set for counteracting load to the maximum power capabilities of the hydraulic booster $(K_p = 1)$. With such a setting in the end positions, the input signal keeps the channels of the switchgear open up to the maximum stroke ofthe slide (*±1,5mm*) — which is a condition for obtaining the static load characteristic in the four quadrants (alternating phases of counteracting and supporting force in both directions).

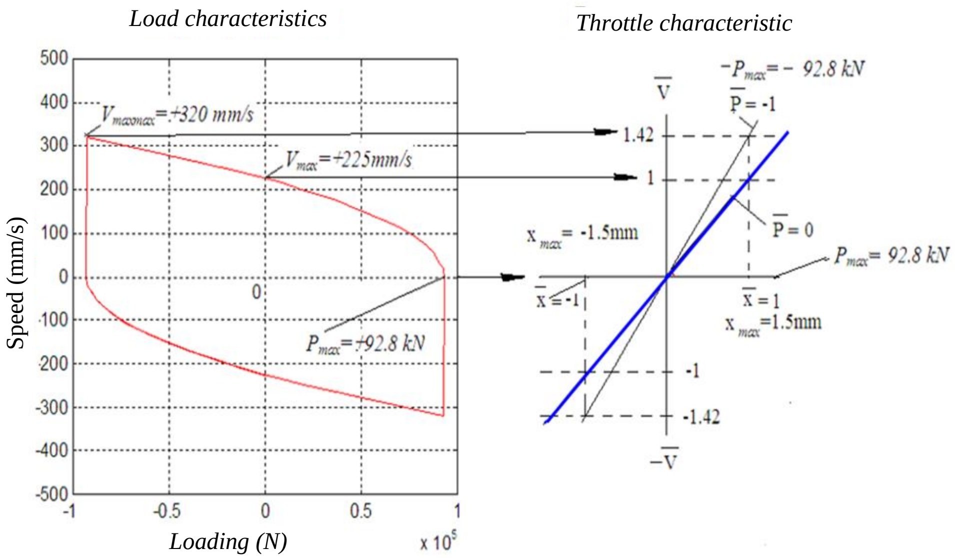


*Fig. 3. Static load characteristics: abscissa- load P(N); ordinate- speed V(mm/s);*
*$P_{max}= \pm 92{,}8$ kN; $V_{max}= \pm 225$ mm/s; $V_{max\ max} \approx \pm 320$ mm/s;*
*Load characteristics $V = f(x)$ at $P = const$.*

Fig. 4 shows the stroke of the distribution valve at the set input signal and the switched off feedback. By characteristic points of the load characteristic ($P_{max}= \pm 92.8$ kN; $V_{max}= \pm 225$ mm/s; $V_{max\ max}= \pm 320$ mm/s) *the throttle characteristic of the hydraulic booster* can also be built.

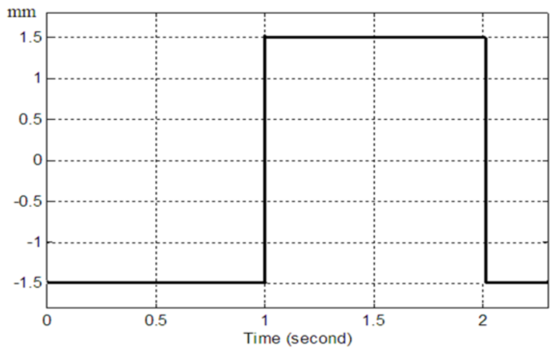


*Fig. 4. Stroke of the camshaft x (mm) with feedback off to model*
*the load characteristic $V = f(P)$ at $x = \pm x_{max}$*

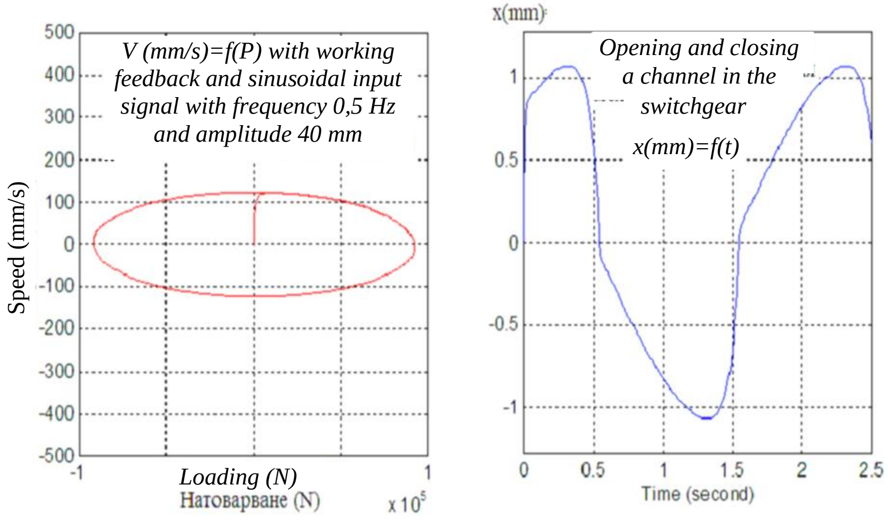


*Fig. 5. Operation of the model with working feedback and input sinusoidal signal*

The role of the feedback can be seen in Fig. 5 when the booster input device moves according to a sinusoidal law with a frequency close to the natural movements of the pilot (one complete deviation of the control and return to neutral for one second).

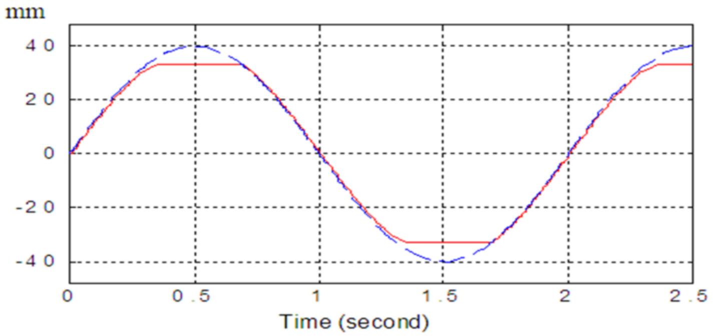


*Fig. 6. Transient with sinusoidal input signal with amplitude 40 mm and frequency 0.5 Hz. The actuator, when overloaded with 20%* $(K_p = 1{,}2)$ *of counteracting force, is visibly delayed by the input signal (dashed line), stops at a "stop" near the end positions* $(\pm 33\ mm)$ *when it reaches* $|P_{max}| = 92800\ N$ *and not can use the entire control range.*

The phenomenon of “stop” is demonstrated by the model of Fig. 6 when operating the power steering as a tracking system (with feedback included). In real practice, this phenomenon can occur even with properly designed aerodynamic rudders, because it is related to the ultimate power capabilities of the booster, and they change with decreasing operating pressure (for example, failure in the control system of the booster pump). The exclusion of such phenomena in practice is done in the design with the selection of a sufficiently strong hydraulic booster (with a load margin).

### Simulation of asynchronous parallel drive

For the purposes of modeling, the model of Fig. 1 is modified in the form of Fig. 7.

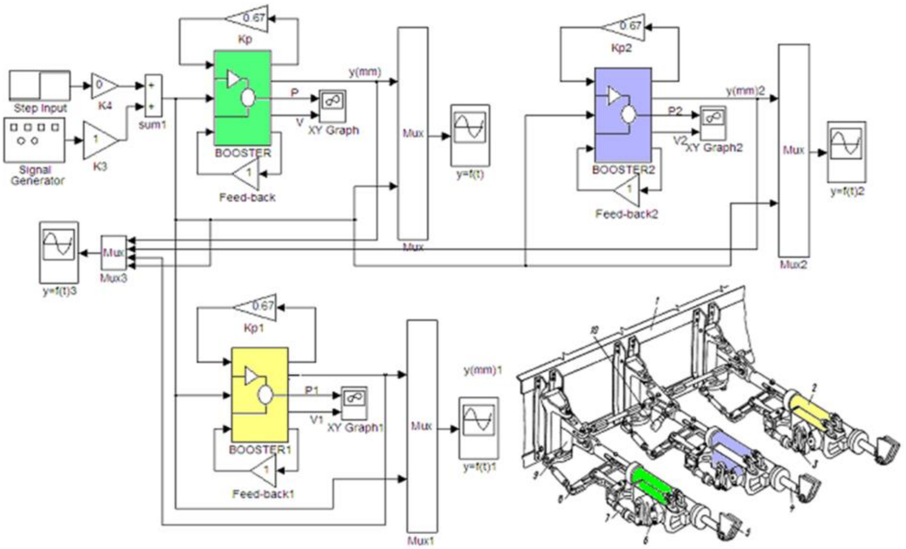


*Fig. 7. Model of multi-chamber parallel drive with the same hydraulic boosters and pressure differences of the hydraulic systems*

Differences in operating pressures affect the force $P_{max}$ and speed characteristics $K_{agr}$.

The different hydraulic systems in the model are set to work with different operating pressures, which hypothetically may be real in the functions that these systems perform. The results shown in Fig. 8 show that if hypothetically the hydraulic boosters are selected in the design process to work without load margin (in the model setting $K_p$, $K_{p1}$, $K_{p2} = 1$), the actuators tend to move at different speeds.

The desynchronization is most noticeable at the end of the turn. This further burdens the drive control, which absorbs these differences and redistributes the load so that slower power boosters receive support from faster ones and vice versa. This synchronization mechanism cannot be modeled with the proposed model, but it can prove that with proper selection of hydraulic boosters (with a margin of 50% by piston rod force) the pressure difference of different hydraulic systems up to 10% does not contribute significant desynchronization in the movements of the actuators (the existing asynchrony is permissible in operating conditions). This is shown in the right graph of Fig. 8 and is achieved by adjusting the load coefficients in modeling $K_p$, $K_{p1}$, $K_{p2}$ with the same value 0,67, which is a ratio between *1* and *1,5* and is recommended by the theory of hydraulic propulsion of aircraft controls [4].

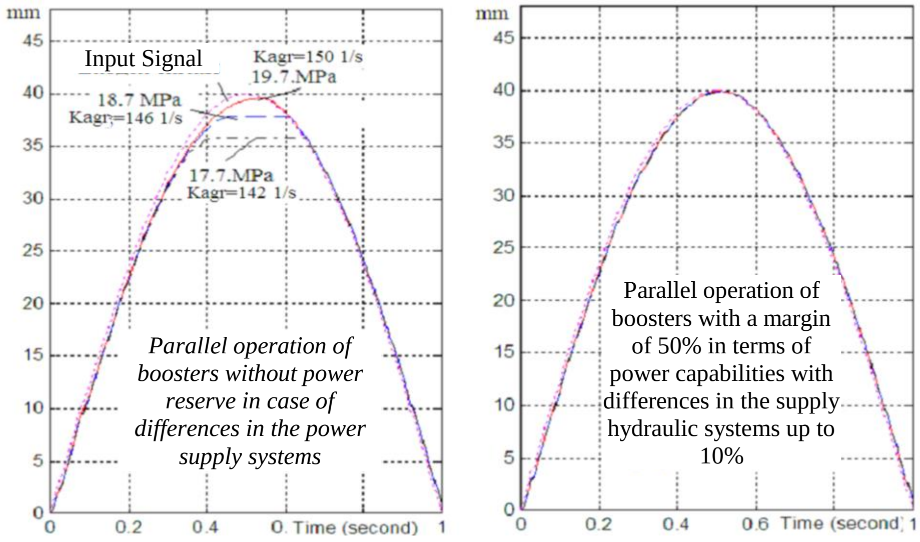


*Fig. 8. Stroke of actuators in parallel operation, when the power supply hydraulic systems have different pressures within the operational admissibility (differences up to 10% ... 15%). The input signal is sinusoidal with a frequency of 0.5 Hz and amplitude of 40 mm*

The location of the operating area in relation to the speed and power limit characteristics, according to these recommendations is shown in Fig. 9 — left graph. The two zones are obtained with the model of Fig. 7 with different setting of two of the modeled boosters and subsequent graphic processing.

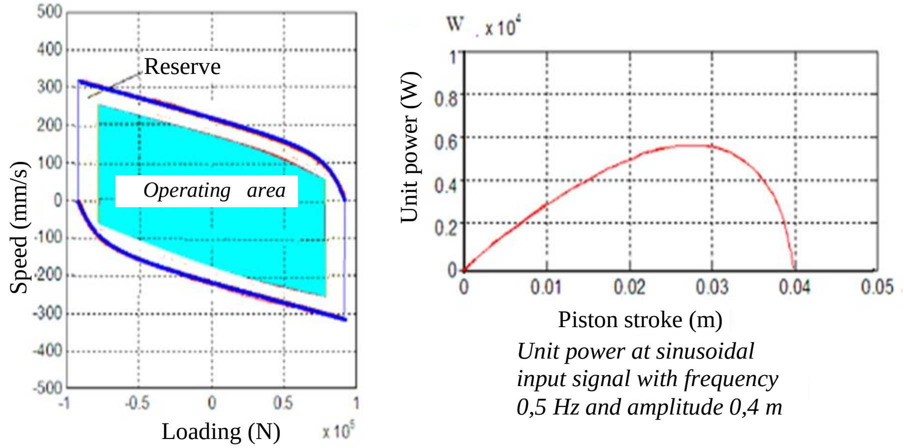


*Fig. 9. Approximate location of the operating area and the actual power capabilities of the booster on the load static characteristic; power of the steering unit (power steering - transmission - steering wheel) in case of steering deviation*

When operating the booster in real conditions, the maximum power is obtained at about 75% of its maximum stroke. The model can also, with some tuning and development of its graphical capabilities with the Sinks library from Matlab-Simulink, confirm this fact known from the theory. The dependence of the power along the stroke of the piston rod is shown in Fig. 9-right graph.

## Conclusion

The work of the model confirms the main idea of the recommendation in the selection of hydraulic actuators: to work with a margin of at least 20% and strength — 50%.

## References


1. AIRCRAFT MAINTENANCE MANUAL – Airbus A320. 1999.
2. Bashta, T. M. Gidroprivod i gidropnevmoavtomatika, izd. “Mashinostroenie”, Moskva, 1972 (In Russian).
3. Gulytjaev, A. K. MATLAB 5.2 Imitacionnoe modelirovanie v srede Windows; Prakticheskoe posobie. Sankt Peterburg. izd. Korona print, 1999 (In Russian).
4. Jordanov, D. Letatelni aparati – sistemi za upravlenie, kniga #16 ot poredicata “Biblioteka na aviacionnija specialist”, katedra “Vyzdushen transport” v Tehnicheski universitet – SofiJa, 1999 (In Bulgarian).
5. Novozhilov, G. V. i dr. Teorija i praktika proektirovanija passazhirskih samoletov, Nauka, Moskva 1971 (In Russian).

# РОЛЯ НА РЕЗЕРВА ОТ МОЩНОСТ ПРИ ПАРАЛЕЛНИ ХИДРОЗАДВИЖВАНИЯ НА САМОЛЕТНИ ОРГАНИ ЗА УПРАВЛЕНИЕ

*Д. Йорданов, Н. Загорски, Ст. Чолаков*

**Резюме**

Статията представя процес на моделиране на паралелно бустерно управление на органи за управление на транспортен самолет, като е демонстрирана положителната роля на запаса от мощност за работата на конструкцията при допустими експлоатационни разлики в наляганията на захранващите системи.

Паралелните хидравлични задвижвания са характерни за големите транспортни самолети, при които един орган (например, кормило за височина или направление) се отклонява от няколко хидроусилватели (бустери). Всеки от тези хидроусилватели се захранва от отделна хидросистема и, естествено, съществуват допустими разлики в работата на задвижващите устройства. Органът за управление, който тези устройства задвижват, е този елемент, чрез който при реални условия се преразпределя общата работа между отделните хидроусилватели. Едните (по-бързите) работят с донатоварване, а други (по-бавните) работят с подпомагащи усилия.

Bulgarian Academy of Sciences. Space Research and Technology Institute.
Aerospace Research in Bulgaria. 34, 2022, Sofia

DOI: https://doi.org/10.3897/arb.v34.e09

# SIMULATION AND MODELS OF ONBOARD SECONDARY POWER SOURCES FOR AERO AND SPACE DEVICES

***Pavlin Gramatikov***

*Space Research and Technology Institute — Bulgarian Academy of Sciences*
*e-mail: pgramatikov@space.bas.bg*

***Keywords:*** *Secondary power sources, Simulation models, Ltspise, Micro-Cap, NI MultiSim*

***Abstract***

*This article discusses the design and evaluation of secondary power sources using simulation models. In a set of circuit experiments, the models allow various parameters to be measured and visualized and aid in the analysis of the results. The models were developed using "NI MultiSim" (for simulation experiments); "Micro-Cap" (for functional experiments) and "LTspise" (for process control). Simulation helps to understand the basic concepts, analysis and tuning of circuit processes and parameters of secondary power supplies.*

## 1. Introduction

The onboard secondary power sources and systems (SPs and SPS) are designed according to the requirements of the specific loads; regulated technical requirements of the standards for space equipment (SE) and space operating conditions [3]. Incorrectly designed SPS can cause: poor electromagnetic compatibility (EMC); errors in the junior bits when we make analogical-digital conversion; noises in analogue data, etc. Analysing heat processes in SPS helps to increase the reliability and resource of SPS [3, 5]. In order to achieve a long-time use of SPS in advance a thorough analysis of their elements with the shortest resource in space conditions is carried out. That are devices with high operating temperature of the hull (which reduces the time of flawless operation of the SPS): electrolytic capacitors and the switched mode elements (diodes and transistors) operating at the high frequency [5]. The analysis of space SPS can be divided into three groups of consecutive activities: design; creation and final corrections after laboratory testing with space methodology and onboard studies in manned and unmanned spacecraft. Specific activities in the synthesis of a particular cosmic SPS are: choice of the element base according to the working conditions; selection of the structure of the SPS; examination of the thermal regimes and parameters of the SPS according to the SE and the scientific experiment.

In this article we distinguish three types of SPS, according to their application for: manned spacecraft, unmanned spacecraft and unmanned aerial vehicles (UAV):

• For board analysis of the SPS in unmanned spacecraft the means for telemetric control and ground processing of the data, as well as software control from the boarding computers are used. The weight characteristics in the space conditions of use are not in the foreground-in the case of interplanetary flights double and triple reservation [1, 3] shall apply.

• The abilities of the astronaut as operator [11] of the SPS and the scientific apparatus in manual mode (emergency and main) are also used in manned spacecraft. In long term the astronaut performs operation and repair of SPS [3], but the time and means of repair are regulated. SPS for manned spacecraft has a specific construction and specific qualities of materials.

• In case of SPs or SPS for UAV in the development of one product is invested scientific work in order to minimize the weight and volume of the power supply-including cables and achieve satisfactory EMC. The reliability and the resource of the equipment used must be satisfactory for the short flight time, usually within 24 hours. In the UAV is not necessary the reservation of SPS and the multiannual reliability. The SPS technical indicators require the EMC to ensure the functioning of the specific UAV (rather than the functioning of a complex of work and scientific Apparatus as in space SPS) and high energy efficiency.

## 2. Main types of SPs for aero and space purposes.

In SPS with space application is obligatory to use SPs with galvanic isolation not only in relation to the input/output compounds, but also to the casing, control and telemetry circuits [3]. In The UAV minimizes weight and is usually administered SPs without galvanic isolation, without a choke or a single choke. Depending on the structure of the impulse transducers with galvanic isolation are:

• Mono-phase: forward converter with one or two semiconductor keys and a reverse “flyback” converter with one or two semiconductor keys;

•Two-phase (half bridge and full bridge circuit);

• Multi-phase converters.

Impulse converters according to the mode of switching are: forward and flyback; single-phase and multiphase, resonant, quasi-resonant and etc.

## 3. Simulation methods for analysis and synthesis of SPs

### 3.1. Program Product “LTspise”

With this software are possible the following analyses of SPs: “Transient analysis” (Transitional processes after start of supply voltage); “AC small signal” (amplitude and phase frequency analysis in small signal); “DC sweep” (DC regime in dependence of constant voltage or current); "DC transfer function" and "DC_op_pnt" (DC working point).

In Fig. 1 and Fig. 2a are given one model and times diagrams for one driver for MOS transistor, controlled by optical cable. In Fig. 2a are given next parameters in different colors: in the yellow is the voltage Vui at the input to the U3 comparator; the 5 V green is Vc at the input to the U1; the red is Vdr at the input to the FET Driver and the 12 V green is the Vg of the gate of the transistor. Two different resistors R1 and R2 are used for charge and discharge of the gate. After comparing Vdr and the Vg can be seen about 3 times greater delay between open and closing processes the MOS transistor, because R1 is repeatedly bigger than R2. In the positive front of the Vg there is a short sharp peak due to the discharge of the parasitic capacity (between the gate and the drain) and it is specific characteristic of the high voltage MOS transistors in impulse mode.

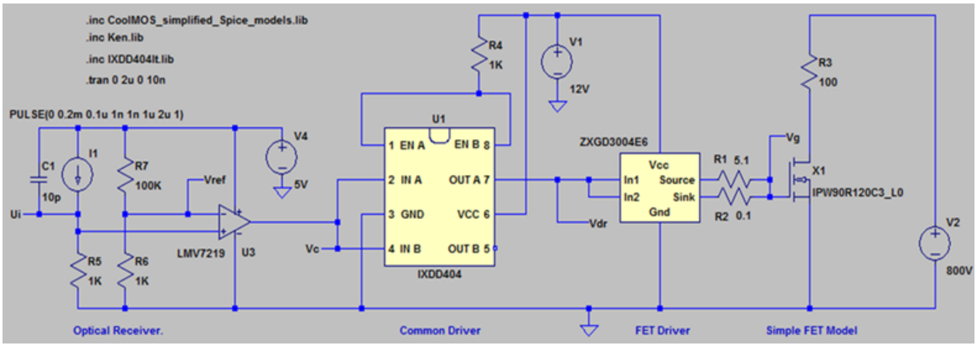


*Fig. 1. Model with "LTspise" for one driver for MOS transistor*

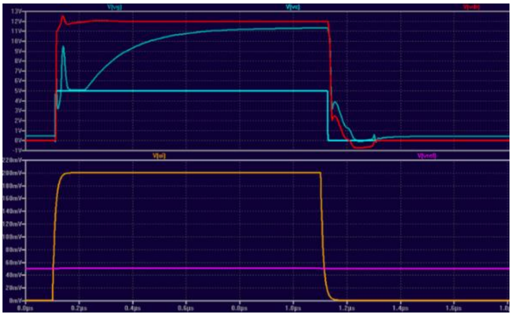

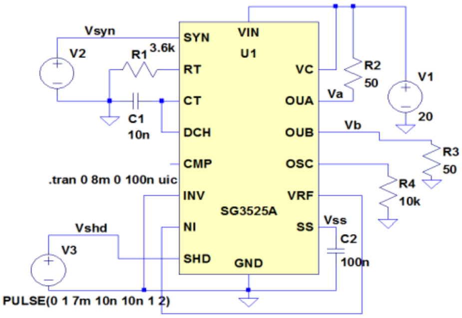


*Fig. 2a. Times diagrams with "LTspise" for one driver for MOS transistor*

*Fig. 2b. Controller with "LTspise"*

In Fig. 2b a full functional model of the controller (SG3525A) for SPs is presented. This model can be used to synthesize and optimize the schemes of management of SPs. With time and value controlled generators $V_1$, $V_2$ and $V_3$ are simulated the power, synchronization and authorization of the controller.

Fig. 3 show a model of the flyback converter with controller UC3842 and two feedbacks: from the output voltage $V_{out}$ and from the current of the key transistor $I_{SNS}$. The following time diagrams are shown in Fig. 4a: with purple color $V_{out}$; with green color the voltage of the feedback VR6; with blue color, the voltage at the output of the controller $V_{mdrv}$; with a red color the current of the key transistor $I_{SNS}$. For the time interval $\Delta t_2 = 0 \div 4$ ms voltage $V_{out}$ is smoothly increased, because with the peak current of the primary winding is limited by comparator S3 to the level $I_{lim} = V_{lim}/R_{sns} = 1$ V/0.25 $\Omega$ = 4 A. This is the way to charge output capacitor $C_{FILT}$ = 2200 µF. In Fig. 4b magnifier software was demonstrated, allowing detailed examination of processes from Fig. 4a: in time $\Delta t_3 = 3 \div 3.2$ ms we observed negative and positive halfwave of over-regulation of negative feedback that causes the voltage exceeding the output voltage $V_{out}$ (above the nominal value 12,00 V) — up to 12.3 V. This process is undesirable and should be removed after optimization the feedback for current and voltage on the SPS.

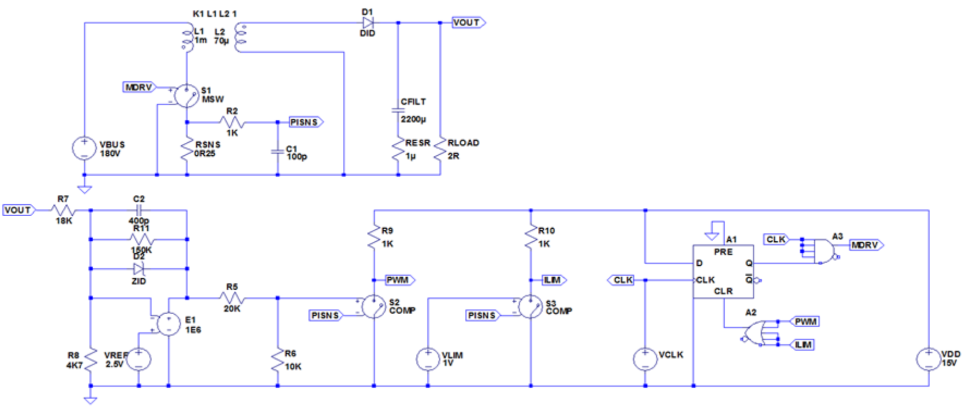


*Fig. 3. Simulation of the converter with feedback and controller UC3842*

Fig. 5 shows the Flyback model built with the UC3842B controller [2]. It can be seen that the feedback does not regulate the output voltage VR9, and follow the rectified voltage U1 off the secondary winding L2. The startup process from Fig. 8 can be analyzed with the presented simulation data. When U1 = 16 V the controller UC3842B turns on and began the discharge of the starting capacitor C6 to 11 V. At the moment t = 62 ms diode D2 is beginning to conduct and charge the capacitor C6 from 11 V to U1 = 12 V, set by the feedback resistors R2, R3 and U1. Generator V1 simulate work levels for voltage DC supply.

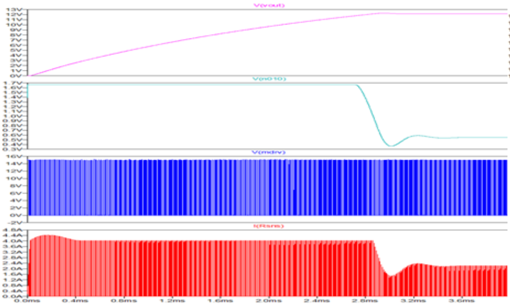

Fig. 4a. Start process at Ts=0÷4 mS

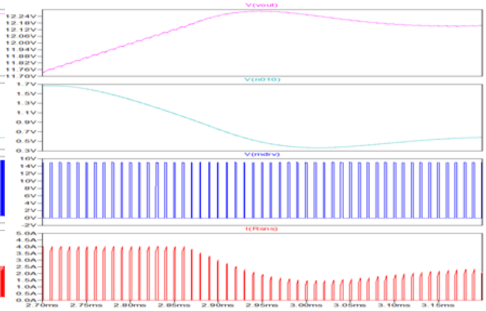

Fig. 4b. Start process at $T_s$=2,7÷3,2 mS

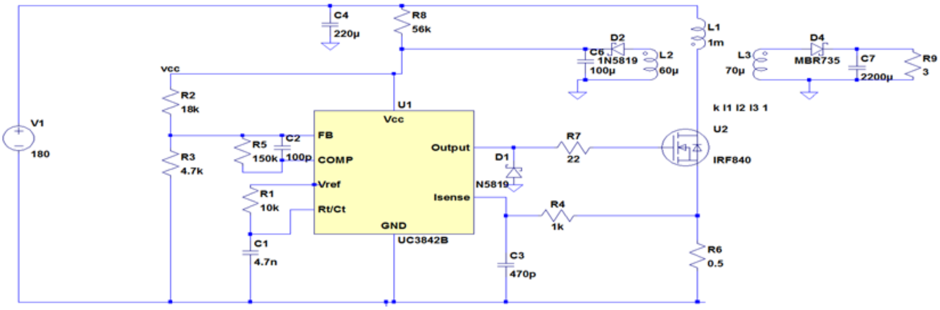


Fig. 5. Flyback model built with the UC3842 controller

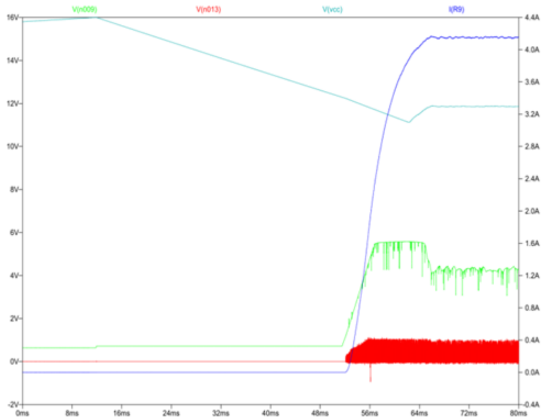


Fig. 6a. Startup process from Fig. 7

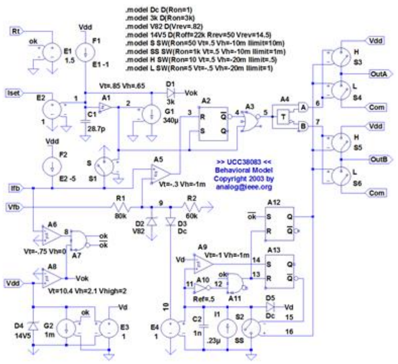

Fig. 6b. Model of the new generation Controller UCC38083

In examining the tension by $V_{comp}$ (in green) from controller U1, Fig. 6a we see five curves: zero level; positive front, horizontal front; the negative zone and horizontal level when feedback is working. In time interval Δt4 = 50÷56 ms Vcomp sets growing smoothly his level which is reflected in the gradual increase of the amplitude of the current of transistor of U2. We see 10 undesirable waves of Vcomp with resonant frequency of 1 KHz in the adjustment zone Δt5 = 66÷80 ms. This undesirable pulsation of the closed system for voltage regulation U1 must be minimize.

In Fig. 6b the structure of the model of the new generation controller UCC38083, simulating its internal structure and all its functions, is shown. This controller is built entirely with MOS technology, has very low consumption in the excluded and active state. It is suitable for use in the synthesis of new management schemes for SPS.

### 3.2. Program Product "Micro-cap"

With this software, the following analyses are possible: transient processes; small signal frequency analysis: amplitude and phase frequency analysis and Bode's diagram; transmission function on constant voltages and currents: transmission function; V-A characteristic and family static transmission characteristics; dynamic analysis of constant voltages and currents; analysis of the sensitivity of the equivalent scheme for constant voltages and currents to change the parameters of the component.

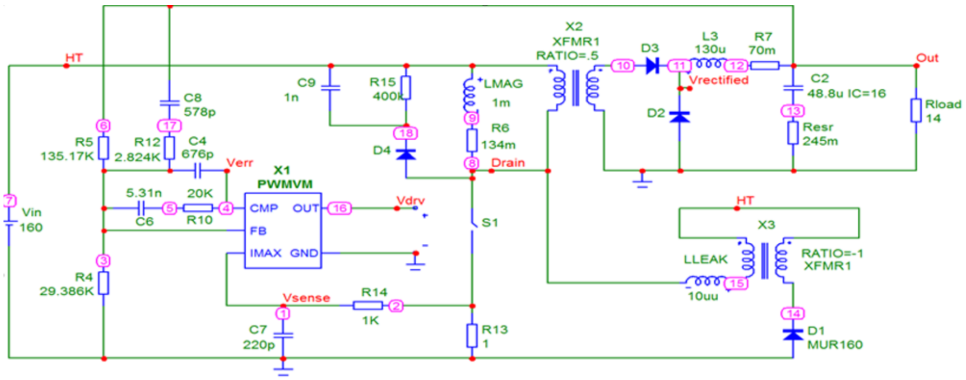


*Fig. 7a. Model of Transformer Forward converter*

Additional types of analyses are: calculations when modifying one or more parameters; calculation of modification of parameters in a specified tolerance for statistical processing; Fourier analysis; calculation of the graphs of various dependencies and examination of the temperature instability of the model.

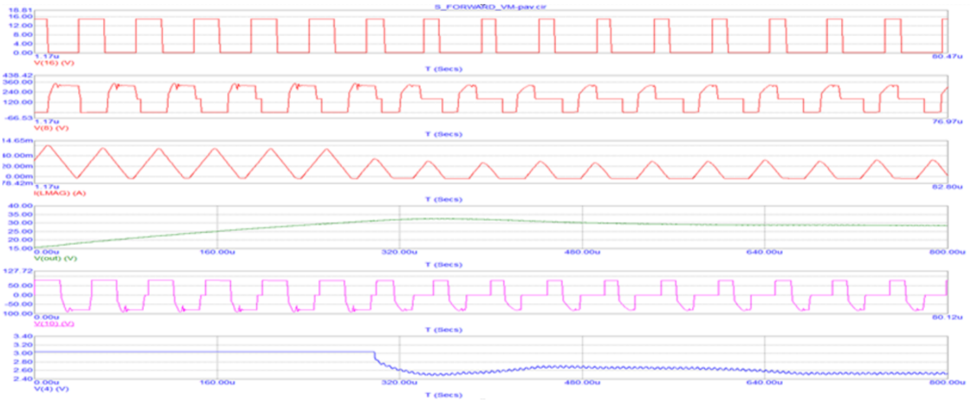

*Fig. 7b. Time diagrams of Transformer forward converter*

In Fig. 7a it is a model of Transformer Forward converter, in which is used a function equivalent of a X1 controller, operating in a voltage mode of regulation. In Fig. 7b are visualized some of the parameters from Fig. 7a: geit voltage V16 and drain voltage V8 of the function equivalent of MOSFET transistor S1; current $I_{Lmag}$; output voltage Vout; secondary voltage V10 and output voltage V4 of the error amplifier CMP. The analysis of the Vout graph shows an overshoot to a peak value of 35 V, with a nominal 24 V, which proves an abnormal mode of operation of the voltage feedback and the need for further optimization of its performance. Other wise there is a danger of damage to the user, powered by this SPs.

### 3.3. Program Product "Multisim".

The library of elements of this program contains more than 2000 "SPICE" pattern. It is possible that through the sub-program "Utiboard" to synthesize and analyze the construction of the PCB, as well as to present in the 2D and 3D appearance of the individual elements.

The resistance of the virtual resistors can have an arbitrary value. Multiple models can be used for a single component. For building blocks, an "SPICE" analysis is usually used. "Multisim" has a rich set of virtual instruments for analyzing the processes [4, 6, 7, 8]. There are two types in the component library, both real and virtual. You can set the time of emulation. In Fig. 8. is a model of SPs for the camera of the multichannel spectrometric system "Spectar-256" [9, 10, 12]. For the visualization of the processes are selected: two virtual oscilloscopes XSC1 (green for source current off Q1transistor and gelb for secondary winding of T1) and XSC2 (blue for gate voltage of Q1 and red for voltage of a soft start of the controller DA1); multimeter XMM2 and wattmeter XWM1. Interactive elements are used: switch S1 (for restart of DA1) and X1 light diode indicator.

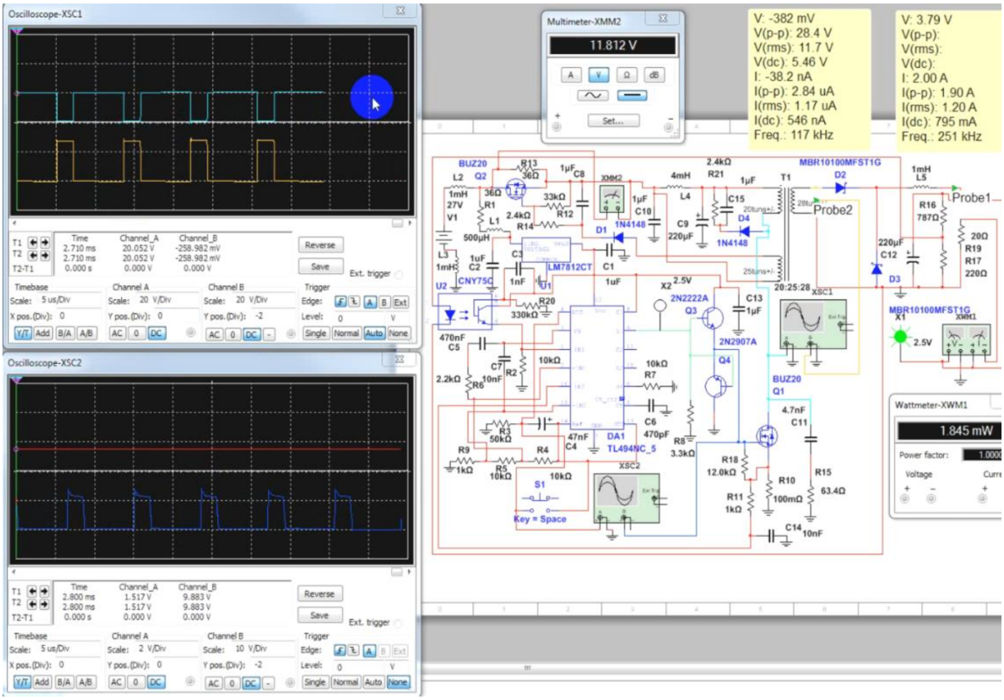

*Fig. 8. Model of SPs for the multichannel Spectrometric system "Spectar-256"*

## Results and Discussions

It was synthesized an author's model, allowing an interactive simulation of the dynamic processes of SPs for the Spectrometric complex "Spectar-256". The dynamic regimes were tested in three more models of SPs. It was simulated: basic diagrams of stabilized pulse converters, dynamic parameters; protections and feedbacks; voltage and current pulsation. Modern methods and tools are used for research and design of SPs for board aero and space Equipment – analysis by simulation of complete functional models of power supply sources and their components. The simulation of SPs and SPS allows to reduce the errors in synthesis and by analysis to shorten the time of development.

## References


1. Avanesov, G. A., B. I. Bonev, F. Kempe, *et al.* Television observations of Phobos. *Nature*, volume 341, Issue 6243, 1989, 585–587, DOI 10.1038/341585a0
2. Braun, M., Naruchnik po tokozahranvashti ustrojstva, Izdatelstvo "Tehnika", SofiJa, ISBN 9540304946, 1998, 240 p. (In Russian).

3. Ishodnye tehnicheskie trebovaniJa k apparature i oborudovaniju – ITT2. Kompleks celevyh nagruzok. ITT KCN RS MKS P 34240–515, Raketno-kosmicheskaJa korporacija “Energija” imeni S.P. Koroleva, sentJabry 2000, 111 p. (In Russian).
4. Charles Schuler, Electronics: Principles and Applications w/Multi Sim CD, Book, McGraw-Hill, Inc. New York, NY, USA, m ISBN-10:0073316512, ISBN-13:9780073316512, 2007, 566 p. https://www.semanticscholar.org/paper/Electronics%3A-Principles-and-Applications-w%2FMulti-CD-Schuler/6b81fac2e4885a5605acfa9a515d5d7e6e97fe8e
5. Zjagina, S. S., M. V. Roshtina. Obespechenie teplovyh rezhimov pechatnogo uzla istochnika vtorichnogo elektropitanija, zhurnal “Trudy mezhdunarodnogo simpoziuma nadezhnosty i kachestvo”, tom 2, 2009, pp. 200–201 (In Russian). https://cyberleninka.ru/article/n/obespechenie-teplovyh-rezhimov-pechatnogo-uzla-istochnika-vtorichnogo-elektropitaniya
6. Mahata, S.; A. Maiti ; C. K. Maiti, Cost-effectiveweb-based electronics laboratory using NI MultiSim, LabVIEW and ELVIS II, 2010 International Conference on Technology for Education, IEEE, 2010, 242–243, DOI: 10.1109/T4E.2010.5550110
7. David Báez-López and Félix E. Guerrero-Castro, Circuit Analysis with Multisim, 2011, Copyright © 2011 by Morgan & Claypool, ISBN: 9781608457564 paperbacks, ISBN: 9781608457571 ebook, Print 1932-3166 Electronic 1932-3174, 198 p. DOI 10.2200/S00386ED1V01Y201109DCS035
8. Gramatikov, P., A. Gramatikova, Izpolzvane na programata MULTISIM za poluchavane na volt-amperna harakteristika na diodi, International Conference “Enganging tools for science Education”, Sofia, 31 oktomvri-1 noemvri 2014 g.
9. Mishev, D. N., Kovachev, S. T., Yanev, T. K., & Krezhova, D. D., The multichannel spectrometric system “Spectrum 256”onboard the manned space station ‘MIR’and afterwards. 10 Years from the Space Project Schipka 1998, 104–110.
10. Borisova, D. Izsledvane na spektralnite otrazhatelni harakteristiki na skali, Doktorska disertacija. Sofia, 2015, 105 p. (In Bulgarian)
11. https://ras.nacid.bg/api/reg/FilesStorage?key=afcbb445-7745-4dd0-be63-8b642b8fa764&mimeType=application/pdf&fileName=PhD_text_3(3)(3)_J111_dop_KK.pdf&dbId=1
12. Getzov, P., Z. Hubenova, Reliability Study of Operators Within a Complex Ergatic System, JOURNAL SCIENTIFIC AND APPLIED RESEARCH, Vol. 5, ISSN 1314-6289, 14; ISSN 1314-6289, EBSCO, 2014, 7–14. http://www.rst-tto.com/docs/journal-scientific-and-applied-research-vol-05.pdf
13. Gramatikov, P. SECONDARY POWER SUPPLY SYSTEM FOR MULTICHANNEL SPECTROMETRIC SYSTEM “SPECTRUM-256”. Proceedings SES2018, Space Research Technology Institute — BAS, 2018, ISSN:2603-3313, 217–220. http://www.space.bas.bg/SES/archive/SES%202018%20DOKLADI/2_Aerospace%20Technologies/16_Gramatikov.pdf

# СИМУЛАЦИЯ И МОДЕЛИ НА БОРДНИ ВТОРИЧНИ ЕЛЕКТРОЗАХРАНВАЩИ ИЗТОЧНИЦИ ЗА АЕРОКОСМИЧЕСКИ ПРИБОРИ

***П. Граматиков***

**Резюме**

В статията се разглежда проектирането и оценката на вторични източници за електрозахранване с помощта на симулационни модели. При набор от схемни експерименти моделите позволяват да се измерят и визуализират различни параметри и спомагат при анализа на резултатите. Моделите са разработени с помощта на “NI MultiSim” (за симулационни експерименти), “Micro-Cap” (за функционални експерименти) и “LTspise” (за контрол на процесите). Симулацията спомага за разбирането на основните концепции, анализа и настройката на схемните процеси и параметри на вторични източници за електрозахранване.

Bulgarian Academy of Sciences. Space Research and Technology Institute.
Aerospace Research in Bulgaria. 34, 2022, Sofia

DOI: https://doi.org/10.3897/arb.v34.e10

# SYSTEMS FOR SECONDARY ELECTRIC POWER SUPPLY OF THE INSTRUMENTS "ZORA" AND "NEUROLAB-B" — SPACE MEDICINE

***Pavlin Gramatikov[1], Rumen Nedkov[1], Raicho Todorov[2]***

*[1]Space Research and Technology Institute — Bulgarian Academy of Science*
*[2]LTD RAIT — AEROSPACE — FPLEASR*
*e-mail: pgramatikov@space.bas.bg*

***Keywords:*** *Secondary power supply system, Space medicine instrumentation, "Mir" Space Station, International Space Station*

***Abstract***

*The "Zora" and "Neurolab-B" instruments solved problems related to the study, control and prediction of astronaut health. The "Zora" instrument is a computer system for collecting and processing data from complex neurophysiological experiments: "Statokinetiks", "Labyrinth", "Potential"; "Leisure Time"; "Questionary", etc. The system for complex research of the psychophysiological state of astronauts "Neurolab-B" is used for scientific experiments with the help of a number of international crews. Engineering solutions are proposed according to the investigated specificity of the powered devices. Both systems have been operating on board the Mir space station — "Neurolab-B" from 1996 to 2000. New space medicine instruments used on the Russian sector of the international space station are considered. Since 2000, four new secondary power systems for space instruments have been developed at the Institute of Space Research and Technology — Bulgarian Academy of Sciences. They are applicable in both space physics and space medicine.*

## 1. Secondary power supply systems of the instrument "Zora"

The requirements of the Mir Space Station (Mir SS) for the secondary power supply system (SPS) of the "Zora" instrument, Fig. 1a, are as follows [1, 2, 3]:

- The service life shall be a minimum of 5 years.
- The average time to failure of the equipment shall be 300 h.
- Full operability at Ta = +5 to +35°C.
- The "Zora" instrument must operate under voltage ripple generated by the on-board network (BN) with parameters according to Tab. 1.
- The level of electromagnetic noise generated by the scientific instrumentation (SI) of the BN shall not exceed the levels shown in Fig. 2a and Fig. 2b.

The "Zora" structure, Fig. 1a, consists of four modules:

• Aluminum housing;
• Laptop “GRiD Compass”, or microprocessor system (MPS1).
• SPS cartridge.
• Digital and analogue circuit boards.

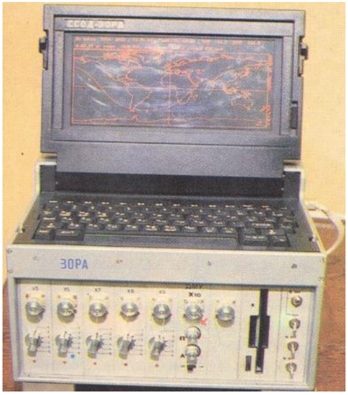

*Fig. 1a. “Zora” instrument https://rait-aerospace.com/photogalery/011.jpg*

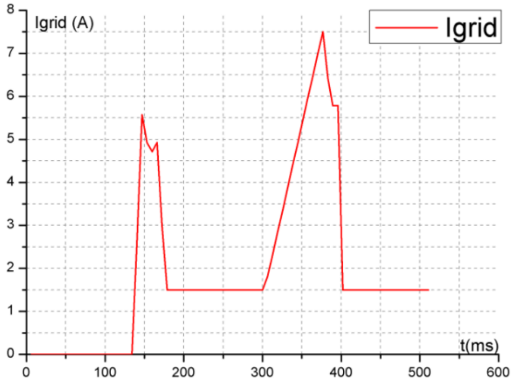


*Fig. 1b. MPS1 start process in circuit +16 Vgrid*

*Table 1. Sinusoidal ripple current and voltage generated by the BN at the Mir SS, [1]*

| Current frequency | Current sensor voltage, RMS |
|---|---|
| 10÷25 [Hz] | 0,25 [V] |
| 25÷60 [Hz] | 0,25÷0,1 [V] |
| 60÷250 [Hz] | 0,1 [V] |
| 250÷1700 [Hz] | 0,1÷0,15 [V] |
| 1700÷6500 [Hz] | 0,15 [V] |
| 6,5÷150 [KHz] | 150÷0,5 [mV] |
| 0,15÷1[MHz] | 500÷100 [µV] |
| 1÷100[MHz] | 100 [µV] |
| Voltage frequency | Voltage [V], RMS |
| 10÷25 [Hz] | 0,8 [V] |
| 25÷60 [Hz] | 0,8÷0,3 [V] |
| 60÷250 [Hz] | 0,3 [V] |
| 250÷1700 [Hz] | 0,3 [V]÷1 [V] |
| 1700÷2000 [Hz] | 1 [V] |
| 20÷150 [KHz] | 1÷0,15 [V] |
| 0,15 ÷ 1 [MHz] | 0,15÷0,003 [V] |

Structurally, the instrument SPS, Fig. 3a, consists of five circuit boards: the PSA; PSW; PSD and PSC and an automatic start-up circuit (ASS). Two identical

PSA and PSW sources (each 24 W) power the most important consumer (MPS1) and have the following characteristics:

- Using the “hot” and “cold” reserve mode of the MPS1.
- Two-stage auto start and dynamic current limiting.
- Automatic shutdown when the voltage of the BN is exceeded or reduced;
- Suppression of current ripple and inrush current of MPS1 in BN.

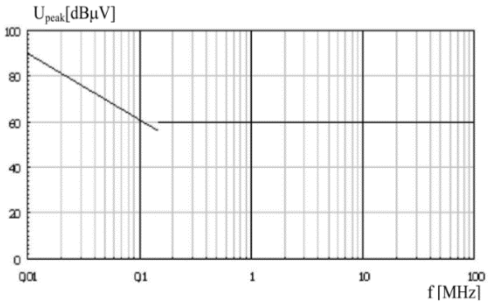


*Fig. 2a. Radio frequency levels noises created by SI in BN of the Mir SS [1]*

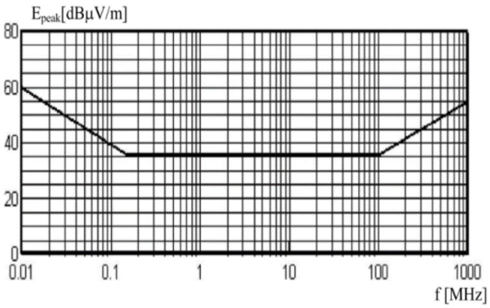


*Fig. 2b. Electric field strength of radio noises, created by the SI in the Mir SS [1]*

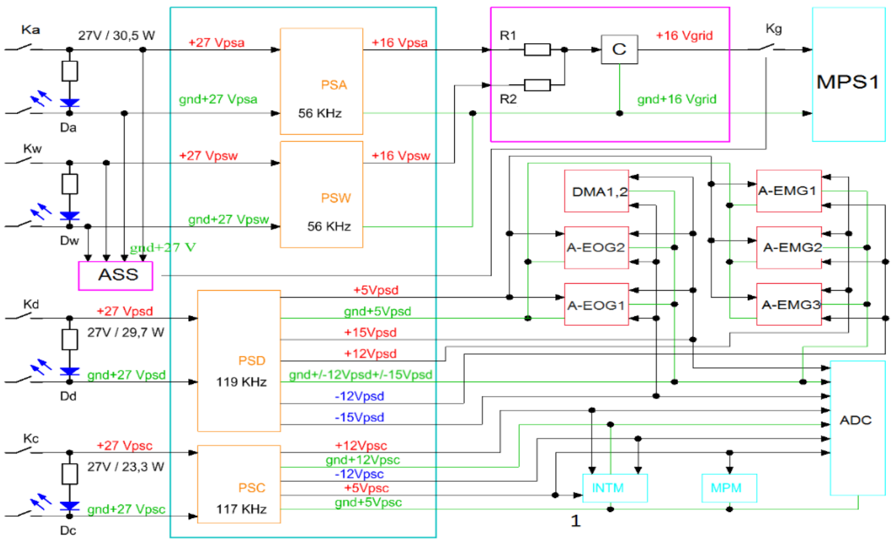


*Fig. 3a. Functional diagram of the SPS of the instrument “Zora”*

When the Ka switch is turned on, the Da indicator for PSA lights up. For a time of 0,5 s to 1 s, the safety circuit automatically turns off the PSA if: the +16 Vpsa voltage is higher than a set upper level, lower than a set lower level, or a short circuit has occurred in its outputs. A circuit solution has been chosen to sum the voltages +16 Vpsa and +16 Vpsw to a single voltage +16 Vgnd across the R-C filter board. A voltage of +16 Vgrid across contact Kg of the polarized relay from ASS is supplied to power MPS1. When both switches (Ka and Kw) are on, PSA and PSW operate in “hot” reserve mode. For some of the planned experiments, operation of PSA, PSW and MPS1 alone is sufficient. As needed in different experiments, the Kc and Kd switches power the PSC module most often and the PSD module less often. In this way, the resources of the power supply and the “Zora” elements are saved. The results for the starting current of MPS1 at Vgrid = 16 V are shown in Fig. 1b. According to these measurements, unacceptable currents will be obtained in the BN, so an R-C circuit (R1, R2 and C) has been added.

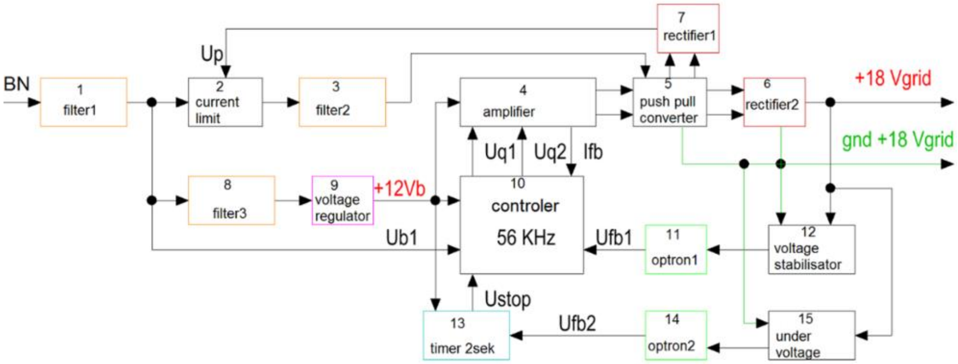


*Fig. 3b. Functional diagram of PSA and PSW of the instrument “Zora”*

Conventionally, at time zero a command is given to turn on Kg, but the relay closes at time T = 130 ms when the charging process of part of the capacitors in MPS1 starts and the pulse converter for the digital part built into MPS1 is started. At the moment T = 300 ms, the second start-up process in MPS1 (high voltage converter for the display) starts and continues until T = 400 ms. Once the voltage is applied to BN 4, 9, 10 and 13 are powered, see Fig. 3b. The voltage at Ub1 is used for negative feedback of the board voltage and for undervoltage estimation of BN. When Ub1 exceeds 14 V, operation of 10 is enabled and the PSA start-up process is enabled. When the +18 Vgrid output voltage exceeds the value of 13 V during normal startup within 2 *s*, 10 and 14 generate the Uvb2 signal, which stops the operation of 13 and disables the Ustop signal, at which the PSA operates normally. In an emergency, when the +18 Vgrid voltage drops below 13 V for a time greater than 100 ms, Uvb2 drops out and the Ustop signal disables the PSA from operating continuously. This condition is maintained until the Ka switch is opened. To reduce the EMC emissions radiated by the PSA and PSW, the two collectors of the power key transistors and their common heatsink are galvanically connected to the BN plus bus.

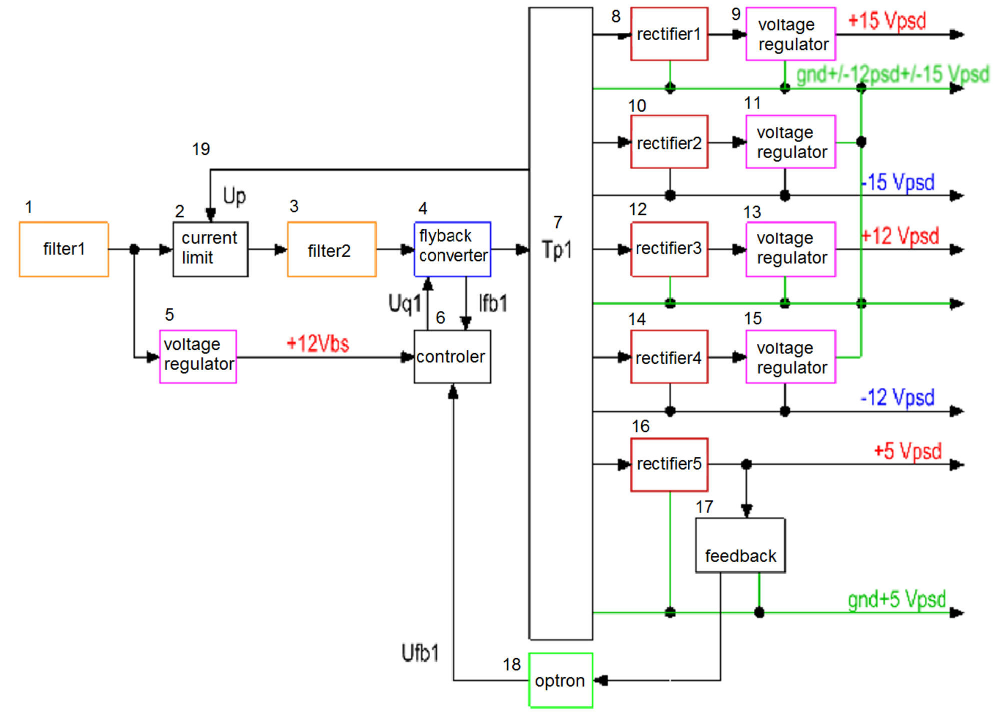


*Fig. 4a. Functional diagram of the secondary power supply PSD of the instrument "Zora"*

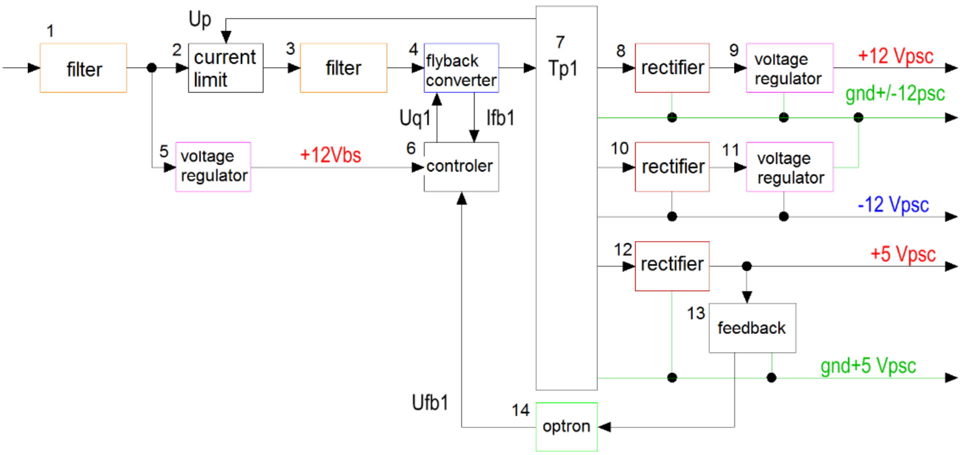


*Fig. 4b. Functional diagram of the PSC of the instrument "Zora"*

Fig. 4a shows the functional diagram of the PSD. The PSD is designed to power the digital telemetry, MPS2 and ADC (INTM, MPM and ADC respectively).

The functional diagram of the PSC is shown in Fig. 4b. The PSC is designed to power analog ICs in the boards for: electromyography; electrooculography; dynamometry (EMG, EOG and DMA) and ADC. The same principle and mounting scheme are used for the PSC and PSD, but the PSC does not mount the +/-15 Vpsd elements. From "Zora" were made 5 pieces: trainer, LK-1, LK-2, LK-3 and LK-4, one of the flying specimens was used for a long time on board of the Mir SS [4, 5, 8].

## 2. Secondary power supply systems of instrument "Neurolab-B"

Fig. 6 shows the functional diagram of "Neurolab-B" instrument, where the average power dissipated by individual users is given. The Neurolab-B (fig. 5a and 5b) system consists of three main power consumers:

- Digital part (2, 3, 4, 5, 6, 7, 8), fed by SPS-D: (1, 9).
- Analogue part (11, 12, 13, 14, 16, 17, 18, 19, 20) fed by SPS-A: (10, 15). The main consumption for 10 is from the operational amplifiers (11 and 12).
- Laptop 22 powered by SPS-20: (21).

*Fig. 5a. Neurolab-B instrument https://rait-aerospace.com/photogalery/_016.jpg*

*Fig. 5b. SPS for the Neurolab-B instrument https://rait-aerospace.com/photogalery/_018.jpg*

Prior to the 21 design, the following power supply parameters were measured (under different 22 modes at +20 V):

- 11,4 W with display off.
- 17 W when the display is on. The current ripple is 280 Hz and has an amplitude of +/-18 % with respect to the average value of 0,85 A;
- 19 W with display and hard drive included. Current ripple amplitude is +/-18.4% of the mean value of 0.95 A at 280 Hz.

Under these conditions, the performance of the SPS-20V was measured at four BN voltage values: 22 V, 24 V, 27 V, and 34 V. For these voltages the following efficiency values were measured for the SPS-20V: 73 %, 73.5 %, 74.5 % and 76 %.

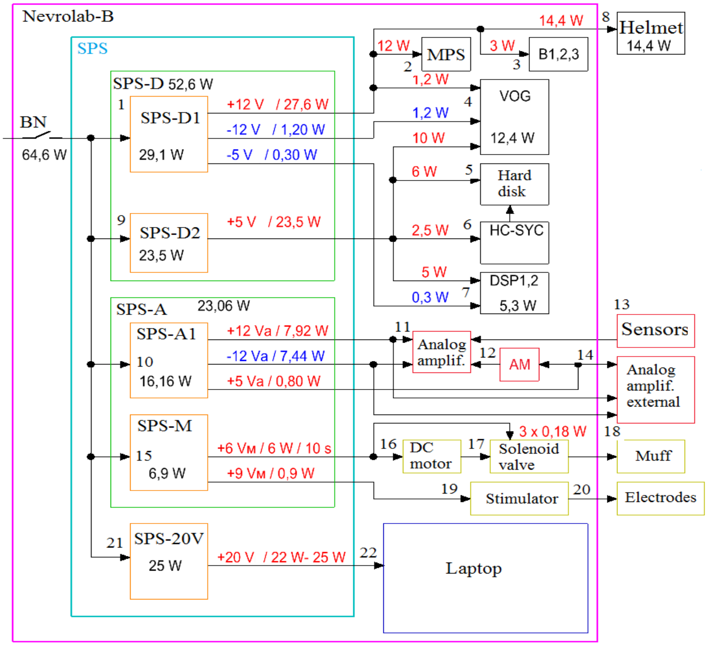


*Fig. 6. Functional diagram of the SPS of the instrument "Neurolab-B"*

The SPS-M provides +6 Vm to power the DC motor of the blood pressure pump and +9 Vm to power the stimulator for high-voltage pulses that are applied to the human body via electrodes. This motor runs for a maximum of 10 s and makes a minimum pause of 60 s. The air pressure created by it is passed by three electromagnetic pneumatic valves (17) to the cuff (18) of the astronaut's arm.

The rotor resistance is 5.5 Ω, the power at start-up is 6,54 W, and at idle it consumes 1,38 W. The average power while maintaining the maximum cuff pressure is 2,4 W. Then the motor current ripple measured in the supply lines has a frequency of 480 Hz and its power varies 1,5÷2,58 W. An L-C filter is used to minimize the current ripple. It has a frequency of 94 Hz, with capacitor and inductance values of 2,2 mF and 1,3 mH. In the off state, the SPS-M consumes only 0,648 W of BN. For one of the "Stimulation" modes in transceiver tests, three consumptions were measured (for three BN voltage values: 23 V; 27 V and 34 V, respectively on the "Neurolab-B"- LK-1: 72,45 W; 68,85 W and 68,02 W. The Neurolab-B-LK-2 protocol (for three BN voltage values: 23 V; 27 V and 34 V, respectively) records three power consumptions: 62,1 W, 62,1 W and 64,6 W. These data show a weak dependence of the SPS efficiency when changingthe BN voltage 23÷34 V. Five units have been fabricated from "Neurolab-B": laboratory sample and four flight samples — LK-1, LK-2, LK-3, LK-4 [6, 7, 9].

“NEUROLAB-B” was built by the Bulgarian Space Agency BASA, together with the German DOS-software NEURON (SpaceBit GmbH. Balin), provided by the German Space Agency DARA. This system was successfully operated for 4 years on board the Mir SS (1996–2000). The equipment was designed (Nedkov, 1993) to record the electroencephalogram (EEG) in the central scalp line (Fz. Cz. Pz). val and horizontal electrooculogram (EOG), skin conductance (SCL/SCR) (tonic and phase), peripheral digital skin temperature, electromyogram (EMG. forearm rigid, muscle extensor digitorum), pulse transit time (PTT) to the finger of the right hand (plethysmography), electrocardiogram (ECG), blood pressure (hand cuff, oscillography), respiration (thoracic impedance method) and voice parameters” [10].

## 3. Space medicine equipment on board the Russian sector of the International Space Station

Space medicine is a field of biomedical research and technology that studies human interaction with the factors of space (weightlessness, cosmic radiation, artificial environment in a hermetically sealed spacecraft). It is an important element of the practice of manned spaceflight and defines the state of the art and the prospects of human space exploration. The main areas of research in space medicine are [12]:

• Space physiology [14];
• Medical provision;
• Radiation Safety.

Prospective research is the development and creation of:

• Means for medical observation of astronauts;
• System for on-board monitoring, diagnosis, prevention and correction of the mental state of astronauts;
• System for selection and training of astronauts for interplanetary expeditions;
• On-board simulator to support operator activity.

### 3.1. “NEUROLAB-2000M” complex

In 1998, an experimental sample of the psycho-diagnostic complex-simulator “NEVROLAB-2000M” was developed by scientists of IMBP and RKK “Energia” and delivered on board of Mir SS and then to the International Space Station (ISS), Fig. 7a [12]. It has been used since 1998 to conduct 29 studies involving 6 astronauts on the Mir SS and ISS [12]. With this simulator crew members simulate docking and redocking of the Soyuz transport ship and the ISS.

Experimental data showed that the use of the simulator was effective in regaining lost professional docking skills in spaceflight. Test “Manometers” [11], was implemented on the basis of the instrumentation complex “Neurolab-2000M”. It aimed at establishing correlation relations of indicators characterizing the quality (speed and accuracy) of the astronaut's operator activity. It is intended for the study of the processes of information perception and decision-making in conditions of strict time limit [12]. The 2011 space experiment (SE) "Pilot" aimed to investigate individual psychophysiological state regulation and occupational performance reliability of astronauts in long-duration spaceflight [12].

The first SE "Virtual" [12] started in 2013 during the flight of the crew of ISS-37/38 of Ryazansky S. N. and Kotov O. V. on board the Russian sector of the ISS (RS ISS) on (Fig. 7a). The state of the vestibular function of the astronauts after 2 days on board the ISS was observed. The second stage of "Virtual" was launched in 2015 and aimed at the following:

• Studying the effect of weightlessness on visual tracking accuracy and speed performance

• Investigating the impact of visually induced illusions (veccia) in weightlessness on visual tracking accuracy and speed performance;

• Study of visual tracking characteristics in relation to vestibular function status during weightlessness.

The third stage of SE "Virtual" consisted of performing a set of computer tests to study oculomotor responses to visual stimuli — a dot target up to 1° in size (a feedforward stimulus) moving according to a given law both on the non-oriented field of the screen (virtual reality goggles) and against the background of additional retinal optokinetic stimulation — blurred spots (ellipses) displayed on the background of the screen. An RSE Med laptop is used to record eye movement using electro-oculography and virtual reality goggles for visual and auditory stimulation. The start of the SE "Tracking" is planned for 2015–2016.

*Fig. 7a. "Virtual" Space Experiment, "NEVROLAB-2000M" complex, 2013 http://vestibularlab.ru/wp-content/uploads/2013/09/History-10-2.jpg*

*Fig. 7b. "Pilot-T" experiment, "NEIROLAB-2010" complex https://www.energia.ru/ru/iss/researches/images/human24_1.jpg*

### 3.2. "NEUROLAB-2010" complex

Since 2014, the first stage of the SE "Pilot-T" has been underway on the ISS RS. The model of the operator's professional activity is the Six-degrees-of-freedom (6df) program, which simulates manual control of objects with six degrees of freedom and which contains secondary cognitive tests. The qualitative parameters of the occupational activity are compared with the physiological parameters obtained using the hardware complex "Neurolab-2010". An electrocardiogram; pulse wave, electrical resistance and skin temperature of the little finger (left) and a speech signal were recorded using "Neurolab-2010". Currently 16 astronauts have completed the full cycle of the experiment [15].

The study is being conducted from 2015 to 2018, with the crews of Expeditions 43/44-53/54 (13 astronauts) participating in the study. During the flight: 43/44-50/51 ISS-Pilot-T CE is conducted twice a month, and for 51/52-53/54 ISS expeditions - once a month [15].

The SE "Pilot-T" experimental study (Fig. 7b) on board the space stations is designed to assess the expected reliability of cosmonauts during manual docking of the Soyuz or Progress spacecraft (Mir SS and ISS, respectively), [13]. For the SE "Pilot", the following equipment is used: the "Neurolab-2010" complex in the first and second stages; "Neurolab 2010+" in the second stage; a laptop in the second stage; control handles "6df" and "Virtual H"; software "6df" and "Virtual H".

### 3.3. "Sensomotor" set

In SE "Tracking", visual and manual tracking of astronauts in weightlessness is performed. Eye tracking, sensory interactions, stability of adaptive changes during short- and long-term spaceflight are investigated [13]. The kit consists of: a "Sensomotor" device with dimensions: 170x150x70 mm and weight 1 kg; a "Sensomotor" tablet with dimensions: 640x470x50 mm and weight 3 kg; a joystick with dimensions: 250x200x200 mm and weight 1.5 kg; a sensorimotor cart with dimensions: 300x250x190 and weight 0.3 kg; a "Sensomotor Data" device with dimensions: 70x30x10 and mass 0.1 kg [16].

### 3.4. "Pneumocard" complex

It has been used to investigate the influence of long-duration spaceflight factors on the autonomic regulation of blood flow, respiration and contractile function of the heart [12]. During the expeditions from ISS-14 to ISS-28, 94 experimental sessions were conducted and 19 Russian cosmonauts were studied. In 2012, 43 experimental sessions are planned to be conducted during the main expeditions ISS-30, ISS-31/32 and ISS-33/34. The planned completion date for the flight realization of the Pneumocard space experiments 2013. The kit consists of:

the Pneumocard kit 220x220x50 mm, 1.20 kg; consumables (electrodes and wipes) 0.15 kg; data card; ThinkPad A31p RSE-Med medical support laptop [16]:

### 3.5. “Pulse” Set

It is a computer system for monitoring the state of the cardiovascular system in weightlessness and is used for the Pulse KE for new scientific data on the mechanisms of adaptation to prolonged weightlessness, 2007 [16]. The Typology KE investigates the topological characteristics of the operator and the topological features of the operator activity of ISS crews during long-duration spaceflight [13].

The composition of the “Pulse” kit is [16]:

•Electrocardiogram (ECG), pneumotachogram (PTH) and sphygmogram (SFG) recording kit including: pulse device; ECG reading device (DUT); USI PTH; USI SFG; data cable and belt.

•On-board computer and special software.

•Sphygmomanometer TENZO PLUS (standard equipment on ISS RS).

•A “PULS” package designed to provide the experiment with consumables (electrodes, wipes, batteries, magnetic carriers).

Characteristics of instrumentation and equipment used. The “PULS” device has an autonomous power supply sufficient for 4 experiments. The device works with the on-board computer, transmitting information to it via a standard RS-232 port.

### Conclusion

A high lifetime SPS was synthesized for the “Zora” system consisting of: a laptop, a microprocessor system, and medical amplifiers for complex neurophysiological testing. The applied transistor connection scheme reduces the EMC level. Appropriate structuring of the SPS ensures low noise in the analog medical data. For “Neurolab-B” system, parameters and timing diagrams were tested in different modes for the different consumers of the system: laptop; physiological signal amplifier boards; air compressor motor and hard disk. As a result, an SPS tailored to the specific parameters of the “Neurolab-B” was built. By the usage of the fans, the weight of radiators has been reduced and the SPS resource has been increased. After an electromagnetic compatibility analysis in the on-board network, an electromagnetic compatibility filter was designed and added to the SPS. The operation of the SPS in four units of “Neurolab-B” system for more than 4 years has proven stable operation in four locations: on-board the Mir SS and in the cities of Moscow, Berlin and Sofia. After the completion of the experiments with the “Neurolab-B” system, 4 new space SPS have been developed and constructively built on a modular principle at SRTI-BAS, [17–20]. They are applicable to both space physics and space medicine. These new SPS are without fans and heat sinks, which significantly reduces their weight and volume.

## References


1. Osnovnye tehnicheskie harakteristiki avtomaticheskoj universalynoj orbitalynoj stancii AUOS i tehnicheske trebovaniJa dlJa ustanavlivaemoj na nej nauchnoj apparature, AN SSSR, INTERKOSMOS, 1982 g. (in Russian)
2. Dunaev, A. I. Apparatura nauchnaJa, Obshtie tehnicheskie trebovaniJa, OTT-87, Glavkosmos, -M.,1987, 92 str. (in Russian)
3. “Tehnicheskoe zadanie SSOD – “Zora”, KM01.001.00.00 TZ., IKI-BAN, S., 1987. (in Russian)
4. Nedkov, R., S. Tanev, S. Simeonov, P. Trendafilov, A. Spasov, P. Gramatikov, V. Shalamanov. Sistema sbora i obrabotki na danni “Zora”, V KM01.001.03.00, IKI – BAN, Sofia, 1988. (in Russian)
5. Nedkov, R., S. Tanev, S. Simeonov, P. Trendafilov, A. Spasov, P. Gramatikov, R. Todorov, V. Jankov, M. Ivanov, I. Ivanova, V. Shalamanov. Tehnicheskoe i tehnologicheskoe obespechenie mediko-biologicheskoj programmy proekta “Shipka”, Okonchatelynyj otchet BAN, 4, SofiJa, 1990 g. (in Russian)
6. Nedkov, R. Sistema za intelektualna cifrova obrobotka na biomedicinski signali v kosmicheski usloviJa, “Aerokosmicheski izsledvaniJa v B”lgariJa”, SofiJa, IKI-BAN, nomer 10, 1993 g., 65–70. (in Bulgarian)
7. Protokol #01 Kvalifikacionni ispypanij (Etap 2), GNC RF-IMBP, Proekt “Nejrolab”, sistema “Nejrolab-B”, KM 01.055.00.00 zav. #01, Ocenivaemye pokazateli: ElektromagnitnaJa sovmestimosty, 10.11.1995 g. (in Russian)
8. Grigorova, V., A. Manev, L. N. Kornilova. Rezultati ot bylgaro-ruskija kosmicheski eksperiment “Labirint”. Prilozhenija v klinichnata praktika. V: 10 godini kosmicheski proekt “Shipka”, Sofia, Institut za kosmicheski izsledvaniJa, 1999, 128–131.
9. Getsov, P., P. Panova. New possibilities for space research in Bulgaria. *Conference Proceedings, IV Serbian-Bulgarian Astronomical Conference*, Invited lecture, Belgrade, 21–24 April 2004, Publ. Astron. Soc. “Rudjer Boˇskovi´c” No 5, 2005, 59–66. https://adsabs.harvard.edu/pdf/2005PASRB...5...59G
10. Bernd, J., V. Salnitski, P. Wittels. Two Psychophysiological Scales for the Description of “Psychophysiological Load”. *Conference Proceedings, 55th International Astronautical Congress of the International Astronautical Federation, the International Academy of Astronautics, and the International Institute of Space Law*, Published Online: 29 Nov 2012, IAC-04-IAF-G. 5. B. 09. https://doi.org/10.2514/6.IAC-04-G.5.B.09 https://arc.aiaa.org/doi/abs/10.2514/6.IAC-04-G.5.B.09
11. Kuznecova, E. P., S. I. Stepanova. ISSLEDOVANIE KACHESTVA OPERATORSKOJ DEJATELYNOSTI S ISPOLYZOVANIEM TESTA “MANOMETRY”, REALIZUEMOGO NA BAZE APPARATURNOGO KOMPLEKSA “NEJROLAB-2000M”, Institut mediko-biologicheskih problem RAN, ISSN: 0233-528X, AviakosmicheskaJa i ekologicheskaja medicina, Tom: 43 Nomer: 5, (2009): 63–65 str. (in Russian) https://elibrary.ru/item.asp?id=20742622
12. DolgosrochnaJa programma nauchno-prikladnyh issledovanij i eksperimentov, planiruemyh na rossijskom segmente MKS, KNTS Roskosmos, 09 oktJabrJa 2011 g. # 03 (p.3). 84 str. (in Russian) https://www.gastroscan.ru/literature/pdf/dp.pdf

13. Bernd, J, S. V. Bronnikov, J. A. Bubeev, et al. Operator's Reliability During Spacecraft Docking Training on Board Mir and ISS. *Aerospace Medicine and Human Performance*, 92(7), 2021, 541–549.
DOI: https://doi.org/10.3357/AMHP.5745.2021
14. Landon, L. B., K. J. Slack, E. Salas. *Psychology and Human Performance in Space Programs: Extreme Application.* 1st Edition, eBook Published 9 October 2020, Pub. Location Boca Raton, Imprint CRC Press, Pages 338, eBook ISBN 9780429440854, p. 294.
https://books.google.bg/books?hl=bg&lr=&id=A5v6DwAAQBAJ&oi=fnd&pg=PA284&dq=NeuroLab-2010&ots=4gSfheMl4_&sig=F-lkEy3jcINYQ3lkUJ4rj1BmQn0&redir_esc=y#v=onepage&q294=NeuroLab-2010&f=false
15. Bubeev, Ju. A., T. I. KotrovskaJa, D. V. Schastlivceva. Kosmicheskij eksperiment "Pilot-T" dlJa ocenki nadezhnosti raboty kosmonavta. GNC RF-IMBP RAN. (in Russian)
http://inno.imbp.info/library/%D0%9A%D0%BE%D1%81%D0%BC%D0%B8%D1%87%D0%B5%D1%81%D0%BA%D0%B8%D0%B9%20%D1%8D%D0%BA%D1%81%D0%BF%D0%B5%D1%80%D0%B8%D0%BC%D0%B5%D0%BD%D1%82%20%D0%9F%D0%B8%D0%BB%D0%BE%D1%82-%D0%A2.pdf
16. Roskosmos, Centralynyj nauchno-issledovatelyskij institut mashinostroenija, Nauchnye eksperimenty na bortu RS MKS, Koordinacionnyj nauchno-tehnicheskij sovet, eksperimenty. (in Russian)
https://tsniimash.ru/science/scientific-experiments-onboard-the-is-rs/cnts/#1
17. Gramatikov, P., V. Guineva. SECONDARY POWER SUPPLY SYSTEM OF SPACE EQUIPMENT "ASLAV". *Proceedings SES2017*, Space Research Technology Institute — Bulgarian Academy of Sciences, 2017, ISSN:1313-3888, 144–148.
http://www.space.bas.bg/SES/archive/SES%202017_DOKLADI/2_Aerospace%20Technologies/6_Gramatikov.pdf
18. Gramatikov, P., SECONDARY POWER SUPPLY SYSTEM OF SPACE EQUIPMENT "AMEF-WB". Proceedings SES2017, Space Research Technology Institute - Bulgarian Academy of Sciences, 2017, ISBN:1313-3888, 149–152.
http://www.space.bas.bg/SES/archive/SES%202017_DOKLADI/2_Aerospace%20Technologies/7_Gramatikov.pdf
19. Gramatikov, P., R. Nedkov, G. Stanev. Secondary power supply system for spacecraft potential monitor DP-1 and DP-2, "OBSTANOVKA" Project, International Space Station. *Aerospace Research in Bulgaria*, 31, 2019, ISSN:1313-0927, 108–116.
DOI: https://doi.org/10.3897/arb.v31.e09
http://journal.space.bas.bg/arhiv/n%2031/Articles/9_Gramatikov.pdf
20. Kirov, B. Report on FA8655-08-1-3006 Langmuir probes for "OBSTANOVKA" Experiment aboard the Russian Segment of the International Space Station, August 04, 2010, 1–8.
https://apps.dtic.mil/sti/pdfs/ADA525750.pdf

# СИСТЕМИ ЗА ВТОРИЧНО ЕЛЕТРОЗАХРАНВАНЕ НА УРЕДИТЕ “ЗОРА” И “НЕВРОЛАБ-Б” – КОСМИЧЕСКА МЕДИЦИНА

*П. Граматиков, Р. Недков, Р. Тодоров*

**Резюме**

Приборите “Зора” и “Невролаб-Б” решават проблеми, свързани с изучаването, контрола и прогнозирането на здравето на астронавтите. Приборът “Зора” е компютърна система за събиране и обработка на данни от сложни неврофизиологични експерименти: “Статокинетика”, “Лабиринт”, “Потенциал”, “Свободно време”, “Въпросителна” и др. Системата за комплексно изследване на психофизиологичното състояние на космонавтите “Neurolab-B” се използва за научни експерименти с помощта на редица международни екипажи. Предложени са инженерни решения в съответствие с изследваната специфика на захранваните устройства. И двете системи са работили на борда на космическата станция “Мир” - “Невролаб-Б” от 1996 до 2000 г. Разгледани са нови инструменти за космическа медицина, използвани в руския сектор на международната космическа станция. След 2000 г. в Института за космически изследвания и технологии – Българска академия на науките, са разработени четири нови системи за вторично захранване на космически прибори. Те са приложими както в космическата физика, така и в космическата медицина.

Bulgarian Academy of Sciences. Space Research and Technology Institute.
Aerospace Research in Bulgaria. 34, 2022, Sofia

DOI: https://doi.org/10.3897/arb.v34.e11

# IDENTIFYING BATCH PROBLEMS IN AIRCRAFT FIELD RELIABILITY ANALYSIS

***Kolyo Kolev, Angel Tanev***

*Aviation Faculty, Air Force Academy, Dolna Mitropoliya*
*e-mail: ang_tanev@abv.bg*

***Keywords:*** *Aircraft, Aviation safety, Batch problems, Reliability*

***Abstract***

*In practice, a very important task is to monitor the field reliability of aircraft systems, especially the ones related to aviation safety, and to take relevant actions to prevent from potential consequences. Zooming in that task, one can state that a very important step in that analysis is to identify batch problems where the failure mode only affects a subset of the fleet. The Weibull distribution typically provides the best fit of life data obtained either from test or from field. This is due in part to the broad range of distribution shapes that are included in the Weibull family. As well as, there are many other distributions which are included in the Weibull distribution's family either exactly or approximately- for example, the normal, the exponential, the Rayleigh, and sometimes the Poisson and the Binomial. This paper presents a practical approach for those aviation professionals dealing with monitoring and analyzing the aircraft field reliability.*

## Introduction

Weibull distribution has been invented by Waloddi Weibull in 1937. His statement was that this distribution can be applied to a large variety of engineering problems. And, on other hand, his first experience showed that it had not always worked. In fact, history has shown that Waloddi Weibull was correct in both of these statements [10]. The author found a very important advantage that the Weibull method works with extremely small samples, even two or three failures for engineering analysis (in engineering practice such situation often happens). This characteristic is important and very useful in different domains including aerospace safety problems and in development testing with small samples (one should note that, for statistical relevance, larger samples are needed). In aircraft operation, the presence of defects and occurrence of failures may have a potential impact on flight safety. Today, with the increasing number of flight objects (e.g. unmanned aerial vehicles), the problem with the operational reliability becomes even more complex [12–14], especially for batch issues identification and detection [16–18].

**Theoretical Background**

From the reliability engineering theory [1, 2], it is well-known that a product/component failure rate often exhibits 3 periods in the usage/field (Fig. 1).

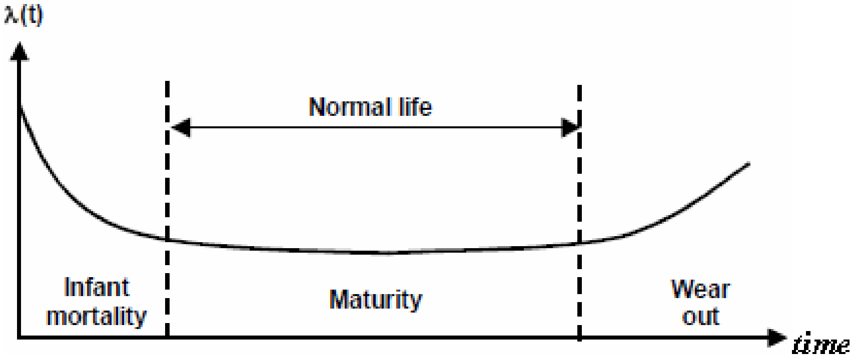


*Fig. 1. Failure rate over product/component lifetime*

One of the most flexible distributions which may adequately describe the bathtub curve (Fig. 1) is the Weibull distribution. Let's review some of the most basic characteristics of the Weibull distribution. Suppose the random variable *X* has Weibull distribution with scale parameter and shape parameter. The Weibull probability density function is defined by the following expression [5–9]:

(1) $$f(t) = \frac{\beta t^{\beta-1}}{\alpha^{\beta}} exp\left(-\left(\frac{t}{\alpha}\right)^{\beta}\right), t \geq 0,\ \ \alpha, \beta > 0$$

where: the two defining parameters of the Weibull line are:

- The slope, β (beta: shape parameter), and the characteristic life, alpha (scale parameter, where 63.2% of cumulative failures will occur up to this point).

The slope of the line, β, is particularly significant and may provide an idea about the physics of the failure [3, 4]. From bathtub's point of view, the failure classes present can be split to the following 3 regions (see Fig. 1):

- $\beta < 1$ indicates "infant mortality" (e.g. process issues)
- $\beta = 1$ indicates "random failures" (independent of age; e.g. overstress failures)
- $\beta > 1$ indicates "wear out" failures (e.g. capacitance/resistance drift).

The characteristic life, alpha, is the typical time-to-failure in Weibull analysis.

Therefore, the failure behavior of a risk system is described by several equally suitable functions: the cumulative distribution function $F(t) = P(T \leq t)$, the Survival function $R(t) = 1 - F(t)$ or failure rate function $\lambda(t)$ [1, 6, 15]. The rate at which failures occur in the interval $t_1$ to $t_2$, the failure rate $\lambda(t)$, is defined as the ratio of probability that failure occurs in the interval, given that it has not occurred prior to $t_1$, the start of the interval, divided by the interval length [7]. Therefore, it is expressed by:

(2) $$\lambda(t) = \frac{R(t_1) - R(t_2)}{(t_1 - t_2)R(t_1)}$$

The Weibull model used for the failure rate modelling is as follows [8]:

(3) $$\lambda(t) = \frac{\beta t^{\beta - 1}}{\alpha^{\beta}}$$

The Weibull distribution usually provides the best fit of life data. This is due in part to the broad range of distribution shapes that are included in the Weibull family [10]. Many other distributions are included in the Weibull family either exactly or approximately, including:

- the normal,
- the exponential,
- the Rayleigh,
- the Poisson and the Binomial.

One should remember that the choice of distribution is also dependent on the best fit [9]. Therefore, in practice the analyst should follow these rules of thumbs:

- If the Weibull fit is poor, other distributions should be considered.
- The data may be plotted utilizing other forms of probability to determine which distribution best fits the data.

**Methods**

In practice, identifying batch problems can be done by applying the following batch analysis methods [11]:

1. Compare Beta MRR (Median Rank Regression) with MLE (Maximum Likelihood).

- MLE Beta is normally steeper (the MLE Bias for small sample-size). If a Batch issue is present, then the MLE Beta will be lower than MRR Beta.

2. Present Risk, calculated on 90% Lower Confidence, should be lower than your current number of defects.
   - If 90% Lower Risk is higher than the Real number of Defects, then this would be a Batch indication
3. The actual number of defects is smaller than the expected number of failures.
   - Aggregated Cumulative Hazard (ACH) plot should show the percentage of the population that is affected by the failure-mode – the Batch size.
4. Other Batch indication clues:
   - Relatively large number of late suspensions; only the youngest units fail.
   - Steep slope followed by shallow.
   - Close serial numbers of the failures.
   - All failures from one supplier (of the multiple suppliers for this unit).
   - All defects after start-up of full production or in a certain timeslot.
   - All failures at one customer/one country.

**Practical Application**

Next, for our further example showing the practical application of the proposed batch analysis approach, we will focus on the application of the first method- Compare Beta MRR (Median Rank Regression) with MLE (Maximum Likelihood Estimation). For more information on the estimation methods [6, 10].

In our example, we are considering a seal defect with failures and suspensions gathered from the field observations (such seal failure may cause an oil leakage leading to an aircraft oil pollution, cabin odor or visible smoke with the use of bleed air and this might have a potential impact on flight safety). The case study we are considering is the following: the age of the seals is measured in weeks, the total failures number is 10 and the suspensions are 25634. As only the youngest seals are failing, it is suspected that something has recently changed in production. If this is the truth, we might only have a part of the total population that is infected with this “virus”, so the damage will be limited. The defects are summarized in the following format: Failures number vs Time-to-Fail (weeks) and are shown in the table below:

*Table 1. Seal Defects vs Time-to-Fail (weeks)*

| **Seal defects** | |
|---|---|
| Time-to-Fail(weeks) | Failures number |
| 14 | 1 |
| 15 | 1 |
| 15 | 1 |
| 20 | 1 |
| 21 | 1 |
| 25 | 1 |
| 26 | 1 |
| 27 | 1 |
| 31 | 1 |
| 31 | 1 |
| Total | 10 |

Running the analysis by means of specialized software tool, first we create an Occurrence CDF (cumulative distribution function) plot for the two slopes based on MRR (Median Rank Regression) and MLE (Maximum Likelihood Estimation) methods:

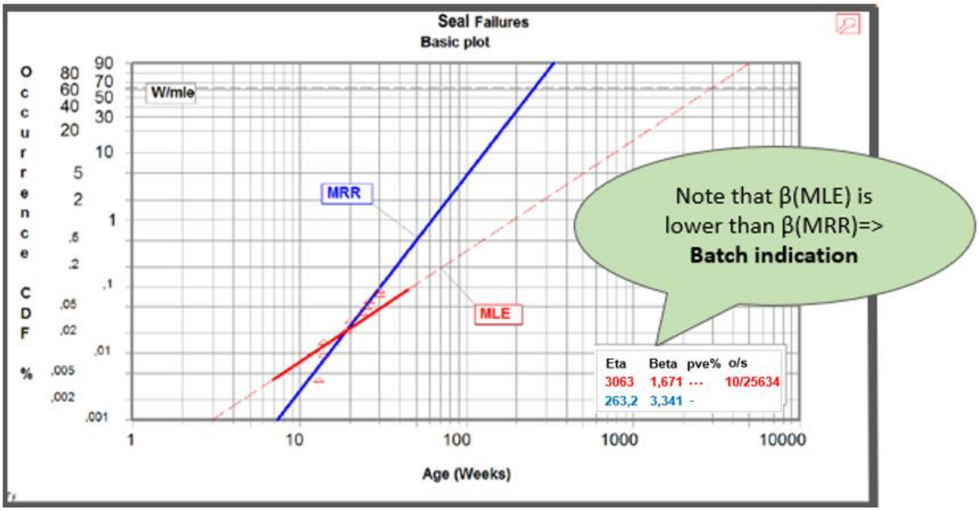


*Fig. 2. Occurrence CDF[%] vs Age(weeks)*

The analysis clearly shows that the slope related to MLE method is lower than the MRR method (see Fig. 2). Another useful plot: creating a histogram "Quantity vs Age (weeks)" which can confirm the presence of batch issue by plotting the presence of many late suspensions (Fig. 3).

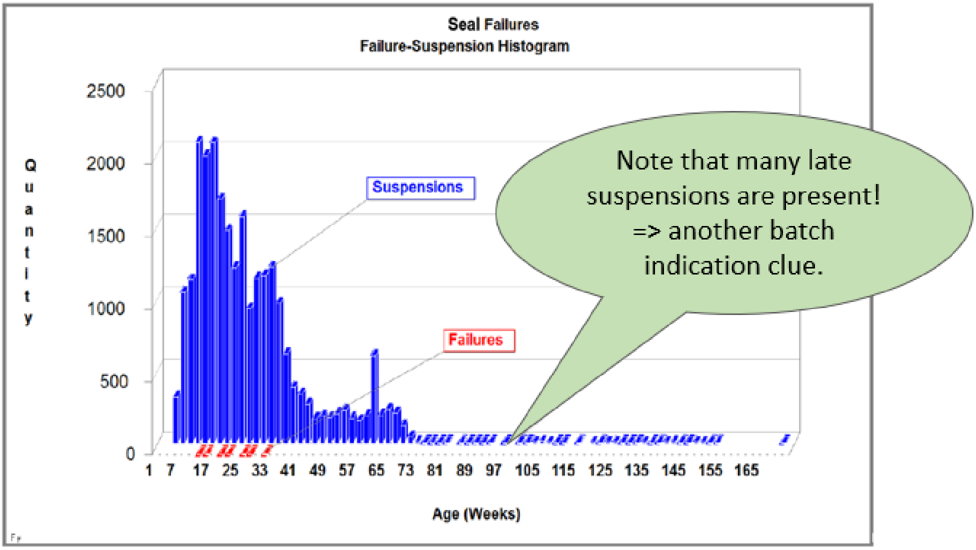


*Fig. 3. Quantity (Failures+Suspensions) vs Age(weeks)*

In our analysis, the early failures occurrence driven by batch issue has been analyzed and confirmed by the two different methods which are very useful in practical applications.

## Conclusion

The following major outcomes can be summarized based on the performed aircraft field reliability engineering analysis:

- In practice, very often problems (e.g. early failures) can be associated with batch issues.
- As a first action, one needs to allocate the batch, find the root-cause and create a solution for the fielded units and the current production.
- After allocating the batch, create a new Weibull analysis plot and then create a failure forecast for the batch only.

## References


1. MIL-HDBK-338B, (1998), Electronic Reliability Design Handbook.
2. MIL-HDBK-217, (1995), Electronic Reliability Prediction Handbook.
3. IEC 62380, (2003), Electronic Reliability Prediction Handbook.
4. FIDES. (2009), Electronic Reliability Prediction Handbook.
5. Kapur, K., L. Lamberson. *Reliability in Engineering Design*. John Wiley & Sons, New York, 1977.
6. Birolini, A. *Reliability Engineering: Theory and Practice*. Springer-Verlag, 2008.
7. Pham, H. *Handbook of Reliability Engineering*. Springer edition, 2003.
8. Nakagawa, T. *Maintenance Theory of Reliability*. Springer edition, 2005.
9. Gindev, E. *Introduction of Reliability Engineering, Part 1*. “M. Drinov” Academic publishing house, Sofia, 2000.
10. Abernethy, R. *The New Weibull Handbook: Reliability and Statistical Analysis for Predicting Life, Safety, Supportability, Risk, Cost and Warranty Claim, 5th ed.* 2006.
11. Schop, R. Reliability Engineering Life Data Analysis using the Weibull distribution. *PLOT Seminar*, October 2008.
12. Valchinov, I., D. Valchinova, G. Mardirossian, S. Zabunov. The unmanned aviation system for radiation intelligence, aerogamma scanning and mapping. *Proceedings SES 2018*, pp. 420–422, Sofia. (In Bulgarian).
13. Zafirov, D., W. Bo, P. Getsov. Impact of the choice of parameters on an electric multi-rotor unmanned aerial vehicles on their main flight characteristics. *Proceedings SES 2020*, pp. 99–102, Sofia (In Bulgarian).
14. Getsov, P., W. Bo, S. Zabunov, G. Mardirossian. Innovations in the area of unmanned aerial vehicles. *Aerospace Research in Bulgaria*, vol. 29, pp. 111–119, 2017, Sofia.
15. Petrov, N. I. *Reliability’s Investigations of Risk Technical Systems*. Trakia University, Publ. House “Uchkov”, 2nd ed., Bulgaria, 2007.
16. Lee, R., J. Yip, V. Shek. *Knowledge Risk and its Mitigation: Practices and Cases*. Emerald Publishing Limited, 2021.
17. Carroll, T. The Fallacy of MTBUR & MTBF as Reliability Metrics. *DoD Maintenance Symposium*, 25 Oct. 2005.
18. Australian Transport Safety Bureau (ATSB), Aircraft Reciprocating-Engine Failure: An Analysis of Failure in a Complex Engineered System, Transport Safety Investigation Report, 2007.

# ИДЕНТИФИЦИРАНЕ НА ПРОБЛЕМИ С ПАРТИДА ПРИ АНАЛИЗ НА ЕКСПЛОАТАЦИОННАТА НАДЕЖДНОСТ НА АВИАЦИОННА ТЕХНИКА

*К. Колев, А. Танев*

**Резюме**

В авиационната практика много важна задача е да се следи надеждността на системите на въздухоплавателните средства, особено тези системи, свързани с безопасността на полета, и да се предприемат съответни действия за предотвратяване на потенциални последици. Навлизайки в дълбочина може да се каже, че много важна стъпка в този анализ е да се идентифицират партидни проблеми, при които отказът засяга само една част от авиационната техника. Разпределението на Вайбул обикновено осигурява най-доброто съгласуване на данните за живота на компонентите, получени от провеждане на тест или от експлоатацията. Това се дължи отчасти на широката гама от форми на разпределения, които са включени в семейството на Вайбул. Също така, има много други разпределения, които са включени в семейството на разпределението на Вайбул, точно или приблизително – например, нормалното, експоненциалното, Релей, а понякога и Поасоновото, и биномиалното. Тази статия представя практически подход за онези авиационни специалисти, които се занимават с мониторинг и анализ на надеждността на авиационна техника.

Bulgarian Academy of Sciences. Space Research and Technology Institute.
Aerospace Research in Bulgaria. 34, 2022, Sofia

DOI: https://doi.org/10.3897/arb.v34.e12

# MATHEMATICAL MODEL FOR OPERATION OF AVIATION SYSTEMS FOR DELIVERY OF SPECIAL MEANS TO AIR AND EARTH OBJECTS

***Milen Atanasov***

*"Georgi Benkovski" Bulgarian Air Force Academy*
*e-mail: maa_69@abv.bg*

***Keywords:*** *Aviation systems, Mathematical model, Delivery of special means*

***Abstract***

*The development of technologies allows the improvement of the algorithms for the operation of aviation systems for the delivery of special means to air and ground objects. The aim is to increase their efficiency, while facilitating the work of the crew in case of lack of time to complete the task. A mathematical model for the operation of this type of aviation systems for the supply of special equipment has been developed, which allows reducing the volume of the existing protocol for the implementation of the crew. It is proposed to use a common ballistic algorithm, combining different groups of special means of delivery to air and ground sites.*

## Introduction

In modern manned military aircraft, full automation of the entire process from target selection to automatic separation of the weapons is essential [1, 6]. The problem is that the wide variety of weapons and their multivariate use creates additional difficulties for full automation [4, 5]. Solving the ultimate task of bringing the weapons to the target requires taking into account the peculiarities in determining the trajectory of each of the groups of weapons — guided with and without motor, unguided with and without motor. What is more, the type of target — aerial, ground (mobile, stationary), flight characteristics of the aircraft must also be taken into account.

This raises the need to create a common algorithm for the operation of the system for release of all types of weapons, taking into account their characteristics.

Unguided weapons are used at a wide range of aircraft heights and speeds, angles and distances to the target, the presence of an angle between the aircraft speed vector and the initial velocity vector of the weapon. In addition, weapons have fundamentally different ballistic schemes. Specific methods are used to solve ballistic problems and various forms of presenting the results of the solutions [2, 7]. It is necessary to synthesize a common ballistic algorithm for all types of unguided weapons, when the type of weapon used is selected on board the aircraft by the crew through a weapon control switch.

**Study area**

To compile a general mathematical model for the release of unguided weapons (UW) is used the general vector scheme determining the destruction of the target — aerial or ground — by the weapon (Fig. 1).

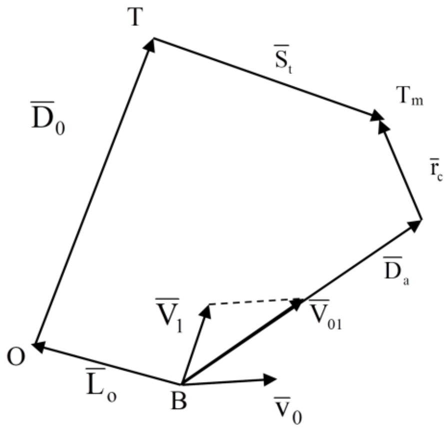


*Fig. 1. General vector scheme of aiming*

1) $\vec{D}_0 = \vec{D}_a + \vec{r}_c - \vec{L}_0 - \vec{S}_t,$

where:

$\vec{L}_0$ is the vector of the base of the weapon;

$\vec{D}_0$ — the target distance vector at the time of the shot;

$\vec{D}_a$ — the vector of the anticipatory distance to the target at the time of the shot;

$\vec{S}_t$ — the vector determining the movement of the target;

$\vec{r}_c$ — the vector determining the deviation of the projectile in the case of a mobile artillery weapon.

The vector equation (1) is represented in scalar form in the connected coordinate system $Ox_1y_1z_1$.

The vector of the base $\vec{L}_0$ of the weapon is determined in the $Ox_1y_1z_1$ coordinate system:

2) $\vec{L}_0 = \vec{L}_{0x1} + \vec{L}_{oy1} + \vec{L}_{0z1}.$

For the synthesis of the general ballistic model, a system of differential equations describing the spatial motion of a weapon in the navigation basis $O_{\eta\zeta\xi}$ is proposed. The axis $O_\eta$ of the navigation basis is oriented along the meridian to the north, the axis $O_\zeta$ is oriented along the local vertical, and the axis $O_\xi$ is oriented so as to form a right coordinate system [3]:

3)
$$\begin{aligned}
&\frac{dV}{dt}=\frac{P}{m}-c_k\frac{m_k}{md^2}H(y)SV^2C_{xe}(M)10^{-3}-g\sin\lambda_b;\\
&\frac{d\lambda_b}{dt}=-g\sin\lambda_b\frac{1}{V}+C_y^{\alpha}(M)(\alpha-\alpha_0)H(y)\frac{\rho_0 V}{2m}S;\\
&\frac{d\eta}{dt}=V\cos\lambda_b;\\
&\frac{d\xi}{dt}=V\sin\lambda_b,
\end{aligned}$$

where:

$P$ is the thrust of the rocket's engine;

$V$ — the speed of the weapon;

$m_k$ — the mass of the rocket after the engine shut down;

$c_k$ — the ballistic coefficient of the rocket in the passive section.

The vector of the anticipatory distance is presented in the connected coordinate system Ox1y1z1 after solving the ballistic problem with the general model of motion — form. (2):

4) $$(\bar{D}_a)_1=\left[A_{\eta\zeta\xi}^{(x_1y_1z_1)}\right]^T\begin{bmatrix}\eta\\ \zeta\\ \xi\end{bmatrix};$$

When firing from a mobile artillery installation, the projectile leaves the barrel with a nutation angle $\delta_0$. In the general case, the initial velocity $\vec{v}_0$ vector of the projectile (relative to the aircraft) and the velocity vector $\vec{V}_1$ do not match.

The deviation of the projectile $r_c$ is determined [3, 5] by the formula:

5) $$(\bar{r}_c)_1=C_r\begin{bmatrix}\cos\beta_s\sin\alpha\sin\beta^/\cos\varepsilon^/-\sin\beta_s\sin\varepsilon^/\\ \sin\beta_s\cos\beta^/\cos\varepsilon^/+\cos\beta_s\cos\alpha\sin\beta^/\cos\varepsilon^/\\ \cos\beta_s\cos\alpha\sin\beta^/\sin\varepsilon^/+\cos\beta_s\sin\alpha\cos\beta^/\cos\varepsilon^/\end{bmatrix},$$

where $C_r=\frac{C_y^{\delta}}{m_{z1}^{\delta}}\frac{d}{l}\frac{\pi\mu}{2\eta_b V_{01}^2}D.$

In the case of a moving target, the following hypothesis for the movement of the target is accepted:

6) $$\dot{\vec{V}}_t=const.$$

The projection of the vector $\vec{S}_t$ on the axes of the connected system $Ox_1y_1z_1$ is determined by the expression:

$$7) \qquad \bar{S}_t = \left\{ \left[A_v^{(1)}\right]^T \begin{bmatrix} V_1 \\ 0 \\ 0 \end{bmatrix} + A_1^{(xDyDzD)} \begin{bmatrix} \dot{D} \\ \omega_{zD} D \\ -\omega_{yD} D \end{bmatrix} \right\} T + \frac{1}{2} \begin{bmatrix} a_{vx1} \\ a_{vy1} \\ a_{vz1} \end{bmatrix} T^2 + \\ + \frac{1}{2} A_1^{(xDyDzD)} \begin{bmatrix} \ddot{D} - D\left(\omega_{yD}^2 + \omega_{zD}^2\right) \\ \omega_{xD}\omega_{yD} D + \dot{\omega}_{zD} D + 2\omega_{zD}\dot{D} \\ \omega_{xD}\omega_{zD} D - \dot{\omega}_{yD} D - 2\omega_{yD}\dot{D} \end{bmatrix} T^2.$$

Putting in form (1) forms (2), (4), (5) and (7) the general system of scalar equations for calculating the distance to the target at the time of the shot is obtained:

$$8) \qquad \begin{bmatrix} D_{0x1} \\ D_{0y1} \\ D_{0z1} \end{bmatrix} = \begin{bmatrix} X_1 \\ Y_1 \\ Z_1 \end{bmatrix} + C_r \begin{bmatrix} \cos\beta_s \sin\alpha \sin\beta^/ \cos\varepsilon^/ - \sin\beta_s \sin\varepsilon^/ \\ \sin\beta_s \cos\beta^/ \cos\varepsilon^/ + \cos\beta_s \cos\alpha \sin\beta^/ \cos\varepsilon^/ \\ \cos\beta_s \cos\alpha \sin\beta^/ \sin\varepsilon^/ + \cos\beta_s \sin\alpha \cos\beta^/ \cos\varepsilon^/ \end{bmatrix} - \\ - \begin{bmatrix} L_{0x1} \\ L_{0y1} \\ L_{0z1} \end{bmatrix} - \left\{ \left[A_v^{(1)}\right]^T \begin{bmatrix} V_1 \\ 0 \\ 0 \end{bmatrix} + A_1^{(xDyDzD)} \begin{bmatrix} \dot{D} \\ \omega_{zD} D \\ -\omega_{yD} D \end{bmatrix} \right\} T - \\ - \frac{1}{2} \begin{bmatrix} a_{vx1} \\ a_{vy1} \\ a_{vz1} \end{bmatrix} T^2 + \frac{1}{2} A_1^{(xDyDzD)} \begin{bmatrix} \ddot{D} - D\left(\omega_{yD}^2 + \omega_{zD}^2\right) \\ \omega_{xD}\omega_{yD} D + \dot{\omega}_{zD} D + 2\omega_{zD}\dot{D} \\ \omega_{xD}\omega_{zD} D - \dot{\omega}_{yD} D - 2\omega_{yD}\dot{D} \end{bmatrix} T^2.$$

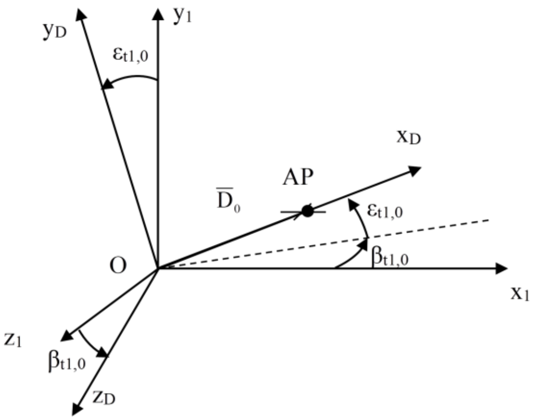


*Fig. 2. Aiming point (AP) and aiming angles*
*of the target $\beta_{t1,0}$, $\varepsilon_{t1,0}$ at the moment of firing and bombing*

In the general case at the moment of firing and bombing, the angles $\beta_{t1,0}$ and $\varepsilon_{t1,0}$ of aiming at the target in the connected coordinate system Ox1y1z1 (Fig. 2) are determined by the formulas:

9) $$\beta_{t1,0} = arctg\left(\frac{D_{0z1}}{D_{ox1}}\right) \qquad \varepsilon_{t1,0} = arctg\left(\frac{D_{0y1}\sin\beta_{t1,0}}{D_{oz1}}\right),$$

where:

10) $$D_0 = \sqrt{D_{0x1}^2 + D_{0y1}^2 + D_{0z1}^2}.$$

The firing of aviation automatic weapons and unguided rockets is performed by the pilot combining the calculated aiming angles of the target $\beta_{t1,0}$ and $\varepsilon_{t1,0}$ with the visually detectable target while observing the allowed firing distance. This distance is determined by the type of the weapon used.

Depending on the combat capabilities of the aircraft, its design features and the perfection of its strike complex, bombing can take place in the visible zone and in the invisible zone.

When bombing takes place in the visible zone, i.e. The Continuously Computed Impact Point (CCIP) method is used, similarly to shooting, the pilot combines the calculated angles $\beta_{t1,0}$ and $\varepsilon_{t1,0}$ in form (9) with the target and depresses the combat button in compliance with safety measures [2, 6].

When bombing into the invisible zone using the Continuously Computed Release Point (CCRP) method, the pilot aligns the aiming grid with the target, as a result of which the calculation of the current coordinates of the target relative to the aircraft begins:

11) $$\begin{cases} \eta_c = \eta_0 - \int_0^t W_{\eta'} dt; \\ \xi_c = \xi_0 - \int_0^t W_{\xi'} dt, \end{cases}$$

where $W_\eta$, $W_\xi$ are the projections of the ground speed of the aircraft, and a $\eta_0$, $\xi_0$ are the initial coordinates of the target.

The bombing is performed in automatic mode when the inequality is fulfilled:

12) $$\eta_c - \eta \leq 0.$$

Based on the abovementioned general mathematical model for combat use of weapons, a general structural scheme of a weapons release system is proposed (Fig. 3).

The general block diagram of a weapons release system consists of:

- targeting unit;

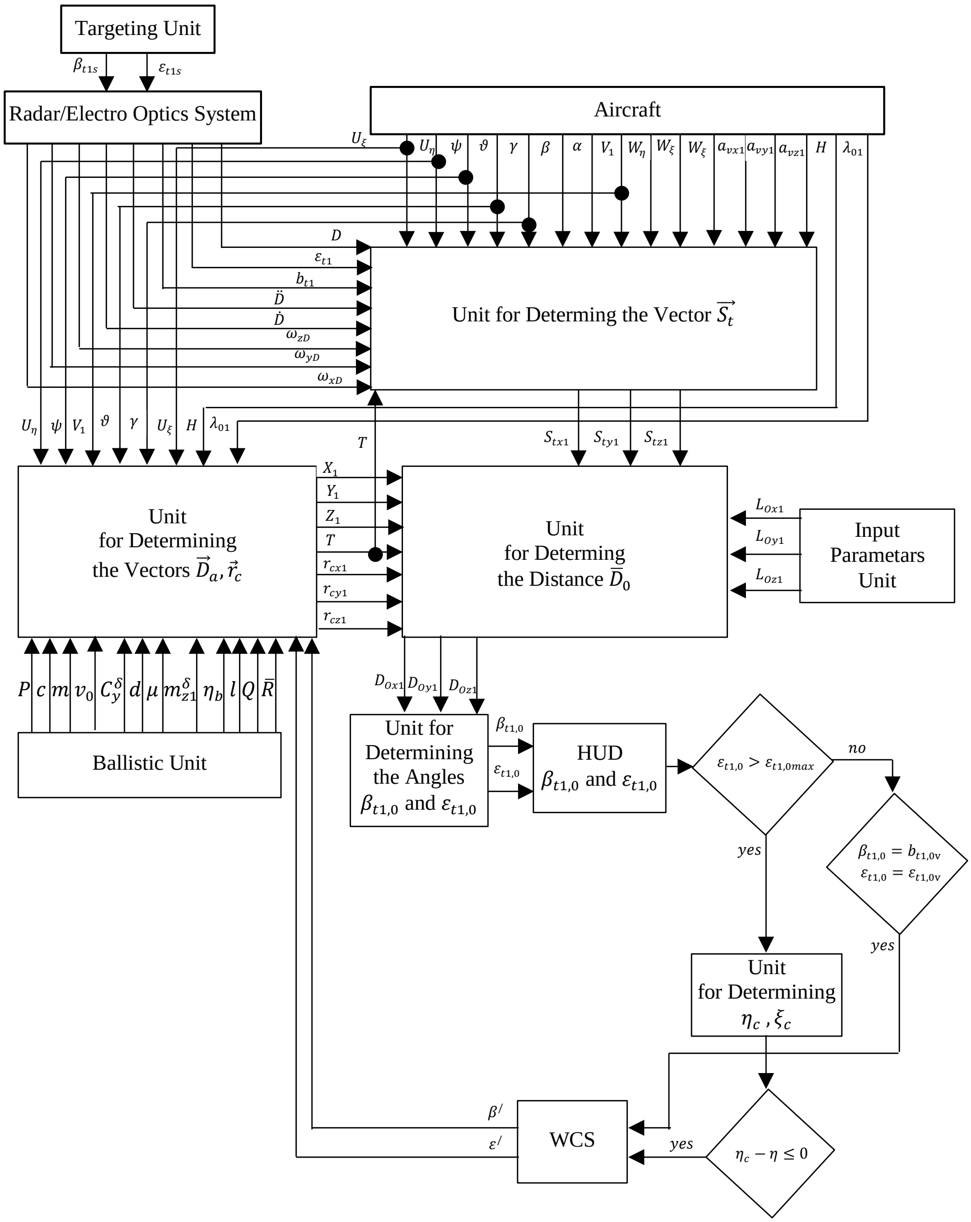


*Fig. 3. General structural scheme of a weapons release system*

- a unit for determining the vector which determines the movement of the target $\overline{S_t}$;

- a unit for determining the vectors of the anticipatory distance $\overline{D_a}$ to the target and the deviation $\overline{r_c}$ of the weapon;

- unit for determining the distance $\overline{D_0}$ to the target at the time of release;

- ballistic unit;

- input parameters unit;

- unit for determining the angles βt1,0 и εt1,0;

- unit for determining ηc, ξc of the current coordinates of the target relative to the aircraft;

- Heads-up Display (HUD).

The azimuth angle βц1 and the angle εц1 of the target location are fed from the targeting unit to the R/OES.

The vector determining the movement of the target $\overline{S_t}$ is calculated after solving the ballistic problem using the system (4) and formula (7) depending on whether the target is aerial or ground.

In the unit for determining the vectors $\overline{D_a}$ and $\overline{r_c}$, they are determined by formulas (4) and (5). Provided that the aviation artillery weapon is stationary, the vector $\bar{r}_c$ is not calculated.

With the help of the obtained formula (8) the distance to the target $\overline{D_0}$ at the moment of release is determined in the respective unit.

The values P, c, m, v0, Cδy, d, μ, mδz1, ηb, l, θ and the coordinates of the point of explosion - Rη, Rζ, Rξ are supplied by the ballistic unit depending on the weapon used.

The base of the aviation artillery weapon $(\overline{L_0})_1$ is supplied by the input parameters unit.

The angles of rotation β′ and ε′ relative to the Ox1y1z1 system are supplied by the weapon control system (WCS).

The target aiming angles βt1,0 and εt1,0 are calculated using form (9) in the relevant unit.

When firing and bombing in the visible zone (CCIP), the calculated angles βt1,0 and εt1,0 are displayed on the HUD. This is the position of the aiming grid. When the aiming grid is aligned with the target, the pilot depresses the combat button, which signals the weapon control system (WCS). In the case of bombing in the invisible zone (CCRP), after aligning the aiming grid with the target, the current coordinates ηt, ξt of the target relative to the aircraft are calculated in the respective unit. Upon fulfilment of the condition $\eta_t - \eta \leq 0$, a signal is sent to the WCS [5].

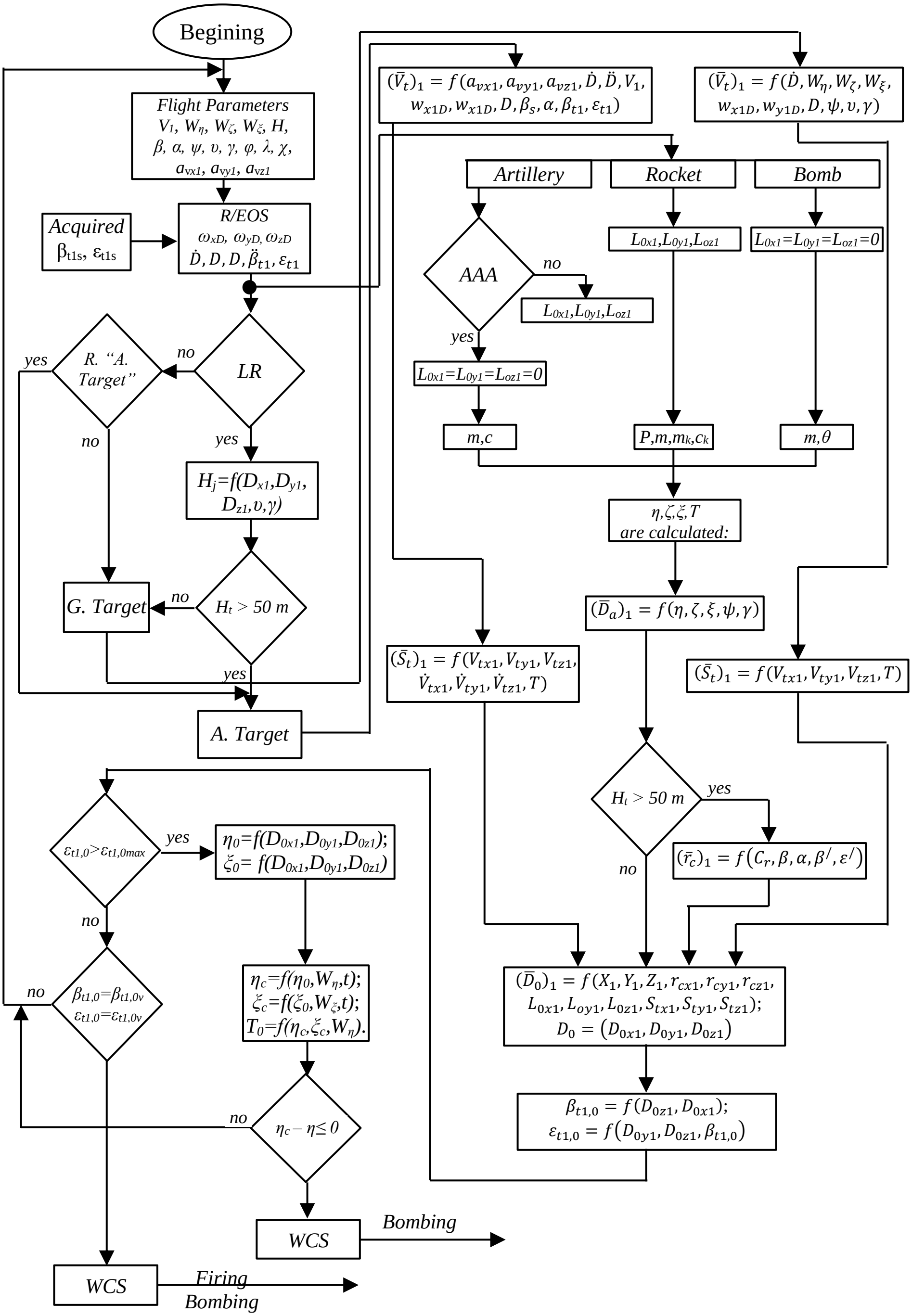


*Fig. 4. Operatoin algorithm for combat when shooting and bombing with unguided weapons*

Based on the developed general mathematical model and general structural scheme of the weapons release system, an algorithm for combat use has been developed (Fig. 4).

After the target is acquired by the radar or the OES, it is automatically determined what the target is — aerial or ground. In case the acquisition is performed by OES, with the help of the laser rangefinder (LR), the distance D to the target is measured and its height Ht is determined using the formula:

13) $$H_t = H_a - D_{x1} \sin\vartheta - D_{y1} \cos\vartheta \cos\gamma + D_{z1} \cos\vartheta \sin\gamma.$$

Provided that Ht > 50 m, a decision is made – it is an aerial target. If the condition is not met – it is a ground target.

When using a radar, the pilot manually selects the “aerial target” or “ground target” mode.

Depending on the type of target, the speed Vt of the target is calculated.

Depending on the target, the pilot selects the type of weapon. Then the respective parameters included in the system of differential equations for the movement of the weapons are submitted. After solving the system, the vector $\overline{D}_t$ of the anticipatory distance to the target at the moment of the shot and the time T of the flight of the weapon are calculated.

In the case of bombing and firing of aviation artillery weapons located along the axis of the aircraft (AAA), it is assumed that the vector of the base on the weapon is: $\overline{L_0} \neq 0$.

When firing a rocket and aviation artillery weapon located in a container attached to the aircraft, it is assumed that $\overline{L_0} \neq 0$.

Depending on the type of target (aerial or ground), the vector $\overline{S_t}$ determining the movement of the target is calculated. Provided the target is stationary $\overline{S_t} = 0$.

Provided that the weapon is mobile ($\beta' \neq 0$; $\varepsilon' \neq 0$) the vector determining the deviation $\overline{r}_c$ of the projectile is determined.

The next step is to calculate the distance vector $\overline{D}_0$ to the target at the time of the shot, from which the angles βt1,0 and εt1,0 of aiming at the target relative to the connected coordinate system Ox1y1z1 are determined.

Provided that shooting or bombing is carried out in the visible zone (εt1,0 < εt1,0max) and after aligning the aiming grid with the target (βt1,0 = βt1,0v; εt1,0 = εt1,0v) a signal is sent to the weapon control system, followed by firing or bombing.

Provided that the bombing is carried out in the invisible zone (εt1,0 > εt1,0max), the initial η0, ξ0 and the current coordinates ηt, ξt of the target relative to the aircraft are determined.

When the condition $\eta_t - \eta \leq 0$ is met, the bombing is performed automatically.

Provided that $\eta_t - \eta > 0$ or $\beta_{t1,0} \neq \beta_{t1,0v}$; $\varepsilon_{t1,0} \neq \varepsilon_{t1,0v}$ then the process continues and returns to the starting position.

**Conclusion**

The creation of a common model of a weapons release system, including a common ballistic model of weapons will lead to:

- shortening the operating time of the pilot in case of combat use;
- increasing the efficiency of the use of weapons by expanding the range of conditions of combat use.

**References**


1. Mitev, S. Accuracy of Navigation Complexes, Scientific Research and Education in the Air Force — AFASES 2018, Publishing House of "Henri Coanda" Air Force Academy Str. Mihai Viteazu 160, Brasov 500183, Romania — 2018, ISSN: 2247-3173, DOI:10.19062/2247-3173.2018.20.
2. Petrov, N., Sv. Asenov, D. Guinchev, N. Zagorski, Ang. Chzhgova. Assessment of the rate of increase of the legally defined technical resources to the aviation system. *International Journal of Mathematic Sciences and Engineering Applications (IJIMSEA)*, Vol. 7, No VI 9 (November 2013), ISSN 0973-9424, pp. 1–6.
3. Stojkov, O., M. Atanasov. *Aviacionni pricelni sistemi — Part 1*. VGC, D. Mitropolija, 2009, ISBN 978-954-713-093-7 (in Bulgarian).
4. Stojkov, S. Analiz na prichinite vliyaeshti na efektivnostta na boĭnoto izpolzvane na aviatsionnite bombi, NVU "V. Levski", fakultet "Aviacionen", D. Mitropolija, "Godishna mezhdunarodna nauchna konferentsiya", pp. 300–303, 2019, ISBN 978-954-713-123-1 (in Bulgarian).
5. Zagorski, N., Ang. Chozhgova, Research on neural network for identification of the status of complex technical objects. *Anniversary Scientific Conference on Aeronautics, Automotive and Railway Engineering and Technologies BulTrans-2013*, 16–18 October, Sofia, Proceedings, pp. 161–164.
6. Zagorski, N. Problemi na nadejdnostta na aviatsionni sistemi i nejnoto vlianie varhu bezopasnostta na poleta, Monografia, IK "Rakursi" - Plovdiv, 2021, ISBN 978-619-7599-03-9, 213 p. (in Bulgarian).
7. Zagorski, N. Priblijeni modeli za optimizatsia na parametrite za eksploatatsia i technichesko obslujvane na aviatsionnite sistemi s otsenka na tochnostta i dostovernostta na poluchavanite rezultati, Journal of the Technical University at Plovdiv "Fundamental Sciences and Applications", Vol. 14(2), 2009, pp. 359–364 (in Bulgarian).

# МАТЕМАТИЧЕСКИ МОДЕЛ ЗА РАБОТА НА АВИАЦИОННИ СИСТЕМИ ЗА ДОСТАВКА НА СПЕЦИАЛНИ СРЕДСТВА ДО ВЪЗДУШНИ И ЗЕМНИ ОБЕКТИ

***М. Атанасов***

**Резюме**

Развитието на технологиите позволява усъвършенстване на алгоритмите за работа на авиационните системи за доставка на специални средства до въздушни и земни обекти. Целта е да се повиши тяхната ефективност, като същевременно се улесни работата на екипажа при недостиг на време за изпълнение на задачата. Разработен е математически модел за работа на този тип авиационни системи за доставка на специални средства, който позволява намаляване на обема на съществуващия протокол за изпълнение от екипажа. Предложен е за използване общ балистичен алгоритъм, обединяващ различните групи специални средства за доставка до въздушни и наземни обекти.

Bulgarian Academy of Sciences. Space Research and Technology Institute.
Aerospace Research in Bulgaria. 34, 2022, Sofia

DOI: https://doi.org/10.3897/arb.v34.e13

# COMPARATIVE ANALYSIS OF THE ACCURACY OF BOMB RELEASE AND THE PROBABILITY CHARACTERISTICS OF THE ERROR OF BOMBING OF DIFFERENT METHODS SOLVING THE PROBLEM OF AIMING

***Stoyko Stoykov***

*Faculty Aviation, Bulgarian Air Force Academy, Dolna Mitropolia, Bulgaria*
*e-mail: sos_23@abv.bg*

***Keywords:*** *Aviation, Air bomb, Accuracy of bomb release, Probable deflection*

***Abstract***

*An approximate method for estimating the accuracy of bomb release of new methods solving the problem of targeting compared to existing ones is proposed. A comparative analysis of the Root mean square deviation, the expected value and the second starting point of the bomb release error for new and existing methods of the targeting task was performed.*

## Introduction

In certain areas of use of different methods for solving the targeting problem, it is possible to perform a comparative analysis of the accuracy of bomb release of these methods by the probable deviations of the drop points of the bombs.

The probable deviation is calculated according to the formula [3]:

1) $$E = 8H + 0{,}08V_1(1+\sin\lambda)$$

where: H is the height of bomb release, km,
$V_1$ — speed of bomb release, km/h,
$\lambda$ — diving angle.

The following expressions (method 1, existing and method 2, new) are used to perform a comparative analysis of the probabilistic characteristics of the bomb release errors of different methods:

2) $$\Delta\sigma\Delta x = \sigma\Delta x1 - \sigma\Delta x2$$
$$\Delta M[\Delta x] = M[\Delta x1] - M[\Delta x2]$$
$$\Delta\alpha 2x = \alpha 2x1 - \alpha 2x2$$

where: - $\sigma\Delta x1$, $M[\Delta x1]$, $\alpha 2x1$ are the standard deviation, the mathematical expectation and the second starting point of the bomb error for method 1.

- $\sigma\Delta x2$, $M[\Delta x2]$, $\alpha 2x2$ are the standard deviation, the mathematical expectation and the second starting point of the bomb error for method 2.

**Results**

To calculate the probable deviation E of Method 2, the following formula is proposed:

3) $E_2 = P_п E_п + P_{ип} E_{ип}$,

Where: - $E_п$ и $E_{ип}$ are probable deviations during bomb release during or exiting diving;

- $P_п$ и $P_{ип}$ – probabilities for bomb release during or exiting diving.

Probable deviations are calculated by a formula (1) where H, V1 and λ are the average values taken for the respective bomb-dropping areas.

Release probabilities are defined as the ratio of the area to the total area of the bomb-dropping area for a given method.

To determine the percentage increase in the accuracy of bomb release when using method 2 compared to method 1, the following ratio is used:

4) $$E\% = \frac{E_{см} - E_{ум}}{E_{см}} 100$$

Based on the resulting areas [4] of possible bomb release conditions for method 2 and method 1, the average values for the bomb release conditions ($H_0$, $V_{1,0}$, $\lambda_0$) of the respective areas are determined (Fig. 1, 2, 3, 4). The same figures also determine the probabilities of during or exiting diving release Pn and Rip (Table 1).

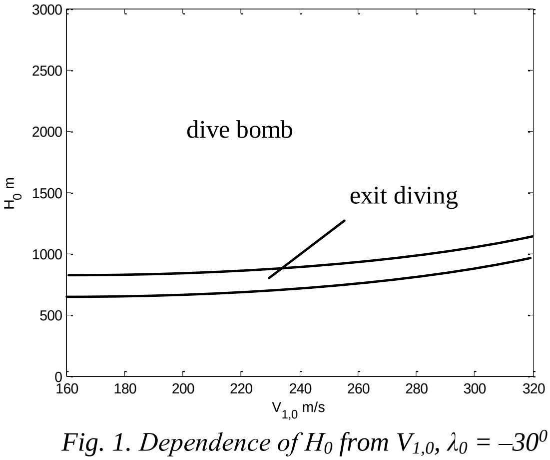


*Fig. 1. Dependence of $H_0$ from $V_{1,0}$, $\lambda_0 = -30^0$*

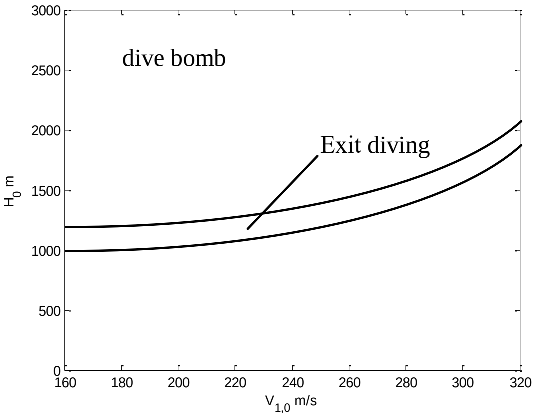


*Fig. 2. Dependence of $H_0$ on $V_{1,0}$, $\lambda_0 = -50^0$*

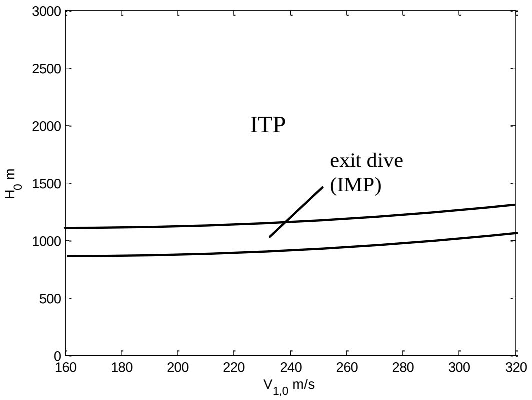


*Fig. 3. Dependence of $H_0$ from $V_{1,0}$ $\lambda_0 = -30^0$*

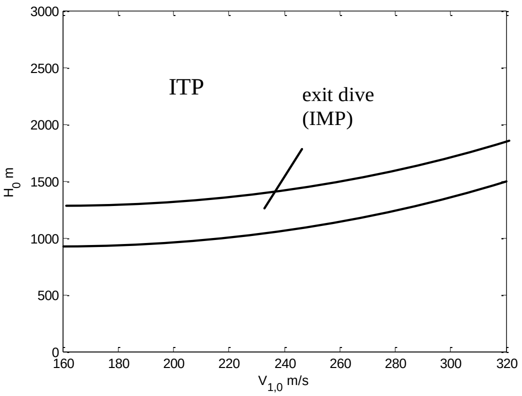


*Fig. 4. Dependence of $H_0$ from $V_{1,0}$, $\lambda_0 = -50^0$*

*Table 1*

| | $\lambda_0 = -30^0$ | | | | $\lambda_0 = -50^0$ | | | |
|---|---|---|---|---|---|---|---|---|
| | ***Diving*** | | ***Exit diving*** | | ***Diving*** | | ***Exit diving*** | |
| | **M2** | **M1** | **M2** | **M1** | **M2** | **M1** | **M2** | **M1** |
| $\mathbf{V_1}$ | 800 | 900 | 850 | 900 | 900 | 900 | 950 | 950 |
| **H** | 0,7 | 1,8 | 0,5 | 0,7 | 1,5 | 2 | 1 | 1,3 |
| $\boldsymbol{\lambda}$ | $-30^0$ | $-30^0$ | $-12^0$ | $-12^0$ | $-50^0$ | $-50^0$ | $-20^0$ | $-20^0$ |
| $\boldsymbol{P_п}$ | 0,94 | 0,94 | | | 0,88 | 0,72 | | |
| $\mathbf{P_{ип}}$ | | | 0,06 | 0,06 | | | 0,12 | 0,28 |
| $\mathbf{E_п}$ | 33,6 | 50,4 | | | 28,8 | 32,8 | | |
| $\mathbf{E_{ип}}$ | | | 48,4 | 62,63 | | | 58,01 | 60,40 |
| $\mathbf{E_2}$ | 34,5 | | | | 32,34 | | | |
| $\mathbf{E_1}$ | 51,13 | | | | 40,56 | | | |
| | $E\% = \frac{E1 - E_2}{E_1}100 = 32.\,\%$ | | | | $E\% = \frac{E1 - E_2}{E_1}100 = 20,\,\%$ | | | |

It can be seen from Table 1 that the accuracy of the bomb release of method 2 at $\lambda_0 = -30^0$ is with 32% greater than that of method 1, and at $\lambda_0 = -50^0$ — by 20%.

Table 1 shows that the circular probable deviation of Method 2 for solving the targeting task is closer to the required E = 30 m [4]. The resulting percentage increases of accuracy calculated by the proposed formula (1) and by the root mean square deviations (2) are close in value (for $\lambda_0 = -30°$, $\sigma_{\Delta x}\% = 28.63\%$; for $\lambda_0 = -50°$, $\sigma_{\Delta x}\% = 19.55\%$).

As a result of the mathematical modeling of the aiming process, the probabilistic characteristics of the bomb release error are determined. ($\sigma_{\Delta x}$, $M[\Delta x]$) from diving.

The differences $\Delta\sigma_{\Delta x}$ are given in Table 2 during bomb release at diving angle of $\lambda = -30°$. The difference $\Delta\sigma_{\Delta x}$ varies within the limits of 1.9 m and 5.3 m.

*Table 2*

| $\Delta\sigma_{\Delta x}$ m, $\lambda = -30°$ | | | | | |
|---|---|---|---|---|---|
| | **$V_1$ = 170 m/s** | **200** | **220** | **240** | **270** |
| **H = 650 m** | 2.7 | 3.15 | 3.4 | 3.65 | 3.9 |
| **1000** | 1.9 | 2.4 | 3.2 | 4.30 | 4.8 |
| **1350** | 2.2 | 2.2 | 2.7 | 3.8 | 5.3 |
| **1700** | 3.4 | 2.6 | 2.6 | 3.5 | 5.2 |
| **2100** | 5.7 | 3.5 | 2.5 | 2.8 | 4.4 |

The difference $\Delta M[\Delta x]$ varies within the limits of 2.00 and 14.60 m for observed bomb release conditions (*Table 3*).

*Table 3*

| $\Delta M[\Delta x]$ m, $\lambda = -30°$ | | | | | |
|---|---|---|---|---|---|
| | **$V_1$=170 m/s** | **200** | **220** | **240** | **270** |
| **H=650 m** | 6.18 | 5.36 | 4.41 | 3.32 | 2.00 |
| **1000** | 6.86 | 6.56 | 5.82 | 4.65 | 3.04 |
| **1350** | 8.47 | 7.73 | 6.66 | 5.30 | 3.62 |
| **1700** | 11.02 | 8.86 | 6.93 | 5.27 | 3.84 |
| **2100** | 14.60 | 9.95 | 6.64 | 4.55 | 3.70 |

The difference $\Delta\alpha_{2x}$ assumes its maximum value in the range of conditions under which the method 1 is used — MRD “moment of release display” ($\Delta\alpha_{2x}$ = 684 m$^2$), and its minimum value ($\Delta\alpha_{2x}$ = 124 m$^2$) is assumed in the range of conditions, under which the method 1 is used — DPD “drop point display” (Table 4). At heights H = 1700–2100 m, $\Delta\alpha_{2x}$ assumes minimal effect within the range of speeds, at which method 1 is changed from DPD to MRD. With the increase of height H, the second initial moment of the error $\alpha_{2x2}$ decreases in relation to $\alpha_{2x1}$.

*Table 4*

| $\Delta\alpha_{2x}$ m$^2$, $\lambda = -30^0$ | | | | | |
|---|---|---|---|---|---|
| | **$V_1$ = 170 m/s** | **200** | **220** | **240** | **270** |
| **H = 650 m** | 139.99 | 136.56 | 133.01 | 128.88 | 123.77 |
| **1000** | 154.91 | 169.24 | 183.50 | 197.95 | 212.65 |
| **1350** | 223.60 | 219.63 | 228.03 | 251.86 | 292.46 |
| **1700** | 383.56 | 302.31 | 265.77 | 278.66 | 344.56 |
| **2100** | 683.95 | 431.35 | 295.03 | 266.87 | 351.15 |

The difference $\Delta\sigma_{\Delta x}$ varies within the limits of 1.95 to 4.60 m (Table 5) at $\lambda = -50°$.

*Table 5*

| $\Delta\sigma_{\Delta x}$ m, $\lambda = -50°$ | | | | | |
|---|---|---|---|---|---|
| | **$V_1$=170 m/s** | **200** | **220** | **240** | **270** |
| **H = 650 m** | 2.26 | 2.21 | 2.13 | 2.03 | 1.95 |
| **1000** | 2.27 | 2.73 | 2.99 | 3.06 | 2.92 |
| **1350** | 2.28 | 3.06 | 3.55 | 3.79 | 3.69 |
| **1700** | 2.31 | 3.18 | 3.79 | 4.13 | 4.21 |
| **2100** | 2.36 | 3.11 | 3.71 | 4.16 | 4.60 |

The expected value $M[\Delta x_2]$ of the bomb release error $M[\Delta x_1]$ for the considered conditions of bomb release, where the difference $\Delta M[\Delta x]$ varies within 3.20 and 8.90 (Table 6). With the increase of speed $V_1$ of bomb release $\Delta M[\Delta x]$ decreases, and with the increase of the height H the difference $\Delta M[\Delta x]$ increases.

*Table 6*

| $\Delta M[\Delta x]$ m, $\lambda = -50^0$ | | | | | |
|---|---|---|---|---|---|
| | **$V_1$ = 170 m/s** | **200** | **220** | **240** | **270** |
| **H = 650 m** | 5.32 | 4.56 | 3.93 | 3.43 | 3.20 |
| **1000** | 6.45 | 5.77 | 5.20 | 4.73 | 4.38 |
| **1350** | 7.41 | 6.78 | 6.25 | 5.81 | 5.47 |
| **1700** | 8.20 | 7.61 | 7.08 | 6.66 | 6.32 |
| **2100** | 8.90 | 8.22 | 7.71 | 7.27 | 6.91 |

The second starting point $\Delta\alpha_{2x2}$ of the bomb release error is smaller than $\Delta\alpha_{2x1}$ (Table 7).

*Table 7*

| $\Delta\alpha_{2x}$ m$^2$, $\lambda = -50^0$ | | | | | |
|---|---|---|---|---|---|
| | **$V_1$ = 170 m/s** | **200** | **220** | **240** | **270** |
| **H = 650 m** | 87.23 | 77.50 | 69.68 | 63.21 | 57.64 |
| **1000** | 132.06 | 132.63 | 131.51 | 127.93 | 120.53 |
| **1350** | 176.04 | 188.29 | 196.48 | 198.72 | 193.33 |
| **1700** | 216.49 | 237.79 | 254.46 | 265.13 | 267.72 |
| **2100** | 251.69 | 274.12 | 296.65 | 317.58 | 335.62 |

For the full range of conditions, the accuracy of method 2 for bomb release is higher than that of existing methods 1. The relative increase of bomb release accuracy of method 2 varies between 34% and 56%.

## Conclusion

A formula for calculating the probable deviation of the bombing error is proposed for newly developed methods for solving the targeting problem. As an example, the probabilistic characteristics of the dive bomb release error were calculated and a comparative analysis was performed for different methods solving the task of bomb release targeting.

## References

1. Atanasov, M. Mathematical model and algorithm of operation of system for release of load from airplane. *Aerospace Research in Bulgaria*, 32, 2020, Sofia, pp. 64–74.
2. Stoykov, S., M. Atanasov. Calculating Technical Scattering Full Error for External Suspended Bombs at Free Release. *International conference of scientific, Brasov, AFASES*, 2015, pp. 487–490, ISSN L 2247 3173.
3. Stoykov, S., A. Stoilkov. Calculation of the probabilistic characteristics of the accuracy of bomb release without forced release of the bomb. *VI International scientific and technical conference, Engineering, Technologies, Education, Security*, Proceedings, Volume I, Military Science and Security, pp. 30–32, Veliko Tarnovo, 2018, ISSN 2535–0315.
4. Stoykov, O., M. Atanasov. Determining the areas of use of the methods indication of the point of fall and indication of the moment of launching during bombing. *UNK, NMU "V. Levski", Faculty "Aviation", D.M.*, pp. 91–96, 2014, ISBN 978-954-713-216-8.
5. Mardirossian, G., D. Danov. Preliminary analysis or the ballistic parameters of a penetrator for ecological studies. *Aerospace Research in Bulgaria*, 16, 2001, pp. 89–96.

## СРАВНИТЕЛЕН АНАЛИЗ НА ТОЧНОСТТА НА БОМБОПУСКАНЕ И НА ВЕРОЯТНОСТНИТЕ ХАРАКТЕРИСТИКИ НА ГРЕШКАТА НА БОМБОПУСКАНЕ НА РАЗЛИЧНИ МЕТОДИ, РЕШАВАЩИ ЗАДАЧАТА НА ПРИЦЕЛВАНЕ

***С. Стойков***

### Резюме

Предлага се приблизителен метод за оценяване на точността на бомбопускане при нови методи, решаващи задачата на прицелване спрямо съществуващите такива. Извършен е сравнителен анализ на средно квадратичното отклонение, математическото очакване и втория начален момент на грешката за нов и съществуващ метод на задачата на прицелване.

Резултатите могат да се използват и при проектиране на пенетратори за екологични изследвания.

Bulgarian Academy of Sciences. Space Research and Technology Institute.
Aerospace Research in Bulgaria. 34, 2022, Sofia

DOI: https://doi.org/10.3897/arb.v34.e14

# AFM ANALYSIS OF ALUMINIUM ALLOY 7075

***Anna Bouzekova-Penkova[1], Silviya Simeonova[2]***

*[1]Space Research and Technology Institute — Bulgarian Academy of Sciences*
*[2]Department Physical Chemistry Faculty of Chemistry and Pharmacy Sofia University St. Kliment Ohridski*
*e-mail: a_bouzekova@space.bas.bg, fhsss@chem.uni-sofia.bg*

***Keywords:*** *Atomic Force Microscopy (AFM,) Aluminium alloy 7075, Cosmic ray and gamma radiation.*

***Abstract***

*In this paper we present the results of atomic force microscopy (AFM) characterization of the surface morphology new type of composite based on the high-tensile aluminium alloy 7075 strengthened with nanoparticles of diamond powder and tungsten is developed, stored for 28 months under different conditions. One sample was stored on Earth at room temperature and second one was mounted on the outer side of the International Space Station.*

## Introduction

Requirements for the materials and them properties which are used in extreme conditions leads to new materials development and using. One of the conditions for exploitation is that they are light and hard. These materials need to have determined properties — heat resistance, high modulus of elasticity, wear, low density and other useful property for space materials engineering application. They must work in non-standard conditions — temperature fluctuations, cosmic radiation and mechanical stress: acceleration, vibration and others. To function in outer space, which is why it is extremely important to produce appropriate materials.

Due to the unique combination of properties, the aluminium and its alloys are one of the most important materials of today's aviation, aerospace and missile/rocket industry [1–3]. They are also called "space materials" because they meet the requirements that apply to space materials.

The aluminium alloy AA 7075 is the most widely used alloy for the production of high strength structures operating in extreme conditions. These aluminium alloys have a complex chemical composition, and refers to the four component system Al-Zn-Mg-Cu- highly hardened by heat treatment [4–6].

Due to the fact that the alloy AA 7075 is used in extreme conditions and is used in modern aeronautical structures and space techniques, it is especially proposed additional introduction of nanodiamond particles and other alloying additives to improve the properties of alloy.

In the presented scientific development a new composite material based on aluminium AA 7075 was investigated, with quantitative addition of ultrafine diamond powder (UDPD) [7] and Tungsten (W). The material is suitable, has the necessary properties and for this purpose the “OBSTANOVKA” experiment is planned and performed in the Russian module of the International Space Station (ISS) [8–9].

## Materials and Methods

### Materials

Two types of samples were prepared and studied of aluminium alloy AA 7075 with additions of ultra-dispersed diamond powder (UDDP) and Tungsten. Some specimens were stored as a “reference” under natural terrestrial conditions for 28 months, while other specimens were subjected to “space” conditions — outside the International Space Station (ISS) for the same period.

The “space” sample was subjected to space radiation [10], which changed rapidly in intensity and type, depending on the coordinates, geophysical and helio-physical conditions, during orbiting of the station around the Earth

The temperature changes varied over a wide operating temperature range from −120 to +150°C for 2 hours over a period of 2 years and 4 months.

The above composite was obtained by casting and subjected to subsequent heat treatment. Cylindrical samples were made from it. For the presented below studies cylindrical specimens were cut with a diameter of 6 mm and a height of 6 mm. The analysed surfaces for both types of samples are performed in the centre, periphery and end. By periphery is meant the middle between the centre and the end along the radius.

### Characterization methods

AFM imaging was performed on the NanoScope V system (Bruker Ltd, Germany) operating in tapping mode in air at room temperature. We used silicon cantilevers (Tap 300Al-G, Budget Sensors, Innovative solutions Ltd, Bulgaria) with 30 nm thick aluminium reflex coatings. According to the producer’s datasheet the cantilever spring constant and the resonance frequency are in the range of 1.5 to 15 N/m and 150 ± 75 kHz, respectively. The tip radius was less than 10 nm. The scan rate was set at 1 Hz and the images were captured in height mode with 512×512 pixels in JEPG format. Subsequently, all images were flattened by using NanoScope software. The same software was also used for section analysis and roughness.

## Results and Discussions

Atomic Force Microscopy (AFM) can be applied to measure the surface topography with great accuracy and thus facilitate the quantification of material roughness. Measurements of three samples from the “reference” R-1, R-2, R-3 and three samples from the “space” samples S-1, S-2, S-3 were performed. For each type of sample measurements were made in the centre, periphery and edge. The topography of a surface consists of structures of different length scales. The surface roughness caused by these structures plays a decisive role in interfacial properties.

Fig. 1 and Fig. 2 present the AFM images in 2D and 3D format of the samples. These images are accompanied by cross sections (Section) on the surface of the materials.

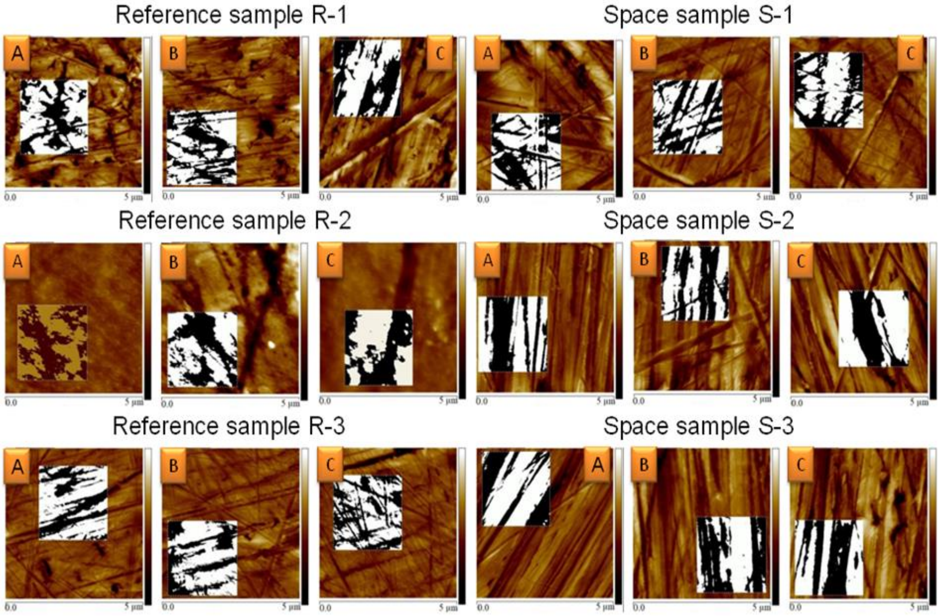


*Fig. 1. 2D AFM images 5 µm of the Roughness of the aluminium alloy 7075 strengthened with nanoparticles of diamond powder and Tungsten: from left in the images – “reference” sample, the right of the image – “space” sample, (A) centre, (B) periphery and (C) edge*

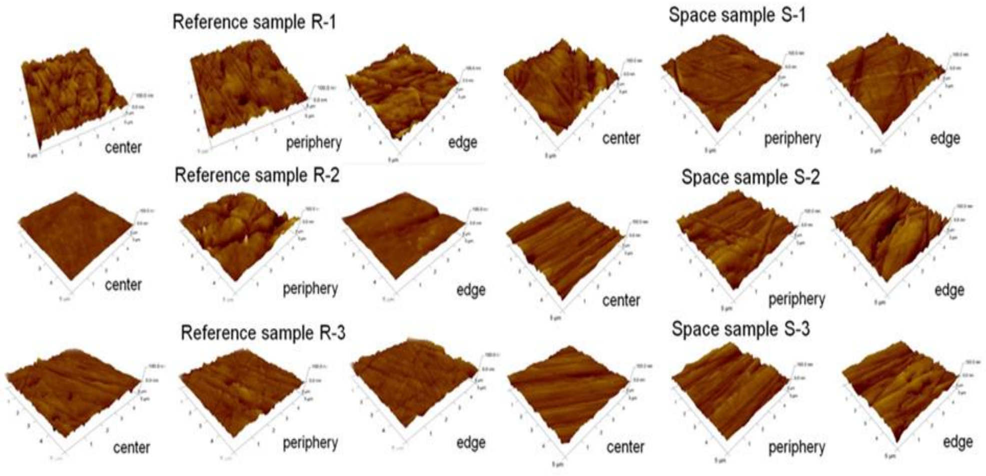


*Fig. 2. 3D AFM images 5 µm of the surface of aluminium alloy 7075 strengthened with nanoparticles of diamond powder and Tungsten: from left in the images – "reference" sample, the right of the image – "space" sample*

Images from three independent locations of the samples were taken for reproducibility purposes. From the applied roughness analysis statistical values according to the relative heights of each pixel in a particular AFM image are calculated. The roughness analysis gives the value $R_a$, which is an arithmetic average of the absolute values $Z_i$ of the surface height deviations measured from the mean plane, i.e.

1) $$R_a = \frac{1}{N}\sum_{i=1}^{N}|Z_i|$$

while the image $R_q$ is the root mean square average of height deviations taken from the mean image data plane, expressed as

2) $$R_q = \sqrt{\frac{1}{N}\sum_{i=1}^{N} Z_i^2}$$

The obtained values for the roughness of the two types of samples are shown in Table 1 and Fig. 3.

*Table 1. Values of surface Roughness for the "reference" and "space" sample*

| Surface Roughness (*size scanned area*) | Reference sample R-1 | | | Reference sample R-2 | | | Reference sample R-3 | | | Space sample S-1 | | | Space sample S-2 | | | Space sample S-3 | | |
|---|---|---|---|---|---|---|---|---|---|---|---|---|---|---|---|---|---|---|
| | center [nm] | periphery [nm] | edge [nm] | center [nm] | periphery [nm] | edge [nm] | center [nm] | periphery [nm] | edge [nm] | center [nm] | periphery [nm] | edge [nm] | center [nm] | periphery [nm] | edge [nm] | center [nm] | periphery [nm] | edge [nm] |
| $R_q$ (*5μm x 5μm*) | 16.5 | 12.3 | 16.1 | 15.4 | 15.2 | 24.7 | 8.95 | 8.32 | 8.98 | 13.4 | 7.35 | 9.46 | 9.13 | 10.3 | 16.9 | 10.4 | 11.1 | 14.0 |
| $R_a$ (*5μm x 5μm*) | 12.0 | 8.84 | 12.3 | 11.9 | 11.1 | 16.2 | 5.87 | 5.76 | 5.65 | 10.0 | 5.53 | 7.34 | 7.22 | 8.16 | 12.5 | 7.95 | 8.78 | 11.2 |
| $R_{max}$ (*5μm x 5μm*) | 167 | 178 | 210 | 108.8 | 151 | 248 | 273 | 193 | 239 | 166 | 76.8 | 93.1 | 77.4 | 94.3 | 124 | 90.0 | 96.2 | 118 |

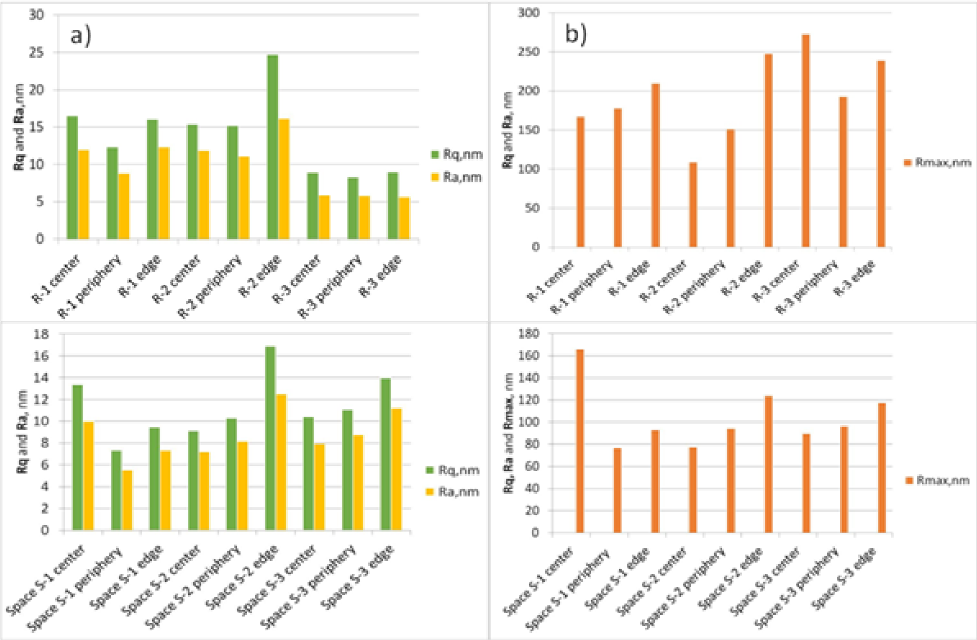


*Fig. 3. Analysis of the roughness of AFM images 5 μm for the aluminium alloy 7075 strengthened with nanoparticles of diamond powder and Tungsten: $R_q$ and $R_a$ for "reference" sample and "space" sample (a) and $R_{max}$ for "reference" sample and "space" sample (b)*

From the analysis of the surface roughness performed for the "reference" and "space" samples shown in Fig. 3, as well as in Table 1, it was found that the "reference" sample R-1 has a rougher surface $R_q$ compared to the "space" sample S-1 at three points of analysis. The difference in roughness of R-1 compared to S-1 on the measured surfaces is 3.1 nm in the centre and respectively 6.64 nm higher roughness at the end of the image. The "reference" sample R-2 has a rougher surface $R_q$ compared to "space" sample S-2 at the three analysis points. The difference in roughness for R-2 compared to S-2 on the measured surfaces is 6.27 nm in the centre and respectively 7.8 nm higher roughness at the end of the image. For "reference" sample R-3 were found, that the values for $R_q$ to be approximately comparable to those values for sample S-3. The difference in roughness for S-3 compared to R-3 on the measured surfaces is not large and is in the order of 1.45 nm in the centre and respectively 5.02 nm higher roughness at the end of the sample.

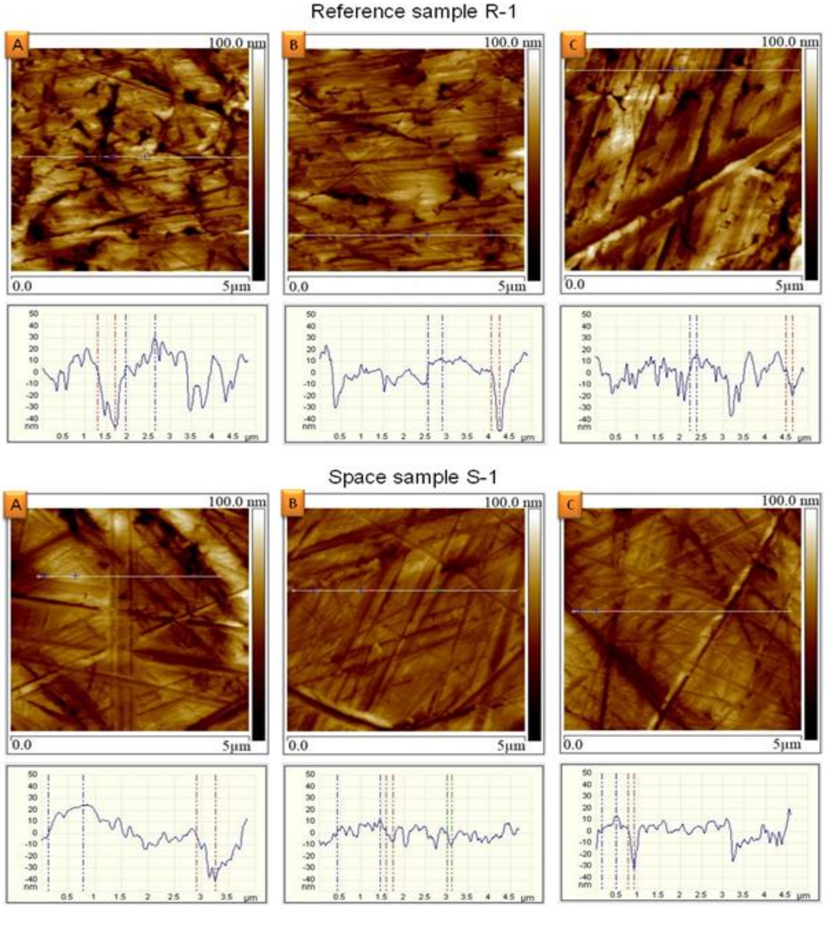


*Fig. 4. Section analysis of the surface of "reference" sample and "space" sample in the centre, periphery and end*

From the measured roughness of the "reference" and "space" samples, the values $R_{max}$ was determined for the two types of samples at three points of analysis — centre, periphery and end. For the "reference" samples R-1 and R-2, the $R_{max}$ values were found to increase from the centre to the periphery and the end, while for the "reference" sample R-3 these values decrease. For the "space" samples S-1, S-2 and S-3, it was found that the values of $R_{max}$ increases from the centre to the periphery and the end.

From the section analysis of the "reference" and "space" samples presented in Fig. 4, it was found that in the "reference" samples microcracks with a diameter of 0.5 microns in the centre, periphery and at the end of the analysed surface were observed compared to the "space" samples.

The differences in the roughness between the "reference" R-1, R-2 and R-3 and the "space" S-1, S-2 and S-3 samples is explained by the environment conditions at which the "reference" material was stored, the terrestrial conditions temperature, atmospheric pressure, radiation, etc.

## Conclusion

From the measurement by an atomic force microscope of "reference" and "space" samples of aluminium alloy 7075 was found that:

1. The "reference" samples R-1, R-2 and R-3 have a rougher surface compared to the surface of the "space" samples S-1, S-2 and S-3 at three points of analysis — in the centre, periphery and the end.
2. For the "space" samples S-2 and S-3, it was found that the values of $R_{max}$ and the values of $R_q$ increases from the centre to the periphery and the end.
3. From the roughness of the sectional analysis for the "reference" R-1 sample it is established presence of microcracks at three points of analysis due to storage conditions

**Acknowledgement:** This work is financially supported by the Bulgarian National Science Fund under the project ДМ17/1.

## References

1. Fridlander, I. N. Memoirs on the creation of aerospace and nuclear technology from aluminum alloys. Moscow, Nauka, 2005, 275 p. (in Russian)
2. Fridlander, I. N. Aluminum alloys in aerospace and nuclear engineering. *Bulletin of the Russian Academy of Sciences*, (2004), 74, 12, 1076–1081 (in Russian).
3. Abidov, A. L. Composite materials in the construction of aircraft. Moscow, Engineering, 1975, 272 p. (in Russian).
4. Friedlander, I. N. High-strength deformable aluminum alloys. — M. Oborongiz, 1960, 291 p. (in Russian).

5. Friedlander, I. N., O. G. Senatorova, E. A. Tkachenko. High-strength alloys of the Al–Zn–Mg–Cu system. *Mechanical Engineering, Encyclopedia 3*. Colored metals and alloys, Moscow, Engineering, 2001, pp. 94–128 (in Russian).
6. Miteva, A. On the microstructure and strengthening of aluminium and aluminium alloys. *Tribological Journal BULTRIB*, Vol. III, 2013, pp. 367–370.
7. BG No 49267 (in Bulgarian). https://patents.google.com/patent/BG49267A3/en?oq=BG+%E2%84%96+49267
8. Klimov, S., V. Grushin, K. Balajthy, *et al.* Studying of space weather electromagnetic parameters of ionosphere in "Obstanovka 1-step" experiment on the Russian segment of the ISS. *Space Engineering and Technology*, 2021, 1, 32, pp. 20–41 (in Russian).
9. Bouzekova-Penkova, A., R. Nedkov, G. Stanev, *et al.* Technological experiment "Environment" on board the International Space Station. *J. BAS*, 2017, 130, 5, pp. 22–26 (in Bulgarian).
10. Dachev, Ts., G. Horneck, D.-P. Häder, M. Schuster, M. Lebert. Expose-R cosmic radiation time profile. *International Journal of Astrobiology*, 2015, 14, 1, pp. 17–25.

## AFM АНАЛИЗ НА АЛУМИНИЕВА СПЛАВ 7075

**А. Бузекова-Пенкова, С. Симеонова**

### Резюме

В тази статия представяме резултатите от Атомно-силова микроскопия (AFM) за охарактеризиране морфологията на повърхността на нов тип композит на базата на високоякостна алуминиева сплав 7075 уякчена с наночастици от диамантен прах и Волфрам, съхранявана за 28 месеца при различни условия. Една серия от образците са съхранявани на Земята при стайна температура, а втората серия образци са били монтирани от външната страна на Международната космическа станция.

Bulgarian Academy of Sciences. Space Research and Technology Institute.
Aerospace Research in Bulgaria. 34, 2022, Sofia

DOI: https://doi.org/10.3897/arb.v34.e15

# SOME AEROSPACE APPLICATIONS OF 7075 (B95) ALUMINIUM ALLOY

***Anna Bouzekova-Penkova, Adelina Miteva***

*Space Research and Technology Institute — Bulgarian Academy of Sciences*
*e-mail: a_bouzekova@space.bas.bg; ad.miteva@gmail.com*

***Keywords:*** *Aluminium alloys, Aluminium 7075 / B95 alloy, Aluminium 7xxxx alloys, Applications, Aerospace applications of 7075 (B95) alloy*

***Abstract***

*Nowadays, aluminium alloys are of growing interest to scientists and are widely used in aerospace and allied industries due to their inherent lightness, high strength to weight ratio, excellent thermal and electrical conductance, good reflectivity and low working cost. Among the conventional structural materials used in aerospace applications aluminium alloys are frontrunners. This is due to the ability of modern aluminium alloys to achieve unique combination of properties, through alloying and heat treatment, tailored to particular applications. Aluminium alloy 7075 (B95) is a high-strength alloy that works in extreme conditions and is used in modern construction of aircraft, spacecraft and satellites.*

*In this mini-review, we will briefly focus on some of the existing and growing applications of some 7xxx aluminium alloys, in particular 7075 (B95), in the aerospace industry. Possible options for continuing work in this area are considered, and some Bulgarian developments are presented.*

## Introduction

The application of aluminium in our life began about 100 years ago. But today aluminium, aluminium (Al) alloys and aluminium-based (Al-based) composites are the most important structural engineering materials and are widely used in aerospace and terrestrial industries, because of their inherent lightness, high strength-to-weight ratio, excellent thermal and electrical conductivity, good reflectivity, low operating costs and to a certain extent good corrosion resistance [1–16]. The use of aluminium alloys in these areas leads to a decrease in the mass of the structure, which leads to an increase in the payload and a greater mass of fuel and, consequently, to an increase in the service life of the spacecraft. The application of lighter aluminium alloys and Al-based composites, instead of the (dominating since 1920s) special steels, reduces the weight of the vehicles and hence fuel and energy savings, reducing exhaust emissions, and improving safety. Among the common structural materials used in aerospace, aircraft, transport and related industries aluminium alloys are in the lead. One of the proofs of this is the huge amount of available literature on aluminium alloys.

The purpose of this mini-review is to define some general concepts of Al alloys and Al-based composites related to the aerospace industry. The most important Al alloys and some of their applications are mentioned, with emphasis on Al alloys 7xxx, 7075 (B95) in the aerospace sector, and finally some of the Bulgarian contributions to the investigation of Al 7075 (B95) alloy are mentioned.

**Al alloys for aerospace and aircraft structures – some history and classification**

The aerospace industry covers the production of aircraft and spacecraft; includes the production of both non-space articles (passenger and military aircraft, helicopters, gliders, balloons, etc.) and space articles (including spacecraft, spacecraft launch vehicles, satellites, planetary probes, orbital stations and shuttles); also includes the manufacture of their parts and accessories used in civil and military applications, as well as in terrestrial space complexes, such as aircraft instruments, navigation and control systems, ignition parts and other electrical parts for internal combustion engines, space radio and telemetry systems and others [17].

The aerospace industry has a long history of using aluminium and aluminium alloys in many applications both civil and military. It is of prime importance to lower the weight of air- and spacecraft, as well as projectiles, to aid in decreasing emissions and increasing fuel efficiency. These changes will result in a lower operational cost as well. Aluminium is an ideal material for use in these applications.

In this article we do not present data on the structure of aluminium and its alloys, as these data are presented in virtually all textbooks, reference books and monographs on metals and materials. Pure aluminium is used little (for electrical conductors and for domestic products) or is not used, due to its insufficient strength and heat resistance. For serious structural/construction use it has to be strengthened by alloying. The chief characteristic of Al and Al-based alloys is their low density, which is why they are so valuable for aerospace and terrestrial industries.

As for the classification and designation systems of Al alloys, it should be noted that currently there is no universal one. Different classifications and designation systems are used in different countries, as well as in Bulgaria [1, 2, 11]. According to Bulgarian State Standard, Al alloys are conditionally denoted by chemical signs of the base metal and the components of the alloy and by the numerical values of the respective composition. But despite the different designation systems for Al alloys, it is not difficult for a specialist to understand what kind of alloy it is (there is enough literature on the subject). To improve the physical, mechanical and technological properties (to obtain Al alloys with different and desired properties), aluminium is alloyed with various elements (copper, magnesium, manganese, silicon, zinc, lithium). In addition to these six basic ones, about 20 other alloying additives are known. Today, the industry mainly uses about 55 grades of aluminium alloys.

The various types of aluminium may be divided into two general classes: (1) casting alloys (those suitable for casting in sand, permanent mould, or die castings) and (2) wrought alloys (those which may be shaped by rolling, drawing, or forging). From these two, the wrought alloys are the most widely used in aircraft and spacecraft construction, being used for stringers, bulkheads, skin, rivets, and extruded sections. The most recently developed of the Al-alloys are Al-Li alloys. Lithium is presented in several Al-alloys, but since it is not necessarily the main alloying element, forged Li-containing Al-alloys can be found in different groups of alloys: 1xxx, 2xxx and finally 8xxx, which are the alloys of this last group, with higher Li concentrations.

The first appearance of Al in aerospace was in 1901, when Wilhelm Kreiss used aluminium for the floats of his triplane, in which he failed to get into the air from a tank in Austria. But the first successful aviation appearance of Al was in the engine of the world's first successfully powered aircraft (operated by the Wright brothers in 1903), whose cylinder block and crankcase were manufactured by Al [2–4].

The development of stronger Al alloys, suitable as structural metals, was accelerated in 1903 by the German metallurgist Alfred Wilm, who discovered age hardening, a phenomenon in which some aluminium alloys, although they remain weak immediately after heat treatment (quenching), slowly harden when left for several days at room temperature. Further work led to the creation of stronger Al alloys, and in 1909 he produced an alloy with properties almost as good as the low-carbon steel, Al-CuMgMn, which he called "duralumin" (from the name of the city Duren — the city where its industrial production was started in 1909). This was the beginning of what we now call the 2xxx series of Al alloys.

About 1920 a second kind of age-hardening alloy emerged, namely the Al-Mg-Si type. This alloy group (the present day 6xxx series) has a tensile strength in its strongest version of some 300 $N/mm^2$, and is thus generally weaker than the 2xxx series. But it has other characteristics that have since led it to become aluminium "low carbon steel".

Then Al-Mg alloys emerged, our current 5xxx series. These are non-heat treatable roll-hardened alloys developed in the UK in the late 1920s and marketed under the name "Birmabright". These alloys have very good corrosion resistance and were successfully used in shipbuilding in the 1930s.

In the 30s of the last century, both of the strongest types of alloys appeared, both of which are heat-treatable alloys and react to artificial aging, i.e. increased aging at elevated temperatures. The first, another alloy of the 2xxx series, was the development of Wilm's duralumin and was named "superdural". It has a tensile strength of over 450 N/mm$^2$ when fully heat treated and high yield strength. The second appeared in 1936, turned out to be even stronger. It was a new type of Al-Zn Mg alloy, the first in today's 7xxx series, with a tensile strength of over 500 N/mm$^2$ and still the strongest form of aluminium commonly used.

By 1939, all of today's major Al alloy series had arrived this way, except for one, namely the weldable 7xxx series alloy. This series was actively developing after the Second World War [4–6, 8–11].

The application that put aluminium on the map as a structural metal was its use in airplanes, first in airships and later in airplanes [4–6]. In 1919, the first duralumin aircraft appeared. A huge step forward for aluminium was its use for military aircraft during the Second World War. But the ubiquitous distribution and use of aluminium in the world, and not only in military aviation, began after the Second World War.

The main areas of application of aluminium and its alloys are aviation, space technology, electrical engineering, and construction. Aluminium alloys make up from 2/3 to 3/4 of the dry weight of the aircraft and from 1/10 to 1/2 of the dry weight of the missiles.

In recent decades there has been a considerable effort to develop Al alloys, possessing improved and/or new desirable properties for new aerospace applications. The structure of these alloys, and therefore their properties, can be modified by changing the concentration of the main components or adding new ones [18, 19], or by application of new/modified technologies [20]. For example, rapidly solidified nano-microcrystalline Al alloys are designed to replace titanium alloys for high temperature applications [20].

The Space Age began October 4, 1957 with the launch of *Sputnik-1* by the USSR. This satellite operated until January 3, 1958. It consisted of an aluminium sphere with a 58 centimetre diameter, two radio transmitters, four antenna and total weight of 83.6 kg.

Today, space systems are available in all sizes and shapes; they work in orbits near the Earth, in geosynchronous orbit and around other planets in our solar system. Some space systems explore the outer limits of the solar system itself. Some large systems, such as the International Space Station (ISS), are the product of multiple launches. And in all these systems, the most common material for aircraft construction is aluminium. Aluminium is rightly called a winged metal. Here is one of many examples: the structural skins of all the modules of the International Space Station are constructed from either AA7075 or AA2219. These have been delivered by US, European and Japanese companies (Source: European Space Agency) [6].

**Examples of some Al alloy applications used in aerospace**

In the literature there are sufficient data for Al alloy applications. The famous dural or duraluminium (it is most often denoted by2024 or sometimes by 2017, or by D16) is an alloy of Al, the main alloying metals of which are copper (4.4% of mass), magnesium (1.5%) and manganese (0.5%). Dural is durable, high-strength and lightweight, resistant to corrosion, deformation and environmental influences, aesthetic and easy to maintain, therefore it is one of the most demanded alloys in modern industry. Light alloy duraluminium is used in various fields such as: aviation, space, technology, electrical engineering, shipbuilding, construction, motor transport, at home. The first application of duraluminium is the manufacture of the skeleton of airships of rigid construction. The new alloy has become one of the main structural materials in the aircraft industry, space technology, nuclear engineering, defence industry, and, of course, for the production of high-speed trains. Despite competition from other materials, Al alloys still make up > 70% of structure of modern commercial airliner.

Design requirements for application of aluminium alloys in aerospace mainly include careful balance of material properties. Components must be lightweight, damage tolerant, durable (corrosion resistant) and cost effective. More specifically, the alloy property requirements vary depending on the application. Severe operating conditions in air and space often limit the possibility of using some of these Al alloys directly and for a long time. These are many harsh factors – gravity, vacuum, neutral particles, plasma, micrometeorites, space debris, radiation etc. in our space environment. Therefore, in order to reduce the impact of unfavourable environmental and space conditions, for successful use in the space industry and transport, aluminium alloys and their products require special surface treatment by coating. Nowadays there is a tremendous interest in extremely stable in space environment Al alloys and Al alloys coatings materials. The evidence is the space programs and enormous space budgets, which almost every country has. Therefore, in order to reduce the impact of severe space conditions and prevent from them, we must study and know how outer space conditions influence the properties of Al alloys together with their coatings.

Typical materials used for the fuselage and wings of civil aircraft are:

• 2000 series aluminium alloys based on the aluminium – copper system;

• 7000 series aluminium alloys based on the aluminium – zinc – copper – magnesium system;

• aluminium – lithium alloys.

The 2xxx series (Al-Cu alloys) are heat-treatable, and possess in individual alloys good combinations of high strength (especially at elevated temperatures), toughness, and in specific cases, weldability; they are not resistant to atmospheric corrosion, and so are usually painted or clad in such exposures. The higher strength 2xxx alloys are primarily used for aircraft (2024) and truck body (2014) applications; these are usually used in bolted or riveted construction. Specific members of the series (e.g. 2219 and 2048) are readily welded, and so are used for aerospace applications where that is the preferred joining method. Booster rockets of the Space Shuttle are 2xxx alloys, originally 2219 and 2419, now sometimes Al-Li "Weldalite" alloy 2195 [4].

Heat treatment plays an important role in aircraft and spacecraft industry. Different heat treatment manufacturing processes are employed in the production of Al alloys in order to change and improve certain properties. For example (see Table 1), you might use heat treatment to make alloy stronger, harder, more durable, or more ductile, depending on what the material needs in order to perform properly.

*Table 1. Heat treatment designations for aluminium and aluminium alloys*

| Term | Description |
|---|---|
| T1 | Cooled from an elevated temperature shaping process and naturally aged |
| T2 | Cooled from an elevated temperature shaping process cold worked and naturally aged |
| T3 | Solution heat-treated cold worked and naturally aged to a substantially |
| T4 | Solution heat-treated and naturally aged to a substantially stable condition |
| T5 | Cooled from an elevated temperature shaping process and then artificially aged |
| T6 | Solution heat-treated and then artificially aged |
| T7 | Solution heat-treated and overaged/stabilised |

The 7xxx (Al-Zn alloys) alloys are heat treatable and among the Al-Zn-Mg-Cu versions provide the highest strengths of all Al alloys. There are several alloys in the series that are produced especially for their high toughness, notably 7150 and 7475, both with controlled impurity level to maximize the combination of strength and fracture toughness. The widest application of the 7xxx alloys is in the aircraft industry. The most common aluminium alloy used in aerospace is 7075, which has zinc as the primary alloying element. It is strong, with strength comparable to many steels, and has good fatigue strength and average machinability, but has less resistance to corrosion than many other aluminium alloys. The atmospheric corrosion resistance of the 7xxx alloys is not high, so in such service they are usually coated or, for sheet and plate, used in an alclad version. The use of special tempers, such as the T73-types, is required in place of T6-type tempers whenever stress corrosion cracking (SCC) may be a problem.

All Al alloys of the Al-Zn-Mg-Cu system (7xxx) exhibit the highest strength. Table 2 shows some mechanical properties of selected aluminium alloys.

The following alloys have the highest tensile strength values that aluminium alloys can have: 7075, 7079 and 7178. In many countries around the world, metallurgical plants produce these alloys due to their properties and high demand.

There are no satellites or spaceships that do not use at least one element made of some aluminium alloy. We will give an example with Ten-Koh (satellite from the Kyushu Institute of Technology in Japan — https://www.n2yo.com/satellite/?s = 43677), which is a 23.5 kg, low-cost satellite developed to conduct space environmental effects research in low-Earth orbit (LEO). The satellite carries a double Langmuir probe, CMOS-based particle detectors and a Liulin spectrometer (designed and developed in Bulgaria, at SRTI — BAS) as main payloads. The main structure of Ten-Koh is composed of a CFRP composite shell with a rigid internal load-bearing structure made of aluminium alloy (Al 6061-T6). The DLP (double Langmuir probe) system is composed of two spherical, 10 μm gold-plated electrodes, made of solid aluminium. Control electronics circuits of DLP are housed in the internal structure of the satellite shielded in a 3 mm-thick aluminium box.

*Table 2. Mechanical properties of selected aluminium alloys*

| Alloy | Temper | Proof Stress 0.20% (MPa) | Tensile Strength (MPa) | Shear Strength (MPa) | Hardness Brinell HB | Hardness Vickers HV |
|---|---|---|---|---|---|---|
| AA2011 | 0 | 35 | 80 | 50 | 21 | 20 |
| | T4 | 270 | 350 | 210 | 90 | 95 |
| | T6 | 300 | 395 | 235 | 110 | 115 |
| | T8 | 315 | 420 | 250 | 115 | 120 |
| AA6082 | 0 | 60 | 130 | 85 | 35 | 35 |
| | T5 | 275 | 325 | 195 | 90 | 95 |
| | T6 | 310 | 340 | 210 | 95 | 100 |
| AA7075 | 0 | 105 | 225 | 150 | 60 | 65 |
| | T6 | 505 | 570 | 350 | 150 | 160 |
| | T7 | 435 | 505 | 305 | 140 | 150 |
| AA7075-R | | | 645 | | | |
| AA7075-S | | | 167 | | | |

### 7075 or B95 aluminium alloy

Al alloy 7075 — Al-Zn-Mg-Cu-Cr alloy — has the widest and longest use of all alloys of the 7xxx series. It was introduced in Japan in 1943, was a big secret and was used to make Japanese military aircraft. Alloy 7075 was originally used for parts and components with a thin cross section, mainly in the form of sheets and extruded profiles. For these products, the quenching rate is usually very high and tensile stresses do not occur in the short transverse direction. Therefore, stress corrosion cracking is not is a problem for such materials with a high-strength T6 state.

Al alloy B95 alloy was developed independently in the former USSR in the middle of the last century for the production of the Tu-16 strategic bomber and other aviation equipment.

Foreign companies produce Al alloy 7075 or B95 under different names, but all are analogues:

- USA – AA7075 (AA = American Association);
- Germany – 3.4365;
- Japan – 7075;
- European Union – ENAW AlZnMgCu;
- former USSR and Russian Federation – B95.

Alloy types 7075/B95 includes:

- zinc — 5÷7 %;
- magnesium – 0.2÷0.6 %;
- copper – 1.4÷2 % and some others.

Usually, Al alloys 7075 and B95 are considered analogous and identical. The same applies to alloys 2024 and D16. They are very similar in composition and properties.

Aluminium alloys used in aircraft construction around the world have approximately the same composition and characteristics (Table 3). Thus, practically the same alloys were used for passenger and transport aircraft in the USA and Russia: in the USA — for the bottom of the wing and fuselage — alloys of the 2xxx series; for the top — alloys of the 7xxx series. In Russia, for the bottom of the wing — alloys D16, 1161, 1163, for the top, alloy B95pch (B95пч); for the fuselage — alloys D16, 1163, D19, 1420.

*Table 3. Chemical composition (weight %) of some American and Russian Al alloys for aviation equipment*

| **alloy grade** | **Zn** | **Mg** | **Cu** | **Mn** | **Cr** | **Fe** | **Si** | **Ti** | **Ni** | **other impurities** |
|---|---|---|---|---|---|---|---|---|---|---|
| 2024 | - | 1.5 | 4.4 | 0.6 | - | 0.5 | 0.5 | - | - | - |
| D16 | 0.3 | 1.5 | 4.35 | 0.6 | - | 0.5 | 0.5 | 0.1 | 0.1 | 0.1 |
| 7075 | 5.6 | 2.5 | 1.6 | - | 0.23 | 0.4 | 0.4 | - | - | - |
| B95 | 6.0 | 2.3 | 1.7 | 0.4 | 0.17 | 0.5 | 0.5 | - | 0.1 | 0.1 |

However, when alloy 7075 is used in products and parts of large size and thickness, it becomes clear that such products and parts, thermally hardened to T6 states, often do not meet the specified requirements. Products obtained by large machining from large forgings, extruded profiles or slabs were then subjected to prolonged tensile stresses in unfavourable orientation. Under such operating conditions, stress corrosion cracking (stress corrosion) occurred quite often.

The solution to this problem was the introduction of the T73 condition for thick and massive products from alloy 7075. The heat treatment that is used to obtain this condition requires a two-stage artificial aging. The second stage is performed at a higher temperature than that used to reach the T6 state. This additional heat treatment reduces the strength to a level below that which the 7075 alloy reaches in the T6 temper.

The T7 state is achieved by overaging, which means that the aging of the alloy continues after reaching the peak of its hardness and strength, in contrast to the T6 states. Numerous experiments and long-term operating experience have confirmed that alloy 7075-T73 has significantly higher stress corrosion resistance compared to alloy 7075-T6. Interestingly, the wheels of the famous Curiosity rover are made of 7075-T7351 alloy by machining from a one-piece forged ring. Hence new alloys with improved properties for use in the aerospace industry were obtained from the Al 7075 alloy by changing the composition and/or applying a special heat treatment (tempering).

B95 (Al 7075 alloy) alloy is used for the manufacture of power components for civil aviation and military equipment, in particular, frames, spars and other parts and assemblies operating under constant compression pressure. The keels of some large aircraft are made of this alloy. B95 is used to produce various blanks and semi-finished products — profiles, bars, etc. B95 is used for the production of rivets and related wires of various sizes.

Fuselage/pressure cabin stringers and frames, upper wing stringers, Airbus A380 floor, beams and seat rails, Upper wing covers, Frames, brackets, stringers, Upper and lower wings skins, bulkheads, door rails — are some of the main applications of Al 7075 alloy. Main features of Al 7075 alloy are: the highest strength; the highest tensile strengths that aluminium alloys can have; a fairly high corrosion resistance, controlled by proper heat treatment and the addition of some alloying materials. Main products and status of Al 7075 alloy are: T6 T73 T76 sheet plate, T651 T7651 T7351 thick plate, T6 T73 T7352 casting and T6511 T3511 extrusion [8]. Many new and superior alloys from the 7xxx series are based on the 7075 (B95) grade [2–6, 8–11]. For example, "Boeing" manufactures the upper wing of the "B777" airplane from 7075-T77 alloy plates, which is an exact copy of the B96-C3 alloy.

In Table 4 are listed several conventional wrought Al 7075 alloys used for commercial aircraft parts.

Conventional (non-lithium-containing) aerospace alloys always require some form of corrosion protection. This can be cladding with (nearly) pure aluminium and anodizing for sheet alloys; anodizing or ion vapour deposition for other types of products; and primer and paint systems [3].

The surface condition has a significant effect on the durability of high strength aluminium alloys. Severe operating conditions in air and space often limit the possibility of using some of these Al alloys directly and for a long time. Therefore, in order to reduce the impact of unfavourable environmental and space conditions, for successful use in the space industry and transport, aluminium alloys and their products require special surface treatment by coating. Nowadays there is a tremendous interest in extremely stable in space environment Al alloys coatings materials [2, 7].

*Table 4. Al 7075 alloys used for commercial aircraft parts*

| **Alloy** | **Temper** | **Application** |
|---|---|---|
| 7075 | T6 | Fuselage skin Empennage (tail),<br>Wing lower panels,<br>Wing lower stringers,<br>Wing upper skin,<br>Wing upper stringers |
| 7075 | T6 and T73 | Fuselage stringers |
| 7075 | T6, T73 and T76 | Aircraft structures |

More than a decade composites have started to be used more widely in large commercial jet airliners for the fuselage, wing as well as other structural components in place of aluminium alloys due their high specific properties, reduced weight, fatigue performance and corrosion resistance. Composite materials based on aluminium, reinforced with fibres of boron, charcoal, SiC, etc. are promising for use in aircraft construction.

In the composite materials (CM) Al alloys + SiC, Al alloys from the systems Al-Cu-Mg, Al-Mg-Si, Al-Cu and others are used as a matrix material. As reinforcing filler, both whiskers and SiC powders with a dispersion of 1 to 20 microns are used. The volume fraction of the reinforcing filler can vary from 5 to 40%. The technology provides a high degree of uniformity of SiC distribution in the matrix material.

A promising material for the cladding of aircraft is a laminated CM, consisting of alternating thin aluminium sheets and interlayers of adhesive prepreg with glass fibres — SIAL (S — glass, A — aluminium) — an analogue of GLARE. SIAL is distinguished by high specific strength and rigidity, satisfactory corrosion resistance, good workability, high resistance to fatigue crack growth [2].

In our Space Materials Science department at SRTI-BAS was synthesized a new type of composite based on aluminium Al-based alloy, namely aluminium alloy 7075 (B95) strengthened with nanoparticles of nanodiamond powder and tungsten (W). Table 5 shows the composition of the thus obtained Al alloy. Several samples of the so modified, with nanodiamonds and W, aluminium alloy 7075 (AA7075+W+ND), were a part of the DP-PM module of the international space experiment “Obstanovka” (carried out in the Russian sector of the International Space Station). The aim of this international space experiment was to study the influence of the space environment on the properties of the new composite (AA7075 + W + ND), after a stay of 28 months in outer space. After this exposure to space, the samples were returned to Earth (space samples AA7075-S) for research and compared with samples of the same material stored in terrestrial conditions (AA7075-R) for the same period. Today, a comparative analysis of the properties of the samples (one of the samples was stored in terrestrial conditions (reference sample) and the other sample was installed on the outside of the International Space Station for the same period (space sample)) has already been done [12–14]. The results obtained will be repeated to see if the data has changed over time.

*Table 5. Chemical composition of AA 7075 (in wt. %)*

| Al | Cu | Mg | Zn | Fe | Si | Mn | Cr | Ti | UDDP + W |
|---|---|---|---|---|---|---|---|---|---|
| 86.2 ÷ 91.5 | 1.4 ÷ 2.0 | 1.8 ÷ 2.8 | 5.0 ÷ 7.0 | 0.0 ÷ 0.5 | 0.0 ÷ 0.5 | 0.2 ÷ 0.6 | 0.10 ÷ 0.25 | 0.00 ÷ 0.05 | 0.1 |

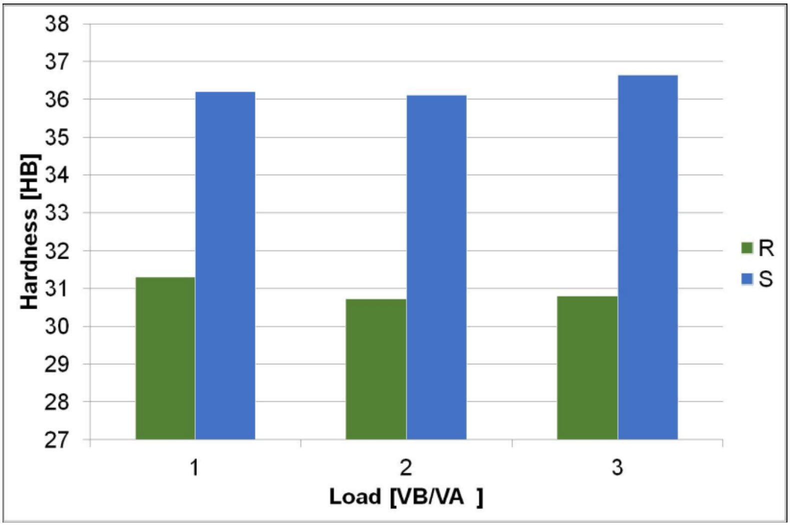


*Fig. 2. Leeb hardness measurement results for three “reference” (R) and three “space” samples (S)*

Fig. 2 shows the average hardness values of three of the two types of samples. Seven measurements were made for each sample. Hardness was measured with a universal digital hardness tester according to Leeb/Al-150A. This is necessary because the studied “space” samples are very small.

The obtained average hardness value for the reference samples is: R1-31.3; R2-30.72 HB and R3-30.8 HB. The same for space samples is: S1-36.2HB; S2-36.11 HB and S3-36.64 HB (Fig. 2). The hardness of space samples is greater than that of reference samples. Based on the results obtained, it can be concluded that the introduced radiation defects and temperature cycles within ~300 °C, leading to the refinement of the material structure on the surface and periphery, are the reason for the higher hardness of the space sample S-36.31 HB compared to the reference R-30.94 HB (see also Table 2).

In our Space Materials Science department at SRTI-BAS we also work on the production of new FGM (functionally graded materials) based on aluminium with high hardness, high density and high thermal stability for different applications. Such materials will be of significant interest for their application in space technology and in particular for aerospace instruments [15, 16].

**Future of aluminium in aerospace industry and conclusions**

The rapid development of the aviation industry contributes to the progress of new materials. Aluminium alloys and aluminium-based composites are very important structural engineering materials widely employed in the aerospace industry. The production and widespread use of Al alloys continues to increase, largely due to the excellent combination of their properties.

7xxx series aluminium alloys (Al 7xxx alloys) are widely used in bearing components, such as aircraft frame, spars and stringers, for their high specific strength, high specific stiffness, high toughness, excellent processing, and welding performance. Therefore, Al 7xxx alloys are the most important structural materials in aviation and aerospace.

Due to the broad and rapidly developing field of Al 7xxx alloys, all their properties and aerospace applications cannot be encompassed in this paper. Nevertheless, here are some of the observations of the authors based on the published research and their own analysis of the subject.

The next generation of Al 7xxx alloys should be higher strength, higher toughness, higher damage tolerance, higher hardenability, and better corrosion resistance. It is urgent requirements to develop or invent new heat treatment regime.

In order for aluminium alloys to remain attractive in the airframe construction and compete with and/or be compatible with currently used polymer composites and titanium alloys, research activities on the improvement of structural performance, weight and cost reductions are needed.

There have been important recent advances in aluminium aircraft alloys that can effectively compete with modern composite materials. It is believed that developments of advanced hybrid materials, like fibre metal laminates could provide additional opportunities for aluminium alloys and new material options for the airframe industry.

As the main part of high strength aluminium alloy, Al 7xxx alloys have been successfully used as the main materials of aircraft structural components. With the application of titanium alloys and composite materials in the fuselage design, the proportion of aluminium alloy has been reduced. In order for aluminium alloys to remain attractive in the airframe construction, research should be necessarily carried out in terms of structural properties, weight reduction, and cost reduction. Therefore, current studies for Al 7xxx alloys contain improvements on mechanical properties; reduction of manufacturing, maintenance, and repair costs; prevention of corrosion and fatigue; and ability to perform reliably throughout its service life.

In recent years, Al 7xxx alloys have successfully improved static strength, fracture toughness, fatigue and corrosion resistance through composition design and control of chemical composition, as well as via the exploitation of more efficient heat treatment methods. It can be seen from this review that the main improvement of Al 7xxx alloys is to optimize the solute content and solute ratio to achieve better balance for the performances. Therefore, for the design of the alloy, the content of Zn will be increased to more than 10%, while the content of Mg and Cu will be reduced. Also, the content of impurity elements such as Fe and Si will be even lower. On the other hand, the addition of trace transition elements like Zr and Er will be more reasonable.

The attractiveness of aluminium is that it is a relatively low cost, lightweight metal that can be heat treated to fairly high-strength levels; and it is one of the most easily fabricated of the high-performance materials, which usually correlates directly with lower costs. Disadvantages of aluminium alloys include a low modulus of elasticity, rather low elevated-temperature capability (≤ 130 °C), and in high-strength alloys the susceptibility to corrosion [1].

Improvements in aluminium manufacturing technology include high-speed machining and friction stir welding (FSR):

• Although higher metal removal rates are an immediate benefit of high-speed machining, an additional cost saving is the ability to machine extremely thin walls and webs. This allows the design of weight competitive high-speed machined assemblies, in which sheet metal parts that were formally assembled with mechanical fasteners can now be machined from a single or several blocks of aluminium plate.

• FSR is a solid state joining process that has the ability to weld the 2xxx and 7xxx alloys, which are not suited to conventional fusion welding. FSR also allows the design of weight competitive assemblies with a minimum number of mechanical fasteners.

There are still more to be done in terms of research to improve the performance of manufacturing processes of Al 7xxx alloys in order to make them more cost effective. Emphasis should be placed on modelling for the design of new Al alloys and coatings that have specific and desirable properties.

There is no doubt that high-strength aluminium alloys are, and will remain, important and indispensable airframe materials in the aerospace industry.

## References


1. Luts, A. R., A. A. Suslina. *Aluminium and Its Alloys*. Samara, Samara state tech. un, 2013, p. 81 (in Russian).
2. Beletskiy, V. M., G. A. Krivov. *Aluminium alloys (composition, properties, technology, application): reference book*. Kiev: Komintech, 2005, p. 365 (in Russian).
3. Rambabu, P., N. Eswara Prasad, V. Kutumbarao, R. Wanhill, J. H. Chapter 2. Aluminium Alloys for Aerospace Applications. Springer Science+Business Media Singapore, N. Eswara Prasad and R. J. H. Wanhill (eds.), Aerospace Materials and Material Technologies, Indian Institute of Metals Series, 2017, p. 595, DOI: 10.1007/978-981-10-2134-3_2.
4. Dwight, J. *Aluminium design and construction*. CRC Press, 1999, p. 301, ISBN 0-419-15710-7 (Print Edition).
5. Weisshaar, T. A. *Aerospace Structures-an Introduction to Fundamental Problems*. Purdue University, USA, 2011, 197 p.
6. Dong, H. (Ed.). *Surface engineering of light alloys: Aluminium, magnesium and titanium alloys*. Cambridge, Woodhead Publishing Limited, 2010, 680 p.
7. Karaguiozova, Z., A. Miteva, A. Ciski, G. Cieślak. Some aerospace applications of aluminium alloys. *Proceedings SES 2017*, 2017, 327–332, ISSN: 1313-3888.
8. Zhou, B., B. Liu, S. Zhang. The Advancement of 7XXX Series Aluminium Alloys for Aircraft Structures: A Review. *Metals*, 2021, 11(5), 718. DOI: https://doi.org/10.3390/met11050718.
9. Gialanella, S., A. Malandruccolo. *Aerospace alloys*. Springer, 2020, 583 p.
10. Davis, J. R. (Ed.). Metals Handbook Desk Edition. Ohio, CRC Press, 1998, 2571 p.
11. Zhang, X., Y. Chen, J. Hu. Recent advances in the development of aerospace materials. *Progress in Aerospace Sciences*, 2018, 97, 22–34. DOI: https://doi.org/10.1016/j.paerosci.2018.01.001.
12. Bouzekova-Penkova, A. Investigations of the mechanical properties of a dispersion-reinforced aluminum alloy intended for outer space. *Proceedings SES 2013*, Sofia, Bulgaria, 2013, 492–496.
13. Bouzekova-Penkova, A., K. Grigorov, M. Datcheva, C. A. Cunha. Influence of the outer space on Nanohardness properties of Al- based alloy. *C. R. Acad. Bulg. Sci.*, 2016, 69 (10), 1351–1354.
14. Bouzekova-Penkova, A., M. Datcheva, R. Iankov. Mechanical properties of the enhanced with nanodiamond and tungsten strengthened aluminium alloy being exposed in the Outer space. *International Journal "NDT Days"*, 2019, II (4), pp. 396–401.
15. Bouzekova-Penkova, A., A. Miteva. Aluminium-Based Functionally Graded Materials. In Bulgarian Academy of Sciences, 2014, 10.

16. Miteva, A., A. Bouzekova-Penkova. Some aerospace applications of functionally graded materials. ibid. *Aerospace Research in Bulgaria*, 2021, 33, 79–86. DOI: https://doi.org/10.3897/arb.v33.e14.
17. Mardirossian, G. *Fundamentals of remote aerospace technology*, Chapters 3 and 4. NBU, Sofia, 2015. ISBN: 978-954-535-882-1 (In Bulgarian)
18. Vencl, A., I. Bobić, M. Stanković, *et al*. Influence of secondary phases in A356 MMCs on their mechanical properties at macro- and nanoscale. *J Braz. Soc. Mech. Sci. Eng.*, 2020, 42, 115. DOI: https://doi.org/10.1007/s40430-020-2197-6.
19. Dyakova, V., Y. Kostova. Influence of TiN and TiCN nanosized modifying compositions on the corrosion behaviour of AlSi7Mg alloy. *Engineering Sciences,* 2019, 3, 72–80, DOI: 10.7546/EngSci.LVI.19.03.07.
20. Lavernia, E. J., T. S. Srivatsan. The rapid solidification processing of materials: science, principles, technology, advances, and applications. *J. Mater. Sci.*, 2010, 45(2), pp. 287–325. DOI: https://doi.org/10.1007/s10853-009-3995-5.

## НЯКОИ АЕРОКОСМИЧЕСКИ ПРИЛОЖЕНИЯ НА 7075 (В95) АЛУМИНИЕВА СПЛАВ

***А. Бузекова-Пенкова, А. Митева***

**Резюме**

В днешно време алуминиевите сплави представляват все по-голям интерес за учените и намират широко приложение в аерокосмическата и свързаните с нея индустрии поради присъщата си лекота, високо съотношение на якост към тегло, отличната топлинна и електрическа проводимост, добра отразяваща способност и ниски експлоатационни разходи. Сред конвенционалните конструктивни материали, използвани за аерокосмически приложения, лидират алуминиевите сплави. Това се дължи на способността на съвременните алуминиеви сплави да постигат уникална комбинация от свойства, чрез легиране и термична обработка, адаптирани към конкретни приложения. Алуминиевата сплав 7075 (В95) е високояка сплав, която работи в екстремни условия и се използва в съвременните конструкции на самолети, космически кораби и сателити.

В този кратък обзор се съсредоточаваме накратко върху някои от съществуващите и перспективни приложения на някои алуминиеви сплави 7xxx, по-специално 7075 (В95) в аерокосмическата промишленост. Разгледани са възможни варианти за продължаване на работата в тази област и са представени някои български разработки.

Bulgarian Academy of Sciences. Space Research and Technology Institute.
Aerospace Research in Bulgaria. 34, 2022, Sofia

DOI: https://doi.org/10.3897/arb.v34.e16

# INVENTOR AND INNOVATIVE WORK AT THE SPACE RESEARCH AND TECHNOLOGY INSTITUTE — BULGARIAN ACADEMY OF SCIENCES

***Georgi Jelev***

*Space Research and Technology Institute — Bulgarian Academy of Sciences*
*e-mail: gjelev@space.bas.bg*

***Keywords:*** *Inventions, Innovations, Space Research and Technology Institute — Bulgarian Academy of Sciences, Patents, Utility models*

***Abstract***

*The current article attempts to present the created inventions at the Space Research and Technology Institute — Bulgarian Academy of Sciences during the last 40 years. In view of this long period of time, there exist patents and awards that were omitted from mentioning.*

*The current paper elaborates on the different types of patent and utility model documents that were issued from Bulgarian Patent Office and other foreign patent offices where Space Research and Technology Institute — Bulgarian Academy of Sciences has registered their inventions. A list of recent awards from local and international forums for inventors has been shown. Mentioned were some of the prominent inventors who worked at the Institute.*

*Finally, the article concludes the need for development of specialized information system to store the patent documents of the Institute and to deliver to the public comfortable means of thorough, detailed and quick inquiries.*

In the National Recovery and Resilience Plan of Republic of Bulgaria [1] two entities are implicitly incentivized: the important role of patent protection of intellectual and industrial properties, and the need for fast transfer of inventions to the industry.

Patent and innovation work is recognized as key activity for the Bulgarian Academy of Sciences (BAS) and one could not with pleasure that gains more and more essential presence in the Institutes of the Academy.

According to a report issued by the Inventor and Innovative Work commission at the BAS's General Assembly, about 67% of all registered inventions in Bulgaria are created in BAS [2]. A motivation supporting the inventor work at BAS is also the funding stimulus for the inventors. The augmentation of the latter has been under consideration lately.


*Fig. 1. Different kinds of our patent protection documents*

The Space Research and Technology Institute at the Bulgarian Academy of Sciences (SRTI-BAS) has long standing traditions and results in the inventor and patent activities. Those are largely incentivized and instigated by the subject and methods of aerospace research and technologies, by the necessity to implement non-standard technological and technical solutions, and last but not the least — by the affinity of our scientists and specialists for innovations. SRTI-BAS occupies one of the leading places in the Academy by the number of patents and utility models. For example, during 2019 the Institute has registered 19 utility models of 27 for the whole Bulgarian Academy of Sciences, while during 2020 — 4 of 19 for BAS [2].

In the course of about 50 years, scientists at the Institute have created more than 100 developments that have received author certificates and patents, as well as over 25 utility model registrations. Besides in Bulgaria, our patents have been registered in USA and Ukraine. Patents authored by scientists from SRTI-BAS have been announced by Bulgarian Patent Office for “Invention of the Month”, and have been nominated for “Invention of the Year”.

Over the years, 5 innovations have been selected for top scientifically applied achievements of SRTI-BAS.

Two inventors from our Institute — Acad. Dimitar Mishev and prof. DSc Garo Mardirossian are winners of the title “Honoured Inventor” and have been written in the “Golden Book” of the Bulgarian discoverers and inventors.

Here we shall mention some of our inventors: Acad. Dimitar Mishev, Acad. Kiril Serafimov, Cor. Mem. Petar Getsov, Prof. Garo Mardirossian, Prof. Zhivko Zhekov, Prof. Yulika Simeonova, Prof. Dimitar Teodosiev, Prof. Boycho Boychev, Prof. Roumen Nedkov, Prof. Georgi Sotirov, Prof. Tsvetan Dachev, Prof. Dimo Zafirov, Prof. Eugenia Roumenina, Prof. Georgi Jelev, Assoc. Prof. Svetoslav Zabunov, Assoc. Prof. Stavri Stavrev, Assoc. Prof. Doyno Petkov, Assoc. Prof. Stefan Chapkanov, Assoc. Prof. Stilian Stoyanov, Assoc. Prof. Stoyan Tanev, Assoc. Prof. Tania Ivanova, Assoc. Prof. Todor Nazarski, Ch. Asst. Prof. Angel Manev, Ch. Asst. Prof. Yuri Matviichuk, Ch. Asst. Prof. Medi Astrukova, Ch. Asst. Prof. Tinka Grozdanova, Ch. Asst. Prof. Rumen Shkevov, etc.

The inventors of the Institute have participated with patents and utility models in a large number of local and international innovation forums in Bulgaria, Belgium, Czech Republic, Hungary, Kuwait, Poland, Portugal, Republic of North Macedonia, Russia, Serbia, Taiwan, etc. High accolades have been received from almost all participations. These include special awards, diplomas, medals, award cups and so on. The following is a part of all participations in national and world forums where the inventors from SRTI-BAS have won bronze, silver and gold medals, diplomas and other distinctions.

- EAST-WEST EURO INTELLECT — EWEI Bulgaria — 1998, 2000, 2001, 2002 and 2003
- Fifth national exhibition “Inventions, Transfer, Innovations” — ITI’2014, 6–8 Nov. 2014, Sofia
- 18th Moscow International Salon of Inventions and Innovative Technologies “ARCHIMEDES”, April 2015, Moscow (Russia) — Silver medal
- “INVENTARIUM SCIENCES” 2015 — FIRST INTERNATIONAL CONGRESS OF INVENTOR’S, INNOVATOR’S AND CREATIVES, PORTUGAL — Lisbon, Parque das Nações, 23–26 April 2015
- 29th International Festival of Innovation, Knowledge and Creation “TESLA FEST”, Oct. 2015, Novi Sad (Serbia) — Diploma and a Gold medal. On this

forum SRTI-BAS received cup GRAND PRIX for overall inventor creativity in 2015.

- 30th International Festival of Innovation, Knowledge and Creation “TESLA FEST”, Oct. 2016, Novi Sad (Serbia) — Diploma and Gold medal.
- 20th Moscow International Salon of Inventions and Innovative Technologies “ARCHIMEDES”, April 2017, Moscow (Russia) — Silver and Bronze medals in the category “Aerospace industry” и “Ground, sea and air transport”, among the presented more than 700 inventions from more than 20 countries.
- XI INTERNATIONAL WARSAW INVENTION SHOW, IWIS 2017, Warsaw, Poland — Gold and Silver medals for inventions in the area of unmanned aerial vehicles.
- Tenth national exhibition “Inventions, Transfer, Innovations” — ITI’2017, 01–03 Nov. 2017, Sofia — Diploma for Gold Plaque.
- “INVENT ARENA” International inventors exhibition, 20–22/June/2018, Třinec/WERK ARENA, Czech Republic — Gold medal for inventions in the area of drones.


*Fig. 2. Some of the innovation and inventor work taking place at the Space Research and Technology Institute — Bulgarian Academy of Sciences. Many patents have won international accolades, while further being scrutinized in scientific articles published in SCOPUS and Web of Science indexed international journals and conferences.*

Some of the areas the Space Research and Technology Institute — Bulgarian Academy of Sciences has it major scientific research and innovative activity are:

- Space apparatuses innovations
- Astrophysics devices innovations
- Radio communications inventions
- Remote sensing means and methods
- Information processing
- Unmanned aerial vehicles innovations

The inventions are often backed with consecutive high rated scientific journals articles, some of which are published in SCOPUS/Web of Science indexed international journals — for such articles from the last 4 years [6–14].

For the purpose of participation in inventions forums and scientific article submission, many of the patented inventions at the Institute were further developed to prototype stage of testing and laboratory experiments. Others have been implemented as final products.

## Conclusions

Due to the ever raising importance of inventions and patents thereof, specifically under the significance of the National Recovery and Resilience Plan of Republic of Bulgaria, the Institute's inventor and innovative activity becomes ever more important. Its demonstration, presentation and encouragement become significant factors influencing positively the scientific, research and development work at the Space Research and Technology Institute. On these ground, the design and development in the immediate future of an information system where visitors and users alike might freely search and read about Institute's innovation and inventor work is highly recommended.

## References


1. National Recovery and Resilience Plan. Council of ministers of the Republic of Bulgaria, 2021. https://www.nextgeneration.bg/upload/58/npvu-15102021.pdf
2. Report of the Invention and Innovation Commission at the General Assembly, Bulgarian Academy of Sciences, Oct. 2021.
3. Space Research and Technology Institute — Bulgarian Academy of Sciences, Patents, http://www.space.bas.bg/bg/about/patents.html
4. Bulgarian Patent Office, e-Services portal, Electronic register, https://portal.bpo.bg/home
5. Bulgarian Academy of Sciences — Patents, http://old.bas.bg/%D0%BF%D0%B0%D1%82%D0%B5%D0%BD%D1%82%D0%B8/
6. Mardirossian, G. Izobretatelskata i patentna deynost na Instituta za kosmicheski izsledvaniya I tehnologii. Spisanie na BAN, Year CXXX, t. 5/2017, pp. 73–74, Prof. Marin Drinov Publishing House of BAS, ISSN 0007-3989 (in Bulgarian).

7. Zabunov, S., G. Mardirossian, R. Miteva, T. Kunchev, R. Pamukoff-Michelson. Internet-of-things Sensor for Ionizing Radiation Inspection in Confined Spaces. *Comptes Rendus de L'Academie Bulgare des Sciences*, vol. 74, iss. 10, 2021, ISSN: 1310–1331 (Print), 2367–5535 (Online), DOI: 10.7546/ CRABS.2021.10.12, pp. 1519–1528.
8. Zabunov, S., G. Mardirossian, R. Miteva, T. Kunchev. Internet of Things 36-rotor Multicopter for Ionizing Radiation Surveying. *International Journal of Aviation, Aeronautics, and Aerospace*, 2021, vol. 8, iss. 2, pp. 1–21, 8, 2, Embry-Riddle Aeronautical University, 2021, ISSN: 2374-6793, DOI: https://doi.org/10.15394/ ijaaa.2021.1585, pp. 1–21.
9. Zabunov, S., G. Mardirossian, K. Strelnitski. Emerald – a 16-rotor multicopter for stereo imaging. *Aircraft Engineering and Aerospace Technology*, 2021, 93(6), pp. 1115–1121, vol. 93, iss. 6, Emerald Publishing Limited, 2021, ISSN: 0002-2667, DOI: https://doi.org/10.1108/AEAT-01-2021-0001, pp. 1115–1121.
10. Zabunov, S., G. Mardirossian. Multistatic passive radar employing magnetic loop antennas. *Comptes Rendus de L'Academie Bulgare des Sciences*, vol. 74, iss. 6, 2021, ISSN: 1310–1331 (Print), 2367–5535 (Online), DOI: 10.7546/ CRABS.2021.06.10, pp. 879–889.
11. Zabunov, S., G. Mardirossian, R. Nedkov. Recent Innovations in Circularly Polarized Antennas for Drone Radio Communication. *Comptes rendus de l'Acad´emie bulgare des Sciences*, vol. 73, iss. 9, 2020, ISSN: 2367–5535, DOI: http://10.7546/ CRABS.2020.09.13, pp. 1286–1290.
12. Zabunov, S., G. Mardirossian. In-flight reconfiguration of lithium-ion cells aimed at extending flight times and range of electrically powered UAVs, *International Journal of Intelligent Unmanned Systems*, vol. 7, iss. 3, 2019, ISSN: 2049-6427, pp. 98–111. DOI: https://www.emeraldinsight.com/doi/abs/10.1108/IJIUS-08-2018-0026
13. Zabunov, S., R. Nedkov. Edge controller – a small UAVs distributed avionics paradigm. *Aircraft Engineering and Aerospace Technology*, vol. 92, iss. 2, 2019, ISSN: 1748-8842, DOI: https://doi.org/10.1108/AEAT-04-2019-0087, pp. 229–236.
14. Zabunov, S., G. Mardirossian. Innovative Dodecacopter Design – Bulgarian Knight. *International Journal of Aviation, Aeronautics*, and Aerospace, vol. 5, iss. 4, 2018, ISSN: 2374-6793, pp. 1–16. DOI: 10.15394/ijaaa.2018.1293,

# ИЗОБРЕТАТЕЛСКАТА И ИНОВАЦИОННА АКТИВНОСТ НА ИНСТИТУТА ЗА КОСМИЧЕСКИ ИЗСЛЕДВАНИЯ ПРИ БЪЛГАРСКА АКАДЕМИЯ НА НАУКИТЕ

***Г. Желев***

**Резюме**

В настоящата статия се прави опит да се представят създадените в Института за космически изследвания и технологии при Българска академия на науките изобретения и иновации от последните около 40 години. Естествено

поради дългия времеви период и големия брой патенти някои от тях не са представени.

В публикацията са илюстрирани различни видове документи за патенти и полезни модели, издавани от Патентно ведомство на Република България, а също така и патенти, регистрирани в чуждестранни патентни ведомства, в които Институтът е участвал. Показан е списък на част от последните награди и грамоти от международни форуми за изобретатели. Споменати са някои от известните изобретатели, които са работили или все още работят в Института.

Накрая в статията се заключава, че съществува нужда от разработване на специализирана информационна система за съхранение на патентните документи на Института и за предоставяне на удобство на обществеността при бърз и изчерпателен достъп до справки относно патентните документи със заявител/притежател Институт за космически изследвания и технологии при Българска академия на науките.

Bulgarian Academy of Sciences. Space Research and Technology Institute.
Aerospace Research in Bulgaria. 34, 2022, Sofia

DOI: https://doi.org/10.3897/arb.v34.e17

# CHALLENGES IN INTERNATIONAL RESEARCH ON CELESTIAL BODIES. THE PROSPECTS OF THE BULGARIAN SPACE POLICY

***Aleksandar Milanov***

*Jindal Global University, India*
*e-mail: amilanov@jgu.edu.in*

***Keywords:*** *Space research, International space cooperation, Space waste, Space politics, Bulgarian space policy*

***Abstract***

*The article explores the present political challenges in international research and exploration of states and private actors of celestial bodies. The lack of shared vision of what type of space activities should be planned and the principles of creating research facilities and scientific missions on the Moon and other celestial bodies is causing uncertainty in future space missions and increases the possibility for a military conflict. The political alliances that exclude specific states will increase the risk of a generation of unnecessary space debris and space waste on celestial bodies. This dangerous outcome could be prevented by agreeing on a shared vision of exploitation and exploration of celestial bodies that preserve the outer space environment and adopting comprehensive guidelines for space activities accepted by the leading space-faring nations.*

## Introduction

The international legal principles of exploration of outer space resources were adopted in the 1960s and culminated as legal norms in the Outer Space Treaty. The primary norm is in article II of the Outer Space Treaty, which foresees that "*outer space is not subject of national appropriation by claim of sovereignty, by means of use or occupation, or by any other means"* [1].

The second relevant international treaty that was supposed to regulate the utilization of the resources on the Moon is in the Moon Agreement. However, the lack of ratifications by leading space-faring nations led to the low status of the treaty and rejection of the legal principles and international institutional mechanisms agreed in it.

Since the 1980s, the preferred way of international regulation of outer space activities has been through soft law documents, which means that the norms are not legally binding. This creates uncertainty and distrust among leading space-faring nations. A recent example of this lack of cooperation and common approach is the adoption of the Artemis Accords with the exclusion of China, withdrawal of

Russia, absence of India and most EU countries. This political rivalry in space activities resulted in a new space race that could potentially lead to a significant conflict that is dangerous for all states and humanity.

### The vision of outer space environment protection

Viikari correctly summarized that the dominating attitude of treating outer space, including celestial bodies, is a mere resource reserve and a dump for the refuse produced by space activities [2]. This attitude is the leading risk concerning polluting celestial bodies, and all space-faring nations share it. The plans to pollute outer space to preserve Earth were clearly expressed by one of the private pioneers in the space industry, the CEO of the space company Blue Origin — Jeff Bezos. Instead of transferring polluting industries in space, states and private actors could transform the industries by introducing holistic economic methods and preserving and being part of the environment. In this case, we could protect both Earth and outer space.

Private companies planning to use celestial bodies for research and tourism activities should be interested in a safe ecosystem and lack of space waste in the long term. The adoption of guidelines on sustainable management and exploration of celestial bodies, which complement the UN Space Debris Mitigation Guidelines, is required before the missions on those celestial bodies are initiated.

### The vision of space research in the Artemis Accords

The Artemis Accords are an essential step for continuing research on the ground and the utilization of material resources on celestial bodies. The Accords are designed as a US-centric form of exploration and exploitation of outer space resources, and this is evident from the NASA official statement about the Artemis program: "*While NASA is leading the Artemis program, international partnerships will play a key role in achieving a sustainable and robust presence on the Moon*" [3]. The fact that the program does not plan to include other leading space-faring nations as equal partners is the stated reason of the representative of the Russian Space Agency to dismiss the program [4]. The format of the accords is not multilateral but instead a collection of several bilateral agreements between NASA and the respective partnering country. The Artemis Accords represent a shift in developing a global space economy [5]. In section 12 of the official document is stipulated a general norm that is relevant to the protection of celestial bodies "*The Signatories commit to limit, to the extent practicable, the generation of new, long-lived harmful debris released through normal operations, break-up in operational or post-mission 7 phases, and accidents and conjunctions, by taking appropriate measures such as the selection of safe flight profiles and operational configurations as well as post-mission disposal of space structures*" [6].

This requirement for limitation "to the extent practicable" does not provide a concrete guideline for the appropriate actions of the operator. The examples of an appropriate measure could serve as a guideline for the treatment of space waste, particularly concerning the disposal of space structures. Additional guidelines are required to cover all aspects of space debris management and waste on celestial bodies. Such a document should include standards and good practices agreed by all space-faring nations and applicable beyond the Artemis Accords themselves.

With respect to following already adopted binding norms in international space law, the Artemis Accords are problematic. NASA confirmed not so much their compliance, but their consideration of the Outer Space Treaty, emphasizing that space resource extraction and utilization "*can and will be under the auspices of the Outer Space Treaty, with specific emphasis on Articles II, VI, and XI*" [7]. The usage of the verb "can" and the phrase "under the auspices" do not provide confidence in NASA's intention to comply with binding international space lawfully. The concretization of only three articles from the treaty is also disturbing for states that are not intending to be part of the Accords regarding the interpretation of the program's intention. Other leading space-faring states that are not part of the Artemis Accords, like China, Russia, and India, have no legal guarantees that the program will not be used in violation of Article IV of the Outer Space Treaty specifically not placing weapons of mass destruction in outer space.

The position of the President of the USA, expressed in Executive order from April 2020 [8], illustrates an understanding of the US government that article II of the Outer Space Treaty permits appropriation of space resources and complete rejection of the Moon Agreement and objection to its capacity to reflect international legal custom [9]. Mosteshar rightly concludes that this is a unilateral attempt to circumvent the Outer Space Treaty and general international law. Even if we accept that the argument that initial bases on the Moon might be in compliance of art. II of the Outer Space Treaty, in time, that national settlement would violate this norm that prohibits national appropriation and occupation on celestial bodies [10]. The norms of Article II of the Outer Space Treaty have been accepted as international legal custom, and they carry the obligations for non-appropriation and non-occupation of the outer space to all states, private organizations and people [11].

Establishing a facility, also named "Moon Base Camp", is also a clear violation of Article II of the Outer Space Treaty, as this is a form of occupation and appropriation of parts of the Moon. The purpose of the rejected Moon Agreement [12] was to avoid such initiatives led by a group of countries competing with other countries. The Russian and Chinese responses to the accords culminated in deeper cooperation between the two states and the formation of a solid Sino-Russian alliance. Both countries initiated the International Lunar Research Station, consisting of a space station in Moon's orbit, a moon base, and mobile rovers and robots on the surface.

Other countries are invited to join this initiative as well. It remains to be seen the attitude of India and most European countries.

### The political strategy of Bulgaria in space research

Bulgaria is a country with severe accomplishments in space research from the 1970s and 1980s. The logical future of space research and national space policy is to be integrated into the European Space Agency as a full member, to participate in the EU Space Program with well-identified research and business capacity to contribute. At the same time, the Bulgarian government could continue its good relationships with Russia and build new relationships with states like India, Japan, China and countries from the Middle East.

A critical red line for the Bulgarian space policy is to be fully compliant with the principles of the Outer Space Treaty, Rescue Agreement, Registration Convention and Liability Convention, which means supporting the Artemis Accords should be avoided.

The Artemis program envisions a fundamentally different approach to utilizing the Moon's resources than the one provided in the Moon Agreement. One of the significant differences is that the Artemis accords are non-binding policy documents implemented by several bilateral agreements [13] between the USA and its partners. In contrast, the Moon Agreement foresees a unique multilateral mechanism and the establishment of an international regime with appropriate procedures [14]. The last aims to achieve equitable sharing by all state parties in the benefits from these resources [15]. Another significant difference of the principles of usage of the resources of the Moon in both documents is that the Moon Agreement considers the interest of the present and future generations, whereas the Artemis Accords do not have such an obligation. The common heritage of mankind principle which is stipulated in the art. 11 of the Moon Agreement, usually foresees the establishment of an international legal regime that considers humankind's interests and considers the interests of all nations [16]. The participation of Australia in both the Artemis Accords and the Moon Agreement brings a lot of controversial issues [17] and ambivalence that ultimately probably will result in Australia withdrawing from the Moon Agreement. Such an act would signify the further deterioration of international space law because of preferences of states to participate in alliances that compete with others instead of participation in mechanisms that legitimize equitable ways of distribution of resources.

The Artemis accords validate the transfer of competition and rivalry of mundane national relations in outer space instead of setting a new global venture which is formed based on the common heritage of mankind principle.

The existence of at least two parallel programs with different participating organizations will result in dispersing all nations' financial, technological, scientific, and human resources into similar activities. This situation would lead to the creation of at least two times more space debris in the Moon's orbit and on the Moon's surface. The risk of accidental collision of assets of either programs or even military conflict on the Moon would result to even more generation of space waste on the celestial surface, and this status quo would lower the safety of both space programs.

## Conclusion

The planning of future missions to the Moon and later to Mars and other celestial bodies should be conducted by states on the principles of global cooperation and inclusiveness instead of the present competition and exclusion of rival states. The adoption of comprehensive guidelines for utilization and scientific exploration on celestial bodies should clarify what type of pollution is legally allowed because of the current development of technologies and what type of pollution should be considered legally as legally banned. The most significant step that should be made to achieve transparency and compliance with international legal norms and soft law guidelines is for states to rebuild their level of trust and strengthen international cooperation by including all relevant stakeholders in the process.

## References


1. Treaty on Principles Governing the Activities of States in the Exploration and Use of Outer Space, including the Moon and Other Celestial Bodies, Article II, 1967.
2. Viikari, L. The environmental element in space law. Martinus Nijhoff, 2008, 14 p. https://www.nasa.gov/specials/artemis-accords/index.html Last access 21.01.
3. https://www.space.com/russia-space-agency-chief-criticizes-nasa-moon-plans, Last access 21.01.2022.
4. Onwudiwe, M., K. Newton. Africa and the Artemis Accords: A Review of Space Regulations and Strategy for African Capacity Building in the New Space Economy. *New Space 9*, no. 1, 2021, 42 p.
5. The Artemis Accords, section 12, pp. 6–7.
6. https://www.nasa.gov/specials/artemis-accords/index.html Last access 21.01. 2022
7. Exec. Order No. 13,914, 85 Fed. Reg. 20, 381 (Apr. 6, 2020).
8. Mosteshar, S. Artemis: The Discordant Accords. *J. Space L.* 44, 2020, pp. 596–597.
9. Salmeri, A. Developing and Managing Moon and Mars Settlements in Accordance with International Space Law. *In Proceedings of the 71st International Astronautical Congress 2020*. International Astronautical Federation, 2020, 4 p.
10. Vylegzhanin, A. N., M. R. Yuzbashyan, M. A. Alekseev. International legal prospects for the use of the natural resources of the Moon and other celestial bodies. 2021.
11. The Agreement Governing the Activities of States on the Moon and Other Celestial Bodies, Resolution 34/68 Adopted by the General Assembly. 89th plenary meeting; 5 December 1979.

12. Tronchetti, F., H. Liu. Australia's signing of the Artemis Accords: a positive development or a controversial choice? Australian Journal of International Affairs 75, no. 3 (2021), 244 p.
13. Art.11 par.5 from the Moon Agreement, 1979.
14. Art 11 par.7 d) from the Moon Agreement, 1979.
15. Hobe, S. Common Heritage of Mankind – An Outdated Concept in International Space Law? Paper Presented at the 41st Colloquium on the Law of Outer Space of the International Institute of Space Law, Bremen, September, 1998, pp. 271–277.
16. Tronchetti, F., H. Liu. Australia's signing of the Artemis Accords: a positive development or a controversial choice? Australian Journal of International Affairs 75, no. 3 (2021), pp. 246–249.

## ПРЕДИЗВИКАТЕЛСТВА НА МЕЖДУНАРОДНИТЕ ИЗСЛЕДВАНИЯ НА НЕБЕСНИ ТЕЛА. ПЕРСПЕКТИВИ НА БЪЛГАРСКАТА КОСМИЧЕСКА ПОЛИТИКА

***Ал. Миланов***

**Резюме**

В статията се анализират настоящите политически предизвикателства в международните изследвания на небесните тела от държави и частни космически компании. Липсата на споделена визия за това какъв тип космически дейности трябва да се планират и принципите за създаване на изследователски съоръжения и научни мисии на Луната и други небесни тела причинява несигурност в бъдещите космически мисии и увеличава възможността за военни конфликти. Политическите съюзи, които изключват отделни държави, ще увеличават риска от генериране на ненужни космически отпадъци върху небесните тела. Този опасен резултат може да бъде предотвратен чрез съгласуване на споделена визия за експлоатация и изследване на небесните тела, които запазват космическата среда, и приемане на изчерпателни насоки за космически дейности, приети от водещите космически нации.